THE MÖSSBAUER EFFECT OF IRON-57 IN SOME MAGNETIC OXIDES

by

J.M.D.Coey

A thesis submitted to the Faculty of Graduate Studies of the University of Manitoba in partial fulfilment of the requirements for the degree of Doctor of Philosophy.

Winnipeg: 16.vi.1971.

THE UNIVERSITY OF MANITOBA

PARTMENT OF PHYSICS WINNIPEG, CANADA

June 14, 1971.

Dr. B. G. Hogg,
Acting Dean,
Faculty of Graduate Studies,
The University of Manitoba,
Winnipeg, Canada.

Dear Dr. Hogg:

I enclose my comments on the thesis submitted by Mr. J.M.D. Coey. I hope this is satisfactory to you and conforms to what you ~~hoped~~ asked me to do in your letter of June 9.

Yours faithfully,

E. W. GORTER.

EWG/lmj

General Opinion

I have read Mr. Coey's thesis with interest. It is my opinion that it is a beautiful piece of work, for which he fully deserves to be granted a Ph.D. Mr. Coey seems not to shun hard work, nor intricate experimental work, nor difficult theory, nor even having original ideas, a combination that is very rare indeed. Experience taught me that people who combine these usually make a brilliant career in scientific research.

Presentation

The thesis is written in good English and the quotations at the head of each chapter show a healthy modesty and sense of humour. It is not for a Dutchman to judge how many of the omitted hyphens, intolerable to the -- intolerant -- European eye, are tolerated in Canadian English.

A very good point is that Mr. Coey often after telling what he is doing, either experimentally or theoretically, then explains why he is doing it, a didactic procedure that helps to make things clear to the reader. This in my experience is also rare in most young research workers.

Contents

All objections I had regarding the contents of the thesis while reading it appeared to have been mentioned and discussed by Mr. Coey himself in his last chapter.

He is fully aware of the fact and agrees with me that the random distribution of Fe^{3+} and Rh^{3+} in the solid solutions of the oxides on which he says his conclusions hinge, is a very hard thing to prove and that the degree of disorder may depend on the method of preparation. Nevertheless, he needs this assumption only to be able to calculate the Mössbauer pattern without and with some long-range order, the fact that there is at least a qualitative agreement between the calculated Mössbauer spectra and those determined might well be aduced as a certain measure of proof that this assumption is justified.

In those parts of the subject with which I feel truly familiar I have not found one omission of a relevant literature reference, nor for that matter the mention of irrelevant ones.

Coey is obviously a very gifted physicist, and his knowledge of chemistry seems to me above average, as it should be for a scientist working in the Mössbauer effect. There are small flaws in the presentation, due to the fact that a physicist will always be a physicist, are found in the chemical subjects.

P 41. Line 8 from below.

Coey uses his own -- or another physicist's -- nomenclature for the Fe^{3+} sites in $SrFe_{12}O_{19}$; the use of the internationally accepted names of lattice sites as given in the International Tables of Crystallography--- makes the sites recognisable for a wider circle of readers.

P. 77a.

The percentage of Rh calculated for Pure Rh_2O_3 is not given for comparison.

In some respects the Rh_2O_3 could be called a very dirty material. The quantities of impurities might appreciably affect other properties, like the magnetic phase boundaries of fig. 35, p. 88; a reason why Coey calls it pure for his purpose is not given, although in an oral discussion he was very well able to tell me why.

P. 44.

He does not tell what material he uses for cutting out and weighing, a common ommission. Some materials absorb a variable quantity of water dependent on the atmospheric humidity, (paper), others are manufactured in sheets of variable thickness.

P. 79.

An R-factor of 13.4% for powder diagrams is nowadays not called reasonable unless reasons are given why in this

P. 79 (continued)

special case it is. In the present case these reasons may be readily produced.

P. 83

NaOH was chosen despite possible Na^+ impurity because, as Mr. Coey told me, $(CH_3)_4NOH$ was tried and did not give the desired product. This should have been mentioned.

P. 169

The use of super-pure raw materials is justified only if reason can be given why a larger amount of impurity than present in the raw material was not introduced during grinding, pressing and further processing, or if a spectrochemical analysis of the product can show this.

P. 177

No reference is given for the origin of the ε-Fe_2O_3 mentioned, which as far as I remember is not a very well-defined material.

to Anna

Preface

Physicians shouldn't say, "I have cured this man", but, "This man didn't die under my care". In physics too, instead of saying, "I have explained such and such a phenomenon", one might say, "I have determined causes for it, the absurdity of which cannot be conclusively proved." - *G. C. Lichtenberg.*

In many ways, magnetism is one of the most attractive departments of physics. It is an experimental science, and, in common with most other aspects of the study of the solid state, it is possible for the experimentalist to plan and perform his own experiments without the need for extremely complex equipment, or the help of teams of technical assistants. The electronic and cryogenic apparatus required is just the modern equivalent of Gilbert's 'terella', the device used in the first modern study of the magnetism of the Earth.

However, like any science, magnetism is learnt by apprenticeship. The greater part of the credit for having understood something of the physical world must invariably be given to one's fellow-physicists who have been willing to discuss, encourage, argue, explain and otherwise prepare one to contribute to the heap of knowledge which is continually

being consolidated into principles and compendia for use in the outside world. The two extremities of theory and application are not so far removed from the middle ground occupied by the experimental student of magnetic oxides as to be quite inaccessible. The electronic devices which surround him use ferrites, the study of which started barely a generation ago. In the opposite direction, the theoretical accounts of the causes of the physical phenomena are not all so esoteric that it is impossible for the experimentalist to appreciate their lack of absurdity. In a way, these two extremes are coupled in the laboratory in the chemical pleasure of searching the periodic table for the right compound to elucidate some physical effect.

The main theme of the work reported in this thesis is the characterization and explanation of the Mössbauer spectra of magnetically-ordered iron oxides in which the iron is replaced, to some degree, by a non-magnetic substitution. The application of static molecular field theory to a randomly occupied cubic lattice is the subject of most of chapter III. This is preceeded by a rather sketchy introduction to the Mössbauer Effect, and transition metal oxides, and a chapter on apparatus and techniques, with some experimental illustrations. Then the Mössbauer spectra of $(Fe_{1-x}Rh_x)_2O_3$ are described, and explanations are

suggested for the behaviour of the hyperfine interaction parameters in the region where the static theory is valid. In chapter VI, the spectra of several other compounds are discussed. They are taken just below the magnetic ordering temperature, a region where relaxation effects may be important. Chapter V is devoted to an investigation of the influence of magnetic order on the total spectrum shift of $(Fe_{1-x}Rh_x)_2O_3$ and $HoFeO_3$. Finally, the last chapter summarises the more important findings.

I am grateful to my supervisor, Professor A. H. Morrish for the support and encouragement which has contributed substantially to the success of this work. I collaborated with Dr. G. A. Sawatzky during the first year of my work in Winnipeg, and benefitted greatly from both this, and the subsequent correspondence. It was he who initiated me into the practical, intellectual and social aspects of research in magnetism. Some of the calculations reported in Chapter IV were performed by him. Thanks are also due to Dr. I. Dezsi, who gave me the ferrous perchlorate crystals, and with whom I have also corresponded. I am grateful to other graduate students and staff members at the University of Manitoba for innumerable discussions and far-ranging help. In particular I wish to mention Dr. R. B. Ferguson, Dr. D. C. Price, Dr. C. W. Searle and

Mr. M. R. Spender. Thanks are also due to the machine and electronics shops for their patience and skill. The excellent typing was done by Mrs. M. West.

I have received financial support during the past three years from both the University of Manitoba and the National Research Council of Canada.

Finally, I must acknowledge my friends who have encouraged, inspired or tolerated my metamorphosis into a professional scientist, and accepted the results of the inevitable specialization of interests.

Contents

Abstract

Experimental and theoretical studies of pure and diamagnetically-substituted iron oxides are presented.

Experimentally, the spectra of the diamagnetically-substituted compounds are found to be of three types. At high temperatures there is a normal paramagnetic spectrum. In the vicinity of the magnetic ordering temperature, mixed spectra appear, with the paramagnetic pattern superimposed on a broad magnetically-split spectrum. At lower temperatures, only the magnetically-split pattern remains, but some line-broadening persists, even at the lowest temperatures. The systems studied were $(Fe_{1-x}Rh_x)_2O_3$, $Y_3(Fe_{1-x}Sc_x)_2[Fe]_3O_{12}$ and $Y_3(Fe)_2[Fe_{1-x}Ga_x]_3O_{12}$.

The randomly-occupied cubic lattice was studied with various concentrations of vacancies, x. For $x \lesssim 0.6$, almost all the occupied sites are connected by nearest-neighbour paths, whereas when $x \gtrsim 0.7$ there are small, isolated clusters. A local molecular-field theory was developed to take account of the range of magnetic environments which an ion may have. The theory gives a linear decrease of ordering-temperature with x, in agreement with observation, and also different magnetization curves for ions with different numbers of magnetic nearest-neighbours. It predicts Mössbauer spectra similar to those observed in the low-temperature region, provided that the range of environments for the neighbours of a particular ion is allowed for, and a small, long-range interaction is included to align ions, at the lowest temperatures, which have no magnetic nearest-neighbours.

The structure of αRh_2O_3 was refined by powder methods. It has the same structure as αFe_2O_3, with $a_H = 5.127 \pm 0.001$Å, $c_H = 13.853 \pm 0.004$Å, $x(O) = 0.295 \pm 0.010$ and $z\ (Rh) = 0.348 \pm 0.001$.

The spectra of magnetically-ordered members of the $(Fe_{1-x}Rh_x)_2O_3$ system were analysed on the basis of the distribution of nearest-neighbour environments for an iron ion. Values of the exchange constants J_3 and J_4 were deduced from the local molecular-field theory. They are $-11.0 \pm 1.0^{\circ}K$ and $-15.3 \pm 1.0^{\circ}K$. All the rest of the exchange interactions amount to $-39.1^{\circ}K$. A supertransferred hyperfine field of 7.8 kOe / nearest-neighbour is found from the spectra taken at $20^{\circ}K$, and a covalency parameter $A_{\sigma} = 0.10$ is inferred. It is deduced that the Fe - O bond in αFe_2O_3 is 80% ionic, and the 3d spin of the ferric ion is 2.32. The hyperfine field for a free Fe^{3+} ion is calculated to be 620 kOe, and its isomer shift would be 1.35 mm/s relative to chromium.

The quadrupole coupling and isomer shift, calculated by including overlap distortion of the iron orbitals by the ligand, are in agreement with much of the data for the system, provided that the oxygen parameter varies linearly with x. An abrupt change of 0.2 mm/s in the quadrupole interaction and 0.25 mm/s in the total spectrum shift, with the onset of magnetic order, may be due to a change in the iron parameter at the Néel point T_N.

The temperature dependence of the total spectrum shift was measured in $HoFeO_3$ in the range $99-875^{\circ}K$. No discontinuity is found at T_N, but there is a different temperature-dependence above and below the ordering temperature, which may be explained on the basis of a magnetization-dependent Debye model. An explanation based on a supertransferred process is also considered.

The spectra of the diamagnetically-substituted oxides in the mixed region were studied in large applied magnetic fields. The central peaks are not due to independent paramagentic ions, but rather to ions magnetically coupled in small clusters, whose net moment has a relaxation time of the order 10^{-7} sec. The spectra are analogous to those found for superparamagnetic γFe_2O_3. Central peaks observed in pure $YFeO_3$ were found to be influenced by the atmosphere used during firing.

The quadrupole interaction in $Fe(ClO_4)_2.6H_2O$ changes sign at the transition at 240°K. The spectra at different temperatures in an applied field also show the effect of the polarization of the paramagnetic ferrous ion on the effective field at the nucleus. A hyperfine field of 250 kOe is predicted for the ordered state.

The furnace used for the high-field Mössbauer experiments is described, and the resolution of all five subspectra in $SrFe_{12}O_{19}$ is mentioned as an illustration of its use. An applied field was also used to uncover at separate spectrum for Fe^{3+} on the B-sites of non-stoichiometric magnetite. Its intensity may be accounted for on a pair-localized hopping model, or by assuming that each B-site vacancy traps five Fe^{3+} ions.

MADE IN CANADA 1971

I Introduction

Brevis esse laboro, obscurus fio. - Horace.

1. THE MÖSSBAUER EFFECT.

R. L. Mössbauer [1] discovered that an ^{191}Ir nucleus, when bound in a crystal, can decay to its ground state by emitting a γ-ray with a finite probability of exciting no phonons in the process, the recoil momentum being taken up by the whole lattice. It has been possible to use these photons, whose energy is defined, in one instance, to better than one part in 10^{15}, to study the hyperfine interactions and lattice dynamics of a nucleus in a crystal. Most of the applications of the effect have been in the realm of solid state physics, the nucleus acting as a probe to sample the charge density, electric field gradient and magnetic field at its site. However, if these measurements are to be absolute, it is necessary to know the nuclear radius, quadrupole, and magnetic moments in both the excited and ground states. The spin can usually be deduced from the number of lines in the spectrum itself, but values of the others depend mainly on the accuracy of calculations of the charge density and field gradient in particular crystals, which are not very reliable.

Rather stringent conditions must be satisfied if an isotope is to exhibit the Mössbauer effect, which effectively eliminate all but about 70 isotopes of 40 elements in the periodic table. Of these, all but a handful require an extreme experimental situation. The recoilless fraction, f, is given by

$$f = \exp[-E_\gamma^2 \langle x^2 \rangle / \hbar^2 c^2] \tag{1.1}$$

where E_γ is energy of the gamma decay and $\langle x^2 \rangle$ is the component of the mean square vibrational amplitude of the emitting nucleus in γ-ray direction. It is obvious from this equation that there will be a detectable value of f only if E_γ^2 and $\langle x^2 \rangle$ are not too large. In practice E_γ must be less than 150 keV, and only if it is less than 50 keV can the experiments be performed without cooling the source, to reduce $\langle x^2 \rangle$. Furthermore the effect is essentially restricted to solids, because in fluids $\langle x^2 \rangle$ is indeterminate. It is also necessary that the recoil energy of the particle, of mass M_p, in which the nucleus is bound does not exceed the natural linewidth. Since

$$E_R = E_\gamma^2 / 2M_p c^2, \tag{1.2}$$

the crystallites must typically contain at least 10^4-10^7 atoms. Also the half-life of the excited state should be such that the natural linewidth is about an order of magnitude less than the hyperfine interactions, and finally, the internal conversion must be small so

that the decay is manifest as a photon, and not an electron.

The transition which satisfies these conditions best is the 14.41 keV $\frac{3}{2} \rightarrow \frac{1}{2}$ decay in ^{57}Fe, although ^{119}Sn, ^{121}Sb, ^{125}Te, ^{151}Eu, ^{161}Dy, ^{166}Er and ^{197}Au also have quite suitable transitions. More than half the published work has been on ^{57}Fe, which has an abundance of 2.17% in natural iron and the decay scheme shown in figure 1. Some important parameters are listed in the figure,

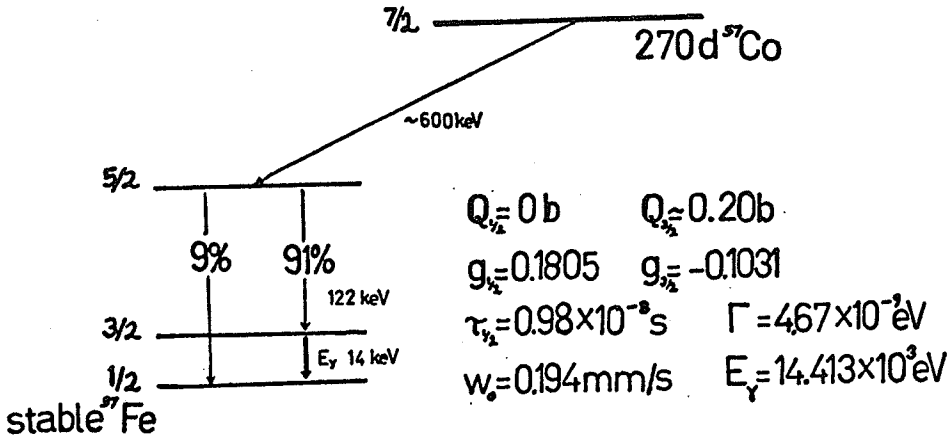

Figure 1. The decay scheme of ^{57}Co, showing the 14 keV Mössbauer transition, and parameters for the I = 3/2 and I = 1/2 nuclear states.

including the nuclear g-factors and the quadrupole moments of the excited and ground states. The natural linewidth, Γ, of the emitted photon is determined by the natural lifetime, $\tau_{1/2}$ of the excited state, and a Lorentzian lineshape,

$$I(E) = I(E_\gamma)[(2(E-E_\gamma)/\Gamma)^2 + 1]^{-1}, \qquad (1.3)$$

is expected. In a spectrum, the emission lineshape of the source is

folded with the absorption lineshape of the absorber so that the minimum possible width for an absorption line is 2Γ. Usually an unsplit single line source is used, and the sample to be studied forms the absorber. $w_0 (= 2\Gamma)$ is expressed in mm/s in figure 1, the conventional Mössbauer energy units. They arise because the hyperfine splitting of the nuclear levels is of the order of 10^{-7}eV, and the energy of the source can easily be modulated by this amount by giving it a small velocity relative to the sample. Then ΔE, the Doppler shift in its energy, is given by

$$\Delta E/E_\gamma = v/c \, . \tag{1.4}$$

v is the velocity of the source in the direction of the γ-rays. 1 mm/s corresponds to 4.804×10^{-7}eV for ^{57}Fe.

2. HYPERFINE INTERACTIONS.

The electromagnetic interaction of a nucleus with the electric and magnetic fields at its site produced by its surroundings is expressed by the following Hamiltonian

$$\mathcal{H}(I) = g_I \mu_N \vec{I}.\vec{H}_{hf} + \vec{Q}_I.\nabla\varepsilon + \frac{2\pi}{5} ZeR_I^2 e\psi^2(0) \tag{1.5}$$

The terms represent the interaction of the nuclear magnetic dipole moment with the hyperfine field, the interaction of the nuclear electric quadrupole moment with the electric field gradient, and the interaction of the nuclear charge with the electronic charge

density due to the finite nuclear radius. Higher order interactions are negligible, and the terms are in order of decreasing magnitude for a magnetically ordered crystal. The eigenvalues of $\mathcal{H}(I)$ are the energy levels of the nucleus in the crystal which derive from the I-level of the bare nucleus. The third term is not quantized, and gives the energy levels a slight isomer shift, δ_i. The total shift of the centre of the spectrum is considered in detail in chapter V.

It should be remarked that if the nucleus, in its excited state, is to respond to a field, the field must remain constant for periods of at least $\tau_{1/2}$. Any component which fluctuates more rapidly will be averaged over the lifetime. Another condition, which is weaker where ^{57}Fe is concerned, is that the fluctuation time of the hyperfine field τ_H must be longer than the Larmor precession time. However the Zeeman splitting is only significant if it is greater than the natural linewidth, so that the condition for well resolved magnetic hyperfine splitting is

$$\tau_H > \tau_{1/2} > \tau_L \qquad (1.6)$$

We will now consider each of the first two terms in (1.5) in the limit in which the other is negligible, and then give a solution which is appropriate when $g\mu_N \vec{I}.\vec{H}_{hf} > \vec{Q}.\nabla\varepsilon$. More general solutions have been worked out [2], but we have no need of them here.

2.1 Magnetic Hyperfine Interaction.

There are four contributions to H_{hf}, some of which vanish in special circumstances. The orders of magnitude cited apply to the 3d transition metals. i) The local field, uniform throughout a domain, is the sum of the applied, demagnetizing and Lorentz fields. The latter two exactly cancel for spherical, single-domain particles. This part of the field is written as

$$H_\ell = H_{ap} - DM_b + \frac{4\pi}{3} M_d \qquad (1.7)$$

M_b and M_d are the bulk and domain magnetizations. H_ℓ may be several kiloersteds. ii) The electronic orbital contribution is of order 10^4Oe if the orbital angular momentum is completely quenched by the crystal field. It is zero for S-state ions, for which $L = 0$. iii) The dipolar field produced by the moments on surrounding atoms is also about 10^4Oe, except if the surroundings have perfect cubic symmetry when it is zero. There is also a dipolar field from the nucleus' own electrons. iv) The Fermi contact interaction is the direct interaction between the nuclear moment and the s-electrons, which are the only ones with an appreciable density at the nucleus. It may be represented by a delta function term in the one-electron Hamiltonian including ii), iii) and iv)

$$\mathcal{H}_1 = -gg_I\mu_B\mu_N \left\{ \frac{\vec{L}.\vec{I}}{r^3} + 3\,\frac{(\vec{S}.\vec{r})(\vec{I}.\vec{r})}{r^5} - \frac{\vec{S}.\vec{I}}{r^3} + \frac{8\pi}{3}\,\delta(r)\vec{S}.\vec{I} \right\} \qquad (1.8)$$

The contact interaction would be zero for all ions, except those with half-filled s-shells, if many-electron effects could be neglected. In fact very large hyperfine fields, in the range 10^5-10^6 Oe do occur in ions with no unpaired s-electrons, and in iron metal and high-spin iron ions the hyperfine field is directed oppositely to the electronic moment [3]. The core polarization mechanism for a $3d^n$ ion is shown schematically in figure 2. The partly filled d-shell with spin S lies outside the 1s and 2s shells, but just inside the 3s shell. The exchange between the 3d↑ and ns electrons causes the s-orbitals to be spin-polarized, with an excess

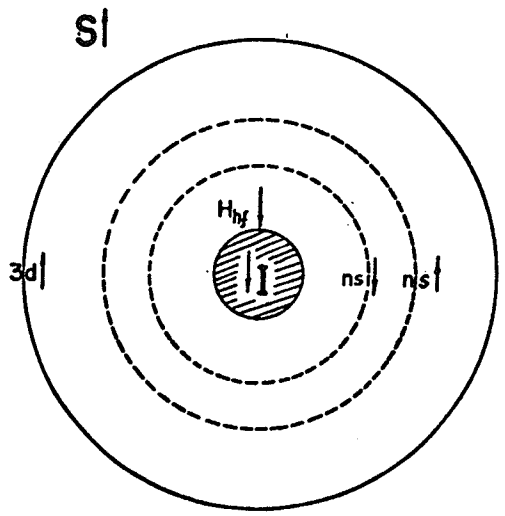

Figure 2. Schematic representation of the core polarization which produces the hyperfine field in a 3d ion.

of ↓ spin at the nucleus. Extensive calculations by Watson and Freeman [4, 90] using the unrestricted Hartree-Fock approach are capable of giving the correct sign, and roughly the right magnitude of the contact field in a free ion. A representative example of

Table 1. Contributions to the Contact Field in an Fe^{3+} Free-Ion.

Shell	Magnetic Field	Difference	Total
		kOe	
1s↑	2845159	-50	
1s↓	2845208		
2s↑	260336	-1792	-632
2s↓	262128		
3s↑	37235	+1210	
3s↓	36025		

their calculations, for Fe^{3+}, is given in table 1. Note that small differences of large numbers must be taken to find the net contact field.

The Zeeman splitting of the 3/2 and 1/2 nuclear levels of ^{57}Fe by the hyperfine field is shown in figure 3a. Only $\Delta m_I = 0, \pm 1$ transitions are permitted, and their angular dependence is given in table 2a. The total intensities are integrated over all possible angles, θ, between the field axis and the γ-ray direction and they are appropriate for randomly oriented polycrystalline absorbers which give a symmetrical six-line spectrum with an intensity ratio 3:2:1:1:2:3. Another common situation is a polycrystalline absorber in an external field, sufficiently strong to saturate the material, which is applied parallel to the γ-ray direction so that $\theta = 0$. In this case, only $\Delta m_I = \pm 1$ transitions are allowed, and a four-line spectrum with an intensity ratio 3:1:1:3 results.

Table 2. *Relative Intensities and Angular Dependence of Allowed Transitions.*

a) *Pure Magnetic Splitting*

Transition	m	Relative Intensity	Angular Dependence
$\frac{3}{2} \rightarrow \frac{1}{2}$	-1	3	$\frac{9}{4}(1 + \cos^2\theta)$
$-\frac{3}{2} \rightarrow -\frac{1}{2}$	+1		
$\frac{1}{2} \rightarrow \frac{1}{2}$	0	2	$3 \sin^2\theta$
$-\frac{1}{2} \rightarrow -\frac{1}{2}$			
$-\frac{1}{2} \rightarrow \frac{1}{2}$	+1	1	$\frac{3}{4}(1 + \cos^2\theta)$
$\frac{1}{2} \rightarrow -\frac{1}{2}$	-1		

b) *Pure Quadrupole Splitting*

$\pm\frac{3}{2} \rightarrow \pm\frac{1}{2}$	±1	1	$\frac{3}{2}(1 + \cos^2\theta)$
$\pm\frac{1}{2} \rightarrow \pm\frac{1}{2}$	0	1	$1 + \frac{3}{2}\sin^2\theta$

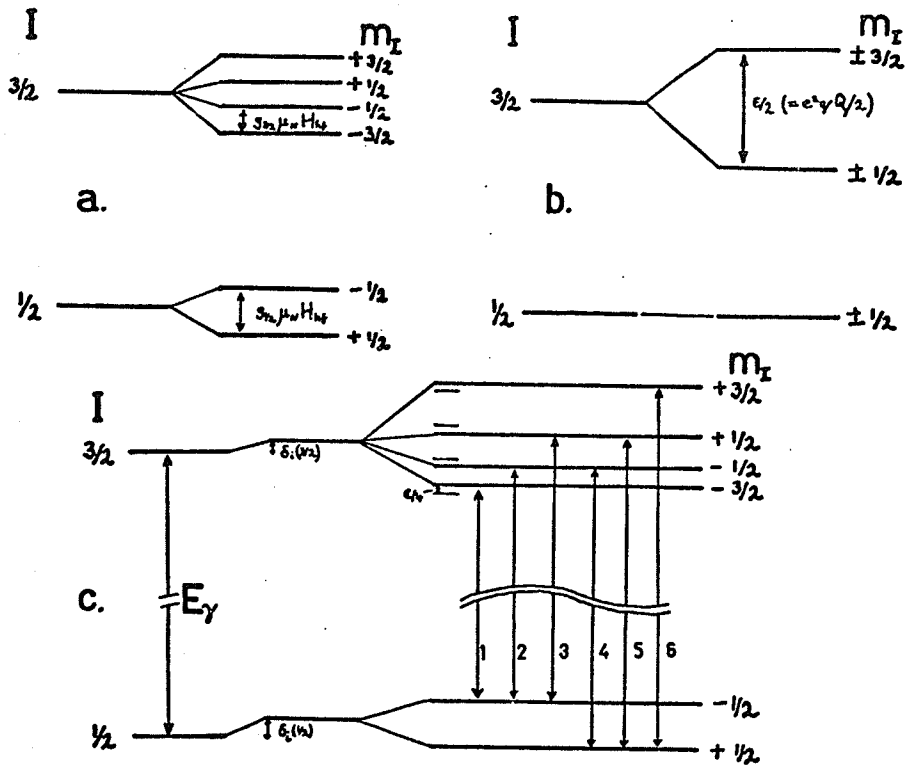

Figure 3. a) *Magnetic Zeeman splitting of the two lowest states of* ^{57}Fe *in a magnetic field.* b) *Electric quadrupole splitting of the same states of* ^{57}Fe *in an inhomogeneous electric field.* c) *Splitting of the states by both electric and magnetic hyperfine interactions, according to (1.12). The vertical scale is greatly distorted because the separation of the two states is about ten orders of magnitude greater than their splitting.*

It is usually found that the hyperfine field in a magnetic insulator has the same temperature dependence as the ionic moment [5]. This shows that the fluctuations of the ionic spin between the different m_S levels is rapid compared to τ_L. The same is usually true of paramagnetic materials as well, and consequently no hyperfine splitting is observable for them. Nevertheless, a few paramagnetic compounds containing S-state ions diluted in a diamagnetic host have been reported to show hyperfine patterns, one corresponding to each m_S state, when the spin-spin and spin-lattice relaxation times exceed $\tau_{1/2}$ [6]. In these circumstances S and I are coupled, and the nuclear levels are characterised by m_F. The effect of relaxation processes on Mössbauer spectra has been treated by several workers [7-12] and is discussed further in chapter VI.

2.2 Electric Hyperfine Interactions.

The electric quadrupole interaction is represented by the term $\vec{Q}.\nabla\varepsilon$ in (1.5). It is usually this term which lifts some of the $(2I+1)$ fold degeneracy of the nuclear levels, and defines the axis of quantization in the paramagnetic region. The electric field gradient is actually a 3×3 tensor which can be reduced to diagonal form by an orthogonal transformation of the co-ordinates. The three diagonal terms, $\partial^2 V/\partial x_i \partial x_i$, are abbreviated to V_{xx}, V_{yy} and V_{zz} (= eq') with the convention $|V_{zz}| > |V_{xx}| \geq |V_{yy}|$. At the nucleus, only s-electrons and relativistic $p_{1/2}$ electrons

whose small components are s-like [13], have a finite charge density. However none of them contribute to the field gradient, on account of their spherical symmetry. There are no other free charges at the nucleus, so Laplace's equation, $\nabla^2 V = 0$, restricts the number of independent components in the field gradient to two, taken to be V_{zz} or q' and an asymmetry parameter $\eta = (V_{xx} - V_{yy})/V_{zz}$ which lies between 0 and 1, and is zero for an axially symmetric gradient.

There are two distinct contributions to $\nabla\varepsilon$. i) The nucleus' own electrons produce a field gradient if they are in aspherical orbits, for example the sixth d-electron in high-spin Fe^{2+}. There can also be a significant contribution from overlap distortion of 2p and 3p orbitals by the ligands [14].
ii) The changes in the rest of the crystal may also produce a field gradient unless the surroundings of the nucleus have cubic symmetry. A quadrupole interaction has recently been reported in metallic iron [15] and it might be evidence of a distortion from cubic symmetry, since it is known that a ferromagnetic material cannot be precisely cubic [16]. The electric field gradient, provided it is axially symmetric, may be written in the form

$$q = q_v(1-R_v) + q_{ov}(1-R_{ov}) + q_\ell(1-\gamma_\infty) \qquad (1.9)$$

The factors R_v, R_{ov} and γ_∞ are shielding factors, discussed by Stemheimer [17], which take account of the modification of the electric field gradient by the nucleus' own electrons. For Fe^{3+},

the lattice contribution is greatly enhanced, but the ionic contributions are slightly shielded. $\gamma_\infty = -0.14$ and $R_v = 0.32$.

It turns out that the quadrupole Hamiltonian may be written as

$$\vec{Q}.\nabla\varepsilon = \frac{e^2q'Q}{4I(2I-1)}\left[3I_z^2 - I(I+1) + \frac{1}{2}\eta(I_+^2+I_-^2)\right] \qquad (1.10)$$

Q is zero for the $I = 1/2$ ground state of Fe^{57}, but the excited state is split into two substates with $M_I = \pm 3/2$ and $\pm 1/2$, which are separated by $\varepsilon/2$ where

$$\varepsilon = e^2qQ = e^2q'Q\sqrt{1 + \eta^2/3} \qquad (1.11)$$

The quadrupole splitting of the nuclear levels is shown in figure 3b, and the relative intensities of the transitions and their angular dependences are given in table 2b. θ' is the angle between the principal axis of the field gradient and the γ-ray direction. All the expressions for the relative intensities of transitions in Table 2 must be multiplied by the recoil free fraction, and the angular dependence will be modified if $f(\theta)$ should be anisotropic. For a polycrystalline absorber, the observed quadrupole spectrum is frequently a symmetric doublet from which it is impossible either to deduce the sign of the interaction, or to estimate V_{zz} and η independently. However it is possible to determine these if single crystals [18] or applied magnetic fields [19] are used.

Analytical solutions of the full Hamiltonian (1.5) cannot generally be found, but in the case where $\vec{Q}.\nabla\varepsilon << g\mu_N\vec{I}.\vec{H}_{hf}$, $\eta = 0$, and the principal axis of the field gradient makes an angle ϕ with with the magnetic hyperfine field, there is the following solution;

$$E(3/2) = g_{3/2}\mu_N H_{hf} m_I + (-1)^{|m_I+1/2|}\frac{e^2qQ}{4}\left[\frac{3\cos^2\phi-1}{2}\right] + \frac{2\pi}{5}ZeR^2_{3/2}e\psi^2(0),$$

$$E(1/2) = g_{1/2}\mu_N H_{hf} m_I + \frac{2\pi}{5}ZeR^2_{1/2}e\psi^2(0) \qquad (1.12)$$

These energy levels are shown in figure 3c), and the information in table 2a) applies to transitions between them. A typical Mössbauer absorption spectrum, for αFe_2O_3, is shown in figure 4. Lorentzian dips at the six allowed energies are superposed on a background which may have a slight linear or parabolic slope due to instrumental effects.

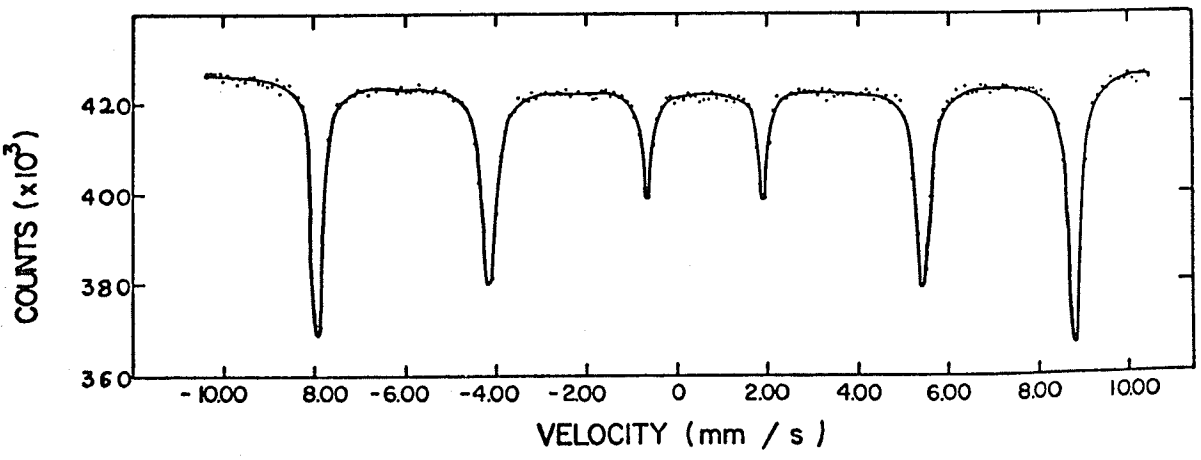

Figure 4. The Mössbauer absorption spectrum of αFe_2O_3.

3. TRANSITION METAL OXIDES.

3.1 Electronic Structure.

The 3d transition metals and oxygen, whose atomic configurations are $(Ar)3d^n4s^2$ and $(He)2s^22p^4$ respectively, will react to form a class of compounds in which the oxygen is ionized to O^{2-}, a (Ne) configuration, and the metals give up two or three electrons to become M^{m+}. Purely ionic bonding would stabilize such a compound by the difference between the ionization energy of the metal and the electron affinity of oxygen plus the electrostatic (Madelung) energy of the crystal.

The simplest compound of this type has formula $M^{2+}O^{2-}$, and the NaCl structure. The unoccupied 4s and 4p orbitals of the metal overlap extensively with the filled oxygen 2s and 2p orbitals to give bonding and antibonding molecular orbitals which extend throughout the crystal. They compose the valence and conduction bands, separated by about 7eV. Hence CaO, for example, which has a binding energy of 0.65eV per formula unit, is an excellent insulator.

The cation d-orbitals have a diameter of about 1.5Å, and since their separation is typically 3Å, they barely overlap each other. There are two completely different ways of describing the d-electrons; they are either collective or localized, and the latter description is the most appropriate one for many transition metal oxides. In this case the 3d electrons are electrostatically trapped by their cations, and an energy U, of the order of an electron volt is required to remove one of them and convert M^{m+} into $M^{(m+1)+}$. In the delocalized, band picture, U becomes negligible

compared to the band width. The energy levels of localized 3d electrons normally lie within the band gap, and they interact with their surroundings to give a set of crystal field multiplets. The electron-electron exchange within an ion is frequently greater than the splitting of the t_{2g} and e_g orbitals by a cubic crystal field, hence Hund's rules apply and high-spin states result. For example, Fe^{3+} as a free ion is in a ^6S state. In a typical crystal field in an oxide, the separation of the t_{2g} and e_g levels is about 1eV, and the interelectronic exchange is several times as great so that a $^6A_{1g}(t_{2g}^3 e_g^2)$ state results. Fe^{2+} is a ^5D ion, and in an oxide it is in a $^5E_g(t_{2g}^3 e_g^3)$ or $^5T_{2g}(t_{2g}^4 e_g^2)$ state depending on whether it is co-ordinated by a tetrahedron or an octahedron of ligands. The point is that the iron ion in the compound bears a local moment due to its unpaired d-electrons which is the same as that of a free ion. Figure 5 summarises the energy level scheme in a transition metal oxide with localized d-electrons.

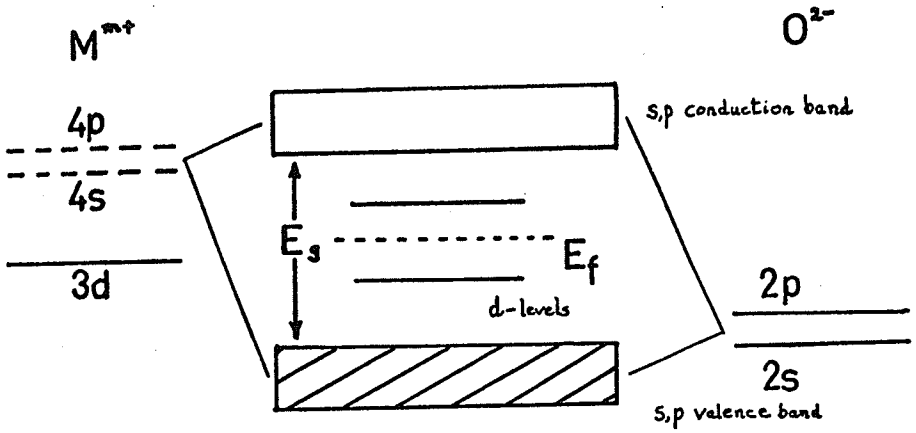

Figure 5. A typical band scheme for an insulating transition-metal oxide.

This picture is a reasonable description of all the compounds to be mentioned later, provided some modifications are made to take account of covalent bonding and overlap distortion of the oxygen 2p and iron 3d orbitals.

3.2 Magnetic Interactions.

The magnetic interactions between neighbouring cations may be of two types: i) direct cation-cation exchange or ii) cation-anion-cation superexchange. Both require appreciable overlap between 3d and 3d or 2p orbitals, and it is possible to predict the sign and strength of the interactions from the d-electron configurations and relative positions of the cations and the anion [20] (The Goodenough-Kanamori rules). For example, Fe^{3+} ions in octahedral co-ordination have a strong antiferromagnetic interaction if the superexchange bond angle is $\sim 135°$ or $\sim 180°$, but a weak one if it is $\sim 90°$. The direct interaction between these ions is weak and ferromagnetic.

The exchange interaction of an ion i with ions in the rest of the crystal is often represented by the Heisenberg-Dirac Hamiltonian

$$\mathcal{H}_i = -2 \sum_j J_{ij} \vec{S}_i . \vec{S}_j \qquad (1.12)$$

Since the overlap of orbitals which do not belong to neighbouring ions is often very small, it is enough just to include nearest neighbours in the sum over j. Another simplification is to replace $\vec{S}_i$ and $\vec{S}_j$ by their z-components so that the magnetic Hamiltonian for the whole crystal is

$$\mathcal{H}_I = -2 \sum_{n.n.} J_{ij} S_{zi} . S_{zj} \qquad (1.13)$$

This is the Ising model, which is soluble in one and two dimensions. However there is no complete solution of either model in three dimensions, although there are a variety of approaches such as effective field theories, spin wave theory, and high temperature series expansions, capable of giving solutions which are approximate or else valid only in a limited range.

The exchange interactions can give rise to a great variety of different ordered spin arrangements. The simplest are the ferromagnetic, antiferromagnetic and ferrimagnetic arrangements which consist, respectively, of a single magnetic lattice, and two opposite magnetic sublattices whose moments are equal, and unequal. In addition to these co-linear arrangements, canted, triangular, spiral and conical structures may occur, particularly when there are several competing exchange interactions of comparable magnitude. A complete classification of crystals, taking into account magnetic properties, is to be found in the 1651 magnetic space groups [21].

They are obtained from the 230 ordinary space groups by combining the time reversal operator, corresponding to a change in spin direction, with the ordinary translation and rotation symmetry operators. Only certain magnetic properties are consistent with each magnetic group, just as only certain physical properties are consistent with each space group [22].

3.3 Crystal Structures.

We conclude this introduction with a few general remarks on the crystal structure of transition metal oxides, although specific structures will be discussed in more detail in later chapters. The large oxygen anions (O^{2-} ionic radius is 1.40Å) often form either a cubic or hexagonal close-packed array, and the smaller cations are accommodated in the small tetrahedral, or slightly bigger octahedral interstices. In each structure there are as many octahedral sites and twice as many tetrahedral sites as there are anions, but usually only a fraction of these are occupied. In the hexagonal close-packed array, two oxygen tetrahedra may share a common face, giving a bipyramidal site which may be occupied by, at most, one cation, either in four- or five-fold co-ordination. Electrostatic repulsion forbids double occupancy. In some structures, pervoskite for example, one simple-cubic oxygen sublattice may be replaced by large cations. In others the oxygen ions are not exactly close-packed. An example is garnet, which has an 8-fold site in addition to the common four- and six-fold ones.

It is a particularly stable structure with almost no tolerance of non-stoichiometry because every interstice in the anion sublattice is occupied by a cation.

With these preliminary remarks, we can now go on to describe our studies of hyperfine interactions in iron oxides using the Mössbauer effect.

II Experimental Apparatus, Methods and Analysis

योगः कर्मसु कौशलम् - *Gita.*

1. MÖSSBAUER SPECTROMETERS.

The bare bones of the experimental arrangement are shown in figure 6. The kernel of the spectrometer is the monochromatic source. It is mounted on a transducer which vibrates it with an

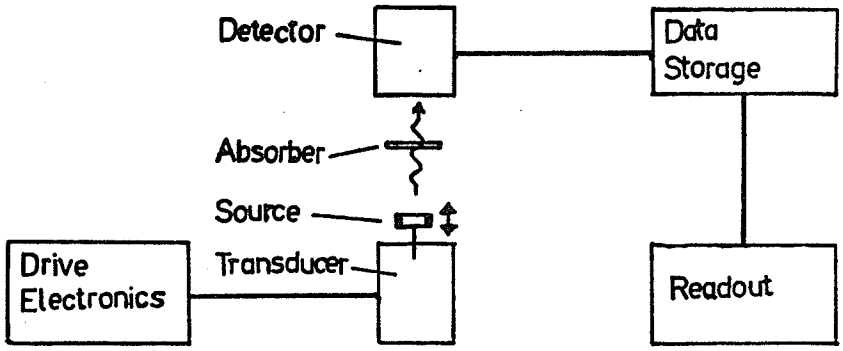

Figure 6. The main components of Mössbauer spectrometers.

accurately controlled velocity, allowing the velocity spectrum to be scanned, either in steps, or continuously. The γ-rays pass through an absorber, which may be mounted in a furnace or cryostat, or subjected to an applied magnetic field. They are detected in a counter, sorted, stored and finally read out. The operation of each of our spectrometers will now be described in a little more detail.

They are entirely manufactured by Elron Electronic Industries except for the Nuclear Data[2] 2200 Series multichannel analysers and the output units.

1.1 Constant Velocity System M-1.

The simplest way of collecting the spectrum is to operate the transducer at constant velocity for a fixed time, usually between 30 and 300 seconds, excluding time taken in flybacks. The counts are fed into a scaler and, at the end of the preset time, the total number of counts is printed out on paper tape. The transducer, which works like a loudspeaker, then runs at a slightly higher velocity, the process is repeated, and the spectrum is accumulated point by point. The counting system must be quite stable over the period of several hours needed to collect the whole spectrum. All three of our spectrometers are capable of operating at constant velocity, but the oldest system, whose components are designated M-1-n, can only operate in this mode. The velocity, set as a number on the three digit scalar M-1-1, is converted into a voltage by a precision digital-to-analogue converter M-1-2. This voltage is amplified, and a current is fed into the driving coil of the transducer by the unit M-1-3. The transducer itself consists of a light central cylinder, mounted so that it can move freely along its axis. The driving and pickup coils are wound at opposite ends in the uniform field of a strong permanent magnet, and the source is fixed to the upper end of the cylinder. There are

mechanical limit switches at each end of the stroke which initiate the flyback. The pickoff voltage is fed back to the transducer driving unit M-1-3, and the driving current is suitably modified. The waveform is shown in figure 9a. A six digit scaler M-1-4, which is inhibited during flybacks, collects the counts, and the total is printed out onto paper tape. The data must then be punched onto cards for computer analysis. The connections for the M-1 spectrometer are given in figure 7, and typical spectra appear in figure 53.

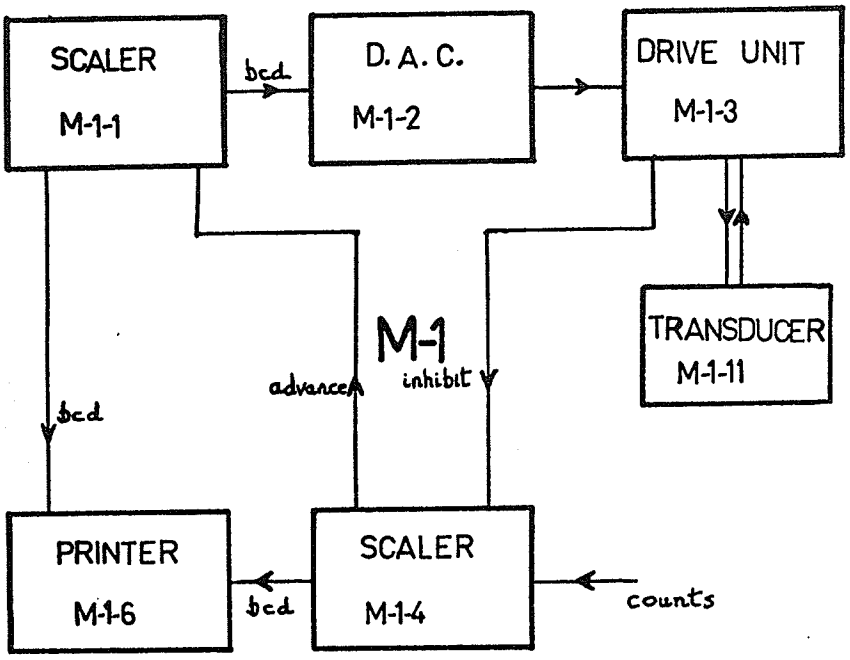

Figure 7. The constant-velocity spectrometer, M-1.

A characteristic of a constant-velocity spectrum is the linear slope on the baseline. It is an instrumental effect, arising in the following way. The γ-rays from the source must be collimated since the Doppler shift in energy, imparted by the movement of the source, is $E_\gamma(v \cos \Psi)/c$. For any finite size of

collimator, it is obvious from figure 8 that the count rate is

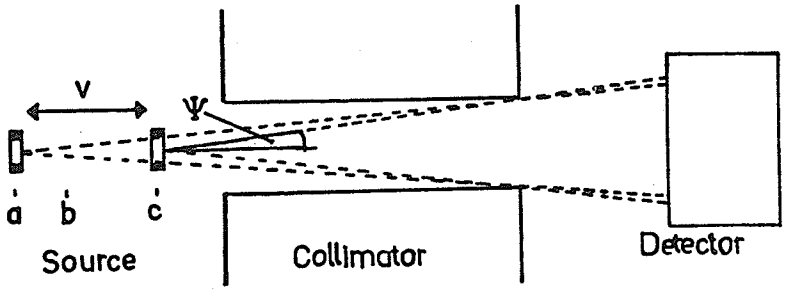

Figure 8. The effect of collimation on the intensity of the γ-ray beam.

greatest when the source is closest to the detector; that is when the half-angle Ψ is greatest. The first part of the stroke, from a to b, is used to regulate the velocity after the flyback, and is dead-time. However for more positive velocities (corresponding to movement of the source towards the detector), a larger section, ab, of the stroke is needed for velocity regulation, hence the source tends to be closer to the detector during the counting section, bc. For negative velocities, cb is now the dead-time section, and it increases for more negative velocities so that the source tends to be further away from the detector during the life-time section. If the limit switches are not set correctly, the transducer traverses a slightly different path for positive and negative velocities, and there will be a discontinuity between the two halves of the spectrum.

1.2 Constant Acceleration Systems.

A more sophisticated and convenient way of collecting the data is at constant acceleration. The source scans the whole range of velocities, from the most negative to the most positive

in a short, double stroke, while the counts obtained at different velocities are stored in different channels of the memory of a multichannel analyser, used in the time mode as a multiscalar. Normally we used the sawtooth velocity profile shown in figure 9b, but the triangular waveform of Figure 9c may be useful if the system is non-linear. It has a lower harmonic content than the sawtooth,

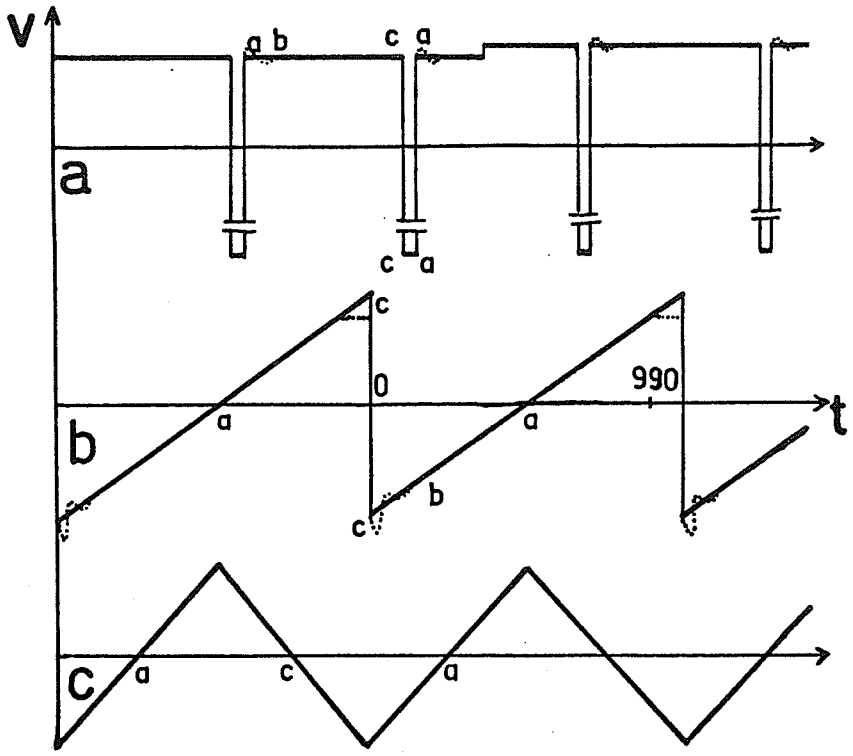

Figure 9. The velocity of the transducer when operating a) at constant velocity, b) at constant acceleration in the sawtooth mode and c) at constant acceleration in the triangular mode. The ideal waveforms are the solid lines, and the deviations found in practice are shown dotted.

but has the disadvantage of requiring twice as many memory channels to store the two mirror-image spectra which result. The baseline of a constant-acceleration spectrum, acquired in the sawtooth mode, is parabolic because the source is closest to the detector when it

is moving with the greatest velocity, whether positive or negative, and it is farthest from it when instantaneously at rest. The letters a, b, c on the waveforms of figure 9 correspond to the positions marked in figure 8. A triangular-mode spectrum has a concave parabola as baseline for the left-hand spectrum and a convex one on the right. Hence, by adding together the two halves, a perfectly flat background can be obtained.

Since there are some differences in the design of the spectrometers M-2 and M-3, they will be described in turn. They share common data output units, and the memory of either multi-channel analyser can be read out onto printed tape or punched tape, or else plotted on an x-y recorder. The punched tape is converted to cards on an IBM 1600 computer.

1.2.1 *M-2*

The spectrometer M-2 is similar in many respects to M-1, and both the scalers on each are interchangeable. In a velocity scan, the three digit scaler runs from 000, corresponding to the most negative velocity to 990, corresponding to the most positive velocity. The reading increases by 2 or 1 as the channel advances, depending on whether a 512 or 1024 channel spectrum is required. The transducer reaches the upper limit of its traverse while moving at velocity 990, and it triggers the photoelectric limit switch. M-2-4 then gives a reset pulse to M-2-1 which in turn issues a start command to the multichannel analyser, set for internal timer operation. When the multiscale sweep begins, the analyser then

gives out clock pulses every 40μs (for a 512 channel scan), and every tenth one of them is fed into the scaler M-2-1 to advance the channel. This is effected by feeding the clock pulses into the first divide-by-ten network of M-2-4, which is set to 'PHA'. When setting up the spectrometer, it is essential to adjust the zero on M-2-3 so that there is a small flat portion at the end of the sawtooth waveform, shown dotted in figure 9b. This ensures that the transducer has finished its scan up to velocity 990 before it reaches the limit. Hence the new scan of the scalar and multichannel analyser can start simultaneously. A consequence is that the zero is always a little to the right of centre.

1.2.2 *M-3*

Spectrometer M-3 incorporates an Elron MFG-3 Mössbauer function generator, and it is more versatile than M-2. Unlike the older spectrometer, it gives out clock pulses to advance the channels in the multichannel analyser, set for external timer operation. There are no constant velocity channels at the end of the scan, so the zero-velocity channel can be exactly in the centre. It can also use the analyser to store a constant velocity spectrum, provided the inhibit level is connected, to take care of dead-time during flybacks. When operating in 512 channels, a dwell time of about 200μs per channel is most satisfactory. The spectrometer also has a facility for making partial and shifted scans, although these are rarely necessary for work with ^{57}Fe. A complete diagram showing the components of the M-2 and M-3 spectrometers is given

in figure 10. Most of the data was collected with this equipment.

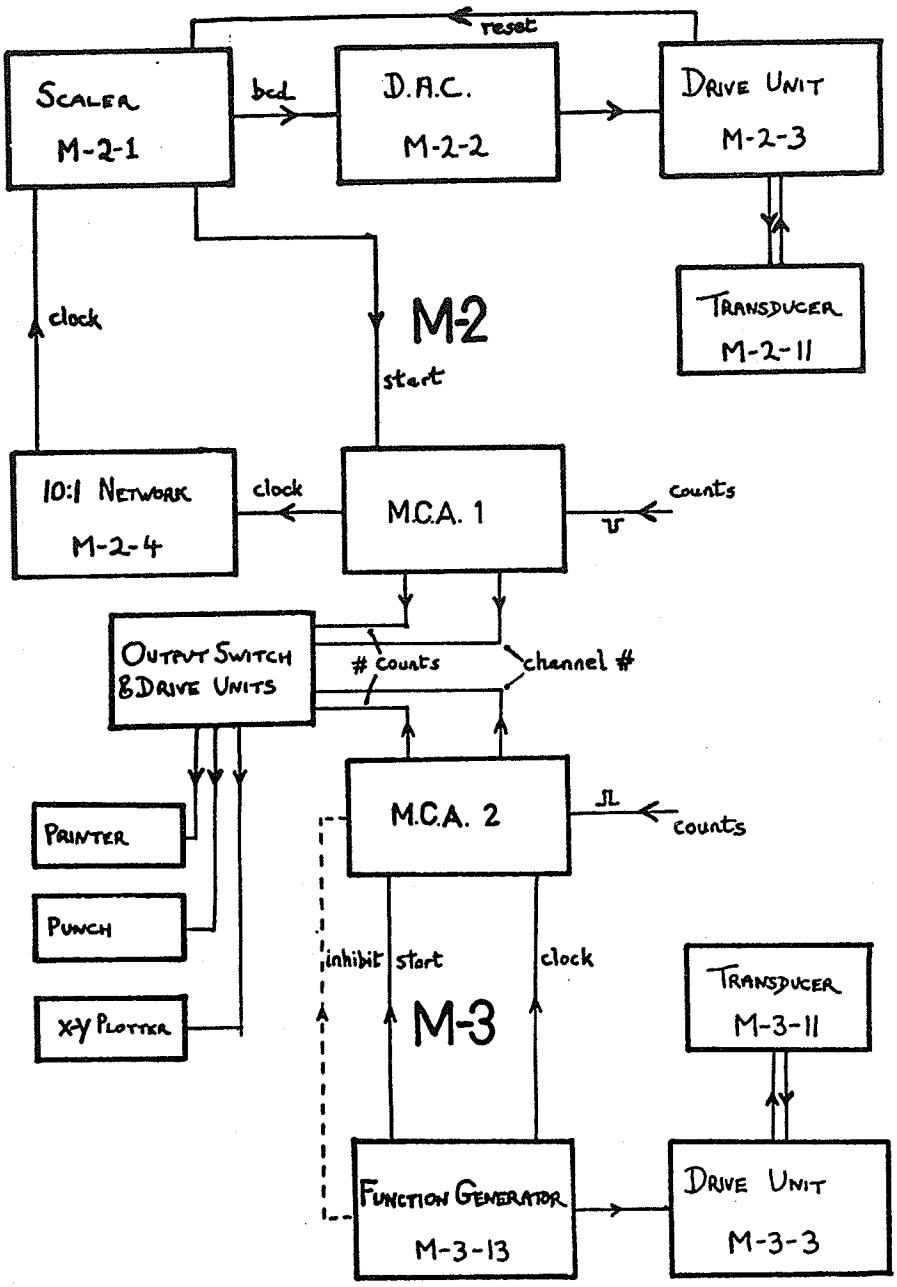

Figure 10. The constant-acceleration spectrometers, M-2 and M-3.

1.3 Sources and Counting Systems.

In a good Mössbauer source, the ^{57}Co nuclei should be embedded substitutionally in a host matrix,in which they experience no electric field gradient or magnetic field. Chromium is a good host material. Since it is body-centred cubic, there is no field gradient at the ^{57}Co nucleus, and neither is there a hyperfine field, in spite of the fact that it is an antiferromagnetic metal. Our sources were initially 10-20 mC of ^{57}Co in Cr, prepared by the New England Nuclear Corporation[3]. Their activity decreases exponentially with time, as indicated in figure 11. A line width of 0.24 - 0.27 mm/s was obtained with a sodium-ferrocyanide absorber.

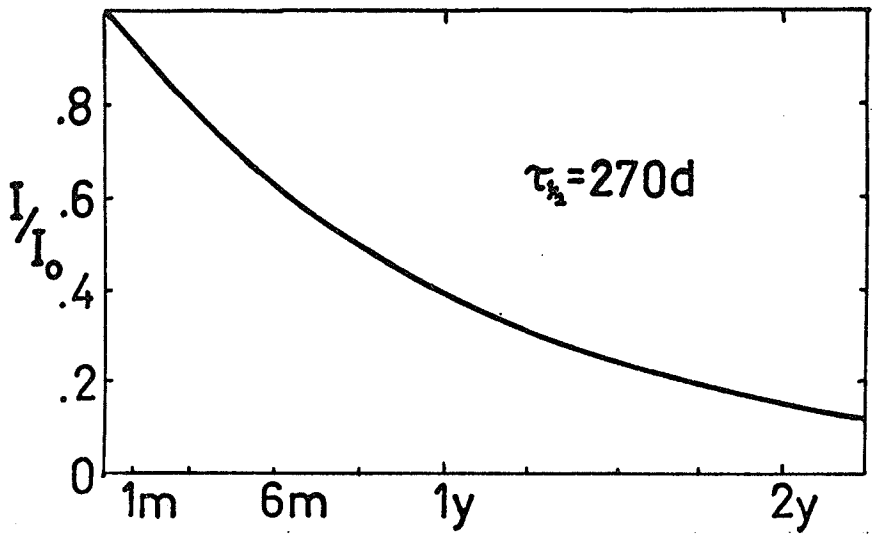

Figure 11. The decay of the radioactivity of a ^{57}Co source.

The pulse detection and counting system used in Mössbauer spectroscopy must be capable of distinguishing the low energy γ-rays of interest from other γ-rays and x-rays. Either proportional, scintillation,or Si(Li) detectors may be used, but the pulses must be proportional to the energy of the photon producing them, so that they can be amplified and then fed into a single-channel

analyser whose gate is set to reject all but the Mössbauer γ-rays. In the case of ^{57}Fe, the detector is chosen to be rather insensitive to the 122 keV 5/2 → 3/2 transition, and the main problem is to separate the 14.4 keV 3/2 → 1/2 γ-ray from the 6.5 keV iron x-ray. Normally the x-ray peak is several times more intense than the γ-ray peak, but it can be substantially reduced by simply putting a few millimeters of lucite (perspex) between the absorber and the detector.

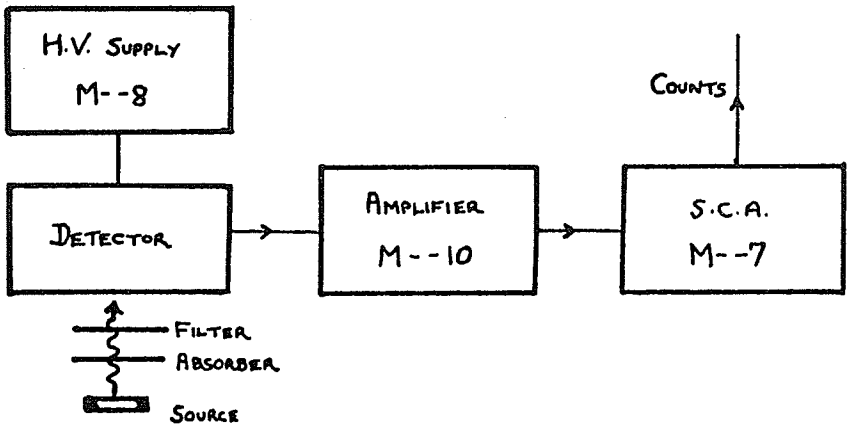

Figure 12. A counting system for 14.4 keV γ-rays.

The counting system is shown diagramatically in figure 12. The detector used was either a proportional or scintillation counter. The proportional counters, manufactured by 20th Century Electronics[4], are filled with a 9:1 mixture of argon and methane, and have 2" × 5" × .010" beryllium windows. Their disadvantage is that use at a counting rate much in excess of 1500 counts per second drastically shortens their life and causes them to drift. They are operated at 1.8 kV, but a slightly higher voltage, up to 2.0 kV, improves the performance of an old counter. These proportional counters last between six months and a year.

The scintillation counter was more satisfactory since it has a much longer lifetime, is less likely to drift, and can be used at count rates of at least 5000 counts per second without pile-up. It was manufactured by Harshaw N.V.[5], and it uses a NaI(Tℓ) crystal 0.2 mm thick, mounted behind a beryllium window window 3.8 cms in diameter. It operates at 1.2 kV. Compared to

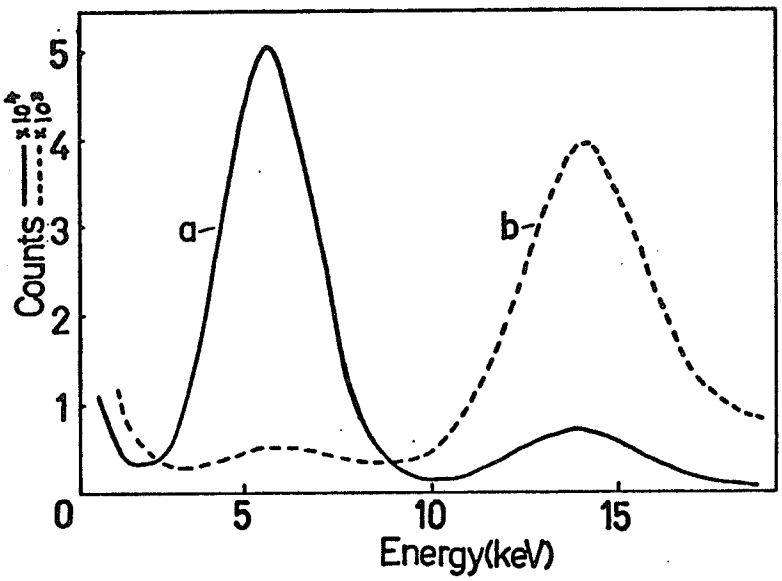

Figure 13. The energy spectrum of a ^{57}Co source, measured using a NaI(Tℓ) scintillation counter, a) without, and b) with a 4 mm thickness of lucite interposed between source and counter.

the proportional counter, it is very sensitive to stray magnetic fields, and cannot be used near the superconducting solenoid. Figure 13 shows the energy spectrum of the source, measured by the scintillation detector, and the effect of a 4 mm thick lucite filter.

2. ANCILLARY MÖSSBAUER EQUIPMENT.

It is often desirable to change the temperature of the absorber or to subject it to high fields.

Our vacuum furnace and liquid nitrogen cryostat have been described in detail in another thesis [23]. The furnace is capable of maintaining the absorber at temperatures up to 900°K. A temperature controller is used to keep the temperature steady to within a degree over periods of several hours. Stability of ±0.1° may be achieved for shorter periods. The sample holder has been modified so that it resembles the one used for the solenoid furnace described in §2.2. The sample is ground to a fine powder and mixed with graphite or boron-nitride, if necessary, to ensure a uniform distribution. It is then clamped between two beryllium discs 0.9" in diameter and 0.02" thick. Two more beryllium discs are clamped on both sides of the sample in good thermal contact with the copper furnace core, so as to ensure thermal homogeneity across the surface of the absorber. The arrangement is shown in figure 16. At the highest temperatures, the outside of the furnace should be cooled with a small air-blower.

A liquid helium cryostat of the 'cold finger' type was used for the lower temperature spectra. Temperatures of 20°K could be attained with a liquid helium consumption of 0.3 ℓ/hr. The liquid nitrogen cryostat was of similar design and the temperature of the sample could be kept constant to ±1° in the range 80 - 300°K using a temperature controller and a heater wound on the sample block.

2.1 Superconducting Magnet.

Axial fields of up to 50 kOe could be generated in a 16,436 turn niobium-zirconium superconducting solenoid, manufactured

by the Westinghouse Electric Corporation[6]. The homogeneity is 1% in a volume 1/4" long and 3/4" in diameter at the centre of the solenoid. The coil is mounted in a dewar designed specially for Mössbauer work, and the design is indicated in figure 14. The storage dewar and the solenoid container are separate, parallel cylinders, joined by a pipe which surrounds a thick copper cold-cylinder. It is connected to the copper nitrogen shield surrounding the coil and is in good thermal contact with the nitrogen reservoir.

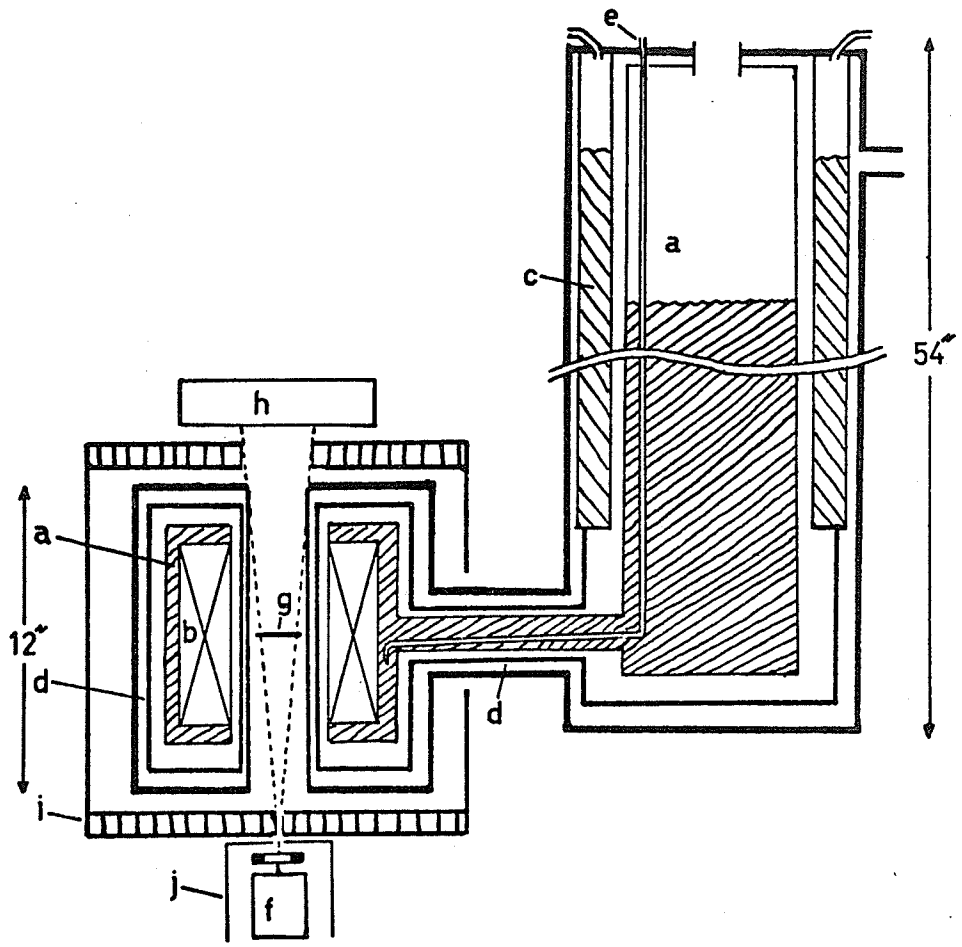

Figure 14. Schematic drawing of the 2" superconducting magnet. a) Helium reservoir and bath. b) Superconducting coil. c) Nitrogen reservoir. d) 77°K radiation shield. e) Helium fill tube. f) Transducer and source. g) Absorber. h) Proportional counter. i) Iron box. j) Conetic shield.

Inside the pipe are tubes connecting the helium reservoir to the solenoid helium bath. The magnet is usually operated with the 2.05" room-temperature bore and the 2.35" nitrogen bore in place inside the 2.65" helium bore of the solenoid. The high field is then in an air space, so the sample may be changed easily, and a cryostat or furnace can be inserted if it is desirable to operate below or above room temperature. The magnet may also be used with the sample at 77°K or 4°K, in thermal contact with the nitrogen or helium bores. In this case, windows are placed across the ends of the bore, and it is necessary to break the vacuum and warm up the magnet in order to change the sample.

Normally, between 8 and 14 litres of helium were used to cool the solenoid from 77° to 4°. The capacity of the dewar is 12 litres and the boil-off varies from 0.5 ℓ/hr when it is full to 0.2 ℓ/hr when it is almost empty.

The resolution in a Mössbauer spectrum becomes better as the number of counts per channel, $y_{obs}(v_i)$, increases. The relative statistical fluctuations are $y_{obs}(v_i)^{-1/2}$ on average, so that the higher the count rate, the more rapidly a good spectrum can be accumulated. The detector should therefore subtend the largest solid angle at the source that is consistent with reasonable collimation. This matter was touched on in §1.1 and will be considered further in §4.2, but $\Psi \sim 7°$ is a reasonable value. The nature of superconducting magnets makes a short source-detector distance difficult to achieve, but if they were placed at opposite ends of the bore of our magnet, Ψ would be 4.8°. However, in practice Ψ was somewhat

smaller, because of the need to shield the transducer and the proportional counter from the large stray field of the solenoid. A massive cubic box was constructed to enclose the cylinder containing the coil. The sides of the box were made of a single layer of soft iron, while the top and bottom were made from six layers, separated by sheets of lucite. The fringing field was thus reduced to about 100 Oe. It is important that the top and bottom of the box are symmetrically positioned, and are in firm contact with the top and bottom faces of the magnet, or else very great strains on the solenoid will result. A special sheath of conetic metal, manufactured by the Perfection Mica Company,[7] fits over the transducer, and with all the shielding in place, Ψ was 4.0°. This corresponds to a count rate of roughly 2500 counts/s with a 15 mC source and no absorber.

In spite of all this shielding, the calibration constant of the spectrometer was significantly influenced by the field, although the linearity remained good, except at the beginning of each sweep. It may be seen from figure 15 that the calibration

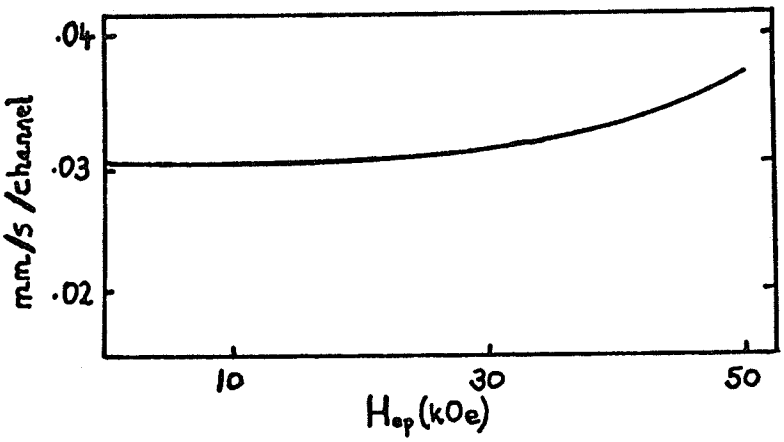

Figure 15. The influence of the fringing field of the superconducting magnet on the calibration constant of the spectrometer M-2.

constant increases rather rapidly at the highest fields. One must calibrate the spectrometer for each field, and be sure that the magnet is in the same position relative to the transducer for both the calibration and sample spectra. The harmonics generated as the velocity stabilises at the beginning of the sawtooth, shown dotted in figure 9b, tend to occupy a greater segment of the waveform in high fields, but this may be counteracted by increasing the dwell time per channel.

2.2 High Field Vacuum Furnace.

We will now describe, in some detail, a furnace which was designed to fit into the room-temperature bore of the superconducting magnet, so that spectra could be collected at high temperatures and in high fields. In addition to the requirement of keeping the sample at a uniform, steady temperature, the design must provide the widest channel for the γ-rays that the unfavourable dimension restrictions will allow, and also it must take into account the requirement that the room-temperature bore of the solenoid may not get any hotter than 100°C.

The simplest way of meeting these requirements is to have the furnace insulated by vacuum and a radiation shield. Ideally the absorber should be a disc 1" in diameter, so that it does not reduce the angle subtended by the γ-ray channel when it is in position at the centre of the bore. However, since we also had to fit the furnace core, heating element, radiation shield and vacuum space into a 2" diameter, we were obliged to reduce the

effective diameter of the sample to 0.8". The corresponding value of Ψ was 3.0°. The furnace is illustrated in figure 16. The furnace core and sheath fit tightly together, and enclose the heating element, 33 turns of Thermocoax[8] type 2 NcNcAc15 with a total resistance of 140Ω. This element contains two nichrome wires, joined at one end, insulated with MgO, and enclosed in a stainless-steel tube whose outer diameter is only 1.5 mm. The sheath is soldered to a bushing in the outer case at the point where the element leaves the furnace. The whole winding is thus vacuum-

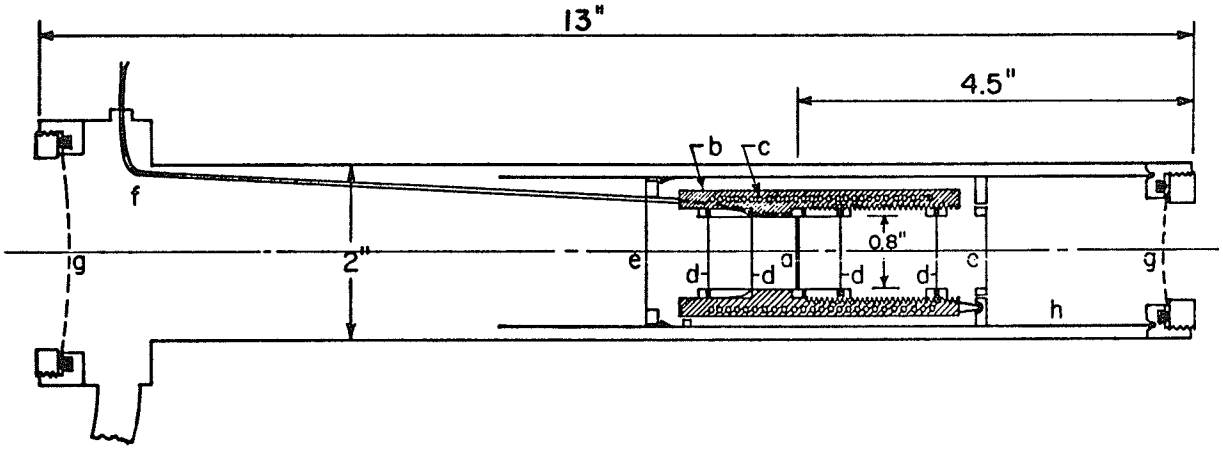

Figure 16. Vacuum furnace for high field Mössbauer experiments. a) Absorber. b) Furnace core. c) Thermocoax heating element. d) Beryllium radiation shields. e) Aluminium radiation shields. f) Thermocoax chromel-alumel thermocouple. g) Lucite windowns. h) Core mount and radiation shield.

tight and non-inductive. Two Thermocoax type 2ABAc10 chromel-alumel thermocouples of a similar design were embedded in the core. One was used to measure the sample temperature and the other was connected to the controller, as shown in figure 17. The connection of the outer case of the furnace to the common side of the power supply is not required for the ordinary furnace.

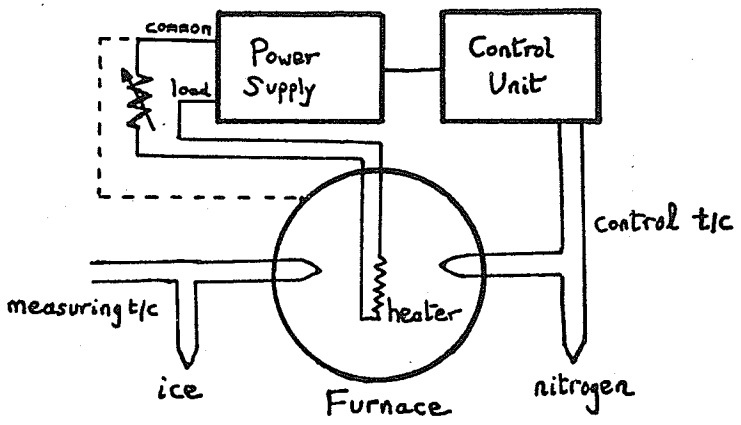

Figure 17. Block diagram of the furnace temperature controller.

The sample is sandwiched between two 0.9" diameter beryllium discs in a stainless-steel sample holder which is held in place by a ring, screwed into the copper core. Two beryllium radiation shields are clamped in place on both sides of the sample holder in the same manner. The core itself stands on three small stainless-steel feet on a shelf inside a 1.7" diameter polished stainless-steel cylinder, which also serves as a radiation shield and is closed at both ends by high purity aluminium foils. The main heat loss is by conduction through the feet, by way of the radiation shield which fits into a groove at the bottom of the outer case. Access to the sample is from below, but the furnace core must be held firmly in a special clamp, inserted through the upper window, when the rings securing the two radiation shields and the sample holder are removed. The windows were made of 1/16" thick lucite, or else 'kepton' film glued between two thin aluminium rings, and they were clamped against O-rings by threaded stainless-steel rings.

Temperatures of 400°C could readily be achieved, and the quality of the temperature control and regulation was estimated

from some spectra of yttrium-iron-garnet. Just below the ordering temperature, the hyperfine field changes very rapidly with temperature, as shown in figure 74. Any variation in the temperature of the sample will greatly broaden the spectral lines, and it is possible to deduce an upper limit for the temperature variation ΔT from the broadening ΔH_{hf}, if the $H_{hf}(T)$ curve is known. Quite simply

$$\Delta T = \left(\frac{\partial H_{hf}}{\partial T}\right)^{-1} \Delta H_{hf} \qquad (2.1)$$

We find that ΔT is less than $\pm 0.02°$ at 280°C.

2.3 Experimental Applications.

There are at least three ways in which a large external field can be used to extract additional information from Mössbauer spectra. i) In ferro- and ferrimagnetic compounds it is possible to determine the direction of the hyperfine fields and resolve lines or spectra which otherwise overlap; ii) in para- and diamagnetic compounds with a large quadrupole interaction it is possible to find the sign of the electric field gradient, and iii) in magnetically ordered and superparamagnetic compounds with fast electronic relaxation rates it is possible to deduce relaxation times. We will give a brief description here of some experiments which exemplify the first two applications, and reserve a discussion of the third for chapter VI.

In ferrimagnetic compounds, the different sites for the

magnetic ions belong to different magnetic sublattices. The Mössbauer spectra of iron on different sites may overlap substantially, particularly if all the iron ions are in the same valence state. However, when a magnetic field which is large enough to overcome the anisotropy is applied, all the ionic moments on the sublattice with the greatest magnetic moment (say the B-sublattice of a simple, two-sublattice ferrimagnet) are aligned parallel to the field, while those on the opposite, A-sublattice, are aligned antiparallel. The measured hyperfine fields will thus be $H_{hf}(A) + H_{ap}$ for the A sites and $H_{hf}(B) - H_{ap}$ for the B sites, because the hyperfine field in iron is oppositely directed to the ionic moment, a fact discovered by Hanna et al. in 1960 when they applied a magnetic field to an iron-foil absorber [3]. In this way overlapping A and B site spectra can be resolved. The first use of this technique was made, in our laboratory, by Armstrong, Sawatzky and Morrish [24], who were able to show that the vacancies in the spinel γFe_2O_3 were on the B-sites. We have confirmed that the A and B-site fields are increased and decreased by exactly the applied field for H_{ap} in the range 10-50 kOe using an absorber of the spinel sulphide Fe_3S_4 [25]. Applications of the technique to two iron oxides will now be discussed briefly to illustrate its usefulness.

2.3.1 $Fe_{3-\delta}O_4$.

A study of the spectra of non-stoichiometric magnetite

has enabled us to draw some conclusions about the conduction mechanism in Fe_3O_4 [26]. The A and B-site spectra are actually quite well resolved in this compound because it is an inverse spinel with only Fe^{3+} on A-sites and a mixture of equal quantities of Fe^{2+} and Fe^{3+} on B-sites. However the sixth d↓ electrons of the Fe^{2+} ions are somehow shared amongst all the B-site cations so that only a single, averaged $Fe^{2+/3+}$ (B) spectrum is seen. Non-stoichiometric magnetites can be prepared, intermediate between Fe_3O_4 and γFe_2O_3, in which there are B-site vacancies and a greater proportion of Fe^{3+}. We obtained spectra of several of these materials, with the general formula

$$(Fe^{3+})[Fe^{3+}_{1+2\delta}Fe^{2+}_{1-3\delta}\square_{\delta}]O_4,$$

and found that it was possible to resolve a third spectrum, with the aid of a 50 kOe field, which was attributed to Fe^{3+} on B-sites which does not participate in fast electron interchange with the other B-site ions. We concluded that conduction in magnetite either proceeds by a 'pair localised' hopping mechanism [27], or if a band picture is to be sustained [28], then each of the vacancies must trap a shell of Fe^{3+} cores and prevent them from participating in the conduction. Typical Mössbauer spectra are shown in figure 18. An area ratio for the Fe^{3+}(A): Fe^{3+}(B): $Fe^{2+/3+}$(B) lines of $1:5\delta:2-6\delta$ is predicted by both models, in agreement with the ratio

observed.

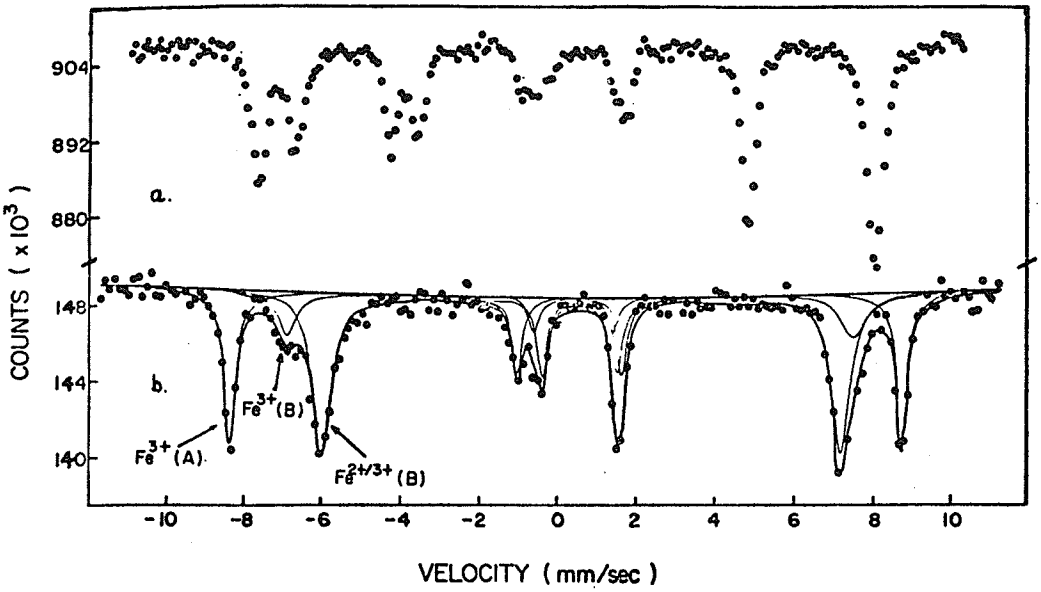

Figure 18. Mössbauer spectra of $Fe_{2.92}O_4$ at 296°K a) without and b) with an applied field of 50 kOe.

2.3.2 $SrFe_{12}O_{19}$.

Another example, this time involving the furnace, is the determination of the temperature dependence of the hyperfine fields in this colinear Néel ferrimagnet [29]. There are five different iron sites I, II, III, IV and V, occupied by 6↑, 1↑, 2↓, 2↓ and 1↑ Fe^{3+} ions respectively.* Sites I, II and IV are octahedral, site III is tetrahedral and site V is a bipyramidal interstice in the hhhcc oxygen array, in which Sr^{2+} has replaced 1/20th of the oxygen. The spectra of iron in the five sites overlap very considerably, particularly II and III, and it is impossible to resolve them all without an applied field [29]. The temperature dependence of the hyperfine fields cannot be obtained from NMR

* In crystallographic notation the sites are: 12k, 2a, $4f_1$, $4f_2$ and 2b.

because the signals are too weak to detect above 300°K [30]. The only way to determine the behaviour of the fields is from Mössbauer spectra in an applied field. Such spectra are simpler than the corresponding ones without a field, because lines 2 and 5 of each subspectrum disappear, and the patterns of sites I and II are well separated from those of sites III and IV. The pattern from site V is completely obliterated for a polycrystalline absorber, because of the statistical distribution of ϕ in (1.12). However, it is rather well resolved in the zero-field spectra. A typical pair of spectra is shown in figure 19.

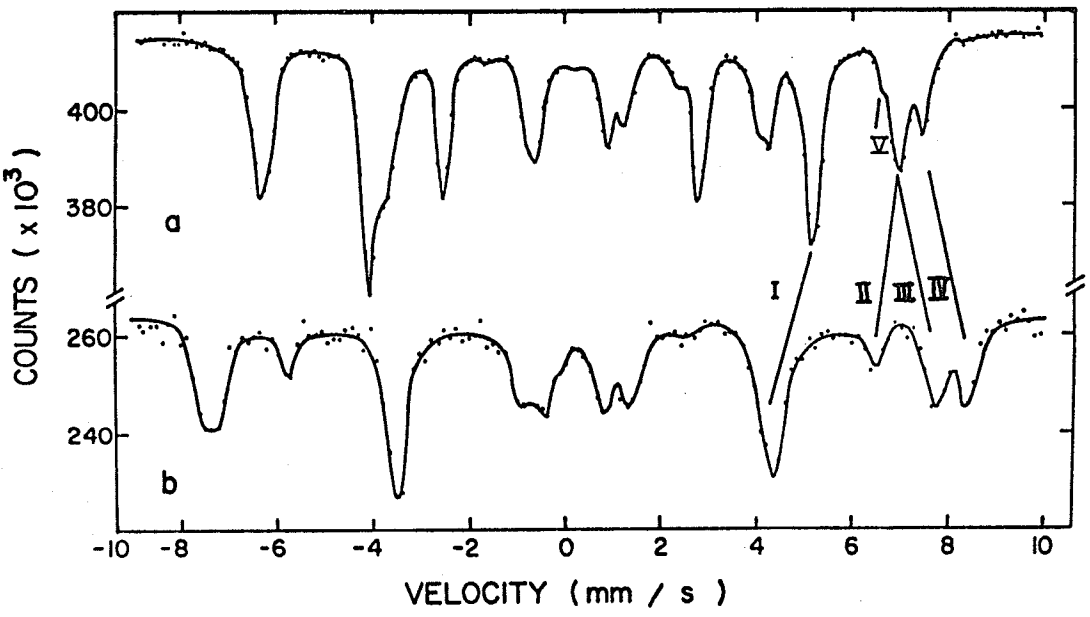

Figure 19. Mössbauer spectra of $SrFe_{12}O_{19}$ at 529°K a) without and b) with an applied field of 50 kOe.

2.3.3 $Fe(ClO_4)_2.6H_2O$.

As an example of the second way in which a large applied field can be used to obtain extra information from Mössbauer spectra we will mention some work on this ferrous salt [31]. It has a

large quadrupole splitting at room temperature which more than doubles at a transition at 240°K. It has been suggested that the transition might accompany a distortion of the octahedron of water molecules surrounding the high-spin Fe^{2+} ion so that the sixth d electron occupies a $|yz\rangle;|zx\rangle$ doublet above 240°K, and a $|xy\rangle$ singlet at lower temperatures [32]. In which case, the principal component of the electric field gradient, V_{zz}, should be roughly $-\frac{4}{7} e\langle r^{-3}\rangle$ at low temperatures and $+\frac{2}{7} e\langle r^{-3}\rangle$ at high temperatures [33].

Collins made the first determination of the sign of a field gradient on a polycrystalline sample, of ferrocene [34]. In an applied field, the line of the quadrupole doublet at lower velocity splits into a triplet and the line at higher velocities

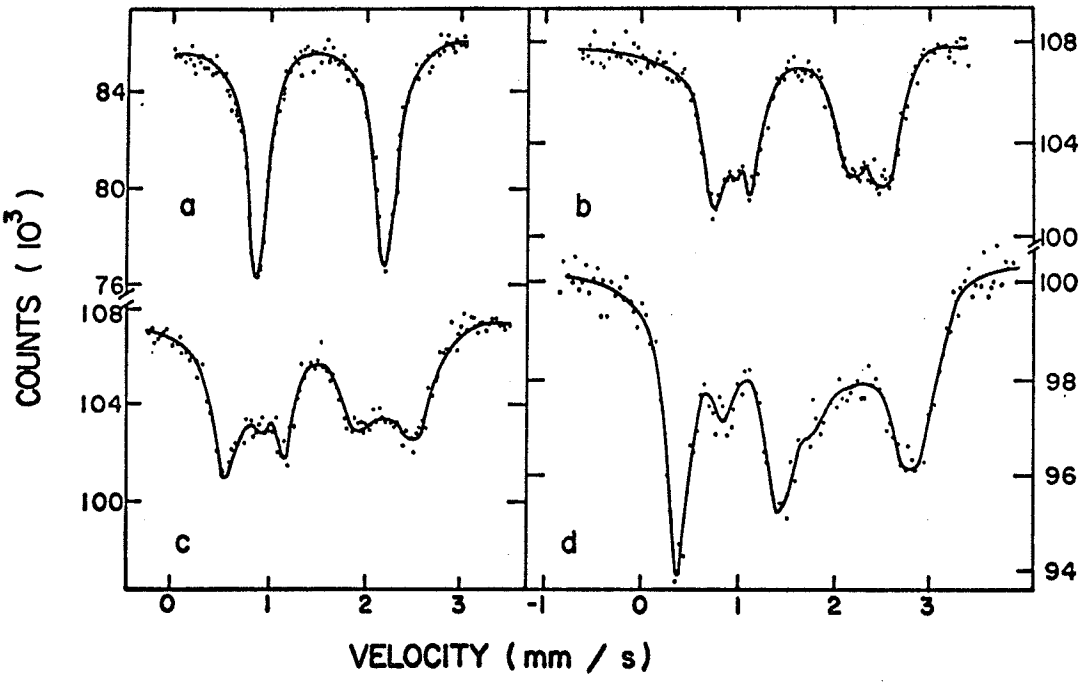

Figure 20. Mössbauer spectra of $Fe(C_2O_4)_2.6H_2O$ at 296°K in applied fields of a) 0 kOe b) 19.4 kOe c) 30 kOe and d) 50 kOe.

splits into a poorly resolved doublet if V_{zz} (or $e^2q'Q$) is positive, and the converse is true if V_{zz} is negative. It is clear from the spectra taken at room temperature, illustrated in figure 20, that V_{zz} is positive. Spectra at 4°K show clearly that V_{zz} is negative, thereby confirming that the ground state has changed from a doublet to a singlet. However, at lower temperatures the susceptibility of many salts increases as 1/T, and the applied field polarizes the iron ions. This has the effect of reducing the splitting of each line in the doublet, and hence the resolution of the experiment, because the induced hyperfine field subtracts from the applied field. A further discussion is given in VI 1.2.1.

3. OTHER EQUIPMENT.

Lattice parameters were determined from powder photographs taken in a 114.6 mm Debye-Scherrer camera with FeKα radiation from a manganese-filtered iron target. Kodak 'No Screen' or Gevaert 'Structurix' film was used, and the parameters were determined by the usual Nelson-Riley extrapolations. The intensities of the reflections were measured on a diffractometer when required, and the areas of the peaks were found by cutting out the traces and weighing them.

X-ray fluorescence was employed to find ratios of ions, and for trace analysis. A 50kV silver target was used together with a conventional goniometer and scintillation counter. The x-ray equipment consisted of a PW 1011/60 generator and a standard

range of accessories[9].

Magnetization measurements were made on a vibrating sample magnetometer[10] which has been described elsewhere [23].

4. DATA ANALYSIS.

It was noted in I.1 that the emitted γ-ray is expected to have a Lorentzian energy profile. The absorption spectrum, y(v), is the sum of N Lorentzians whose full-width at half maximum is the sum of the natural linewidths of the source and absorber. Line broadening effects are discussed in §4.2. The absorption spectrum has the form

$$y(v) = y(v_0)f(v)\left\{1 - \sum_{i=1}^{N} \alpha_i/[(2(V-V_0)/\beta_i)^2 + 1]\right\} \qquad (2.2)$$

where β_i is the full-width of the ith peak, and f(v) is the baseline;

$$f(v) = k_1(v-v_0) + k_2(v-v_0)^2. \qquad (2.3)$$

k_1 is zero for a constant acceleration spectrum and k_2 is zero for a constant velocity spectrum; α_i is the fractional intensity of the ith peak. If v is expressed in mm/s , v_0 is zero; otherwise it is the zero-velocity channel.

Equation (2.2) was fitted to the data using a program which performs a least-squares fit by variable metric minimization. The most frequently used version of the program, 'Monkey', requires

106K core space in the University of Manitoba IBM 360 computer and will fit up to 500 data points and 16 peaks with 30 linear constraints. A larger version, 'Baboon', will fit up to 996 data points and 22 peaks with 40 constraints. Both programs calculate a goodness-of-fit parameter defined as

$$F = \sum_{i=1}^{N_p} (y_{obs}(v_i) - y_{calc}(v_i))^2 / y_{calc}(v_i) \qquad (2.4)$$

where N_p is the number of points in the spectrum. F should be equal to N_p if the calculated curve fits the data exactly, within statistical error, but a fit is satisfactory if $F < 1.5N_p$.

4.1 Calibrations.

The velocity scale of an electromagnetic transducer must be calibrated, and standard absorbers, whose peak positions have been accurately measured on an absolute instrument, are most frequently used. The calibration constant, in mm/s/channel, and the zero-velocity channel are deduced from the calibration spectrum, and the linearity of the spectrometer may be checked. We used αFe_2O_3 and iron foil to calibrate the spectra of magnetically ordered materials, and sodium-nitroprusside for the smaller velocity ranges. The splittings of the outer lines, in mm/s are taken to be 16.70, 10.657, and 1.712 respectively, and the corresponding hyperfine fields for Fe_2O_3 and Fe are 517 and 330 kOe. In order to find the zero-velocity channel, the centre of the spectrum is found by

averaging the positions of the outer four peaks of Fe_2O_3 or Fe, or of the two peaks of $Na_2[Fe(CN)_5NO].2H_2O$. The isomer shift of the absorber with respect to chromium is then subtracted from the position of the centre of the spectrum to give the zero velocity channel. These shifts are shown on the upper scale of figure 21,

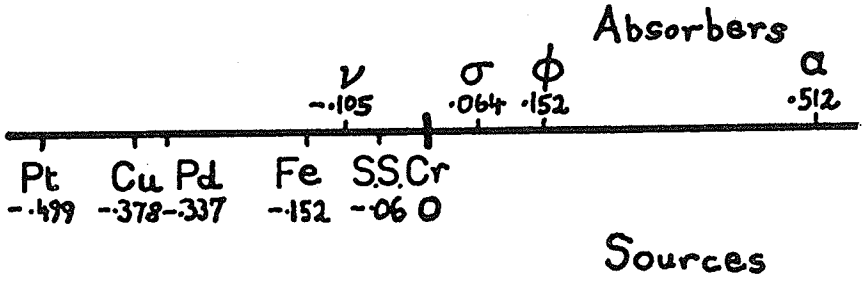

Figure 21. Total spectrum shifts at 296°K of standard absorbers and other sources relative to chromium. The symbols represent: ν, sodium-nitroprusside; σ, sodium-ferrocyanide; φ, iron metal; α, α ferric-oxide; S.S. stainless steel.

together with the peak position of sodium-ferrocyanide, whose single-line spectrum may be used as a marker. The lower scale in the figure shows the isomer shifts of other common sources relative to chromium, to facilitate comparisons with data from other laboratories. To convert an isomer shift relative to some other host into a shift relative to chromium, add the figure shown for the host in figure 21.

4.2 Line Shape.

Several investigators have reported that the shape of a Mössbauer spectral line is not strictly Lorentzian, and that it changes shape as the source ages [35]. We noticed that our computer fits consistently overestimated the absorption in the wings of the

peak, and a better fit was obtained by taking the exponent in the Lorentzians in the spectrum of equation (2.2) as 2.2 instead of 2.0

In addition to instrumental and vibration broadening, and effects in the source, there are two other common causes of broad lines. One is the effect of collimation which was mentioned earlier. The broadening of a line at velocity v is given by

$$\Delta v \simeq v\Psi^2/2 \qquad (2.5)$$

where we have assumed a point source, and Ψ in the half-angle in radians defined in figure 8. For example, a line at 8 mm/s will be broadened by 0.06 mm/s if $\Psi = 7^\circ$. The true source velocity is also modified by a factor $(1 - \Psi^2/2)$, but this is immaterial if Ψ is the same for the sample and the calibration.

The other cause of line broadening is the thickness or 'blackness' distortion [36]. Obviously, the intensity of an absorption peak cannot increase indefinitely in proportion to the absorber thickness. For 'thin' samples, the intensity is proportional to the number of ^{57}Fe nuclei, but for thicker samples the absorption line saturates. The line shape is still approximately Lorentzian, but broadened. Formulae for correcting for finite absorber thickness have been given by Shirley et al [37], but these corrections are negligible for simple iron oxides if the intensity of a particular peak at low temperatures is less than 10%. This corresponds to about 10 mg of natural iron/cm^2 in a magnetically

ordered material with only one site, and half as much for a paramagnetic sample. However, a line *may* be saturated even if its intensity is less than 10%. There are two reasons. If the Debye temperature is low, the recoilless fraction varies rapidly with temperature so that the intensity at absolute zero would be much greater than it is at the temperature of the absorber. Also there can be scattering of the γ-rays in the absorber which tends to destroy the effect, particularly if it contains heavy elements, (elastic scattering cross sections $\sim Z^2$). This problem may be overcome by enriching the absorber with ^{57}Fe so that a much smaller mass of material is required. ^{57}Fe is only 2.17% abundant in natural iron.

III Theory of Hyperfine Fields in Substituted Systems

To know the world, one must construct it.
- C. Parvese.

In this chapter we are going to consider the static hyperfine fields in a compound with a random distribution of two sorts of ions on several sites.

If we denote the ions by f and g, and the concentration of the second species by x, and if each of the ν-sites (e.g. A and B sites in a spinel) has N equivalent neighbouring sites, then we can write down the probability of a particular ν-site ion being surrounded by Z f-ions and (N-Z) g-ions on the neighbouring sites. It is given by the binomial distribution

$$P_N(Z) = \frac{N!}{Z!(6-Z)!} (1-x)^Z x^{N-Z} \qquad (3.1)$$

Some numerical values of these probabilities are given for N = 6 in table 3, and they are plotted for N = 6 and 9 in figure 35.

The assumption of a statistical distribution of ions in a mixed oxide is a fundamental one, and not very easy to prove

Table 3. Nearest-Neighbour Probabilities for a Random Distribution of Two Sorts of Ions in a Lattice with Six Nearest-Neighbour Sites.

z \ x	0.0	0.1	0.2	0.3	0.4	0.5	0.6	0.7	0.8	0.9	1.0
6	1.000	0.532	0.262	0.118	0.047	0.016	0.004	0.001	0.000	0.000	0.000
5	0.000	0.354	0.393	0.302	0.186	0.094	0.037	0.010	0.002	0.000	0.000
4	0.000	0.098	0.246	0.324	0.311	0.234	0.138	0.060	0.015	0.001	0.000
3	0.000	0.015	0.082	0.185	0.277	0.312	0.277	0.185	0.082	0.015	0.000
2	0.000	0.001	0.015	0.060	0.138	0.234	0.311	0.324	0.246	0.098	0.000
1	0.000	0.000	0.002	0.010	0.037	0.094	0.186	0.302	0.393	0.354	0.000
0	0.000	0.000	0.000	0.001	0.004	0.016	0.047	0.118	0.262	0.532	1.000

experimentally. Gross clustering may be detectable by x-ray, neutron, or electron diffraction. If all the lattice sites are equivalent, it should be possible to produce a random distribution of cations by quenching, provided they are the same size. When we come to analyse our experimental data, (3.1) will be assumed. Some workers use a rather different approach, and attempt to verify (3.1) by measuring the shape of the lines in the Mössbauer spectra of mixed systems [38, 39]. Their results, and ours, are certainly compatible with the assumption of a statistical distribution.

The problem now is to calculate the temperature variations and absolute values of the hyperfine fields in all the possible environments of a magnetic ion, whose probabilities are given by (3.1), for a material with some particular value of x. To this end we will use molecular field theory in section 1 to calculate the temperature dependence of the magnetization in each environment,

and then make the assumption [5] that $H_{hf} \propto \bar{S}_z$. In other words the time average of the magnetic moment over τ_L is supposed to be the same as an ensemble average. In section 2, some results on the various contributions to the hyperfine field at $T = 0$ are brought together. Since the *ab initio* calculations of the absolute values of the unpaired spin density at the iron nucleus involve small differences of large quantities (I2.1), calculated within the limitations of Hartree-Fock theory, we will only consider calculations of the changes in H_{hf} from the experimental free-ion value, brought about by the neighbouring ions.

The temperature dependence of the hyperfine fields in mixed systems has not received much attention in the literature, except in the case of small concentrations of magnetic ions in metals [40]. Simple molecular field theory, with nearest-neighbour interactions, plainly predicts that a magnetic ion must have at least one magnetic neighbour if it is to order at all, while more sophisticated effective field theories predict that it should have at least two [41].

1. TEMPERATURE VARIATION OF THE HYPERFINE FIELDS.

Although molecular field theory suffers from some well known defects, it has the virtue of covering the whole range of temperature from $T = 0$ to T_c, the magnetic ordering temperature, and it is not difficult to calculate. Furthermore, Z, the number of nearest neighbours, enters the equations in a direct way.

We will start by taking the usual approach in which a particular ion is isolated from the crystal, and the molecular field acting on it is determined self-consistently. The molecular field equations will be written down for a general situation, and then the results of the theory will be exhibited by calculating the case of nearest-neighbour interactions in a random distribution of magnetic and non-magnetic ions with $N = 6$. The effects of allowing for longer range interactions and the range of environments of the neighbours will be discussed, and then a better model in which the shell of neighbours is treated differently from the rest of the crystal is proposed. Applications to the analysis of experimental data are given in Chapter IV.

1.1 General Molecular Field Equations.

Since our interest is in Mössbauer spectra, we focus our attention on the f-ions which we suppose to be iron. Each ν-site has $N_{\nu i}$ neighbouring sites of type i which may be occupied by either f or g-ions; i labels both different crystal sites and different distance neighbours. A particular f-ion on a ν-site has $Z_{\nu i}$ f-neighbours and $(N_{\nu i} - Z_{\nu i})$ g-neighbours in the ith shell, with $J^{ff}_{\nu i}$ and $J^{fg}_{\nu i}$ as the appropriate exchange constants. The basic approximation of the molecular field theory [42] is to write the Hamiltonian for the magnetic interaction of an ion with its neighbours (1.12) in terms of an effective field H_ν

$$\mathcal{H} = -g\mu_B \bar{S}_z H_\nu \qquad (3.2)$$

H_ν depends on the environment, specified by the set of occupation numbers $\{Z_{\nu i}\}$, and $g\mu_B \bar{S}_{zi}$, the average value of the z-component of the magnetic moment of an ion on the sites of type i. The field is not defined unequivocally, because of the range of environments possible for the neighbours, and it is necessary to take an average, denoted $< >$, over all environments of the central ion which have the same set of occupation numbers, in order to obtain a unique value $H_\nu\{Z_{\nu i}\}$. We may now write the molecular field acting on the central iron ion as

$$H_\nu^f\{Z_{\nu i}\} = \frac{2}{g\mu_B} \sum_i [Z_{\nu i} J_{\nu i}^{ff} <\bar{S}_{zi}^f> + (N_{\nu i} - Z_{\nu i}) J_{\nu i}^{fg} <\bar{S}_{zi}^g>] \qquad (3.3)$$

A similar expression gives the molecular field acting on the g-ions.

The central result of molecular field theory is the relation between the average value of the magnetization of an ion and the molecular field it experiences. For the iron,

$$\bar{S}_{z\nu}^f\{Z_{\nu i}\} = S\mathcal{B}_S(g\mu_B S\, H_\nu^f\{Z_{\nu i}\}/kT), \qquad (3.4)$$

where $\mathcal{B}_S(y)$ is the appropriate Brillouin function, and $\hbar\sqrt{S(S+1)}$ is the angular momentum of the ion. There will be a pair of equations like (3.3) and (3.4) for each of the crystallographic sites, and there is another, similar set for the g-ions if they are also magnetic. A consistent solution of all these equations may be found, at least in principle, so that the averages $<\bar{S}_{z\nu}\{Z_{\gamma i}\}>_{av}$ and $<\bar{S}_{zi}>$ are the same. $<>_{av}$ indicates an average over all suitable sets of occupation numbers. The averaging process

is clear enough when x is so low that occupation numbers of zero have a negligible probability. However, when this is not true, $\langle \bar{S}_{zi} \rangle$ is not identical to the average value of the z-component of the spin of a particular species of ion on a ν-site, because only those ions with the central ion as a neighbour are counted in the $\langle\ \rangle$ average. The straightforward examples, discussed below, will illustrate the averaging process, and show how to take into account the tautology that the nearest neighbours of an f-ion always have at least one f-ion as a nearest neighbour.

From a practical point of view, if the macroscopic averages $\langle \bar{S}_{zi} \rangle$ can be determined experimentally, then equations (3.3) and (3.4) enable us to calculate $\bar{S}^{f}_{z\nu}\{Z_{\gamma i}\}$ for any environment of interest, provided the exchange constants are known. Conversely, if the values of $\bar{S}^{f}_{z}\{Z_{\nu i}\}$ are known for the different environments, then information about the exchange interactions can be deduced.

1.1.1 Ion and Crystal Model. Simple Treatment.

Magnetization curves and Mössbauer spectra will now be calculated for a very simple example. Suppose we have a crystal in which all the cation sites are equivalent, and they are occupied by a random mixture of iron and a non-magnetic substitution, so that x is the probability of finding a non-magnetic ion on any site. In addition, suppose that the only important exchange interactions, J, are between an iron and irons on six neighbouring sites. There are only seven different environments in such a material, $Z = 0, 1, \ldots, 6$, and their probabilities were listed in table 3. The

forest of sub- and superscripts on equations (3.3) and (3.4) vanish and they simply reduce to

$$H(Z) = \frac{2ZJ\langle\bar{S}_z\rangle}{g\mu_B} \tag{3.5}$$

and

$$\bar{S}_z(Z) = S\mathcal{B}_S(g\mu_B S\, H(Z)/kT) \tag{3.6}$$

Only nearest-neighbour ions with the central iron ion as a nearest neighbour are taken into account in the average $\langle\bar{S}_z\rangle$. Thus $\langle\bar{S}_z\rangle = \langle\bar{S}_z(Z)\rangle_{av}$, where the latter average is taken over environments with $Z = 1, 2, \ldots, 6$ only. It is convenient to introduce the reduced variables $\sigma(Z) = \bar{S}_z(Z)/S$, $\langle\sigma\rangle_{av} = \langle\bar{S}_z\rangle/S$ and $\tau = 3kT/2S(S+1)\,\mathcal{J}\langle Z\rangle_{av}$. Equations (3.5) and (3.6) are now combined to give the equation of state

$$\sigma(Z) = \mathcal{B}_S\left(\frac{3S\langle\sigma\rangle_{av} Z}{(S+1)\tau\langle Z\rangle_{av}}\right) \tag{3.7}$$

There is a unique magnetic ordering temperature, T_c, for all the iron in the crystal except the ions with $Z = 0$, which experience no effective field in this approximation, and consequently never order. For materials with $x < 0.5$, $P_6(0)$ is negligible, so that $\langle\bar{S}_z\rangle$ is the average value of the z-components of the spins of all the iron ions, and $\langle Z\rangle_{av} = 6(1-x)$. T_c is proportional to $\langle Z\rangle_{av}$, and it deviates slightly from linearity for $x > 0.5$, as shown in figure 22. The temperature dependence of the hyperfine fields in the different environments in materials with $x = 0.1$, 0.5, and 0.9 is displayed in figure 23, where curves are only shown

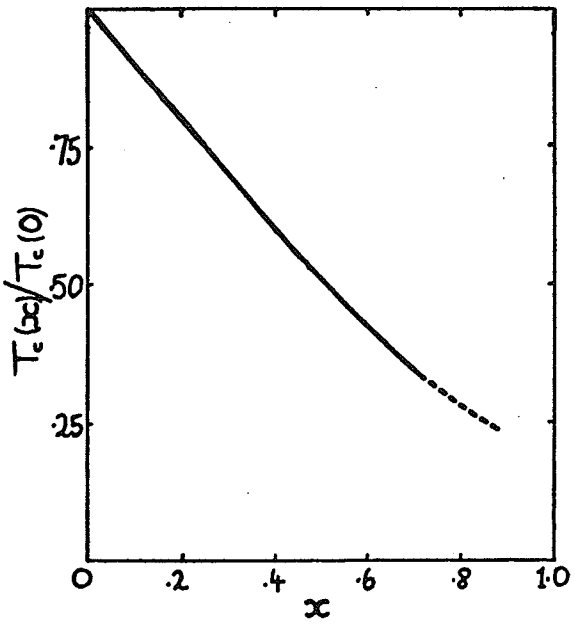

Figure 22. Theoretical variation of the magnetic ordering temperature as a function of concentration in a mixed system.

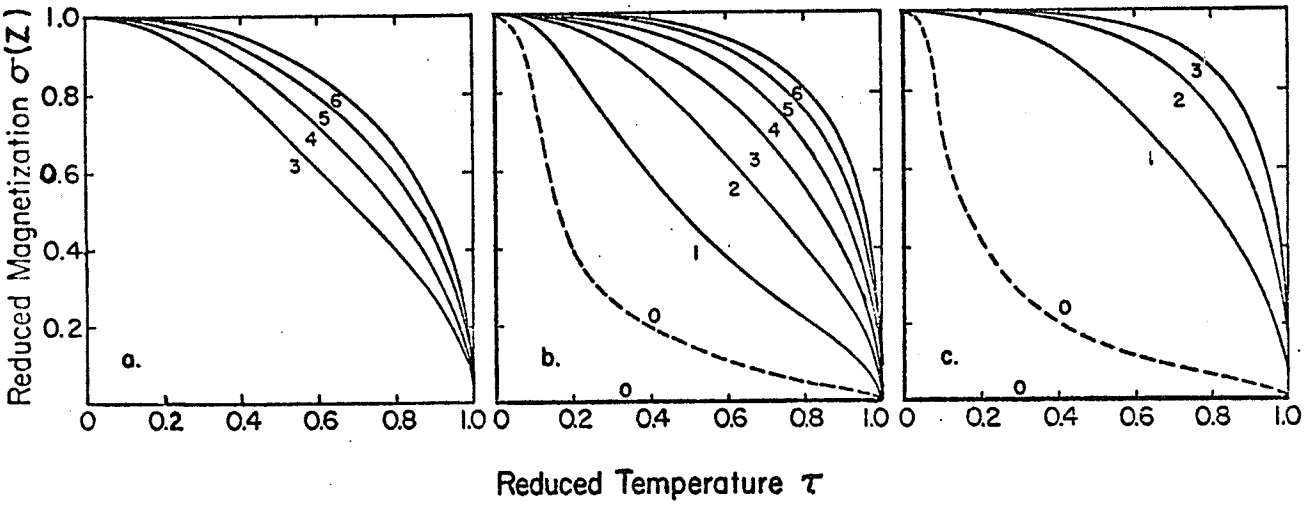

Figure 23. Temperature dependence of the magnetization of an iron ion in environments with various numbers of magnetic neighbours on six nearest-neighbour sites. Curves are drawn for materials with a random non-magnetic substitution of a) 10%, b) 50% and c) 90%. The dotted lines show the effect of a small, long-range interaction on the curve for iron with no iron neighbours.

for environments with a probability greater than 1%. A set of Mössbauer spectra derived from this temperature variation of the hyperfine fields in the material with $x = 0.5$ is shown in figure 24. Each environment is assumed to contribute a pattern of six Lorentzians of equal width and with an intensity ratio 3:2:1:1:2:3. The intensity of the pattern is proportional to the probability of the environment, (3.1), and the quadrupole and isomer shifts are taken to be zero. At $\tau = 0$, $\sigma(Z)$ is assumed to be 1 for all $Z \neq 0$, and an unbroadened six-line pattern results. In

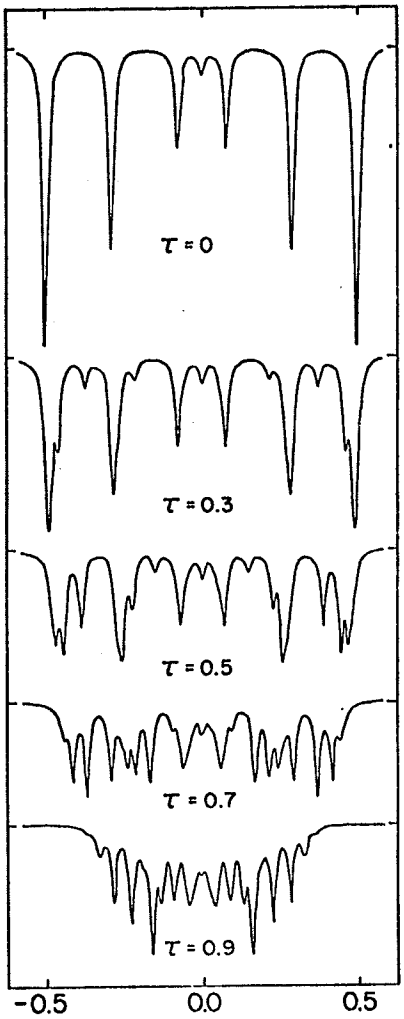

Figure 24. Mössbauer spectra of ^{57}Fe in a material with a 50% random non-magnetic substitution. They are derived directly from the temperature dependence of the hyperfine fields shown in figure 23b.

addition there is a small central peak for the 1.6% of the iron for which $\sigma(0) = 0$.

It must be admitted that the spectra in figure 24 bear only a slight resemblance to the ones that have been observed in mixed compounds. In practice, the numerous sharp peaks are not resolved [57 - 64]; and there is no central peak at low temperatures, even for quite high values of x. The main defects in the simple treatment are the assumptions of equal widths for all the lines, and strict nearest-neighbour interactions. In the improved treatment in the next section, these restrictions will be waived.

Although it is possible to calculate $\sigma(Z)$ for any value of x from (3.7), the model becomes quite unrealistic when $x \sim (N-1)/N$. Since we are assuming nearest-neighbour interactions, many of the iron ions, having no nearest neighbours, are obliged to behave like paramagnetic impurities. Most of the rest of them have only one iron neighbour, and they will be members of rather short chains of interacting ions which may be expected to behave as superparamagnetic clusters. The sizes of connected iron clusters were calculated in a $20\times20\times20$ array for various concentrations of iron distributed at random over the lattice points, and the results are given in table 4.

When $x < 0.67$, corresponding to more than two of the six neighbouring sites being occupied on average, most of the iron ions are connected. The remainder are isolated, or else in small clusters, because the probability of a medium-sized cluster having no ions on adjacent sites is small. When $x \sim 0.75$, there is a range of small

Table 4. Cluster-Sizes in an 8000-Point Cubic Array with Random Distributions of Vacancies.

x	Cluster-size	1	2	3	4	5	6	7	8-9	10-19	20-29	30-49	50-99	100-500	>500	Total
0.40	# of clusters	16		1											1	18
	% of total	0.3		0.1											99.6	100%
0.50	# of clusters	63	4	1	1	3	1								1	74
	% of total	1.6	0.2	0.1	0.1	0.4	0.1								97.5	100%
0.60	# of clusters	156	26	11	2	6	2								1	202
	% of total	4.9	1.6	1.0	0.3	0.9	0.4								90.9	100%
0.65	# of clusters	209	39	20	8	10	4	3	1	5	1				1	301
	% of total	7.5	2.8	2.2	1.1	1.8	0.9	0.8	0.3	2.5	0.8				79.3	100%
0.70	# of clusters	289	59	30	18	16	7	4	8	14	4	1	1	6		457
	% of total	12.2	5.0	3.8	3.0	3.4	1.8	1.2	2.8	8.0	4.2	2.0	2.2	50.4		100%
0.75	# of clusters	348	77	45	26	15	10	13	14	26	4	5	4			587
	% of total	17.7	7.9	6.9	5.3	3.8	3.1	4.6	5.7	17.2	4.6	10.5	12.7			100%
0.80	# of clusters	412	92	55	34	12	13	18	14	13	3	2				668
	% of total	26.5	11.9	10.6	6.6	3.9	5.0	8.8	7.7	9.9	4.8	4.3				100%
0.90	# of clusters	422	81	30	13	2	3		1							552
	% of total	55.4	21.3	11.8	6.8	1.3	2.4		1.0							100%

and medium cluster sizes. Note that the average cluster size is worthless information, except perhaps for x > 0.75 when they are almost all small, and the model is inapplicable.

1.1.2 Ion and Crystal Model. Improved Treatment.

We will first allow for the fact that the molecular field acting on an ion is not precisely defined by Z, but may take a range of values about $H(Z)$ because of the range of environments possible for the *neighbours*. Then the possibility of long-range interactions will be admitted.

The standard deviation in $H(Z)$ is

$$\Delta H(Z) = \frac{2SJ}{g\mu_B}\sqrt{Z \sum_{z=1}^{6} P_6'(Z)[\sigma(Z) - \langle\sigma\rangle_{av}]^2} \qquad (3.8)$$

The probability in this expression is a little different from $P_6(Z)$. The $Z = 0$ environments are ignored because each of the neighbours will always have the central ion as a nearest neighbour, so that $P_6'(Z) = P_6(Z)/[1 - P_6(0)]$. The deviation in $\sigma(Z)$ which corresponds to $\Delta H(Z)$ is

$$\Delta\sigma(Z) = (\partial\sigma(Z)/\partial H(Z))\Delta H(Z) \qquad (3.9)$$

The consequent line broadening, $\Delta\beta$, is $2\Delta\sigma(Z)$ and may be obtained from the last two equations

$$\Delta\beta = \frac{6\gamma S}{(S+1)\langle Z\rangle_{av}\tau}\frac{d\mathcal{B}}{dy}\sqrt{Z \sum_{z=1}^{6} P_6'(Z)[\sigma(Z) - \langle\sigma\rangle_{av}]^2} \qquad (3.10)$$

$\Delta\beta$ is in reduced units, and the constant γ is 1.000 for lines 1 and 6, 0.579 for lines 2 and 5 and 0.157 for lines 3 and 4.

Another source of line broadening is the range of dipolar fields produced by different numbers of magnetic neighbours, but this is small compared with $\Delta\beta$, except close to $\tau = 0$, and will be ignored here.

In insulators, the longer-range interactions are likely to be much weaker than the nearest-neighbour interactions, and arise from ions on many more sites. Hence it is reasonable to represent the longer-range interactions by a small, averaged term in the molecular field, and suppose that the single parameter, Z, is still adequate for defining the environment. The molecular field is now written as

$$H(Z) = \frac{2}{g\mu_B}\left(ZJ + \sum_{i>1} \langle Z_i \rangle_{av} J_i\right)\langle \bar{S}_z \rangle \qquad (3.11)$$

$\langle Z_i \rangle_{av}$ is the average number of iron-neighbours in the ith shell, and J_i their exchange interaction with the central ion. These longer- range interactions will influence the magnetic ordering temperature, and they will contribute a little extra broadening because of the distribution in Z_i. However their greatest effect is on iron ions in sites with no iron nearest neighbours. The magnetization curves of figure 23 were recalculated including a small extra constant term, taken as $0.1\langle Z \rangle_{av} J$, in the molecular field. It turns out that the shape of the curves for $Z > 0$ is barely altered, but the $Z = 0$ curve has the concave form shown by the dashed lines in figure 23b and c instead of following the axes.

Some Mössbauer spectra are shown in figure 25, which were calculated in the same way as the spectra in figure 24 except that the line broadening given by (3.10) and a small long-range interaction given by $\sum_{i>1} \langle Z_i \rangle_{av} J_i = 0.1\langle Z \rangle_{av} J$ in (3.11)

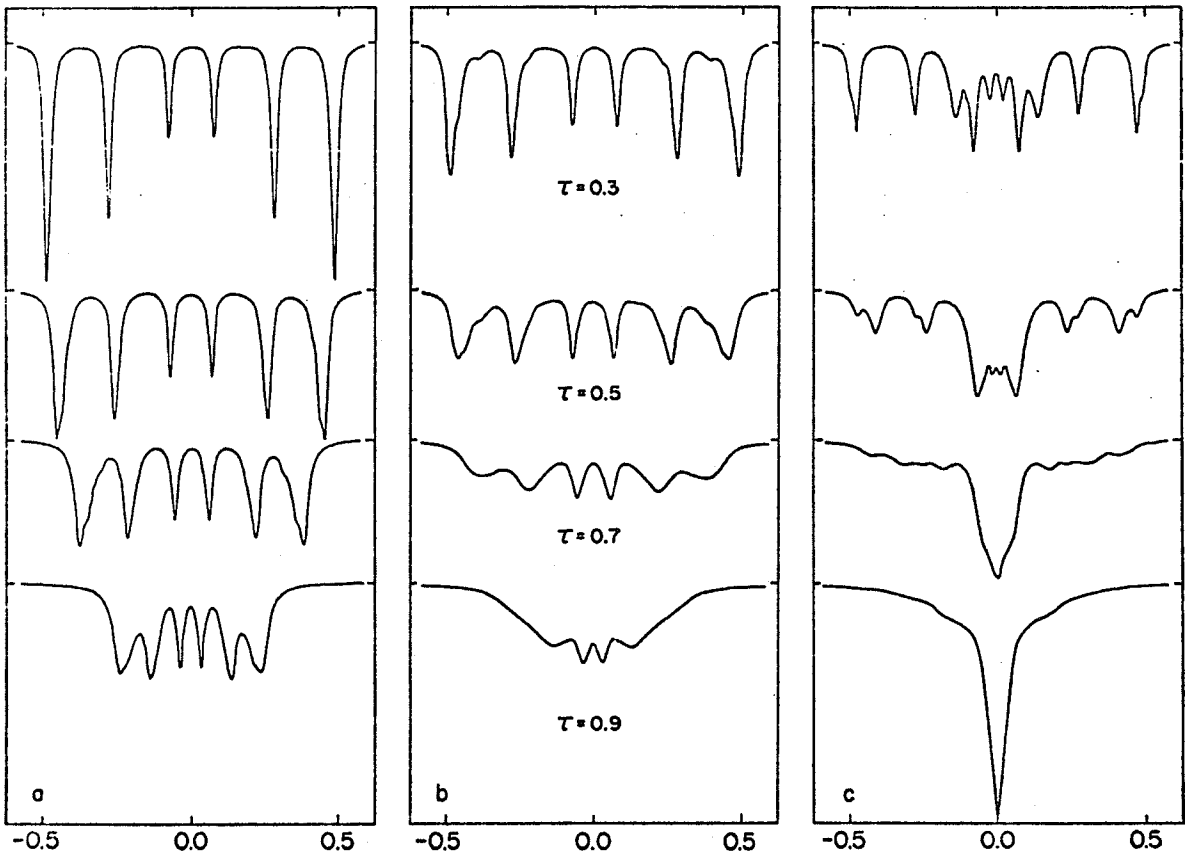

Figure 25. Mössbauer spectra of ^{57}Fe in materials with random, non-magnetic substitutions of a) 10%, b) 50% and c) 90%. They are obtained from the temperature dependence of the hyperfine fields, shown in figure 23, with a small long-range interaction, and the line-broadening effect taken into consideration.

have been taken into account. These spectra now bear a strong resemblence to experimental observations. The broadened lines with some sign of structure, and the 'triangular' spectrum of figure 25b have all been observed, for example, in figure 44. Nevertheless there is a small region of temperature, in the vicinity of the Curie point, where a magnetically ordered spectrum co-exists with a central 'paramagnetic' peak. The static theory given in this chapter is unable to explain these spectra, and an experimental

investigation of them is presented in Chapter VI. They can occur for quite small values of the diamagnetic substitution, x, and even in 'pure' materials. The spectrum in figure 25c which shows a large central peak is not of this type. Rather the peak is simply due to the 53% of the iron with no iron nearest neighbours.

It is desirable to calculate the shape of the magnetization curves just below the Curie point to a better degree of approximation, and this will be done by taking the influence of the central iron on its neighbours into account explicitly.

1.2 Ion, Shell and Crystal Model.

In the last two paragraphs we considered the interaction of a single ion with the rest of the crystal, which is scaled by a factor Z, and adjusted for self-consistency. We now divide the crystal into three parts, shown schematically in figure 26b, instead of the previous two. The usual molecular field equations for the central ion and an ion in its shell of neighbours may be written;

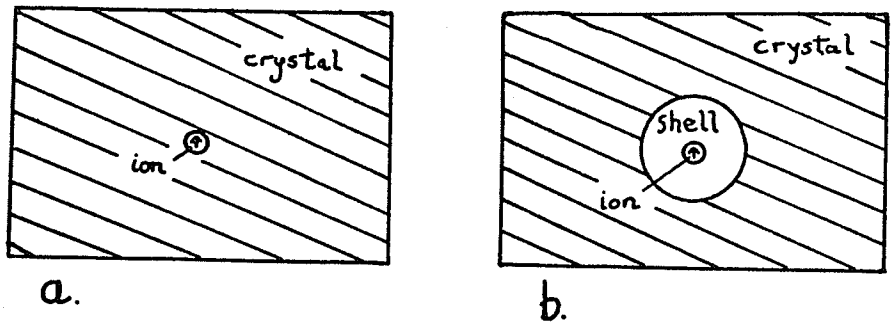

Figure 26. Schematic representations of a) the ion and crystal model, and b) the ion, shell and crystal model.

$$\sigma_{central}(Z) = \mathcal{B}_S(g\mu_B S\, H_{central}(Z)/kT)$$

$$H_{central} = 2ZJS\langle\sigma\rangle_{shell}/g\mu_B$$

$$\langle\sigma\rangle_{shell} = \mathcal{B}_S(g\mu_B S\, H_{shell}/kT)$$

$$H_{shell} = 2[(\langle Z\rangle - 1)JS\langle\sigma\rangle_{av} + JS\sigma_{central}(Z)]/g\mu_B.$$

Combining these equations we find that

$$\sigma(Z) = \mathcal{B}_S\left\{\frac{2ZJS^2}{KT}\mathcal{B}_S\left\{\frac{2JS^2}{KT}[(\langle Z\rangle - 1)\langle\sigma\rangle_{av} + \sigma(Z)]\right\}\right\} \qquad (3.12)$$

The suffix 'central' has been dropped. Equation (3.12) may be solved self-consistently for $\sigma(Z)$. Note that it reduces to (3.7) if $\sigma(Z) = \langle\sigma\rangle_{av}$.

The solution was computed by iteration. For a given value of the parameter J/kT, trial values of $\sigma(Z)$ are used on the right-hand side, $\langle\sigma\rangle_{av} = \sum_{Z=0}^{6} P_6(Z)\sigma(Z)$, and new values of $\sigma(Z)$ are computed. The convergence was rather slow. The calculated curves for $N = 6$ and $x = 0$, 0.3, 0.5 and 0.7 are shown in figure 27. The variation of the magnetic ordering temperature with x is similar to that shown in figure 22. Note that the horizontal scale in figure 27 is proportional to temperature whereas the scale in figure 23 is reduced temperature.

Although the difference between this model and the previous one seems insubstantial - the interaction of the central ion with its shell of neighbours is included explicitly, instead of in an averaged manner - the quantitative differences between the two

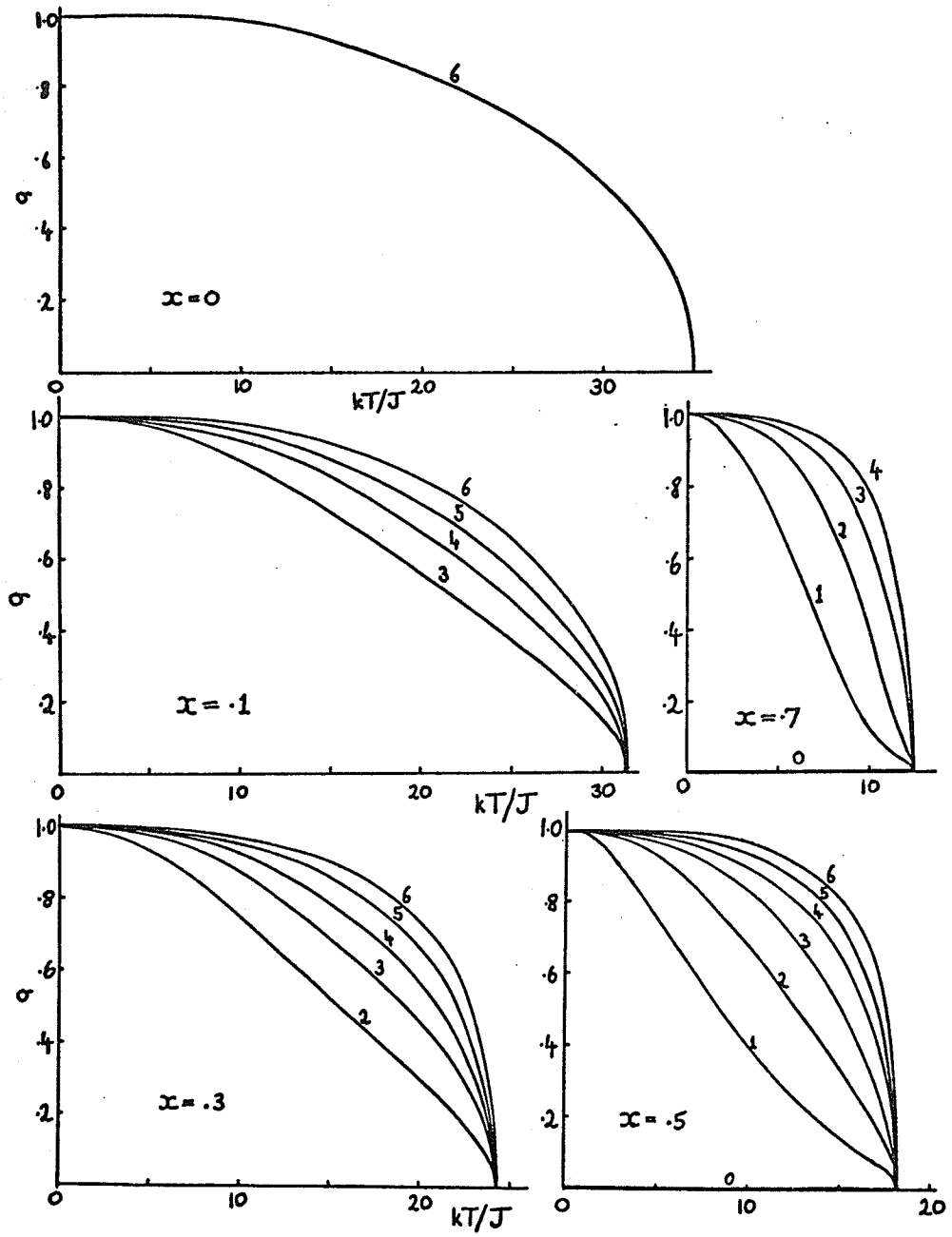

Figure 27. Temperature dependence of the magnetization of an iron ion in materials with various non-magnetic concentrations, calculated on the ion, shell and crystal model.

models are considerable, close to the magnetic ordering temperature. Figure 28 illustrates the fact that the spread of hyperfine fields is larger for the present theory, and the greater tendency towards concave magnetization curves for small values of N. However for $\tau < 0.5$ and $x < 0.5$ the differences are small, and the ion and crystal model will be used because it is easier to calculate.

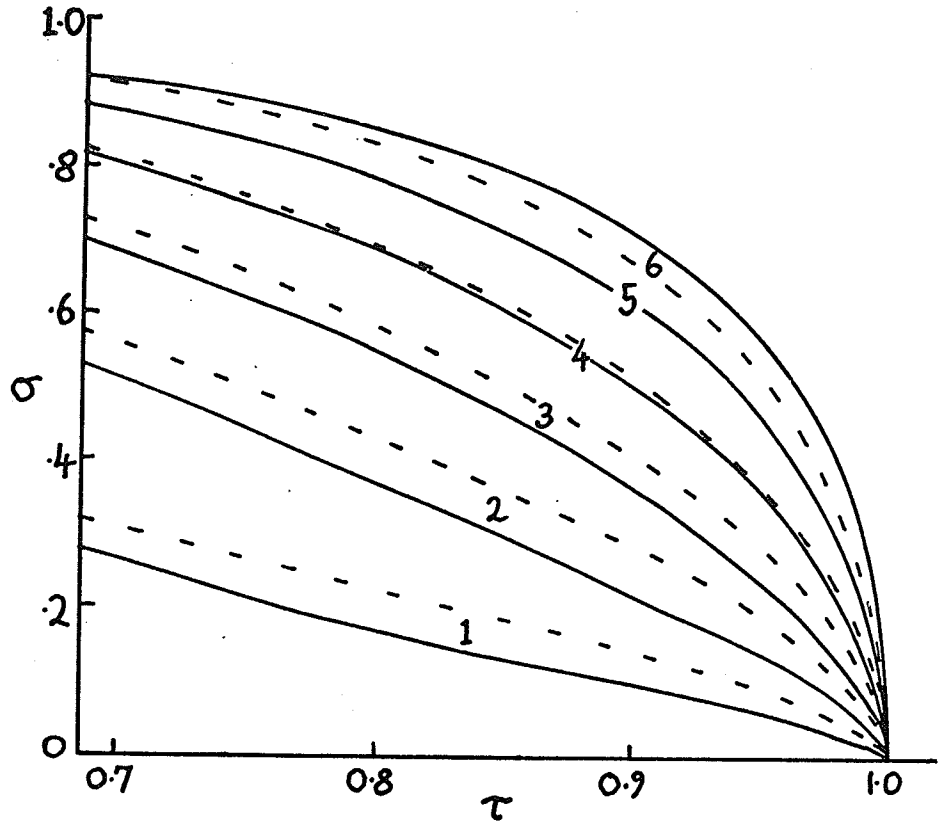

Figure 28. Comparison of predictions of the ion and crystal model, ---------- , and the ion, shell and crystal model, ———————— , for a material with a 50% non-magnetic substitution.

In molecular field theory, there can only be one magnetic ordering temperature, and ions which are very weakly bound to the rest of the crystal, for example ions with Z = 1, or the rare

earth ions in garnets, order at the same temperature as ions with the strongest exchange interactions. It is unlikely that any static effective field theory can predict a range of ordering temperatures, because once the effective field appears, it influences the entire crystal.

As a comparison of theory and experiment, in Figure 29 we have reproduced the hyperfine field data of Czer et al [38] on $(Zn_{0.34}Mn_{0.66})\ Fe_2O_4$ obtained by fitting the absorption spectra to four subspectra whose intensities are given by (3.1), together with the curves predicted by (3.7). $P_6(Z)$ represents the probability that a B-site iron ion will have Z manganese and (6-Z) zinc ions as A-site neighbours, and J is the Fe-Mn superexchange interaction,

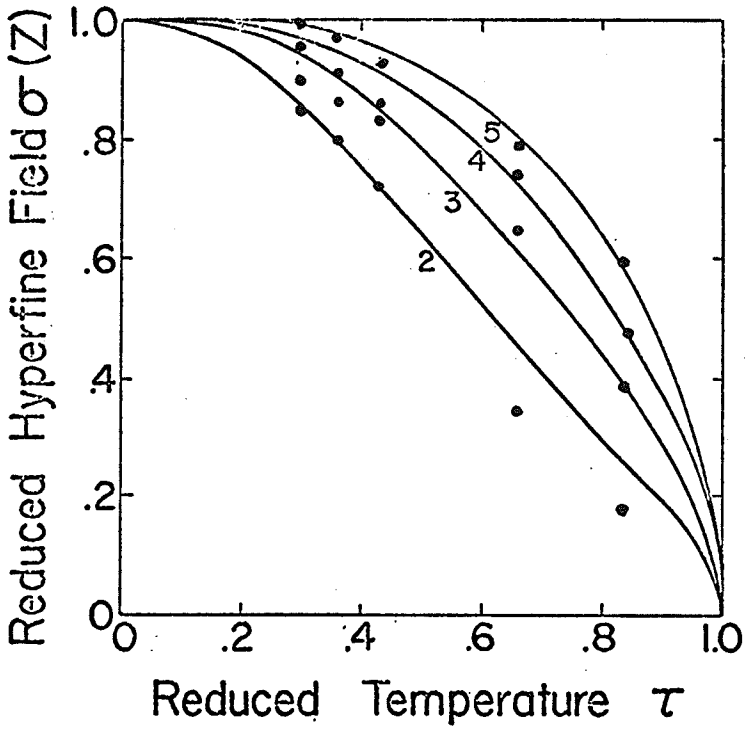

Figure 29. Comparison of the hyperfine fields in $(Zn_{0.34}Mn_{0.66})Fe_2O_4$ with the predictions of equation (3.7).

fixed by the relation $T_c = 2S(S+1)ZJ/3K$. There are no adjustable parameters apart from vertical normalisation, and all the curves are normalised to the same field at $\tau = 0$. The agreement is as good as may reasonably be expected. A concave magnetization curve for $Z = 2$ is in agreement with the theory.

The molecular field theory developed here is capable of predicting the Mössbauer spectra of substituted systems, provided the temperature is not so close to the ordering temperature that dynamic spin fluctuations are important, and provided the concentration of non-magnetic substitution is not too high. Large non-magnetic substitutions may also have the effect of altering the spin arrangement. The main defect of molecular field theory is that it fails to take into account properly the localised nature of the exchange interactions [43]. The molecular field is formally equivalent to an infinite range interaction [44], and it is unable to allow for local time-fluctuations just below T_c. In a dilute system the degree of magnetic order must depend on the geometry of the exchange paths, and the present theory can only approximate the real geometry in a very crude way.

2. HYPERFINE FIELDS AT ABSOLUTE ZERO.

Three factors, which influence the hyperfine field at the nucleus of an ion at $\tau = 0$ according to its magnetic environment, are the dipolar field, the zero-point spin deviation, and the super-transferred hyperfine field. We will briefly review each contribution.

2.1 Dipolar Fields.

If we ignore orbital contributions to the hyperfine field, the dipolar field is obtained by summing the contributions due to the electronic moments on each site.

$$H_{dip} = -gg_I\mu_B\mu_N \sum \left(\frac{3(\vec{S}.\vec{r})(\vec{I}.\vec{r})}{r^5} - \frac{\vec{S}.\vec{I}}{r^3} \right) \qquad (3.13)$$

The sum is over all the lattice sites in the vicinity of the central ion which are occupied by a magnetic ion. It must be extended to fairly distant neighbours because $H_{dip} \sim 1/r_i$, where r_i is the radius of the ith shell. The contribution of a single ion on an adjacent site is $\sim$ 1 kOe, and the total dipolar field $\sim$10 kOe.

At sites with cubic point symmetry in a pure compound, for example the A sites in Fe_3O_4, $H_{dip} = 0$. However H_{dip} may be quite large in a substituted system, although $\langle H_{dip} \rangle = 0$. Even in a pure compound there can be different dipolar fields at sites which are crystallographically equivalent. For example, the dipolar field at room temperature is 2.3 kOe for three-quarters of the B sites in Fe_3O_4 and 4.0 kOe for the remaining quarter.

2.2 Zero-Point Spin Deviations.

It is well known that the correct antiferromagnetic ground state is not the one with alternate spins exactly antiparallel, but there is a small spin deviation, even at absolute zero [45]. There has been some confusion as to whether the zero point spin deviation of a magnetic ion is increased [46] or decreased [47] by a diamagnetic neighbour, but the latter is probably true [48]. However, according

to van der Braak, a diamagnetic neighbour in an antiferromagnet will only change the spin *deviation* by 6%. Thus the net effect is quite negligible. Calculations of the effect have also been made for ferromagnets [49].

2.3 Supertransferred Hyperfine Fields.

Attempts to measure the zero point spin deviation in antiferromagnets led to the postulation of a supertransferred hyperfine field [50]. The interaction $A\,\vec{S}_z.\vec{I}$, where A is the hyperfine coupling constant, may be measured by e.s.r., n.m.r., and the Mössbauer Effect. Attempts to deduce $(S-\bar{S}_z)$ by taking values of A from e.s.r. on paramagnetic salts led to values of $\bar{S}_z/S > 1$. Owen and Taylor [50] suggested that the value of A should be different in dilute and concentrated magnetic compounds because of the transfer of unpaired spin from one magnetic cation to another.

The transfer of spin (and charge) density to a ligand nucleus from an adjacent cation by overlap and covalency produces a transferred hyperfine field [51]. The supertransferred hyperfine field, by analogy with superexchange, is a similar effect, except that it is detected at the cation site, and the anion is an intermediary between two cations. It has been observed in several compounds [52] and a recent study of Sn-doped garnets [53] shows that it is almost exclusively a nearest-neighbour effect.

The influence of the transferred charge density, from oxygen to iron, on the isomer shift is discussed by Simanek [54];

it depends strongly on the iron-oxygen separation. The supertransferred charge density is rather small.

The supertransferred field is a result of the overlap distortion of a central iron's s-orbitals by the s- and p-orbitals of the ligand. These themselves have been partially unpaired by a transfer of spin into a neighbouring 3d orbital. Van der Woude and Sawatzky [55] have given a quantitative expression for the unpaired spin and charge density at an iron nucleus in an antiferromagnet by considering the extended octahedral complex shown in figure 30. A central Fe^{3+} cation with spin ↑ is surrounded by an octahedron of Fe^{3+} nearest neighbours with spin ↓. By forming compound orbitals

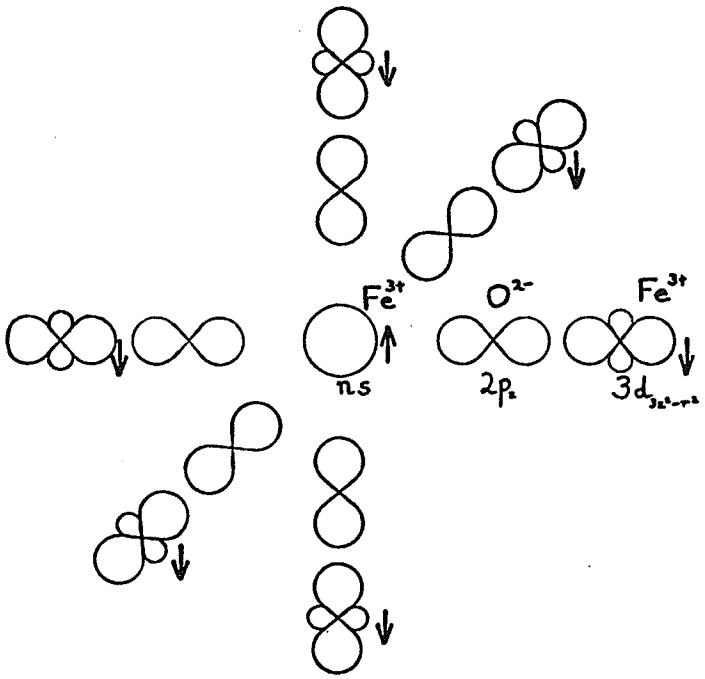

Figure 30. Extended octahedral complex used to calculate the charge and unpaired spin densities at the central nucleus.

with a_{1g} symmetry, the charge and net spin density at the central nucleus may be written, in terms of the electronic charge and spin, as;

$$P = \sum_{n=1}^{3} \{[\phi_{ns}^{\uparrow}(0)]^2 + [\phi_{ns}^{\downarrow}(0)]^2\} + 6N^{\uparrow 2}[-\sum_{n=1}^{3} S_{ns}^{\uparrow}\ \phi_{ns}^{\uparrow}(0) + a_{4s}^{\uparrow}\ \phi_{4s}^{\uparrow}(0)]^2$$

$$+ 6N^{\downarrow 2}[-\sum_{n=1}^{3} S_{ns}^{\downarrow}\ \phi_{ns}^{\downarrow}(0) + a_{4s}^{\downarrow}\ \phi_{4s}^{\downarrow}(0)]^2 \qquad (3.14)$$

and

$$\Sigma = \sum_{n=1}^{3} \{[\phi_{ns}^{\uparrow}(0)]^2 - [\phi_{ns}^{\downarrow}(0)]^2\} + 6N^{\uparrow 2}[-\sum_{n=1}^{3} S_{ns}^{\uparrow}\ \phi_{ns}^{\uparrow}(0)$$

$$+ a_{4s}^{\uparrow}\ \phi_{4s}^{\uparrow}(0)]^2 - 6N^{\downarrow 2}[-\sum_{n=1}^{3} S_{ns}^{\downarrow}\phi_{ns}^{\downarrow}(0) + a_{4s}^{\downarrow}\phi_{4s}^{\downarrow}(0)]^2 \qquad (3.15)$$

In these expressions $\phi_{ns}(0)$ are the s-wave functions of the central Fe^{3+} ion, evaluated at the nucleus, a_{4s} is the transfer coefficient for an oxygen $2p$ electron into the unoccupied $4s$ shell of the central ion, and S_{ns} are the overlap integrals $\langle\phi_{ns}|2p_z\rangle$. The transfer and overlap integrals involving $1s$ and $2s$ electrons are neglected, and the normalization constants $N\uparrow$ and $N\downarrow$ are given by

$$N^{\uparrow 2} = [1 + B_{\sigma}{}^2 + 2B_{\sigma}S_{\sigma} - 6\sum_{n=1}^{3} S_{ns}^{\uparrow 2} + 6\ a_{4s}^{\uparrow 2} + 12\ a_{4s}^{\uparrow}\ S_{4s}^{\uparrow}]^{-1}$$

and

$$N^{\downarrow 2} = [1 - S_{\sigma}{}^2 - 6\sum_{n=1}^{3} S_{ns}^{\downarrow 2} + 6\ a_{4s}^{\downarrow 2} + 12\ a_{4s}^{\downarrow}\ S_{4s}^{\downarrow}]^{-1} \qquad (3.16)$$

where B_{σ} is the transfer integral for oxygen $2p_z$ electrons into the $3d\uparrow$ orbital of the neighbouring iron, and S_{σ} is $\langle 2p_z|3d_{3z^2-r^2}\rangle$.

The first terms in (3.14) and (3.15) are the free-ion charge

and spin densities, and the other terms represent the overlap distortion of the central s-orbitals and the transfer of oxygen p-electrons into the central 4s-orbital and into the 3d orbitals of the neighbouring iron ions.

The supertransferred hyperfine field is really due to the fact that $N\uparrow$ and $N\downarrow$ are unequal, because of the transfer of $2p\uparrow$ electrons from the oxygen into the unoccupied $3d\uparrow$ shells of the neighbouring ions. If we take $S^{\uparrow}_{ns}$ and $S^{\downarrow}_{ns}$ equal to the average overlap integral, $\phi^{\uparrow}_{ns}(0)$ and $\phi^{\downarrow}_{ns}(0)$ equal to their average value and $a^{\uparrow}_{4s}$ and $a^{\downarrow}_{4s}$ equal, then the following expression, [55], gives the supertransferred hyperfine field in kiloersteds

$$H_{Sthf} = -525\, N^{\uparrow 2} N^{\downarrow 2}\, 6A_{\sigma}{}^{2}\left[-\sum_{n=1}^{3} S_{ns}\phi_{ns}(0) + a_{4s}\phi_{4s}(0)\right]^{2} \qquad (3.17)$$

where [56] $A_{\sigma} = (B_{\sigma} + S_{\sigma})$. (3.18)

H_{Sthf} will naturally be zero if the neighbouring cations are diamagnetic.

A discussion of the supertransferred hyperfine field in spinel ferrites is given by Sawatzky et al [56], who show that this factor can explain the difference between the $Fe^{3+}(A)$ and $Fe^{3+}(B)$ hyperfine fields. The contribution at a $Fe^{3+}(B)$ nucleus is 12 kOe for each $Fe^{3+}(A)$ neighbour, so that the supertransferred hyperfine field contributes 72 kOe or 14% of the magnitude of $H_{hf}(B)$ in $NiFe_2O_4$, for example. The corresponding contribution at a $Fe^{3+}(A)$ nucleus is 8 kOe, the difference being related to the greater covalency of the Fe(A) - O bond, as compared to the Fe(B) - O bond.

IV Hyperfine Interactions in the System $(Fe_{1-x}Rh_x)_2O_3$

No investigation, no right to speak. - Mao Tse-tung.

Although a number of investigators have collected Mössbauer spectra of diagmagnetically substituted magnetic oxides, most of the explanations of the observed spectra have been qualitative, and there have been no reports in the literature of a comprehensive investigation encompassing a wide range of temperature and diamagnetic concentration. There have been studies of hematite with Rh [57] and Ga [58] doping, magnetite with Zn [59] and Ga [39] as well as studies of several other spinels [38, 60-62] and garnets [63, 64]. A common feature of the spectra of all these materials, in the magnetically ordered region, are the broad lines with a temperature-dependent linewidth and shape. A theoretical basis for understanding the spectra has been outlined in the last chapter, and we will now describe our experiments on the iron-rhodium oxide system.

The reasons for selecting this particular system for study are that αFe_2O_3 has a single iron site, and consequently a simple six-line spectrum, and also that a complete range of solid solutions of Fe_2O_3 and Rh_2O_3 can be made. The system was first prepared and studied by Krén et al [65], using x-ray and neutron diffraction.

They found that the mixed oxides all had the corundum structure, and that they were homogeneous with no sign of cation ordering. Furthermore, there was no evidence for any change in the magnetic structure of those materials with $x > 0.05$ at room temperature. Some Mössbauer spectra of the compounds were reported by members of the same group [57].

Before discussing our own Mössbauer spectra, it is first necessary to describe the crystallographic and magnetic properties of the system.

1. CRYSTALLOGRAPHY AND SAMPLE PREPARATION.

Rhodium sesquioxide is generally supposed to have the corundum structure, on the basis of an early x-ray study by Lunde [66]. The structure was delineated by Belov in 1945 [67], but there have been no modern refinements. Since we require a knowledge of the cation-oxygen distances in the mixed system in order to interpret the quadrupole interaction and isomer shift data, we need to know the structures of, at least, the two end members. Good single crystal measurements were recently reported for αFe_2O_3 [68] but they are lacking for αRh_2O_3. A determination of the structure of Rh_2O_3 was, therefore, a prerequisite for our work.

1.1 Crystal Structure of αRh_2O_3.

It seems that single crystals of all the corundum structure sesquioxides may be grown, except for Rh_2O_3; thus it was necessary

to resort to powder methods for the structure refinement. A recent attempt, at 65 kbar and 1200°C, led to crystals of an orthorhombic modification [69] which we will call γRh_2O_3. Another orthorhombic form, which we refer to as βRh_2O_3, has also been reported [70]. It is obtained when αRh_2O_3, the usual corundum structure form, is subjected to prolonged heating above 750°C.

The sample used for our x-ray measurements was a grey powder of reagent grade Rh_2O_3 [11], which was reported to contain 80.91% Rh by weight. The only impurities detected by x-ray fluorescence were 0.2% Pd, 0.1% Ru, and 0.1% Sn. Pure Rh_2O_3 is 81.09% Rh by weight.

It was clear from the diffractometer trace that only about 90% of the oxide was in the α-form, the remainder being βRh_2O_3. However, when the orthorhombic powder pattern was subtracted off, all the remaining lines could be assigned indices consistent with the space group $R\bar{3}c$. The overlapping was significant for the hexagonal reflections 012, 104, 110, 024, 211, 134 and 1, 1, 12. All the line positions were measured on Debye-Scherer photographs, while their integrated intensities were obtained from the diffractometer trace. However the intensity of the highest angle reflection, 324, had to be estimated from the powder photographs, because the diffractometer can only scan up to $2\theta = 160°$. All the measurements were made at 23°C using FeKα radiation and the doublet was well resolved at high angles. The powder pattern for αRh_2O_3 is given in Table 5.

We find that $a_H = 5.127 \pm 0.001\text{Å}$ and $c_H = 13.853 \pm 0.004\text{Å}$, the corresponding rhombohedral parameters being $a_R = 5.484\text{Å}$ and

Table 5. X-ray Powder Pattern for αRh_2O_3.

h	k	l	d_{obs}	d_{calc}	I/I_1
0	1	2	3·68 Å	3·738 Å	53
1	0	4	2·731	2·731	88
1	1	0	2·567	2·564	100
0	0	6	2·309	2·309	11
1	1	3	2·242	2·241	7
2	0	2	2·116	2·114	6
0	2	4	1·870	1·869	37
1	1	6	1·717	1·716	53
2	1	1	1·667	1·666	1
1	2	2	1·633	1·631	7
0	1	8	1·615	1·613	2
2	1	4	1·512	1·510	33
3	0	0	1·482	1·480	30
1	2	5	1·436	1·436	1
2	0	8	1·366	1·365	1
1	0	10	1·321	1·322	16
1	1	9		1·320	
2	2	0	1·281	1·282	15
2	1	7		1·280	
0	3	6	1·245	1·246	16
2	2	3	1·236	1.235	1
3	1	2	1·213	1·213	4
1	2	8	1·205	1·205	1
0	2	10	1·175	1·175	17
1	3	4	1·161	1·160	22
0	0	12	1·154	1·154	1
2	2	6	1·121	1·121	25
0	4	2	1·096	1·096	2
2	1	10	1·068	1·068	36
4	0	4	1·057	1·057	12
1	1	12	1·053	1·053	6
3	2	1	1·014	1·016	1
2	3	2	1·008	1·008	4
1	2	11		1·007	
3	1	8	1·003	1·004	5
3	2	4	0·9773	0·9773	90*

* Estimated from photographs.

$\alpha = 55°44'$ The calculated density is 8.02 $g.cm^{-3}$. It is convenient to index the powder pattern in terms of the hexagonal cell, but for some purposes the rhombohedral co-ordinates are more suitable. The structure factor takes a particularly simple form in the rhombohedral system:

$$F_{calc} = 2f_0(\sin 2\pi(h-k)u + \sin 2\pi(k-\ell)u + \sin 2\pi(\ell-h)u); (h+k+\ell)\text{odd}$$

and (4.1)

$$F_{calc} = 2f_0(\cos 2\pi(h-k)u + \cos 2\pi(k-\ell)u + \cos 2\pi(\ell-h)u) + 4f_{Rh} \cos 2\pi(h+k+\ell)w;\ (h+k+\ell)\text{even}.$$

f_0 and f_{Rh} are the atomic scattering factors for O^{2-} and Rh^{3+}, and u and w are the oxygen and rhodium special position parameters. In order to determine these parameters, together with the temperature factor, B_t, we used a computer to minimize the residual:

$$R = \sum|F_{obs}| - |F_{calc}|/\sum|F_{obs}|, \qquad (4.2)$$

where F_{obs} and F_{calc} are the observed and calculated structure factors. The former are related to the intensity of the reflection by the equation

$$I \propto j[(1 + \cos^2 2\theta)/(\cos\theta \sin^2\theta)]F_{obs}^2 \exp[-B_t(\sin\theta/\lambda)^2] \qquad (4.3)$$

where j is the multiplicity of the reflection. No corrections were made for anomalous scattering. Only the 24 lines which were observed, resolved, and did not appreciably overlap rhombohedral lines were used in the calculation of R. The resulting values are $u = 0.295 \pm 0.010$, $w = 0.098 \pm 0.001$ and $B_t = 1.2 \pm 0.4$. The corresponding minimum value of R was 13.4%, which is not unreasonable for this powder refinement. The equivalent hexagonal parameters are $x(O) = 0.295 \pm 0.010$ and $z(Rh) = 0.348 \pm 0.001$. It was also possible to obtain values of u, w; and B_t consistent with these by minimising $\sum W(|F_{obs}| - |F_{calc}|)^2$, regardless of whether W is taken as 1, F_{obs}^{-2}, or a function similar to the one proposed by Evans [71]. Finally we recalculated R using all 33 observed reflections, and found $R = 13.2\%$. The observed and calculated structure factors appear in table 6, and the 24 used for the structure determination are marked with a dagger.

The structure may be regarded as an arrangement of hexagonal close-packed oxygen layers, normal to the c-axis, which is distorted by the presence of small rhodium cations in two-thirds of the

Table 6. Structure Factors for αRh_2O_3.

h	k	l	F_{obs}	F_{calc}	h	k	l	F_{obs}	F_{calc}
0	1	2	52·0	58·4	2	2	3†	27·9	−11·5
1	0	4	96·2	−108·4	1	3	1†	10·5	−3·5
1	1	0	156·9	127·2	3	1	2†	36·4	40·0
0	0	6†	104·7	−85·8	1	2	8†	19·6	20·1
1	1	3†	35·9	26·5	0	2	10†	98·5	98·5
2	0	2†	35·7	38·2	1	3	4	75·8	−74·9
0	2	4	101·8	−107·1	0	0	12†	66·0	61·8
1	1	6†	135·8	−120·0	3	1	5	—	−3·2
2	1	1†	16·7	8·7	2	2	6†	113·4	−92·1
1	2	2†	37·3	38·0	0	4	2†	32·8	42·5
0	1	8†	28·8	29·3	2	1	10†	88·5	95·0
2	1	4†	87·3	−94·9	4	0	4†	70·8	−66·1
3	0	0†	121·3	135·2	1	1	12	48·8	36·4
1	2	5†	13·9	7·4	3	2	1†	11·8	−6·5
2	0	8†	20·5	19·3	2	3	2	—	26·1
1	0	10	—	112·4	1	2	11	—	5·2
1	1	9	—	15·7	3	1	8†	25·2	24·2
2	2	0	—	100·8	2	2	9	—	−9·1
2	1	7	—	6·5	3	2	4	76·1*	−76·9
0	3	6†	68·3	−75·9					

* Estimated.
† These reflexions were used in the determination of u, w and B.

octahedral interstices. Compared to αFe_2O_3 [68, 72], the cations lie closer to the planes mid-way between the oxygen layers, and the oxygen octahedra are more distorted, because Rh^{3+} has an ionic radius of 0.68Å compared to 0.64Å for Fe^{3+}. Within an oxygen octahedron, one of which is shown in figure 31, the distance between adjacent oxygen ions in the same layer is either 2.62 ± 0.09 or 3.14 ± 0.05Å, and the distance between adjacent oxygen ions in different layers is 2.78 ± 0.02 or 2.94 ± 0.02Å. The separation of a c-axis cation pair, r_c, is 2.72 ± 0.02Å, and of a basal plane pair, r_a, is 3.03 ± 0.01Å. In table 7 these distances are compared with those found in the other common corundum-structure sesquioxides, from single-crystal structure refinements [68, 73]. It is interesting to note that the average Rh-O distance and r_a both agree exactly with the values recently predicted for αRh_2O_3 by Prewitt et al [74], but the value of r_c is lower than their

Table 7. Cation-Cation Separations in Corundum-Structure Sesquioxides.

Oxide	Cation electron configuration	r_c	r_c/c_H	r_a	r_a/a_H
Al_2O_3	$2p^6$	2·65 Å	0·204	2·79 Å	0·586
Ti_2O_3	$3d^1$ (t_{2g}^1)	2·59	0·190	2·99	0·581
V_2O_3	$3d^2$ (t_{2g}^2)	2·70	0·193	2·88	0·582
Cr_2O_3	$3d^3$ (t_{2g}^3)	2·65	0·195	2·89	0·583
Rh_2O_3	$4d^6$ (t_{2g}^6)	2·72	0·196	3·03	0·590
Fe_2O_3	$3d^5$ ($t_{2g}^3 e_g^2$)	2·900	0·211	2·971	0·590
Ga_2O_3	$3d^{10}$ ($t_{2g}^6 e_g^4$)	2·835	0·211	2·938	0·590

prediction. A somewhat short cation-cation distance, 2.80Å, is also found in γRh_2O_3 [69]. This suggests that there might be some cation-cation bonding between low spin Rh^{3+} ions.

1.2 Crystal Structure, Preparation and Analysis of the Mixed System.

Part of the corundum structure, the structure of all the oxides in the system, is shown in figure 31. For the sake of clarity, only the oxygen octahedron co-ordinating the central cation, A_1, is shown, and some of the shortest cation-anion-cation linkages are drawn. The remainder may be generated by three-fold rotation about the c-axis. Information about the number and geometry of each sort of linkage, and also the lattice and special position parameters for the end members of the series are given in table 8. The special position parameters x (oxygen) and z (cation) show how distorted the structure is from the ideal of hexagonal close packed oxygen layers, whose spacing is $c_H/6$, with honeycomb cation layers mid-way between them. In this case, $x = z = 1/3$. In fact, half of the cations in each of the honeycomb layers are slightly above, and the other half are the same distance below the planes

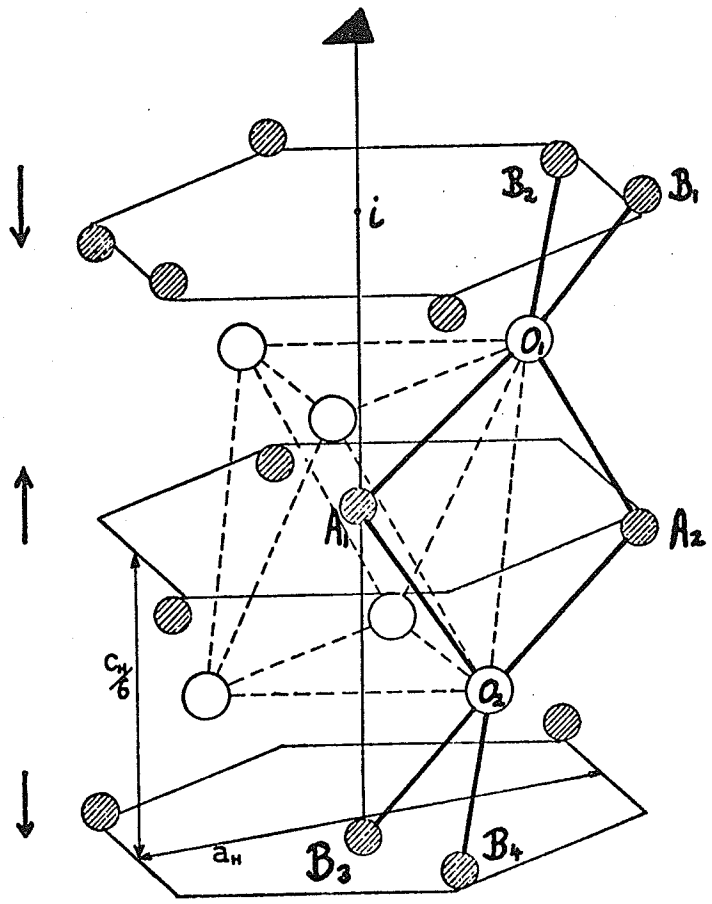

Figure 31. ○ O^{2-} ◍ M^{3+} Part of the hexagonal cell of the corundum structure; the complete cell is six layers high. *i* is a centre of inversion. The octahedron of oxygens co-ordinating the central cation is indicated by dashed lines, and the solid lines show the principal cation-anion-cation linkages. The spin arrangement shown applies to $(Fe_{1-x}Rh_x)_2O_3$ below the Morin Transition.

Table 8. Cell and Bond Dimensions in αFe_2O_3 and αRh_2O_3.

	a_H Å	c_H Å	x(oxygen)	z(cation)	p(= A_1O_1) Å	q(= A_1O_2) Å
αFe_2O_3	5.0346	13.752	0.3072	0.3553	1.941	2.118
αRh_2O_3	5.127	13.853	0.295	0.348	2.07	2.03

Type	Examples	Exchange Constant	Number of equivalent cations	Sign of J	Length	Angle αFe_2O_3	Angle αRh_2O_3
Γ_a	$A_1O_1B_1;A_1O_2B_4$	J_4	6	-	p-q;q-p	131°29'	133°52'
Γ_b	$A_1O_1B_2$	J_3	3	-	p-p	119°59'	117°25'
Γ_c	$A_1O_1A_2;A_1O_2A_2$	J_2	3	+	p-q;q-p	93°54'	94°35'
Γ_d	$A_1O_2B_3$	J_1	1	+	q-q	86°14'	83°50'

mid-way between the oxygen layers. This is indicated in the figure. If i is taken as the origin, the hexagonal co-ordinates of A_1 are (0, 0, -(1/2 - z)). The three oxygens in the O_2 layer form the smallest face of the octahedron co-ordinating A_1, and their co-ordinates are (x, 0, -1/4), (-x, -x, -1/4) and (0, x, -1/4); The three in the O_1 layer, which form the largest face, are at (1/3 - x, -1/3, -1/12), (x - 2/3, x - 1/3, -1/12) and (1/3, 2/3 - x, -1/12).

The samples were prepared in the same way as those of Krén et al. Solutions of 99% pure, reagent grade, $Fe(NO_3)_3.\ 9H_2O$ and $Rh(NO_3)_3.2H_2O$[11] were mixed in the necessary proportions, and NaOH was added to precipitate the mixed hydroxide which was then thoroughly washed, dried, and prefired for several hours at 700°C. Finally the powder was ground, and fired in air at either 800°C or 900°C. The lower temperature was used for materials with $x > 0.6$ because there was a trace of the βRh_2O_3 pattern in a sample with $x = 0.79$, fired at 900°C, but these lines were absent from the powder patterns of all the samples fired at 800°C. All the materials with $x > 0.6$ were enriched with ^{57}Fe [12].

X-ray fluorescence was used to measure x. Eleven known homogeneous mixtures of Fe_2O_3 and Rh_2O_3 powders were taken as standards, and from the ratios of non-overlapping iron and rhodium fluorescence lines with roughly comparable intensities, it was possible to determine x within ±0.01. The following impurities were found in a typical material (x = 0.45) using the same

technique: Ru 0.3%, Zn 0.1%, Mn 0.1%. The samples used in this investigation have $x = 0.00, 0.06, 0.10, 0.14, 0.24, 0.36, 0.46, 0.66, 0.67, 0.79$ and 0.87.

Debye-Scherrer photographs of all the materials showed only lines which belong to the corundum structure. Their positions and intensities varied regularly between those of the two end members. For $x < 0.25$, the lines were sharp, and the FeKα doublet was well resolved at high angles. However, at the other end of the range, there was quite appreciable broadening of the high-angle lines, which is attributed to small particle size. The mean crystallite size, t, is deduced from the relation

$$B \simeq \lambda / t \cos \theta \quad ; \qquad (4.4)$$

B is the broadening of the lines, compared to a Si standard. It was measured for five intense lines in the range $40° < 2\theta < 140°$, and the variation of t with x is plotted in figure 32. Support for the assertion that the line broadening is due to small crystallite

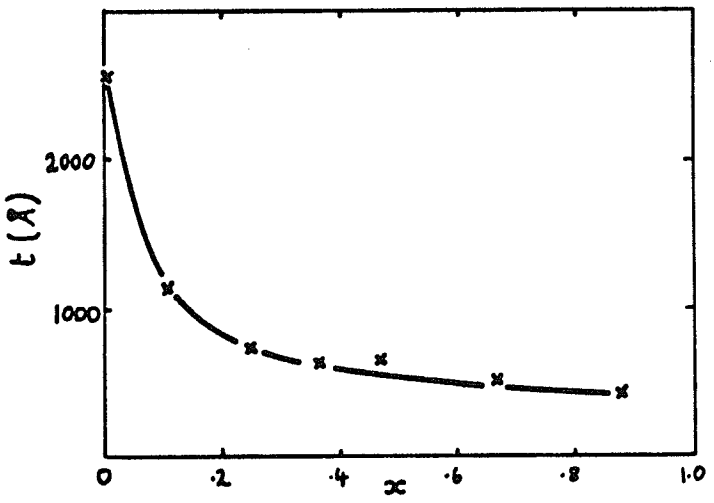

Figure 32. Mean crystallite size in the $(Fe_{1-x}Rh_x)_2O_3$ system, deduced from x-ray powder photographs.

size, rather than strain, was provided by an examination of two of the powders in an electron microscope. Furthermore, pure Rh_2O_3 prepared by the hydroxide method is barely crystalline, and only the strongest low-angle lines are visible in the powder pattern.

The variation of the unit cell parameters, a_H and c_H, is shown in figure 33, where all available data is plotted. The

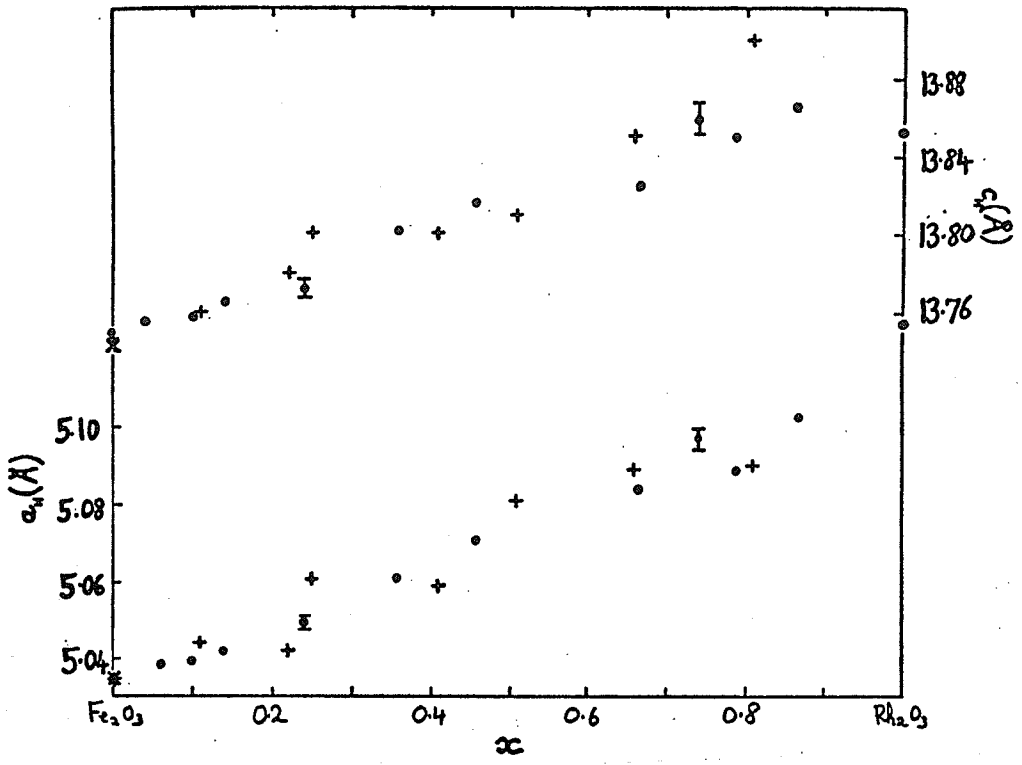

Figure 33. Hexagonal cell parameters of $(Fe_{1-x}Rh_x)_2O_3$; ●, this work; + from reference [65]; ✖ from reference [68].

Fe_1-O_1 and Fe_1-O_2 distances, p and q, will also be needed in §5. Unfortunately, it is impractical to try to deduce three special position parameters, for Fe, Rh and O, from the diffractometer traces of the mixed oxides, so instead we use the data for the end members in conjunction with a plausible assumption. We assume that the cation special position parameters z(Fe) and z(Rh)

have the same values as in the pure oxides. In other words, the position of a cation in an octahedral site depends primarily on whether it is an iron or rhodium ion, and not on its cation neighbours. On the other hand, we assume that the oxygen special position parameter x(0), decreases linearly from 0.307 for x = 0 to 0.295 for x = 1, so that the distortion of the oxygen lattice changes uniformly with the concentration of the larger ion. The resulting dependence of the iron-oxygen separation on rhodium concentration is shown in figure 34.

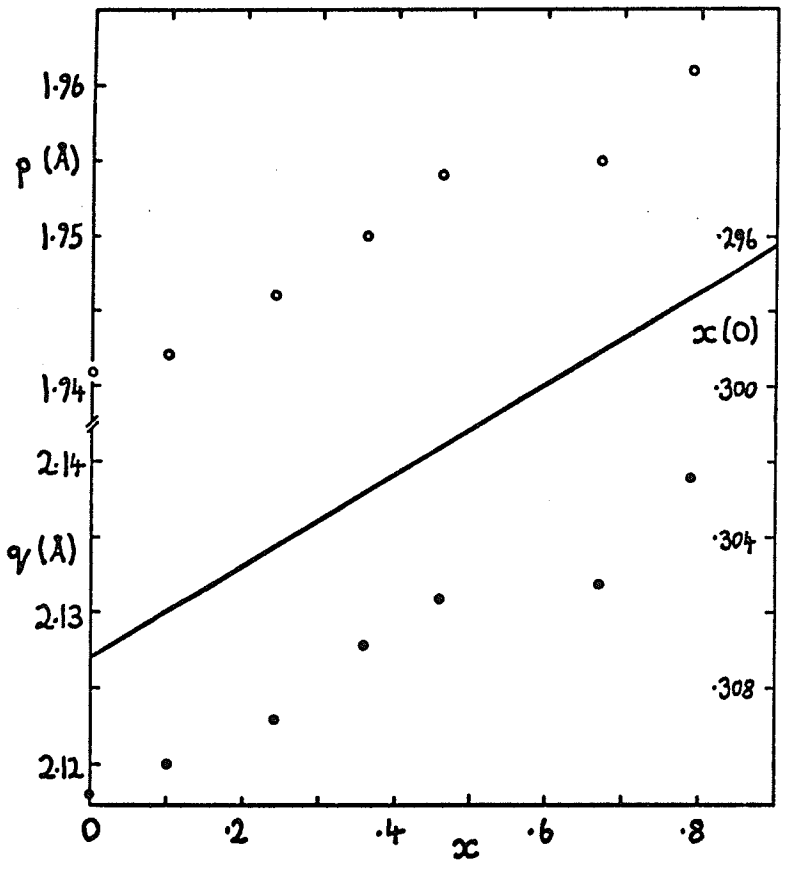

Figure 34. Variation of the two shortest Fe-O distances, calculated by assuming the uniform decrease in oxygen parameter shown by the solid line, and using the measured lattice parameters.

2. MAGNETIC PROPERTIES.

The crystal field at the distorted octahedral cation site has a different effect on Fe^{3+} and Rh^{3+} ions. In the 3d transition metal ions, the Hund's-rule exchange coupling of the d-electrons is the dominant interaction, and for Fe^{3+} the electron configuration $3d^5$ $(t_{2g}^3\ e_g^2)$ gives a high spin state with S = 5/2. However in the 4d transition series, the crystal field splitting predominates over the inter-electronic exchange, so that Rh^{3+} has an electron configuration $4d^6(t_{2g}^6)$, and a low-spin state with S = 0. This is confirmed experimentally by the fact that the susceptibility of Rh_2O_3 is temperature independent [75]. The $(Fe_{1-x}Rh_x)_2O_3$ system, therefore, approximates a random distribution of magnetic and non-magnetic ions on equivalent sites.

The Néel temperature of the system, T_N, measured by neutron diffraction for $0 \lesssim x \lesssim 0.66$, is found to decrease linearly with x [65]. Rh^{3+} is the only trivalent cation which increases the Morin transition temperature, T_M, when it is substituted for some of the iron in hematite. T_M is the temperature above which the spin direction changes from parallel to the c-axis to an angle of about 80° to it [76], and a weak moment appears in the basal plane because of a slight canting of the antiferromagnetic spin arrangement. It increases very rapidly at first with low rhodium doping [77], and then less steeply. A compendium of data on the magnetic phase transitions for the system is given in figure 35. The points from the present study were obtained from Mössbauer spectra, or in the case of x = 0.79, from susceptibility measurements. Morrish and Eatons' point came from an optical domain study, and the rest are

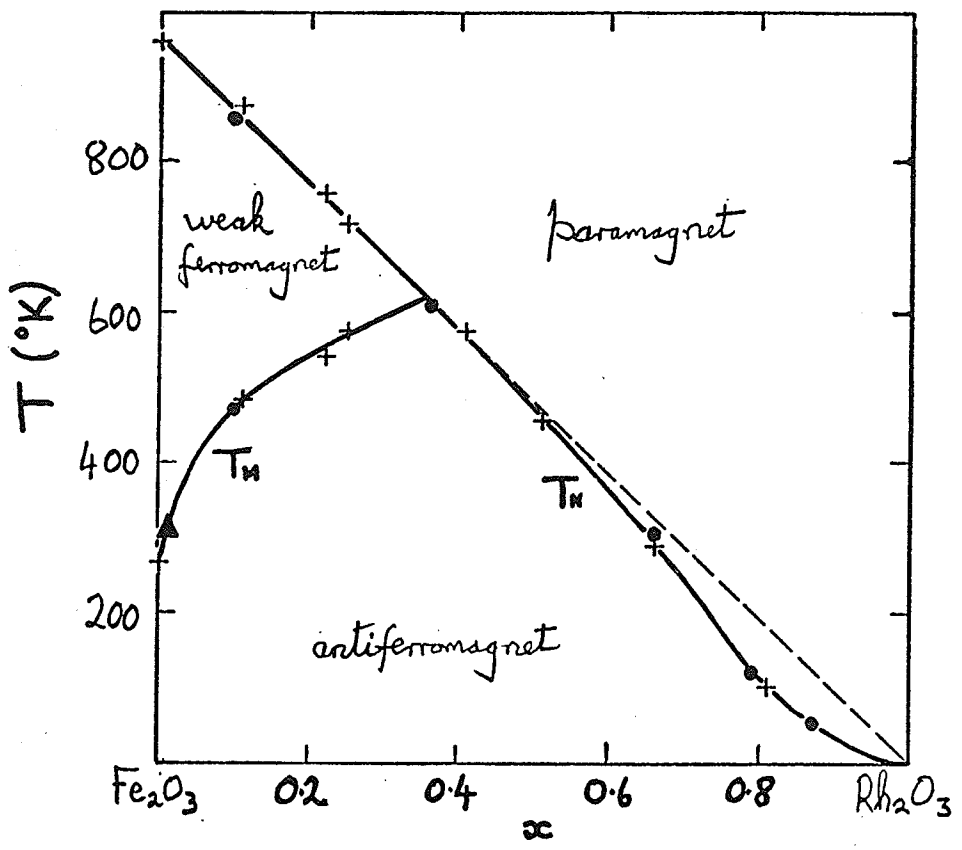

Figure 35. Magnetic phase diagram for the $(Fe_{1-x}Rh_x)_2O_3$ system; ● this work; + from reference [65]; ▲ from reference [77].

from Krén's neutron diffraction work. Nevertheless, we are not particularly concerned with the temperature variation of T_M in this work, because almost all our measurements are made in the antiferromagnetic region. T_N is high enough in αFe_2O_3 for it to be possible to collect spectra in the cold-finger helium cryostat, over most of the range of x, at a reduced temperature sufficiently low for the hyperfine fields to have reached their zero temperature values.

The spin arrangement shown in figure 31 is the one for αFe_2O_3 below the Morin transition. It persists in the mixed system, at least up to x = 0.66, and probably as far as x = 0.81 [65].

Of the cation-cation linkages mentioned in table 8, the six Γ_a ones are probably the most favourable for superexchange, the three of type Γ_b, with an angle of 119°59', may also contribute substantially. Some workers have assumed that an Fe^{3+} ion has nine effective, interacting, magnetic nearest neighbours [78], and this view has received support from the most recent neutron diffraction work on hematite [79] which finds $-J_4 \simeq -J_3 >> J_1, J_2$. These values were obtained at room temperature where $T > T_M$, and they may not be exactly applicable when $T < T_M$, especially as the sublattice magnetization and hyperfine field [80] both change abruptly at the Morin transition, and there is even a small change in lattice parameter [81]. In any case, the Γ_c and Γ_d linkages are unfavourable for superexchange because of the right angle, and direct exchange should be weak and ferromagnetic for the c-axis pair [20].

We will consider two different approximations in the analysis of our experimental data. We suppose that there are either nine, or else six, equal, dominant superexchange bonds, and that in each case the rest of the exchange may be represented by an averaged term proportional to x.

2.1 Six and Nine Nearest Neighbour Approximations.

Some of the results of the ion and crystal model of II 1.1, will be adapted to αFe_2O_3 here. In a two sublattice antiferromagnet, the molecular field acting on an ion in the A-sublattice, say on A_1 of figure 31, is given by

$$H = \frac{2}{g\mu_B}[(J_1 + 3J_3 + 6J_4)\bar{S}_{zB} + 3J_2\bar{S}_{zA}] \qquad (4.5)$$

We will assume, for the present, that only the nearest-neighbour interactions listed in table 8 are important. Setting $\bar{S}_z = \bar{S}_{zA} = -\bar{S}_{zB}$, (4.5) may be abbreviated to

$$H = \frac{2\bar{S}_z}{g\mu_B} \sum_{i=1}^{4} w_i N_i J_i \qquad (4.6)$$

In these equations, S_z is the average component of the spin of a single Fe^{3+} ion along the c-axis. w_i is +1 for i = 2 and -1 for i = 1,3 & 4.

In the mixed system the environment is defined by a set of four occupation numbers $\{Z_i\}$, so that

$$H\{Z_i\} = \frac{2S\langle\sigma\rangle}{g\mu_B} \sum_{i=1}^{4} w_i Z_i J_i \qquad (4.7)$$

(3.4) now reduces to

$$\sigma\{Z_i\} = \mathcal{B}_S[\frac{2S^2\langle\sigma\rangle}{KT} \sum_{i=1}^{4} w_i Z_i J_i] \qquad (4.8)$$

The symbols in this equation were defined in the last chapter, and its significance, namely the ability to predict $\sigma\{Z_i\}$ from $\langle\sigma\rangle$, given J_i; or conversely to deduce J_i from $\sigma\{Z_i\}$, were discussed there. It is possible that (4.8) can predict the variety of hyperfine fields, in the temperature range where dynamic effects are unimportant, with the same sort of accuracy that can be obtained from molecular field theory in simple insulators. However, the equation is rather intractable in its

present form. There are 224 possible different nearest-neighbour environments described by the set $\{ Z_i \}$, and roughly 20% of them have a significant probability for any given x. The Mössbauer data do not justify such laborious analysis, so we simplify the problem by supposing that the variation of only one term in the sum need be taken into account explicitly, and that the rest of the exchange may be represented by an average which is the same for all environments in a particular material. The environment is now defined by a single parameter, Z, the number of dominant exchange neighbours. This averaged term will also include the effect of longer-range interactions. The molecular field has the same form as (3.11), and

$$\sigma(Z) = \mathcal{B}_S[\frac{2S^2}{KT} (ZJ + \langle Z' \rangle J')\langle\sigma\rangle] \qquad (4.9)$$

The six nearest-neighbour approximation assumes that the Γ_a interactions are dominant so that $J = J_4$; $Z = 0, 1, \ldots, 6$; and $\langle Z' \rangle \simeq 7x$. The nine nearest-neighbour approximation assumes that the Γ_a and Γ_b interactions are equally strong so that $J = J_3 = J_4$; $Z = 0, 1, \ldots, 9$; and $\langle Z' \rangle \simeq 4x$. Both of these models involve fitting the data to a sum of several different hyperfine patterns, each of which corresponds to an environment with Z strongly-interacting nearest neighbours. The intensity of each hyperfine pattern is given by the probability $P_N(Z)$, defined in (3.1), provided the iron and rhodium ions are randomly distributed on the

sites. These probabilities are plotted for N = 6 and 9 in figure 36.

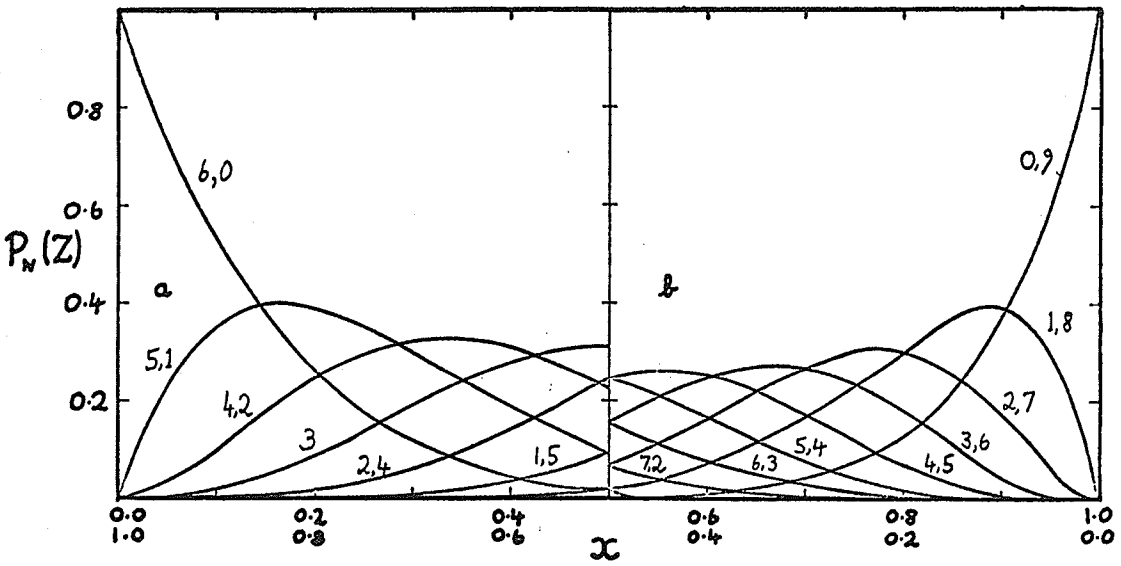

Figure 36. Binomial probability distributions of various numbers of iron neighbours on a) 6 and b) 9 nearest-neighbour sites.

In this approximation, the J_i's are replaced by just two exchange constants J and J', and the Néel temperature is given by

$$T_N = \frac{2S(S+1)}{3k} (\langle Z \rangle J + \langle Z' \rangle J') \qquad (4.10)$$

There is only one magnetic ordering temperature for the whole crystal in molecular field theory, as explained in III 1.2. (4.10) may be used to eliminate $\langle Z' \rangle J'$ from the argument of the Brillouin function in (4.9). The argument, which can be written as

$$y = \langle \sigma \rangle [\frac{15}{7\tau} + \frac{25}{2KT} J(Z - \langle Z \rangle)] \qquad (4.11)$$

is obtained directly for each measured value of $\sigma(Z)$. The substitution S = 5/2 has been made. If we define

$$\eta = \frac{y}{\langle \sigma \rangle} - \frac{15}{7\tau} \quad \text{and} \quad y = Z - \langle Z \rangle,$$

it follows that a plot of $\eta:\zeta$ should be a straight line through the origin with slope 25J/2KT for *all* the materials in the series. The $\eta:\zeta$ graph will give some indication of the validity of the approximations made in this section.

3. MÖSSBAUER SPECTRA.

Some typical sets of spectra for members of the series $(Fe_{1-x}Rh_x)_2O_3$ are shown in figures 37, 44 and 47. The spectra of figure 37 were all taken at room temperature for different members of the system, while those of figures 44 and 47 were taken at different temperatures for a fixed value of x. The values of x and τ are marked on each spectrum. The Néel temperature was taken, rather arbitrarily, as the temperature at which exactly half the absorption was in the magnetically split spectrum. This is almost certainly a lower limit on T_N, and the alternative definition of T_N as the temperature at which the last trace of the magnetically-split absorption disappears would be preferable, were it not much more difficult to measure precisely. A comparison of ferrimagnetic Néel temperatures for diamagnetically substituted garnets, deduced from magnetization and Mössbauer measurements, is given in VI 3. The possible error in τ due to the criterion used to define the antiferromagnetic ordering temperature is insignificant (< 1%) for $x \lesssim 0.6$.

The qualitative features of the sequences of spectra are the same whether x increases at constant temperature or T increases at constant x. In either case, the successive spectra

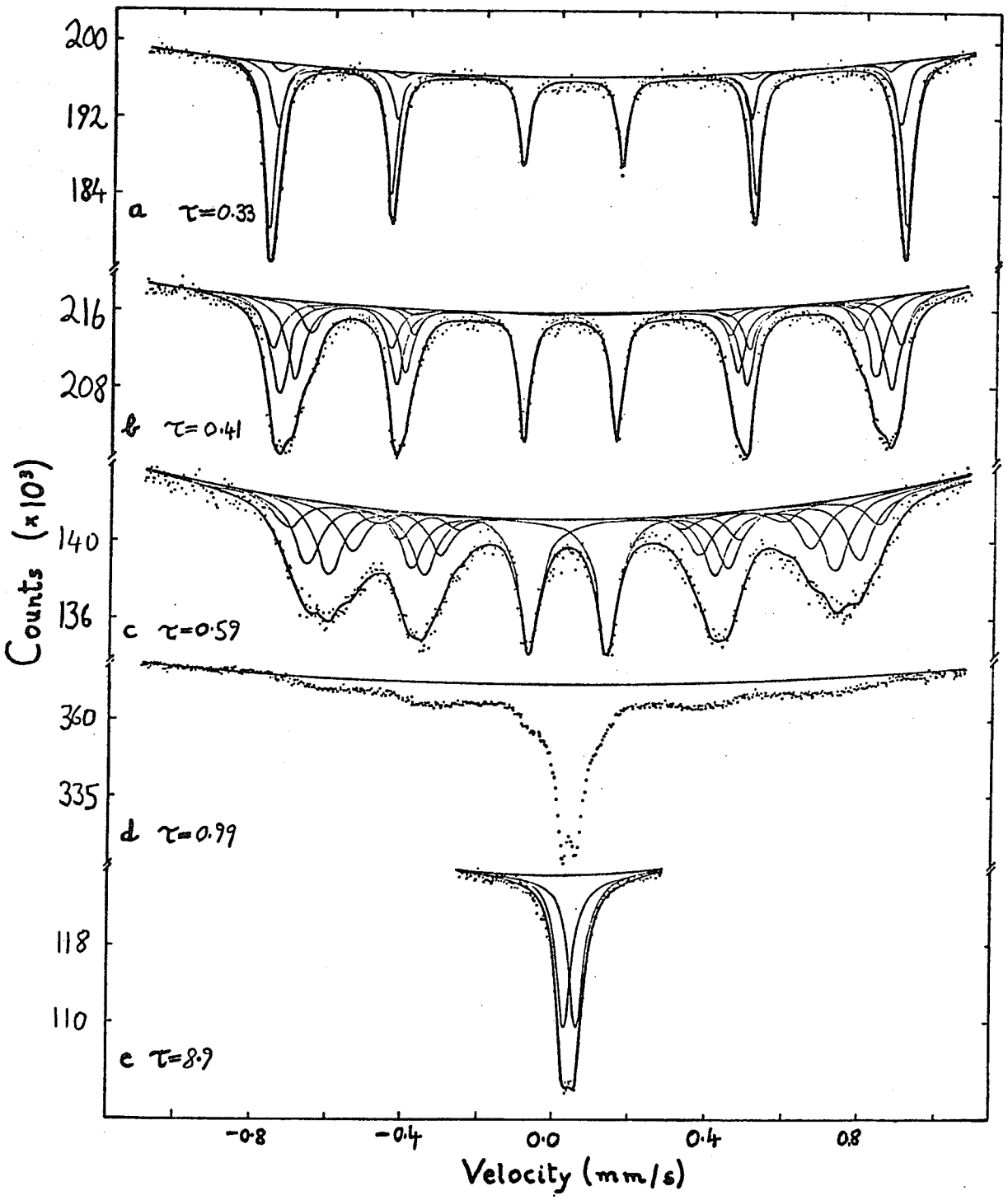

Figure 37. Mössbauer spectra of five members of the $(Fe_{1-x}Rh_x)_2O_3$ system at 296°K. The materials have a) x = 0.06; b) x = 0.24; c) x = 0.46; d) x = 0.66; e) x = 0.87. The fits shown for the first three spectra were obtained on the basis of the six nearest-neighbour approximation, and all the reduced temperatures are marked.

in the diagrams are characterized by an increasing value of τ. At the lowest temperatures, the lines are sharp, yet significantly broader than for pure αFe_2O_3. Then, as x or T increases, the the lines broaden and begin to show some structure. In a region below T_N, $\tau_b < \tau < 1$, a central peak (actually a close doublet) coexists with the magnetically-split spectrum. The reduced temperature, τ_b, at which the mixed spectra first appear decreases with increasing x as shown in figure 78. As τ increases from τ_b, the paramagnetic peaks increase at the expense of the magnetically split spectrum until the two parts of the mixed spectra have equal areas at $\tau = 1$. The vestiges of the magnetically split spectrum disappear very rapidly at higher temperatures, leaving only the paramagnetic doublet, split by a small quadrupole interaction.

Although the range of temperature for which the spectra of the $(Fe_{1-x}Rh_x)_2O_3$ system are mixed increases with increasing x, it is noteworthy that the central peaks have completely disappeared at 20°K, the lowest temperature attainable in the cold-finger cryostat, for x as high as 0.79. 30% of the absorption for the x = 0.87 sample was still in the central peaks at 20°K, but it seems probable that a purely magnetic spectrum would be seen at lower temperatures.

3.1 Data Analysis.

Most of the spectra were fitted to the sum of Lorentzians on a parabolic baseline, as described in II 4. The following constraints were used in the regions $\tau > 1$, $\tau_b < \tau < 1$ and $\tau < \tau_b$.

In the pure paramagnetic region, the close doublet was fitted to two Lorentzians of equal intensity and full width at half maximum.

In the mixed region, the broad lines of the magnetically-split spectrum were fitted to a single six-line pattern, opposite lines of which were constrained to have the same intensity and full width. The central doublet was fitted as in the paramagnetic region.

In the pure antiferromagnetic region, the broadened lines were fitted on the basis of both the six and nine nearest-neighbour approximations. Up to five overlapping six-line patterns, whose intensities are proportional to $p_N(Z)$, were fitted to the data, but only patterns with a relative intensity greater than 0.04 were included. Opposite lines in each pattern were constrained to have the same intensity and full width, and all the members within a peak were further constrained to have the same full width. However, members of different peaks could have different full widths, and the ratio of the peak intensities (but not of the members within each peak) is unconstrained. Since the positions of the four outer lines of a six-line pattern are sufficient to determine H_{hf}, ε and δ_t, each of the two middle peaks were fitted to just a single Lorentzian. Even with this simplification, 22 separate Lorentzians are needed for most of the fits in this region.

Good values of the F-parameter (2.4), in the range $1.0 < F < 1.5$, were obtained for all the fits except for those in the mixed region,

for which F > 2. It is hardly surprising that the complex, magnetically-split spectra are inadequately represented by a single six-line pattern, however broad the lines, and the only useful information to be had from these fits is the position of the central doublet. Typical fits for the pure antiferromagnetic region are shown in figure 37 a-c, and for the paramagnetic region in figure 37e. In both regions the data is well represented by the solid curve.

It is impossible to discriminate decisively between the six and nine nearest-neighbour approximations on the basis of F-value, because the fits obtained using $P_6(Z)$ and $P_9(Z)$ to constrain the relative intensities of the six-line patterns in the pure antiferromagnetic region differ insignificantly. Furthermore, the averages $\langle H_{hf} \rangle$, $\langle \varepsilon \rangle$, and $\langle \delta_t \rangle$ are almost identical in the two cases. $\langle \phi \rangle$ is defined as $\sum_{z=0}^{N} P_N(Z)\phi(Z)$. It is interesting that the values of H_{hf}, ε and δ_t found by fitting a single six-line pattern to the data turn out to be very close to $\langle H_{hf} \rangle$, $\langle \varepsilon \rangle$ and $\langle \delta_t \rangle$ obtained from the six or nine nearest-neighbour fits, notwithstanding the fact that the lines in such a fit are broad, and the goodness of fit is poor. The conclusion is that the average values of the hyperfine interaction parameters in the region $\tau < \tau_b$ are rather insensitive to the method of data analysis. It is a fortunate conclusion, because most of the data is in the pure antiferromagnetic region, and much can be learnt from the variation of these averages across the system.

Values of $\sigma(Z)$, deduced from the room temperature spectra of the samples with x = 0.06, 0.10, 0.14, 0.24, 0.36 and 0.46 were

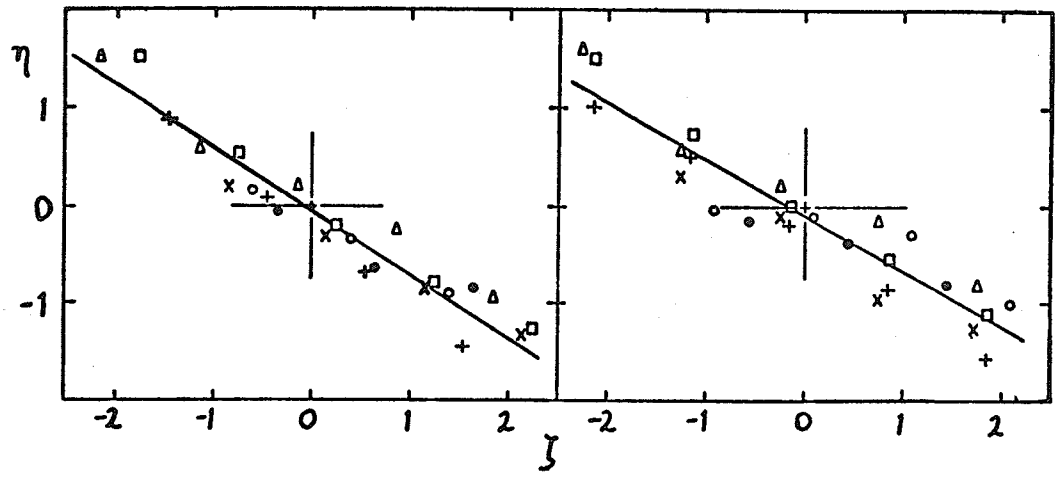

Figure 38. η:ζ plots obtained from the fits using a) the six nearest-neighbour approximation, and b) the nine nearest-neighbour approximation. The plot is explained in §2.1, and the symbols are defined in the caption of figure 41.

used for the η:ζ plots suggested in the last section. τ is sufficiently low for all of these materials, except perhaps x = 0.46, to be well described by the ion and crystal model. The plots are shown for the six and nine nearest-neighbour fits in figure 38 a and b. A least-squares fit of the straight line $\eta = c\zeta$ to the points gives a regression coefficient of 0.970 in the first case, and 0.936 in the second. The lines drawn on the diagram are the best fits to the data, and it is clear that the line in a) passes closer to the origin than the one in b). Accordingly the six nearest-neighbour results will be presented, since we have an indication that the six nearest-neighbour approximation is to be preferred for the analysis of our experimental data. Nevertheless it is worth repeating that most of the results, in particular the supertransferred hyperfine field and the average values of the hyperfine interaction parameters, are virtually independent of whether the six or nine nearest-neighbour approximation is used in the data analysis.

3.2 Hyperfine Field Data.

Spectra were obtained for all the materials in the series at 296°K, and for a representative selection at 20°K. In addition the complete temperature dependence of the Mössbauer spectra of materials with x = 0.10, 0.36 and 0.79 was determined. 1,000 channels were used for the spectra of magnetically ordered materials at 20° and 296°K, and 500 channels at other temperatures. Some of the results of the data analysis are given in tabular form in tables 9 and 10, but they will be described in more detail in the following paragraphs, and a discussion of the results follows in the next section.

3.2.1 20°K.

All the spectra taken at this temperature, except for x = 0.87, resemble the one for x = 0.36, shown in figure 44a. The outer peaks are roughly 0.20 mm/s broader than they are for x = 0, and the variation of linewidth with concentration, when each peak is fitted as a single line, is shown in figure 39. The magnetization

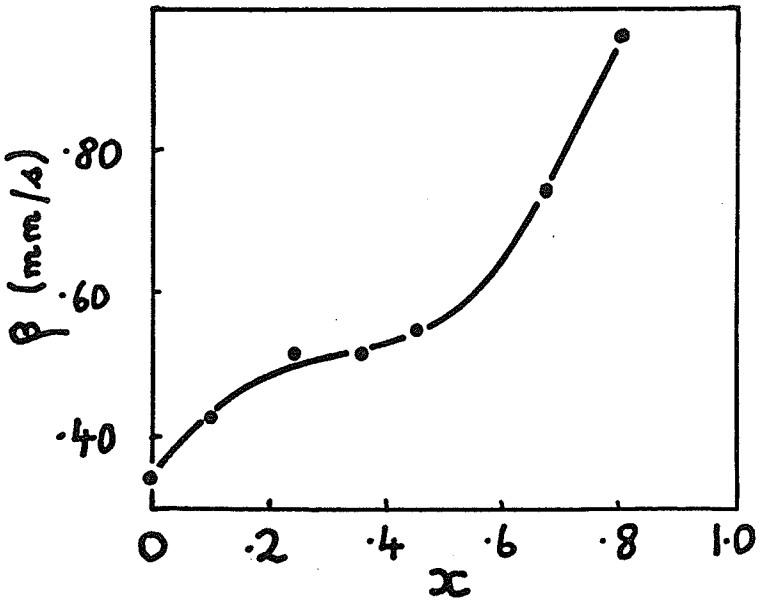

Figure 39. Variation of the width of the outer lines of the 20°K spectra.

Table 9. *Hyperfine Interaction Parameters from the Six Nearest-Neighbour Fits.*

x	T °K		Z 6	5	4	3	2	1	< >
0.06	296	H_{hf}	518.1	505.9	496.0				513.9
		δ_t	.510	.513	.480				.510
		ϵ	.790	.803	.563				.784
0.10	20	H_{hf}	537.3	530.2	524.7				533.4
		δ_t	.642	.642	.620				.640
		ϵ	.751	.930	.836				.825
	83	H_{hf}	535.1	532.9	526.2				533.3
		δ_t	.674	.680	.679				.677
		ϵ	.733	.872	.829				.794
	213	H_{hf}	529.8	521.2	509.7				524.5
		δ_t	.682	.641	.640				.663
		ϵ	.781	.867	.863				.821
	296	H_{hf}	516.7	505.3	492.9				510.0
		δ_t	.513	.515	.513				.514
		ϵ	.801	.847	.751				.812
	448	H_{hf}	473.7	457.0	449.7				465.0
		δ_t	.401	.417	.437				.411
		ϵ	.770	.779	.592				.754
	503	H_{hf}	454.0	435.1	412.3				442.6
		δ_t	.401	.410	.421				.406
		ϵ	-.126	-.196	-.196				-.159
	605	H_{hf}	413.2	392.0	357.7				399.5
		δ_t	.327	.322	.286				.321
		ϵ	-.448	-.452	-.561				-.462
0.10	711	H_{hf}	353.2	324.2	291.2				335.9
		δ_t	.235	.231	.293				.240
		ϵ	-.418	-.287	-.387				-.367
	755	H_{hf}	312.7	275.9	242.7				291.8
		δ_t	.199	.283	.237				.233
		ϵ	-.361	-.252	-.287				-.314
			δ	ϵ					
	887		.254	±.128					
0.14	296	H_{hf}	515.2	502.7	488.3	472.0			504.2
		δ_t	.511	.515	.520	.498			.514
		ϵ	.773	.803	.784	.843			.790
0.24	20	H_{hf}	538.0	533.1	521.8	516.4	512.9		528.0
		δ_t	.642	.642	.648	.640	.637		.643
		ϵ	.644	.731	.771	.777	.768		.733
	296	H_{hf}	512.3	497.6	474.0	446.8	436.8		485.4
		δ_t	.522	.515	.517	.520	.500		.517
		ϵ	.834	.751	.744	.718	.685		.759
0.36	20	H_{hf}	538.4	535.7	525.1	516.7	508.2		524.4
		δ_t	.647	.638	.634	.651	.631		.643
		ϵ	.634	.627	.708	.775	.803		.704
	80	H_{hf}	543.8	535.2	523.9	514.1	501.8		524.9
		δ_t	.589	.628	.613	.623	.628		.619
		ϵ	.805	.652	.714	.757	.752		.721
	135	H_{hf}	537.5	528.3	517.5	506.8	492.5		517.9
		δ_t	.685	.673	.663	.670	.669		.669
		ϵ	.686	.657	.744	.772	.854		.739

0.36	175	H_{hf}	531.5	520.5	507.3	493.5	472.3		506.6
		δ_t	.551	.547	.535	.539	.544		.541
		ϵ	.863	.710	.729	.777	.710		.774
	229	H_{hf}	521.7	509.2	494.0	478.0	455.8		493.1
		δ_t	.566	.549	.555	.551	.567		.555
		ϵ	.940	.662	.782	.700	.686		.734
	296	H_{hf}	508.4	491.6	473.8	455.2	423.7		470.0
		δ_t	.513	.513	.526	.513	.502		.516
		ϵ	.788	.762	.740	.712	.764		.744
	368	H_{hf}	496.1	464.7	441.4	414.7	382.4		439.2
		δ_t	.442	.476	.482	.483	.451		.475
		ϵ	1.005	.737	.751	.729	.645		.748
	447	H_{hf}	474.5	426.8	393.5	361.3	317.2		392.0
		δ_t	.485	.462	.444	.469	.469		.460
		ϵ	.632	.786	.724	.689	.838		.735
	523	H_{hf}	450.0	375.6	309.5	256.2	213.8		311.6
		δ_t	.265	.294	.312	.185	.305		.271
		ϵ	.945	.784	.848	.309	.308		.642
	551	H_{hf}	426.1	335.3	266.0	207.4	150.2		266.4
		δ_t	.196	.197	.243	.278	.105		.223
		ϵ	1.147	1.152	.588	.632	.774		.789
			δ	ϵ					
	620		.235	.882					
0.46	20	H_{hf}		531.3	522.3	512.3	503.4	496.6	514.9
		δ_t		.642	.638	.655	.657	.642	.648
		ϵ		.555	.666	.620	.773	.736	.663

0.46	296	H_{hf}		481.4	449.2	412.2	374.1	334.4	419.2
		δ_t		.511	.522	.517	.517	.482	.515
		ϵ		.738	.688	.640	.598	.323	.637
			δ	ϵ			δ	ϵ	
0.66	296		.51	.73	0.67	296	.544	.795	
0.74	296		.547	.724	0.80	296	.546	.746	
0.87	296		.554	.682					

Table 10. Hyperfine Interaction Parameters from the Nine Nearest-Neighbour Fits.

x	T °K		Z 9	8	7	6	5	4	3	< >
0.06	296	H_{hf}	519.3	509.4	497.2					513.8
		δ_t	.511	.509	.511					.510
		ϵ	.775	.821	.622					.775
0.10	20	H_{hf}	540.4	531.5	523.6	520.2				533.1
		δ_t	.637	.644	.631	.620				.638
		ϵ	.753	.873	.836	.801				.816
	296	H_{hf}	518.5	508.9	499.5	487.5				510.0
		δ_t	.511	.515	.511	.509				.512
		ϵ	.784	.840	.827	.747				.811
0.14	296	H_{hf}	517.5	507.4	489.3	477.5				502.2
		δ_t	.513	.509	.520	.504				.512
		ϵ	.731	.823	.779	.816				.787
0.24	20	H_{hf}	539.2	537.7	529.0	520.2	513.6			528.0
		δ_t	.646	.642	.644	.651	.659			.648
		ϵ	.653	.672	.760	.766	.764			.731
	296	H_{hf}	514.8	507.9	489.2	467.9	440.2			484.7
		δ_t	.520	.511	.520	.511	.511			.515
		ϵ	.845	.806	.755	.758	.727			.772
0.36	20	H_{hf}		539.4	534.2	525.4	517.5	509.9		524.3
		δ_t		.634	.640	.638	.651	.638		.641
		ϵ		.607	.631	.690	.784	.777		.706
	296	H_{hf}		510.8	490.0	474.5	458.2	429.7		470.6
		δ_t		.485	.524	.517	.515	.504		.513
		ϵ		.779	.733	.744	.714	.701		.731
0.46	20	H_{hf}	531.3	524.3	515.4	507.6	498.3	514.8		
		δ_t	.638	.640	.657	.655	.653	.650		
		ϵ	.586	.666	.627	.701	.755	.666		
	296	H_{hf}	481.6	456.8	424.5	391.2	348.5	419.0		
		δ_t	.524	.513	.520	.515	.493	.514		
		ϵ	.655	.731	.633	.607	.410	.616		

is saturated for $x \gtrsim 0.5$, since $\tau \gtrsim 0.05$. The plot of $\langle H_{hf} \rangle : x$, given in figure 40, shows a steady decrease for $x < 0.5$ which is therefore *not a temperature effect*, although the steeper decline for $x > 0.5$ may be, in part, due to the fact that the hyperfine

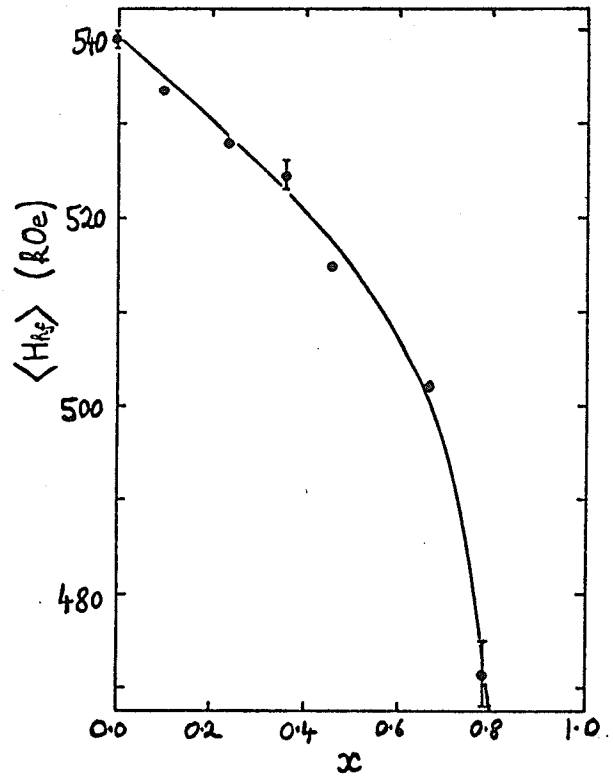

Figure 40. The average hyperfine field at 20°K.

field in these materials has not quite reached its saturation value. In figure 41a the hyperfine field data from the six nearest-neighbour fits is presented, as a function of Z, for the materials with $x = 0.0$, 0.10, 0.24, 0.36 and 0.46. There is a decrease of 7.8 kOe for each non-magnetic neighbour, which seems to be independent of x. This value is also consistent with the initial decrease of $\langle H_{hf} \rangle$ with x shown in the previous figure.

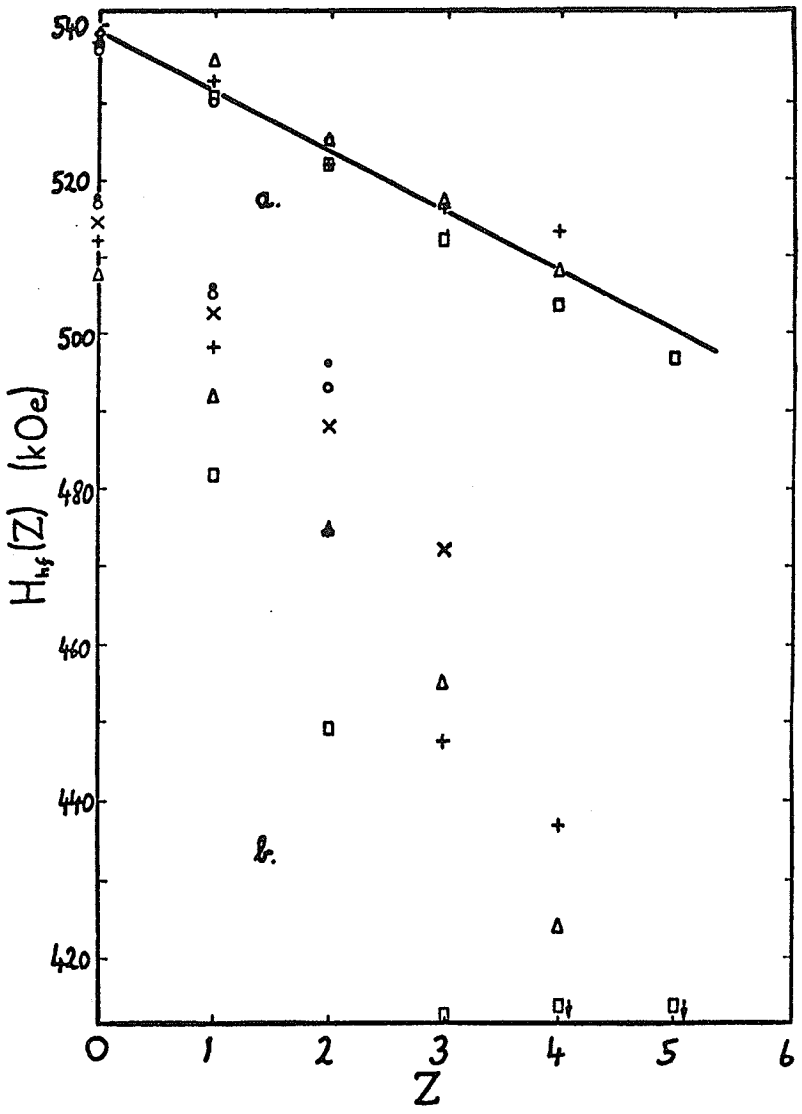

Figure 41. The hyperfine fields for iron in different environments a) at 20°K and b) at 296°K. The symbols represent materials with different rhodium concentrations. ◆, x = 0.00; ●, x = 0.06; o, x = 0.10; ×, x = 0.14; +, x = 0.24; Δ, x = 0.36; □, x = 0.46.

On the basis of the nine nearest-neighbour fits, the average decrease in hyperfine field in 7.9 kOe. This is the average of the slopes of the lines, one for each material, drawn through data like that in figure 41a. It is impossible in this case to draw one good line through all the points from all five materials.

3.2.2 296°K.

The hyperfine fields as a function of Z for materials with $x \lesssim 0.46$ are shown in figure 41b. From the slopes and intercepts of y:Z graphs, it is possible to deduce the exchange constants J and J' of equation (4.9). They are listed in table 11, where the errors are one standard deviation. The average values for all materials with $x \lesssim 0.46$ are more reliable, and they are best deduced from the slopes of the $\eta:\zeta$ graphs and T_N. From figure 38a

Table 11. Molecular Field Exchange Constants for $(Fe_{1-x}Rh_x)_2O_3$.

x	6 nearest-neighbour model J/k	6 nearest-neighbour model J'/k	9 nearest-neighbour model J/k	9 nearest-neighbour model J'/k
0.06	-11.8±3.4°K	-12.7±2.8°K	- 7.3±2.0°K	-22.9±4.8°K
0.10	-12.3±1.1	-12.4±1.2	- 5.5±3.4	-27.9±6.3
0.14	-12.4±0.3	-12.2±0.4	-13.7±2.3	- 7.7±5.8
0.24	-17.4±2.0	- 7.4±1.9	-15.9±1.1	- 2.7±2.3
0.36	-12.6±2.4	-12.9±1.3	-12.6±3.1	-13.2±5.7
0.46	-16.7±2.5	- 8.8±1.2	-15.5±1.4	- 5.0±2.5
average†	-15.3±1.0	-10.3	-13.9±1.0	9.8

†deduced from the graphs in figure38.

we find $\langle Z\rangle J/k = -91.8°K$ and $\langle Z'\rangle J'/k = -72.0°K$ for x = 0. The values from figure 38b are $\langle Z\rangle J/k = -124.7°K$ and $\langle Z'\rangle J'/k = -39.1°K$. We infer that $J_4 = -15.3°K$, $J_3 = -11.0°K$ and the remainder of the exchange, which may be due to the Γ_b and Γ_c linkages and also longer-range interactions, is -39.1°K. The errors in J_4 and J_3 corresponding to the standard deviation in the slope of the $\eta:\zeta$ graphs are ±1.0°K,

but the error is probably greater, because the assumption in the six nearest-neighbour model that <Z>J >> <Z'>J' is not a very good approximation. When comparing these results with the exchange constants found by inelastic neutron scattering [79], it should be remembered that these values are extrapolated from a whole series of materials, all below their Morin transition, whereas the neutron work on αFe_2O_3 was done on a pure single crystal, above T_M. Furthermore, exchange constants from molecular field theory are habitually lower than those found by other methods [82].

The reason why $H_{hf}(6)$ for x = 0.06 and 0.10 is greater than 517 kOe, the value for x = 0, even though τ is higher for these materials, is because there is a discontinuity of 8 kOe at T_M in pure αFe_2O_3 [80].

3.2.3 x = 0.10.

The temperature dependence of the hyperfine-interaction parameters in this material is similar to that found by van der Woude in pure αFe_2O_3. As the temperature increases through T_M (470°K), the quadrupole interaction is halved, and changes sign. A decrease of roughly 12 kOe in H_{hf} is also observed, although the transition is spread over a much more extended temperature range than in the pure material, perhaps because of the effect of the range of small crystallite sizes [83], or possibly because the doping is somewhat inhomogeneous. The temperature variation of $H_{hf}(Z)$, $\langle\varepsilon\rangle$ and $\langle\delta_t\rangle$ is given in figure 42. The decrease in H_{hf} at T_M is not obvious from

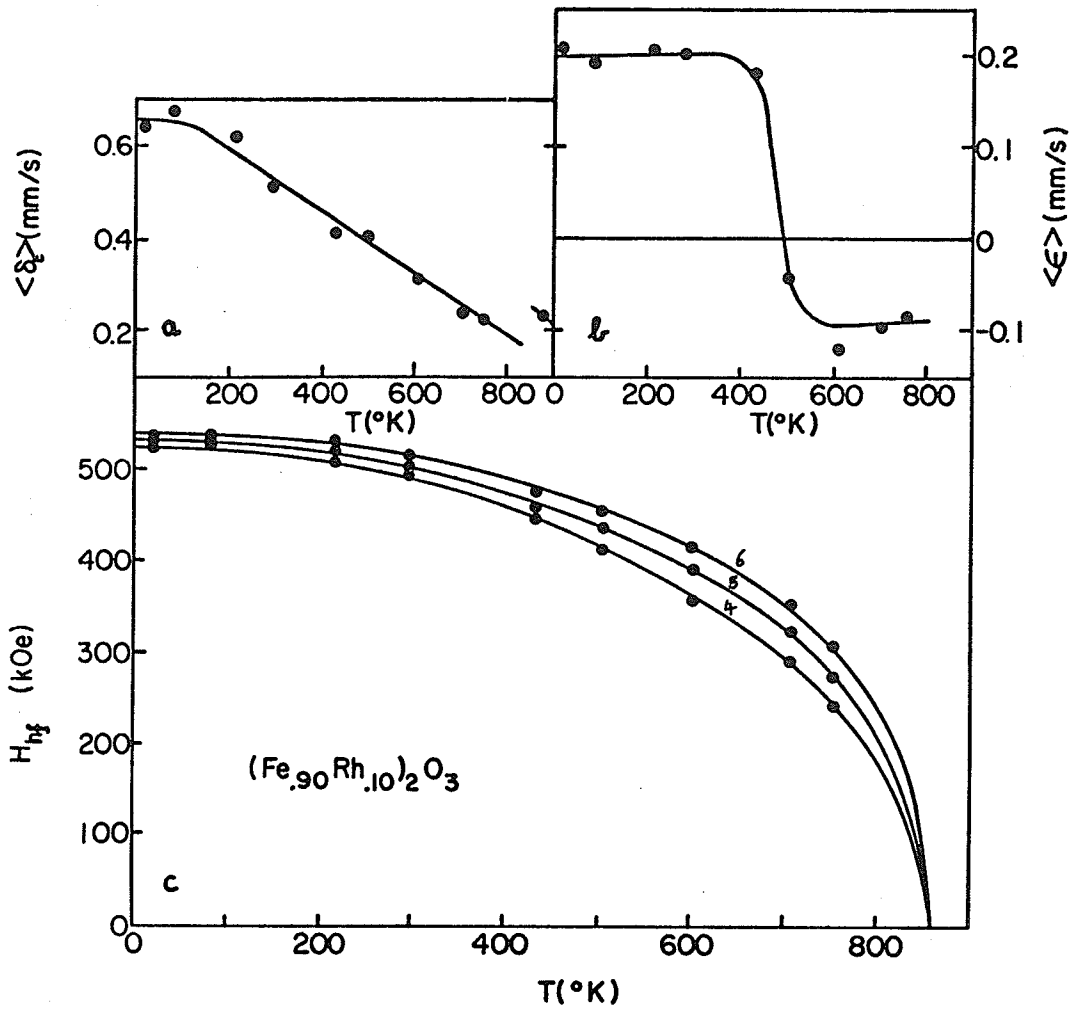

Figure 42. Hyperfine interaction parameters in $(Fe_{0.9}Rh_{0.1})_2O_3$ as a function of temperature; a) the total spectrum shift, b) the quadrupole interaction parameter, and c) the hyperfine fields, deduced from six nearest-neighbour fits.

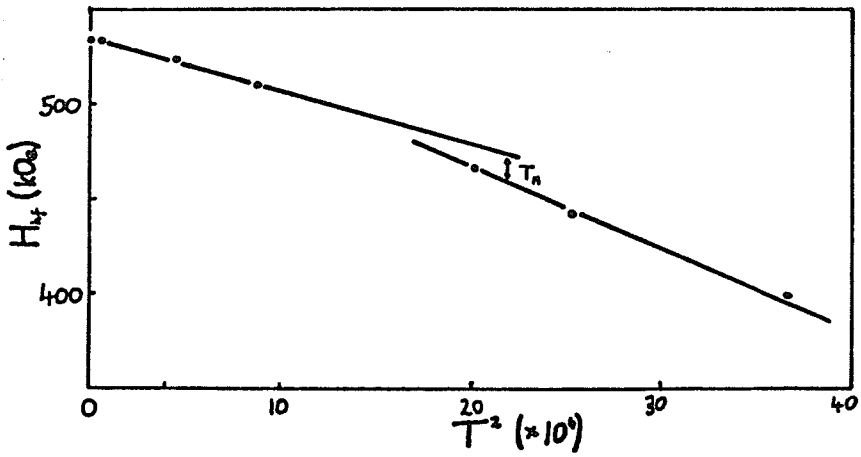

Figure 43. The average hyperfine field in $(Fe_{0.9}Rh_{0.1})_2O_3$ as a function of T^2. T_M is the centre of the Morin transition region.

this figure, but it may be seen in the $H_{hf}:T^2$ plot of figure 43. The errors on many of the points are rather large because the statistics were poor on the spectra with T > 296°K.

3.2.4 x = 0.36.

At this concentration of rhodium, the antiferromagnetic spin arrangement persists up to T_N (608°K). The temperature dependence of the Mössbauer spectrum is illustrated in figure 44.

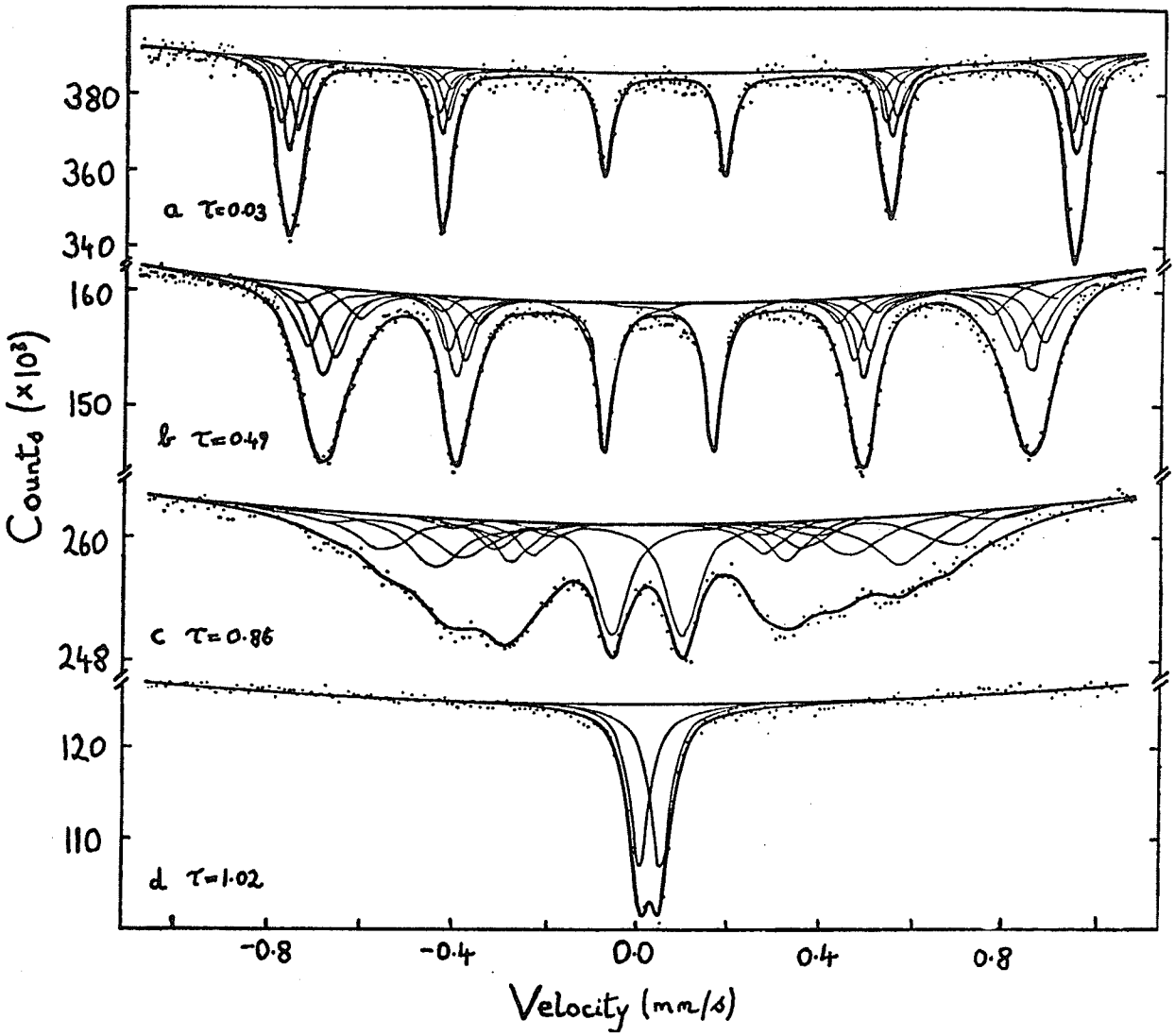

Figure 44. Mössbauer spectra of $(Fe_{0.64}Rh_{0.36})_2O_3$ at different temperatures; a) 20°K, b) 296°K, c) 523°K, and d) 620°K. The six nearest-neighbour fits are shown for a), b) and c), and all the reduced temperatures are marked.

At about 500°K, the peaks have become so broad that they overlap appreciably. The broadening is greatest for the outside lines, so the spectrum begins to look a bit 'triangular', even though the central peak does not appear until 560°K (τ_p = 0.92). The spectrum shown in figure 44c was taken at 523°K, and the fit is quite satisfactory in spite of the fact that some of the elements of peaks 2 and 5 lie outside some of the elements of peaks 1 and 6. The area ratio of the peaks is 3.0:2.0:1.3, in good agreement with the expected 3:2:1.

The hyperfine fields in the environments with Z = 6, 5, 4, 3 and 2 were obtained from spectra taken at ten different temperatures. The results are shown in figure 45, where it can be seen that widely different magnetization curves are followed by ions in different environments. In particular, the experimental curve for Z = 6 does not differ much from that of pure αFe_2O_3, and if extrapolated, it would give a transition temperature of roughly 850°K. It appears that the magnetization of an ion depends mainly on its nearest neighbours, except in the critical region, characterized by central peaks, where spin fluctuations occur, and the magnetization is determined largely by the bulk composition, x. The solid lines are the result of a molecular field calculation using the average values for J and J' in (4.9). Each curve is normalized to the smoothed value of $\sigma(Z)$ at T = 20°K. The data is adequately reproduced only up to 400°K, τ = 0.66.

The same set of spectra were also fitted on the basis of the nine nearest-neighbour approximation, and the resulting data,

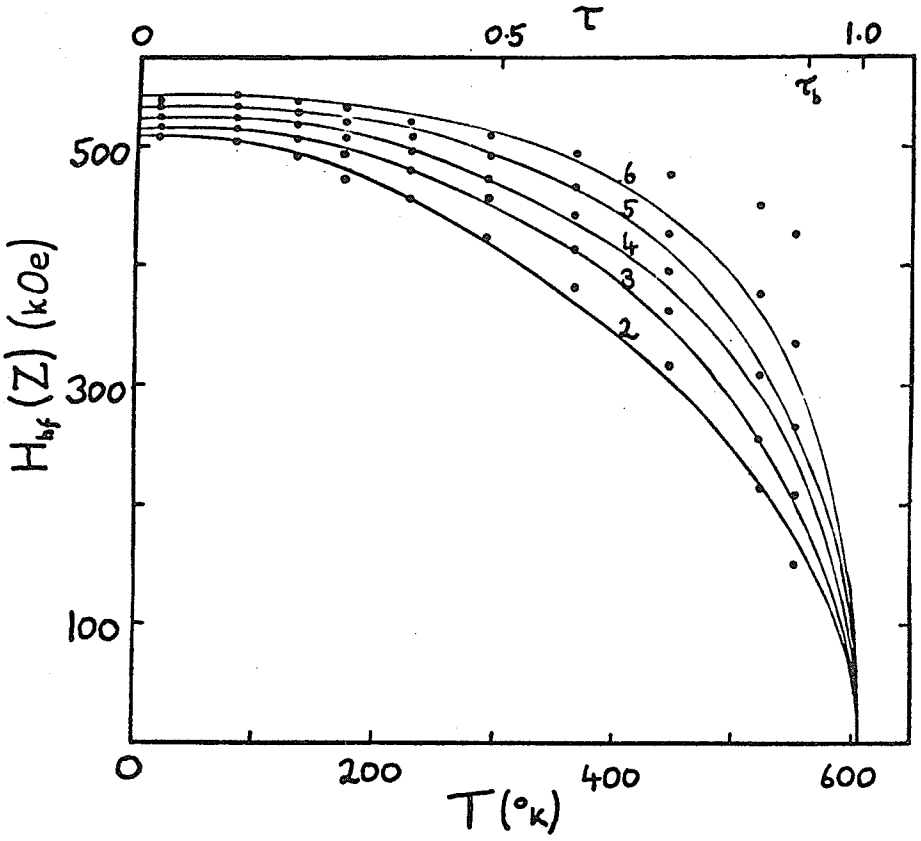

Figure 45. Hyperfine fields in the different environments in $(Fe_{0.64}Rh_{0.36})_2O_3$ deduced from the six nearest-neighbour fits. The solid curves are calculated using the ion and crystal model.

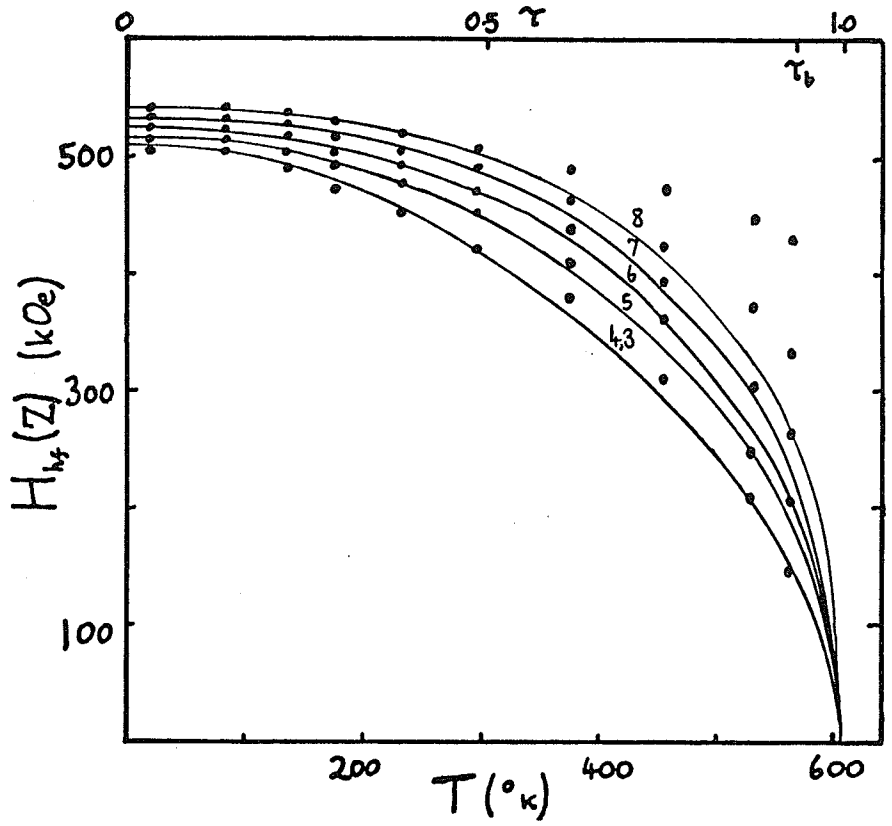

Figure 46. Hyperfine fields in the different environments in $(Fe_{0.64}Rh_{0.36})_2O_3$ deduced from the nine nearest-neighbour fits. The solid curves were calculated using the ion, shell and crystal model.

shown in figure 46, is virtually identical. The solid curves were obtained using the ion, shell and crystal model, but they do not give a better fit to the points.

3.2.5 $x = 0.79$.

The temperature dependence of the Mössbauer spectrum, shown in figure 47, is qualitatively the same as for x = 0.36. However T_N and τ_b are much lower, 120°K and 0.3, respectively. Nevertheless, at 20°K there is no sign of the central peaks, even though the probability of an iron ion having 0 or 1 iron neighbours is

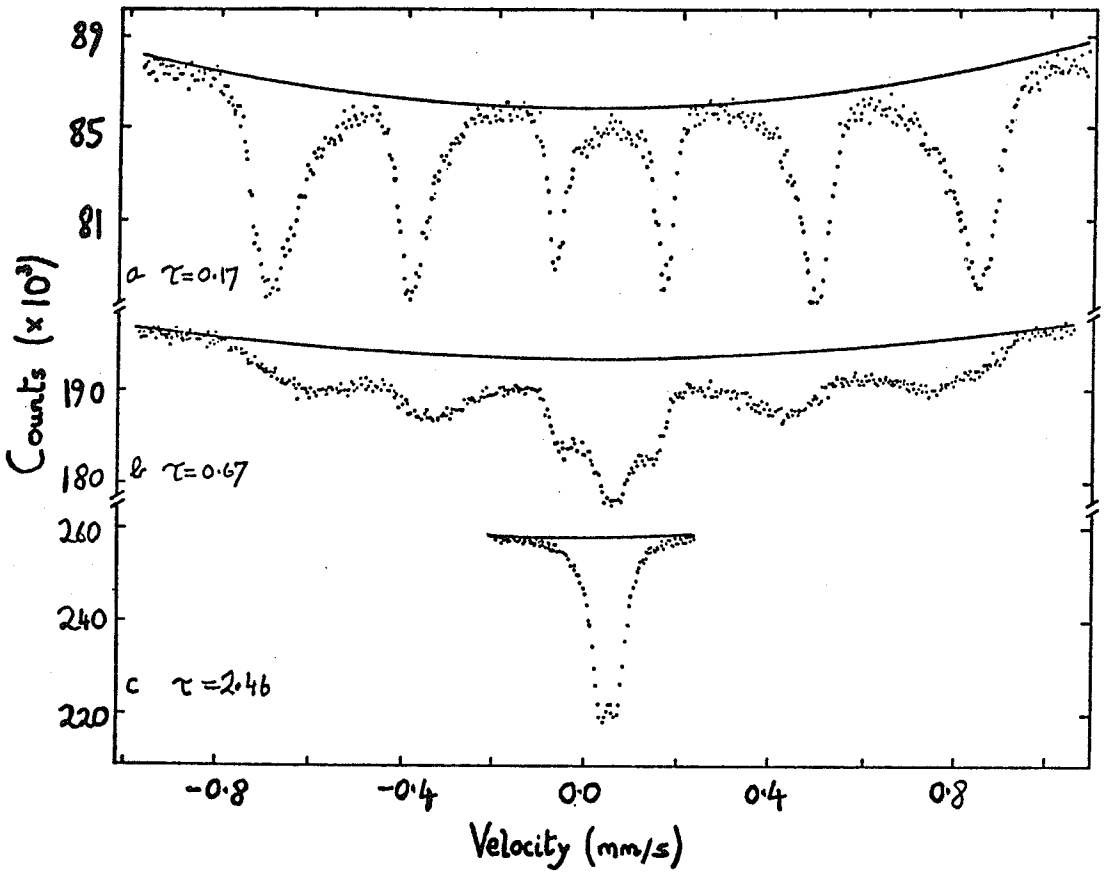

Figure 47. Mössbauer spectra of $(Fe_{0.21}Rh_{0.79})_2O_3$ at different temperatures; a) 20°K, b) 81°K, and c) 296°K. The corresponding reduced temperatures are marked.

25% or 38%, (12% or 29% if we assume nine dominant interactions). If there are any central peaks, they account for at most 2% of the total absorption, so unless there is great inhomogeneity in the cation distribution, this suggests that the magnetic interactions in the mixed system extend beyond nearest neighbours. The possibility of an alternative, dynamic explanation of the mixed spectra is considered in chapter VI. Additional evidence for long-range interactions is provided by the behaviour of T_N as a function of x. The almost linear variation, even at high non-magnetic concentrations, shown in figure 35, is indicative of long range interactions [84]. Furthermore, some calculations by Murray [85] for a dilute Heisenberg ferromagnet (which has only nearest-neighbour interactions), give critical concentrations of $x \sim 0.6$ for the formation of the ordered state in certain simple lattices.

The influence of the rhodium ions on the iron-iron exchange interactions is probably small, but this is not certain. A number of spinel rhodates $M^{2+}Rh_2^{3+}O_4$ have been reported [86]. They all have the normal cation distribution, on account of the predelection of Rh^{3+} for octahedral co-ordination and a low-spin state. The spinels with M = Co, Cr, Mn, Ni and Cu have $T_N \sim 20°K$. The ordering temperature is low because the M-M distance is $\sim 4\text{Å}$, and the A-A exchange is weak. There is a static Jahn-Teller distortion when M = Ni or Cu, and probably also when M = Fe, although there is no published work on ferrous rhodate. However, $CoRh_2S_4$ is also a normal spinel, but is has a Néel temperature of 400°K. The explanation is probably that the picture of localised electrons does not apply to the sulphide.

4. DISCUSSION OF THE HYPERFINE FIELDS.

We found that the magnitude of the hyperfine field decreases by 7.8 kOe at T = 0 for every iron nearest neighbour replaced by rhodium. Most of this change must be due to the supertransferred hyperfine field, because the dipolar field from the Γ_a and Γ_b neighbours is only -0.14 and -0.46 kOe, respectively. The change in the antiferromagnetic zero-point spin deviation due to a non-magnetic defect in the antiferromagnetic lattice is expected to be small [47], and will be neglected.

The configuration of figure 30, which was used to deduce the expression (3.17) for the supertransferred hyperfine field, is not quite appropriate for αFe_2O_3. The six O^{2-} anions are not equidistant from the central iron, and the six Γ_a linkages are not straight. As an approximation, we will replace the factor 6 in (3.14 - 17) by the sum over Γ_a linkages. For example, (3.17) becomes

$$H_{Sthf} = -525N^{\uparrow 2}N^{\downarrow 2}\sum_{i=1}^{6} A_\sigma^{i2}\cos^2\theta_a\left[-\sum_{n=1}^{3} S_{ns}^{i}\phi_{ns}(0) + a_{4s}^{i}\phi_{4s}(0)\right]^2 \qquad (4.10)$$

where θ_a is the Fe-O-Fe angle.

Taking H_{Sthf} as 7.8 kOe per iron neighbour, we can determine A_σ from (4.10). Actually the six Γ_a linkages split up into two groups of three, with slightly different values of A_σ and S_{ns}, but this difference is neglected. The bond geometry of αFe_2O_3 is assumed. The overlap integrals S_{ns}, and $\phi_{ns}(0)$ for $n \lesssim 3$ were calculated from Watsons O^{2-} [89] and unrestricted Fe^{3+}[90] Hartree-Fock

wave functions. S_{4s} and $\phi_{4s}(0)$ were determined from Clementi's wave functions for iron in the configuration $3d^5 4s^2$ [91]. We chose $a_{4s} = 0.15$, and solved (4.10) using (3.18). The total 4s occupation, $6(N^{\uparrow 2} + N^{\downarrow 2})a_{4s}^2$, is equal to 0.17, $A_\sigma^2 = 0.10$, $S_\sigma = 0.062$ and $B_\sigma = 0.253$. Some of the overlap integrals and nuclear electron densities, in atomic units, are given in table 12.

Table 12. s-Electron Wave-Functions Evaluated at the Nucleus, and s-p Overlap Integrals for αFe_2O_3.

	n = 1	2	3	4	
$\phi_{ns}^{\uparrow}(0)$	73.3324	22.1825	8.3892	2.363	
$\phi_{ns}^{\uparrow}(0)$	73.3330	22.2587	8.2517	2.187	
$S_{ns}^{\uparrow}$ *	.00286	.02089	.09950	.29186	S_σ*
$S_{ns}^{\uparrow}$ *	.00286	.02068	.10006	.29186	.062475

* Average over p and q iron-oxygen separations.

Taking $A_\sigma^2 = 0.10$, we can calculate the change of charge and spin densities of purely 3d character for the ion. In atomic units, they are respectively $-6(S_\sigma^2 + B_\sigma^2) = -0.40$ and $\frac{6}{2}(S_\sigma^2 - B_\sigma^2) = -0.18$. Thus the total spin of 3d character is 2.32, and the charge of an 'Fe^{3+}' ion is 3.0 - 0.40 - 0.17 = 2.43. The last term is the 4s occupancy. For charge neutrality, the charge on the O^{2-} ion must be -1.62. These values for the charge depend rather critically on the value chosen for a_{4s}. For example if a_{4s} was 0.10 or 0.20,

the ferric charge would come out as 2.51 or 2.35. The charge distribution in αFe_2O_3 is important in the calculation of the electric field gradient, required to deduce the quadrupole moment of the excited state of ^{57}Fe [92, 93], and it would be interesting to see if these charges give a reasonable gradient.

We can use the modified form of (3.15) to calculate the change in hyperfine field in αFe_2O_3, compared to the free-ion value. We take into account the supertransferred hyperfine field, the field produced by the spin polarization of the 4s electrons, the change in field due to overlap distortion of the core 4s electrons, and the dipolar field. $\phi^{\uparrow}_{4s}(0)$ and $\phi_{4s}(0)^{\downarrow}$ are chosen to give a field of 420 kOe for the two 4s electrons. Then, with $a_{4s} = 0.15$, the total contribution from (3.15) is 62 kOe. The change in field caused by the reduction of the 3d spin is 45 kOe and the dipolar field is -10 kOe, so the total change is +97 kOe, but this is also very sensitive to the value chosen for a_{4s}. However, if the free ion field is taken to be -630 kOe, the net result of the unrestricted Hartree-Fock calculations shown in table 1, then the measured change is +90 kOe, and the agreement is good.

5. QUADRUPOLE INTERACTIONS.

The average quadrupole interaction data at 20°K and 296°K is plotted in figure 48 a and b; $\langle\varepsilon\rangle$ is defined as $\sum_{z=0}^{6} P_6(Z)[\Delta_{16}(Z) - \Delta_{25}(Z)]$ in the ordered region, and it is just 2x(splitting of the doublet) in the paramagnetic region. It is clear that the magnitude

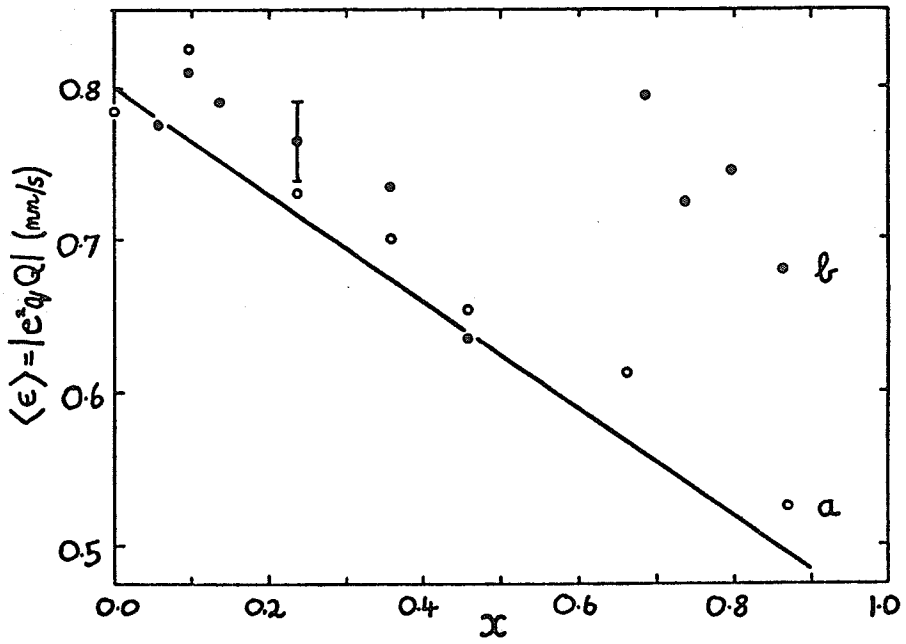

Figure 48. The average quadrupole interaction in $(Fe_{1-x}Rh_x)_2O_3$, a) O, at 20°K and, b) ●, at 296°K. The solid line is calculated taking into account the change in lattice parameters and overlap distortion of the iron p-orbitals throughout the system.

of the quadrupole interaction decreases with x at both temperatures, except for the sharp break between the antiferromagnetic and paramagnetic regions at room temperature. The critical concentration is x = 0.67 at 296°K. The most obvious explanation would be that ϕ, the angle between the hyperfine field and the principal axis of the electric field gradient tensor, (the c-axis), depends on x. It may be seen from (1.12) that the quadrupole interaction in the magnetically ordered state varies as $(3\cos^2\phi - 1)$, so that it would decrease if ϕ changed from 0° with increasing rhodium concentration. However, since no such effect was detected in the neutron diffraction study of the system [65], the obvious explanation is untenable. It also follows that quadrupolar line broadening, caused by a range of ϕ, may be discounted. Furthermore, the

decrease in quadrupole interaction with x persists in the paramagnetic region, so another explanation for the dependence of $|e^2qQ|$ on x must be found.

It is likely that the answer lies in the variation of the iron and oxygen special position parameters z(Fe) and x(O). It has been pointed out, [92], that a 1% increase in these will decrease the electric field gradient in αFe_2O_3 by 88.0% and 11.8% respectively, so that a change in z(Fe) of only three parts in a thousand could be enough to account for the jump between the antiferro- and paramagnetic regions in figure 48b. A change of this magnitude seems quite feasible in view of the fact that there is even a slight change of lattice parameter at T_M [81]. The sign of the quadrupole interaction is positive in the ordered region, but an attempt to determine its sign in the paramagnetic region by applying a magnetic field failed,because the splitting of the doublet is too small.

The variation of the electric field gradient with rhodium concentration could be explained as follows: We assume, as proposed at the end of §1.2, that z(Fe) is the same as for pure αFe_2O_3, but that x(O) decreases linearly as x increases, as shown in figure 34. Most of the electric field gradient at an excited ^{57}Fe nucleus arises from the surrounding anions, so that it depends mainly on z(Fe) and x(O), but is not greatly influenced by the special position parameters of the more distant cations. The electric field gradient (1.9), may be written as

$$q = q_\ell(z(Fe), x(O))(1-\gamma_\infty) + q_{ov}(z(Fe), x(O))(1-R) \qquad (4.11)$$

There is no q_v term for Fe^{3+}. q_ℓ is the lattice (point ion and induced dipole) contribution determined by Artman et al [92], and q_{ov} is the contribution to the field gradient due to overlap distortion of the iron 3p and 2p orbitals by the surrounding ligands [14].

The solid line in figure 48 was calculated from (4.11). The fact that it fits the data fairly well, lends support to the assumption that the oxygen special position parameter depends linearly on rhodium concentration.

The quadrupole interaction, as a function of temperature for $x = 0.36$, is given in figure 49. It is constant, within experimental

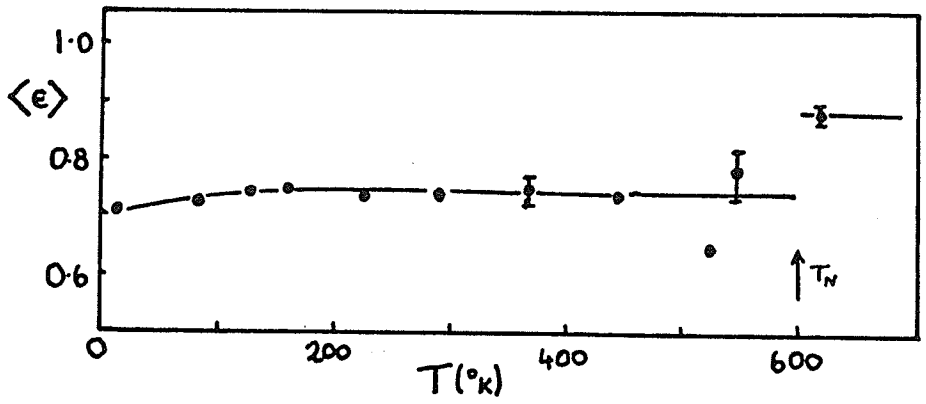

Figure 49. The temperature dependence of the quadrupole interaction in $(Fe_{0.64}Rh_{0.36})_2O_3$.

error, throughout the magnetically ordered region, but it changes abruptly at T_N. This data may be taken as extra evidence for a change in special position parameter when the compounds become magnetically disordered. The change $|e^2qQ|$ is 0.15 mm/s, compared to a change of 0.20 mm/s in the room-temperature data of figure 48b. No conclusions will be drawn from the variation of ε with Z, except to note that there seems to be a tendency for it to decrease at

20°K and increase at 296°K, showing that the interaction depends to some degree on the cation neighbours.

The total spectrum shift data for the whole system will be presented and discussed in the next chapter.

The work on $(Fe_{1-x}Rh_x)_2O_3$ shows that the spectra of a substituted system may be analysed quantitatively on the basis of a random distribution of cations, and that quite a variety of information can be deduced, particularly from the supertransferred hyperfine field, which comes directly from the low-temperature spectra.

V The Influence of Magnetic Order on the Total Spectrum Shift

A fact in science is not a mere fact, but an instance. - *B. Russell.*

1. THE TOTAL SPECTRUM SHIFT.

Up to now, we have been mainly concerned with hyperfine fields, and to a lesser extent quadrupole interactions, in mixed oxides. In this chapter will will give some consideration to the third hyperfine interaction parameter; the isomer shift. Unlike the other two, the Mössbauer effect is virtually the only technique available for measuring it. The difficulties involved in extracting an absolute value of the solid state parameter (the s-electron density at the nucleus) from the measured hyperfine interaction are greatest in the case of the isomer shift, not least because the measured total spectrum shift, δ_t, is actually the sum of two components which arise in quite distinct ways. One is the isomer shift δ_i, and the other is the second order Doppler shift which we denote by δ_D, rather than the 'SODS' of some writers. This second component is also known as the thermal shift.

A complete study of the total spectrum shift in the vicinity of the magnetic ordering temperature has been made by Preston for metallic iron [94, 95]. Anomalous behaviour of δ_t, in the form of a discontinuity of 0.03 mm/s occurring in a temperature interval of less than 0.3° below the Curie point, was taken as an indication that the ferromagnetic phase transition might be first order [95]. However, alternative explanations of the effect in terms of band theory have also been proposed [96]. It was of interest to discover whether similar effects of magnetic order could be observed in insulators, and we have approached the problem in two ways, in an attempt to distinguish between the effects of temperature and magnetization on the total spectrum shift. We first made a careful study of the temperature dependence of δ_t in the orthoferrite $HoFeO_3$ [97], and then we measured the concentration dependence of δ_t in the mixed system $(Fe_{1-x}Rh_x)_2O_3$ [98]. Although it is more difficult to measure the total spectrum shift accurately for the mixed oxides, there is the advantage that the strong temperature dependence of δ_D does not affect data obtained at constant temperature.

Before describing the experimental results, we will give some further explanation of the two contributions to δ_t, and their possible magnetization dependence.

1.1 Isomer Shift.

The third term in (1.5) represents the Coulomb interaction of the electronic charge with the nucleus, assumed to be a uniformly

charged sphere of radius R_I. The energy shift, shown schematically in figure 3c, will be the difference of two such terms for the ground and excited states. If the isomer shift is measured relative to the source, then the complete expression is

$$\delta_i = \frac{2\pi}{5} Ze^2(R^2_{3/2} - R^2_{1/2})(\psi^2_A(0) - \psi^2_E(0)) \qquad (5.1)$$

where $\psi^2_A(0)$ and $\psi^2_E(0)$ are the electron densities at the absorbing and emitting nuclei. The first bracket is often written as $2R^2(\Delta R/R)$, and the isomer shift calibration can be expressed as the fractional change of radius when the nucleus is excited to the I = 3/2 state. R is given by the usual formula, $R = 1.20A^{1/3} \times 10^{-13}$cm. For ^{57}Fe, $R_{3/2} < R_{1/2}$, so that δ_i decreases with increasing s-electron density. The original iron isomer shift calibration of Walker, Wertheim and Jaccarino [99] was based on a comparison of the isomer shift difference between ferrous and ferric compounds and s-electron densities obtained from free ion Hartree-Fock wave functions. They found $\Delta R/R = -1.8 \times 10^{-3}$, so that an increase in s-electron density of 1 a_o^{-3} would decrease the isomer shift by 0.5 mm/s. More recent estimates of $\Delta R/R$ are given by Gol'danskiĭ [100] and Šimánek and Wong [101] who discuss data on the pressure dependence of δ_t in $KFeF_3$, and find $\Delta R/R = -5.2 \times 10^{-4}$, so that 1 a_o^{-3} corresponds to -0.15 mm/s. The smaller value of $\Delta R/R$ is probably the best. We shall show in §3.1 that chemical bonding greatly influences $\psi^2_A(0)$, so that it is not very realistic to use free-ion charge densities.

Measurements of the isomer shift are invaluable for dis-

tinguishing between high and low-spin ions, and different valence states [102]. The electron density at the nucleus decreases in going from Fe^{3+} to Fe^{2+}, mainly because of the additional screening of the 3s shell by the extra 3d electron. The isomer shift usually increases in order Fe^{IV}; Fe^{III}; Fe^{II}; Fe^{3+}; Fe^{2+}, where the Roman numerals denote low-spin iron, and systematic studies of series of compounds may give information about valence and bond type.

The isomer shift and quadrupole interaction together may be used to characterize a diamagnetic or paramagnetic compound. It may then be possible to determine the ratios of phases of the same element present in an unknown mixture. The Mössbauer effect has advantages and disadvantages compared to conventional x-ray techniques for the analysis of soils, rocks and sediments [103]. Briefly, the advantages are that it is selective, responding only to one isotope in the sample, it is capable of distinguishing between valence states even if an unambiguous determination of the compounds present is impossible, and good spectra may be obtained when the crystallite size is too small for x-ray analysis to be effective. The disadvantages are that there are only a very small number of elements with suitable isotopes, and the differences between spectra of materials in the same class, such as high-spin ferric compounds, are often rather slight, so it may be difficult to unravel overlapping spectra.

Magnetic order can influence the isomer shift in several ways. If the onset of order is accompanied by magnetostriction, changes in bond length, or a crystallographic transition, then the s-electron density will probably be affected. Also, if there is

a change in band structure or electrical properties, such as a metal-insulator transition, the isomer shift will probably change as well, because of the change in 4s-like occupation [104].

There will be a small component of the charge density at the nucleus of an insulator which changes with magnetic order, even when the lattice parameters and bond lengths are unaffected. If we make the approximations described in connection with (3.17), equation (3.14) may be rewritten as

$$P_a = P_0 + 6(N^{\uparrow 2} + N^{\downarrow 2})[- \sum_{n=1}^{3} S_{ns}\phi_{ns}(0) + a_{4s}\phi_{4s}(0)]^2 \qquad (5.2)$$

P_0 is the free ion electron density at the nucleus, P_a is the density in the antiferromagnetic state and P_p is the density in the paramagnetic state. If we replace the six $\downarrow$ cations in figure 30 by three $\uparrow$ and three $\downarrow$, then

$$P_p = P_0 + 12N^2[- \sum_{n=1}^{3} S_{ns}\phi_{ns}(0) + a_{4s}\phi_{4s}(0)]^2 \qquad (5.3)$$

where

$$N^2 = [1 + \tfrac{1}{2}(B_\sigma - S_\sigma)^2 - 6 \sum_{n=1}^{3} S_{ns}^2 + 6a_{4s}^2 + 12a_{4s}S_{4s}]^{-1} \qquad (5.4)$$

The difference between (5.2) and (5.3) is ΔP, the charge density difference between the ordered and disordered states. It works out as $0.0004a_o^{-3}$ in αFe_2O_3. If the differences between $S_{ns}^{\uparrow}$ and $S_{ns}^{\downarrow}$ and $\phi_{ns}^{\uparrow}(0)$ and $\phi_{ns}^{\downarrow}(0)$ are also taken into account, ΔP still has the same order of magnitude.

If the reduced sublattice magnetization is σ, then the general charge density, P, is $P_a + (1-\sigma)P_p$. In other words, the isomer

shift is of the form

$$\delta_i(\sigma) = \delta_i(0) + A\sigma. \tag{5.5}$$

A is the isomer shift corresponding to ΔP, and even if the original calibration is used, it is only -0.0002 mm/s, or about 1/1000 of a linewidth, which is much too small to measure on our spectrometers. However, the calculations are rather sensitive to the values of the spin-polarized Hartree-Fock wave functions in the outer, overlap region so the effect might be more important than this calculation suggests. The main result is (5.5), which is true to first order regardless of the precise values of the overlap integrals and charge densities at the nucleus.

1.2 Second Order Doppler Shift.

The second order Doppler shift is a relativistic effect connected with the nuclear vibrations associated with phonons in the lattice [105, 106]. The relativistic expression for the Doppler shift is

$$h\nu_0 = h\nu(1 - \frac{V_E}{c}) \Big/ \sqrt{1 - \frac{V_E^2}{c^2}} \tag{5.6}$$

V_E is the velocity of the emitting nucleus in the direction of the γ-ray. Since phonon frequencies are 10^{12} or $10^{13} s^{-1}$, much higher than the frequency associated with the lifetime of the excited nuclear state, the term V_E/c averages to zero in the course of a lifetime. However, V_E^2 and similarly V_A^2 have non-zero averages. It follows from (5.6) that

$$\frac{\Delta E_\gamma}{E_\gamma} = -\frac{1}{2}\frac{\bar{V}_E^2}{c^2}. \tag{5.7}$$

or, in terms of u, the energy of a monatomic solid per atom of mass M,

$$\delta_D = -\frac{1}{2}\frac{E_\gamma u}{Mc^2} . \tag{5.8}$$

The temperature variation of the thermal shift δ_D, expressed in energy units, is

$$\frac{\partial \delta_D}{\partial T} = -\frac{1}{2}\frac{E_\gamma C_p}{Mc^2} . \tag{5.9}$$

where C_p is the lattice specific heat, at constant pressure. An alternative derivation of these equations was given by Josephson [106], who considered the effect of the relativistic mass loss E_γ/c^2 of the emitting nucleus on the phonon energies.

Some approximation must now be made to the lattice dynamics. u or C_p is usually expanded in terms of a characteristic temperature using the Einstein or Debye models. In the latter case, (5.8) becomes

$$\delta_D = \frac{-9kTE_\gamma}{4Mc^2}\left[\frac{1}{4}\frac{\Theta}{T} + 2\left(\frac{T}{\Theta}\right)^3 \int_0^{\Theta/T} \frac{x^3 dx}{e^x - 1}\right] \tag{5.10}$$

If δ_D is to be in mm/s, then the factor $-9kE_\gamma/4c^2$ is equal to -0.0624, with M in atomic units. The first term in the bracket is the contribution due to the zero-point motion of the nuclei, and the second term is the temperature-dependent part. A universal curve for δ_D/Θ as a function of T/Θ is given in figure 50. It is calculated from (5.10), taking $M = M_a = 56.94$, but it may be used for any other value of M if the vertical axis is scaled by M_a/M. Both the low-temperature and high-temperature asymptotes are drawn in the

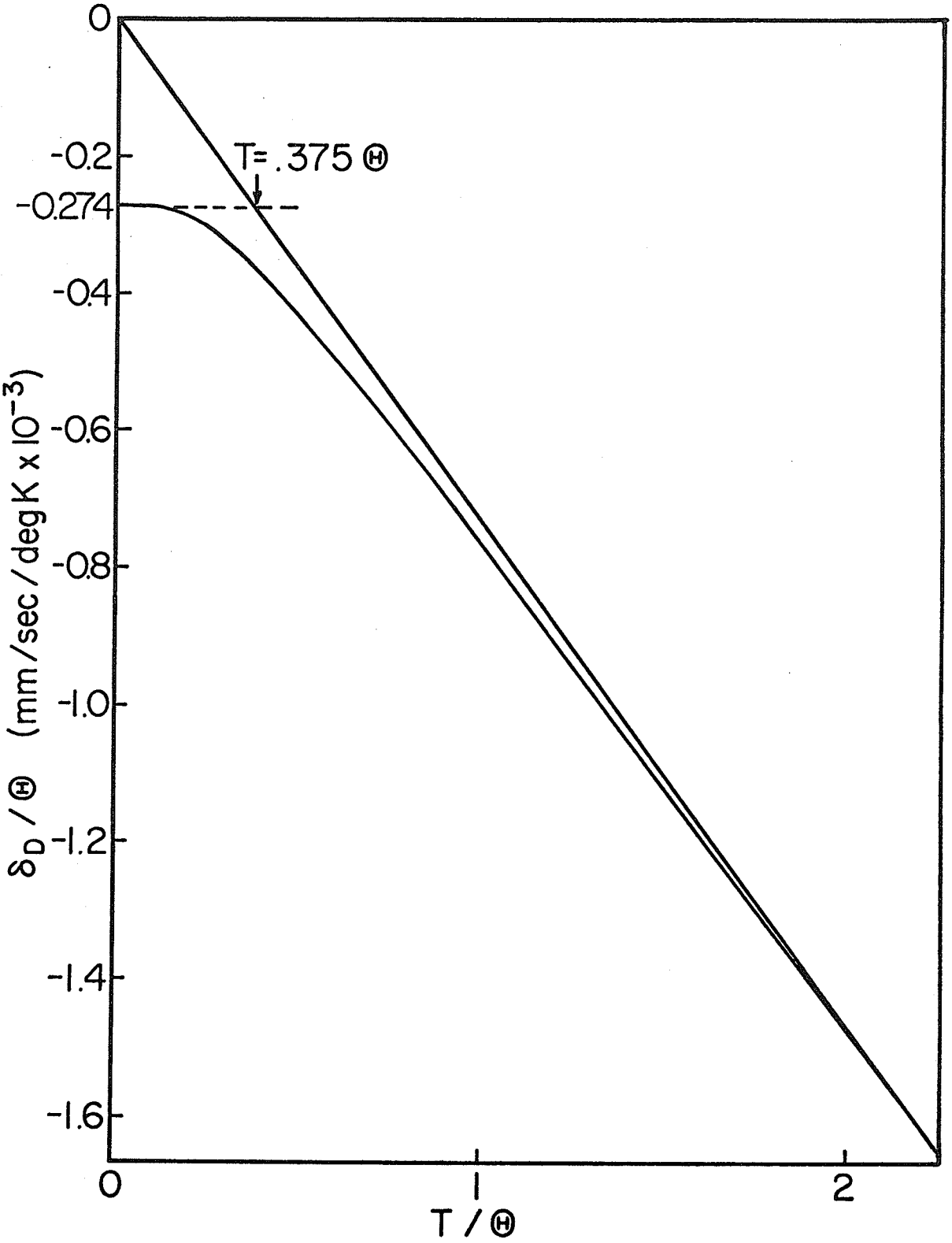

Figure 50. The behaviour of the second order Doppler shift, calculated on the Debye model. The curve may be used for any Debye temperature, and is appropriate for the mass of ^{57}Fe.

picture. They have the form

$$\delta_D = -0.0156\ \Theta/M \qquad (5.11)$$

and

$$\delta_D = -7.31 \times 10^{-4} T \qquad (5.12)$$

The latter corresponds to the classical value, $C_p = 3k$ in equation (5.9), with M = 56.94.

These two asymptotes intersect at $T = 0.375\Theta$, a fact which has been used to measure Θ [107]. Some drawbacks in this method are worth pointing out. An accurate knowledge of the total spectrum shift is required at low temperatures, and also for $T \gtrsim 2\Theta$. The curve does not reach its asymptote at lower temperatures, and if the tangent is taken at lower temperatures, for example in the range $\Theta < T < 2$, Debye temperatures will be obtained which may be 20% too high. It must also be assumed that Θ and δ_i are the same at high and low temperatures, and that the same value of M is appropriate in both limits. All these assumptions are dubious, except possibly for metallic iron. A better method of determining Θ is from the variation of the recoilless fraction in some limited temperature range [108]. An example is given in §2.3.

So far, the discussion of the second order Doppler shift has been for a monatomic lattice. In a polyatomic lattice or solid solution the equations must be modified. Iosilevskiĭ has distinguished two limits for multi-component systems, [109]. The first is the low temperature limit, when the phonon wavelength is much greater than the interatomic spacing. Then M in (5.8) - (5.11)

should be taken as $\bar{M}$, the average mass of an atom in the crystal, and the Debye temperature is related to the value which determines the low-temperature specific heat by the equation $\Theta = (\bar{M}/M_a)^{1/3}\,\Theta_{s.h.}$. In the other limit, when the temperature is high, M in the equations should be replaced by M_a, the mass of the Mössbauer atom. The characteristic temperature may be rather different from the value deduced from low-temperature specific heat, and may even be different for iron ions in different sites in the same crystal [110]. The two limits are characterized by $T \ll \Theta$ and $T \gtrsim \Theta$ respectively.

It is also worth noting that the thermal shift is not particularly sensitive to the details of the vibrational spectrum. If $T > \Theta/3$, a good approximation to (5.8) is

$$\delta_D = \frac{-3kTE_\gamma}{2Mc^2}\left(1 + \Theta^2/CT^2\right) \qquad (5.13)$$

This is true whether the Debye or Einstein model is used, the only difference being that the constant C is 20 for the one and 12 for the other [111].

The influence of magnetic coupling of the ions on the second order Doppler shift of a crystal has been calculated by Bashkirov and Selyutin [112]. Their expressions for δ_D as a function of temperature and magnetization may be rewritten as

$$\delta_D = \frac{-9kTE_\gamma}{4Mc^2}\left[\frac{1}{4}\frac{\Theta'}{T} + \left(\frac{T}{\Theta'}\right)^3\int_0^{\Theta'/T}\frac{x^3\,dx}{e^x - 1}\right] \qquad (5.14)$$

The only difference between this equation and (5.10) is that Θ

has been replaced by Θ', where

$$\Theta' = \Theta\sqrt{1 + B_o\sigma^2} \qquad (5.15)$$

The full expression given by these authors for $(\Theta'/\Theta)^2 - 1$ is $B = -8\pi^2 \langle S_i.S_j \rangle a^2/C_\phi^2 M J''(a)$. C_ϕ is the velocity of sound and $J''(a)$ is the second derivative of the exchange integral, evaluated at the interionic separation. We have assumed that $\langle S_i.S_j \rangle \sim \sigma^2$. They suggest that $B > 0$ in both ferromagnetics and antiferromagnets, and also that $B_o \simeq 1$. In other words, the magnetic order is taken into account through a magnetization-dependent characteristic temperature Θ', which they expect to be considerably greater than Θ at low temperatures, when $\sigma \sim 1$. They predict that δ_D will be 0.01 - 0.10 mm/s less in the magnetically ordered region than it would be if the behaviour above the magnetic transition could be extrapolated to lower temperatures. Provided the lattice parameters do not change, no discontinuity in δ_D is expected at T_N because there is no discontinuity in $\langle S_i.S_j \rangle$.

A set of curves for δ_D for increasing B_o, or equivalently, increasing σ or Θ is shown in figure 51. According to the theory, δ_D should follow one of the lower curves at low temperatures, diverge slightly above it as T increases, and move rather sharply towards the $B = 0$ curve just below T_N.

We will now describe our experimental results, and examine them in relation to the theories we have discussed.

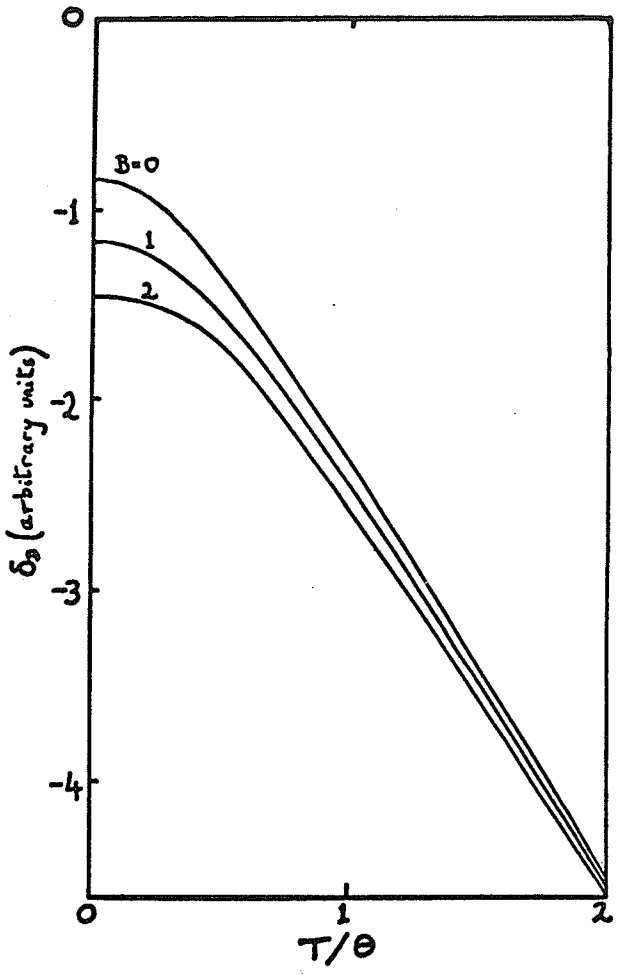

Figure 51. The second order Doppler shift for several values of B, a parameter which depends on the degree of magnetic order and the form of the exchange integral. B = 0 in the paramagnetic state.

2. RESULTS FOR $HoFeO_3$

Holmium orthoferrite was chosen as a candidate for an accurate determination of the total spectrum shift in an insulator for three reasons. i) It has a single iron site in its distorted pervoskite structure [113]. ii) The Néel point is roughly 350°C, so that a good range of temperatures above and below T_N is accessible using the vacuum furnace. iii) $\bar{M}$ differs from M by only 6%, so that the magnetization-dependent effects are unlikely to be

obscured by the variation of M in (5.14). The rare-earth orthoferrites have been extensively studied by various techniques, including the Mössbauer effect [107, 114]. They have interesting magnetic properties, among them are their weak ferromagnetic moments [115] and bubble domains [116], neither of which concern us here.

2.1 Experimental Procedure.

The samples were prepared from a mixture of 99.9% pure $HoFeO_3$ and Fe_2O_3. The powders were ground, pelleted, and prefired for 4 hours at 900°C. They were then reground, repelleted and refired for 10 hours at 1400°C in air. The powders were enriched with $^{57}Fe_2O_3$ [12] so that 27% of the iron was the Mössbauer isotope. X-ray photographs agreed with the published powder pattern [117].

More than a hundred spectra were taken in the range 99-875°K using the M-1 and M-2 spectrometers. Any non-linearity in the spectrometers could have disastrous effects when comparing data in the magnetically ordered and paramagnetic regions. However, the error in the measured total spectrum shifts due to non-linearity was found to be less than 0.002 mm/s, from calibration spectra with an iron foil. Furthermore, data was obtained using both spectrometers in much of the temperature range, and no systematic differences were detected.

In order to measure the total spectrum shift accurately, it is necessary to keep track of the zero drift, and collect the spectra in a time during which the zero changes by no more than

0.002 mm/s. Two different methods of monitoring the zero were used in this experiment. When operating the spectrometer M-1 at constant velocity, the number of flybacks in 100 seconds were counted electronically in each of the twenty channels around the zero. The exact position was found to within a tenth of a channel (≃ ±0.001 mm/s) by interpolation. A typical result is shown in figure 52. An

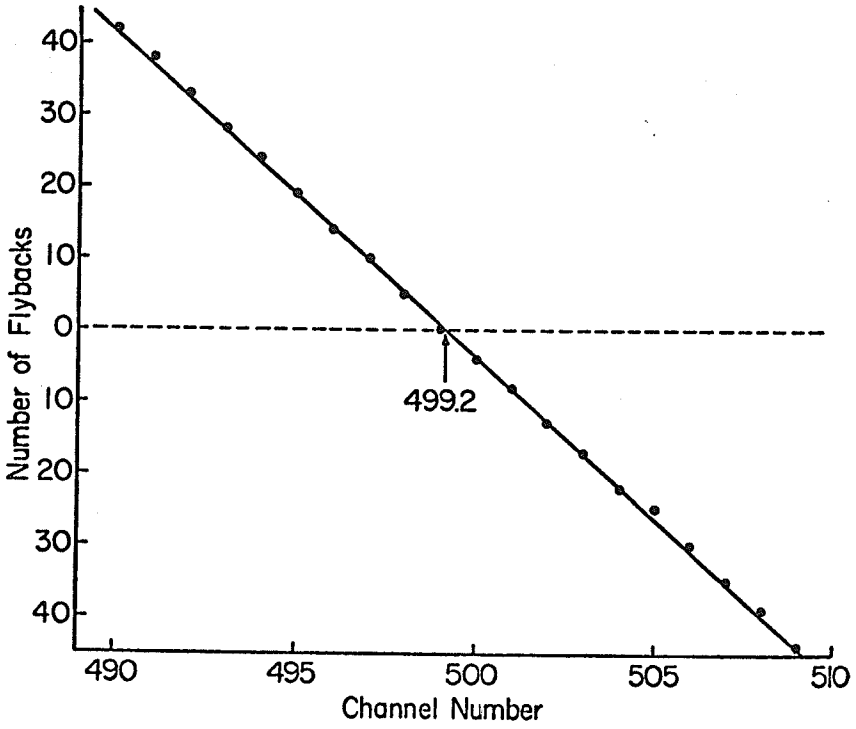

Figure 52. Location of the zero of the constant velocity spectrometer by counting flybacks.

alternative, and slightly less accurate method was used when operating at constant acceleration with the spectrometer M-2. A sodium-ferrocyanide absorber at room temperature was placed between the furnace or cryostat and the counter. The quadrupole splitting in this material is so small that the spectrum is essentially a single-line marker, and the positions of the $HoFeO_3$ lines may be

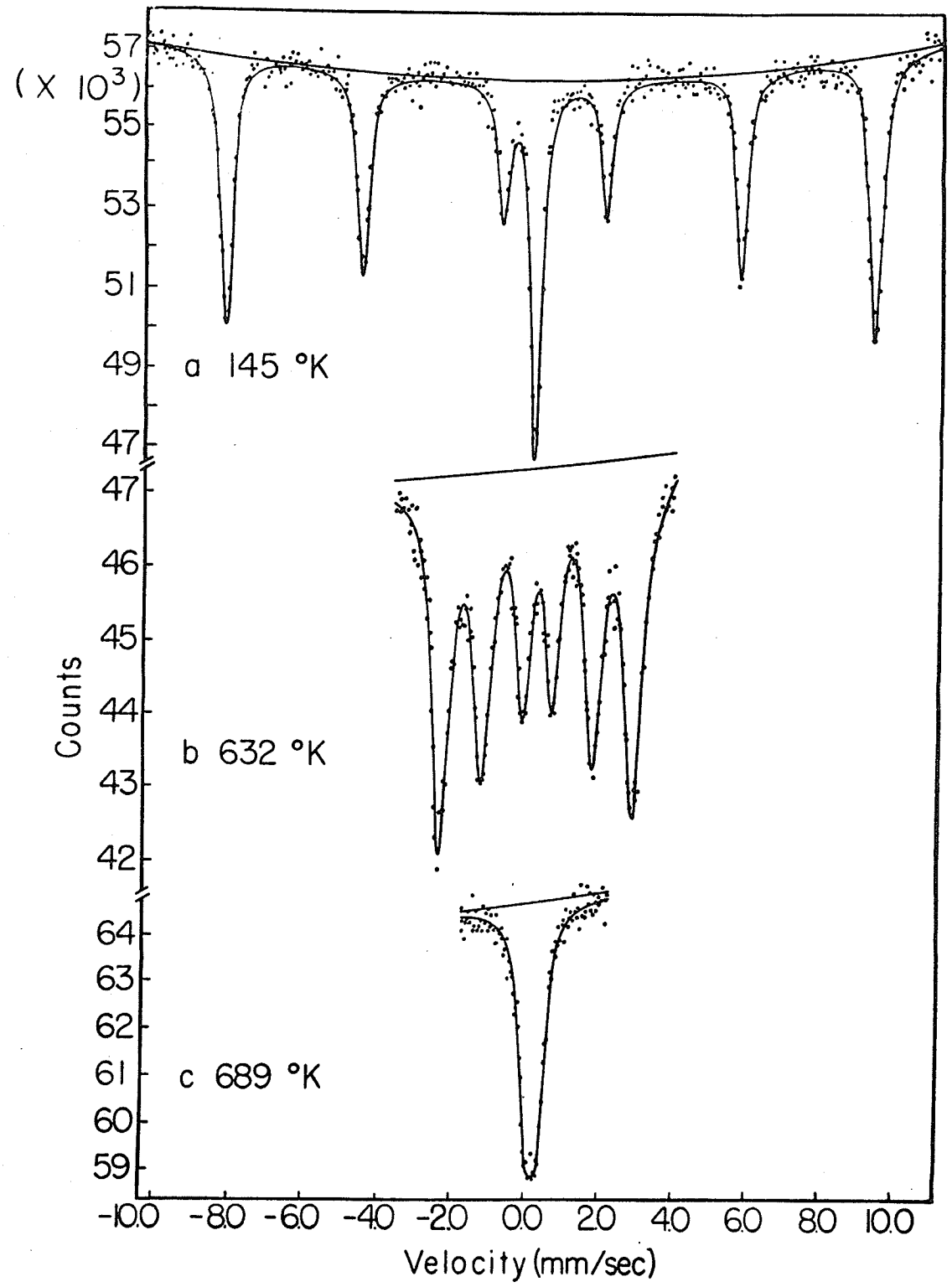

Figure 53. Mössbauer spectra of $HoFeO_3$. a) was collected at constant acceleration with a sodium-ferrocyanide spectrum super-imposed. b) and c) were collected at constant velocity. The least-squares fits are shown.

measured relative to it. This technique is most useful well below T_N where the marker is well separated from the middle lines of the orthoferrite pattern. δ_t may then be determined to within 0.003 mm/s.

Some typical spectra are shown in figure 53. The one in figure 53a was taken at constant acceleration with the ferrocyanide marker, while those in figure 53 b and c were obtained at constant velocity, and the zero was measured before and after each spectrum by counting flybacks. The data was analysed in the usual way, fitting Lorentzians to the peaks by the method of least squares. The solid lines drawn in the figure are the fits. Above T_N, the spectrum is a close doublet with a quadrupole splitting $\varepsilon/2 = 0.309 \pm 0.005$ mm/s. Below T_N, ε is less than 0.05 mm/s and decreases towards zero as $T \rightarrow T_N$.

When fitting the paramagnetic doublets, the two lines were constrained to have the same intensity and full-width at half maximum. No other constraints were used except that the two middle peaks of the spectra taken with the sodium-ferrocyanide marker were also constrained to be equal. Below T_N, the quadrupole shift, hyperfine field and total spectrum shift were deduced from the six peak positions by a weighted least squares fit.

2.2 Hyperfine Fields.

The hyperfine field data, although incidental to the main object of the experiment, is copious and complete. It is shown in figure 54, together with the Brillouin function curve for S = 5/2. It deviates from the data by less than 3% when $T < 500^{\circ}K$. The fields

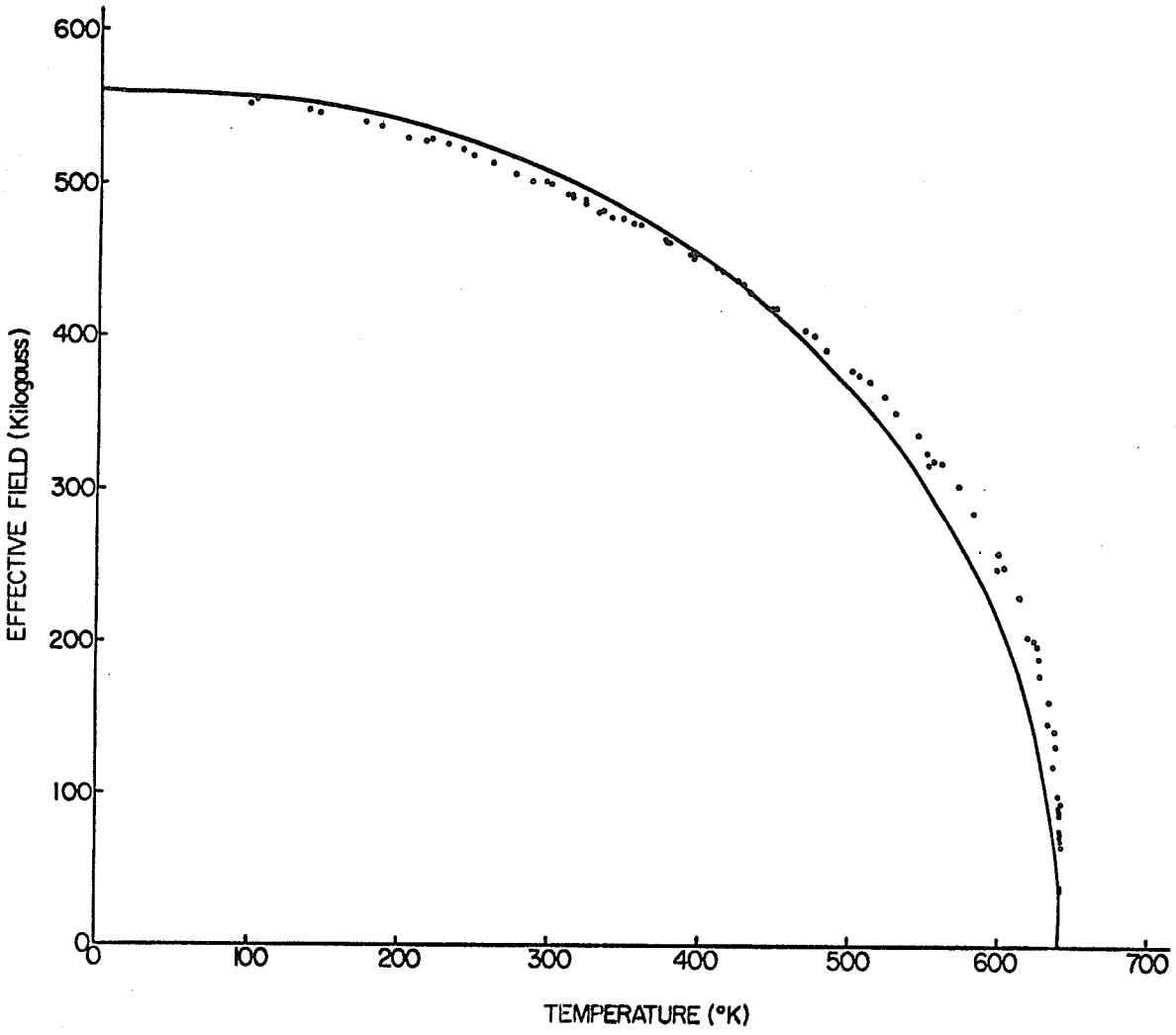

Figure 54. Temperature dependence of the hyperfine field in $HoFeO_3$. The solid curve is obtained from the Brillouin function for $S = 5/2$.

for $T < 450°$, $\tau < 0.7$ are also plotted against T^2 in figure 55. According to simple spin wave theory in an antiferromagnet [118],

$$\sigma = 1 - 1.590 \times 10^{-3} k^2 T^2 / 4J^2 \qquad (5.16)$$

The straight line, which is a good fit to data in the whole temperature range, has a slope corresponding to $J = 17.9°K$. The value of J deduced from T_N using the molecular field equation $J = 3kT_N/2S(S+1)N$ (5.17) is 18.4°K.

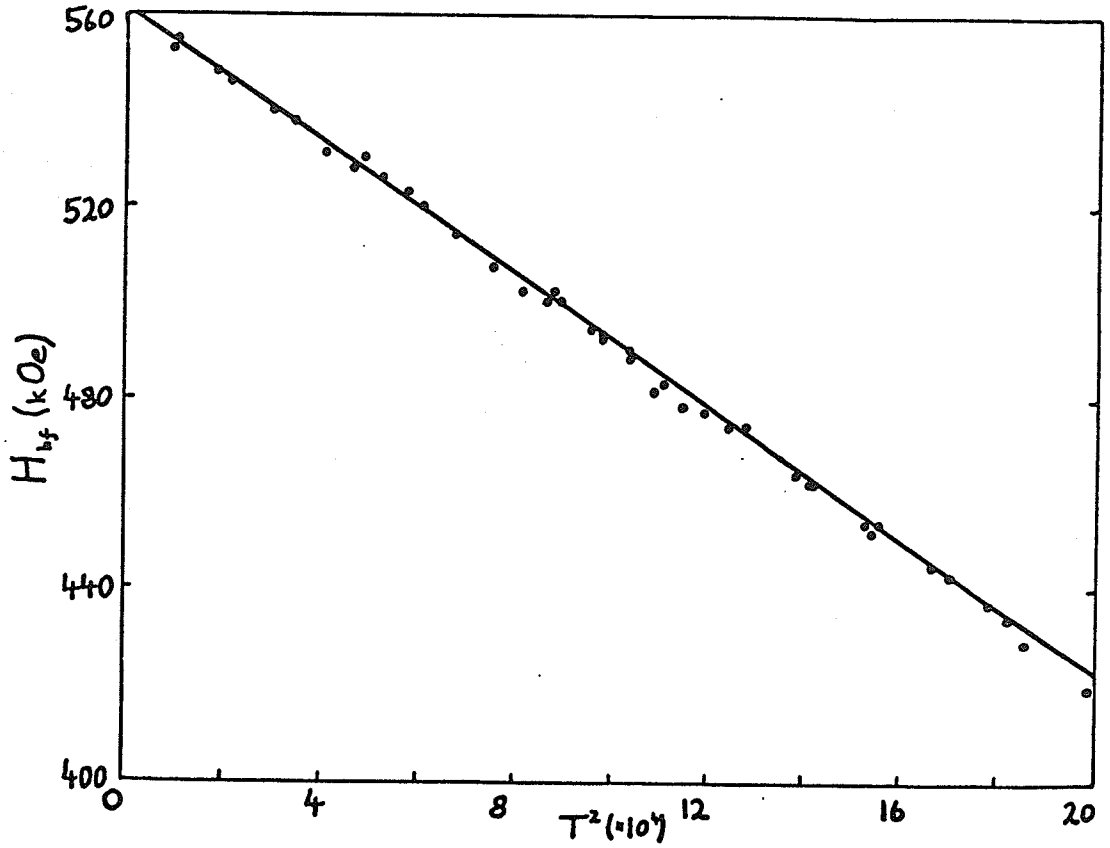

Figure 55. The hyperfine field in $HoFeO_3$ as a function of T^2.

The Néel temperature was measured in two ways. H^3 is plotted against T for $\tau > 0.995$ in figure 56, and a value of 642.7°K was found. Alternatively we carried out a thermal scan at a small positive velocity corresponding to the paramagnetic peak position. The result is shown in figure 57, and a value of 642.5°K was found. The agreement between the two different techniques is pleasing. A slightly lower value, 639°K, was previously reported for $HoFeO_3$ [107]. In our material, mixed spectra were observed in a 2° temperature interval below T_N.

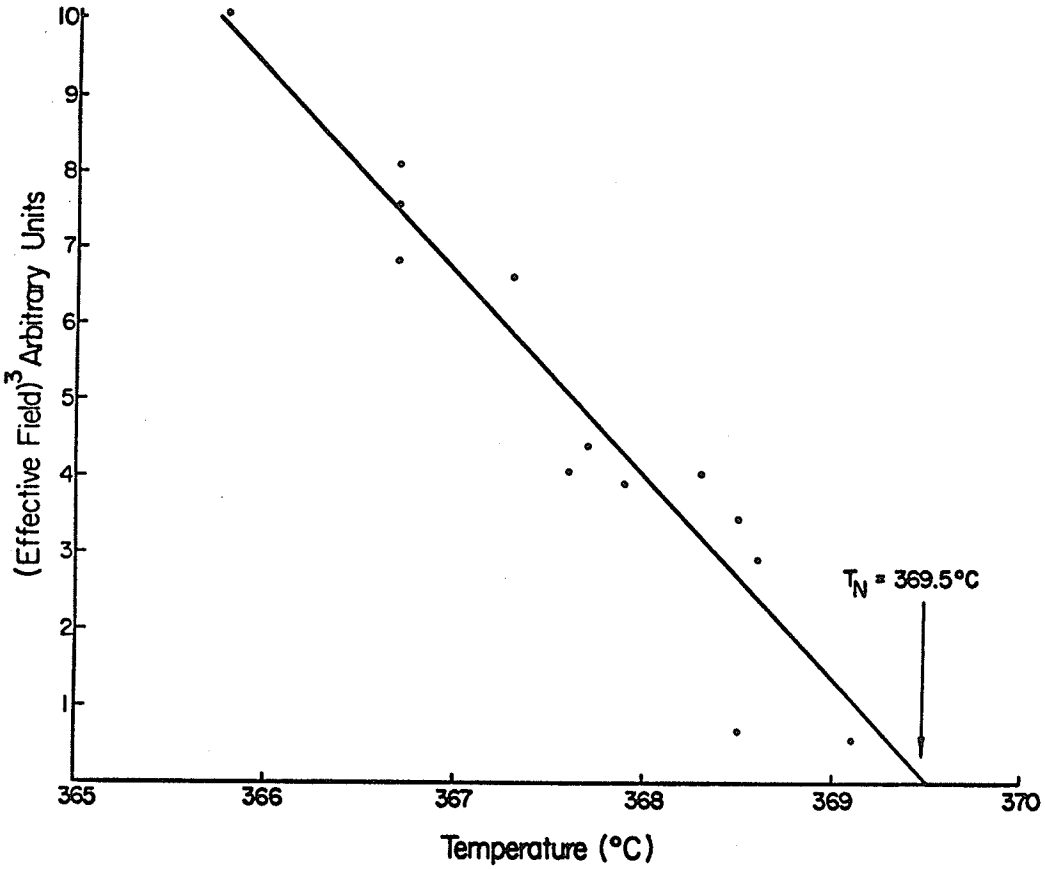

Figure 56. The cube of the hyperfine field plotted as a function of temperature to determine the Néel point.

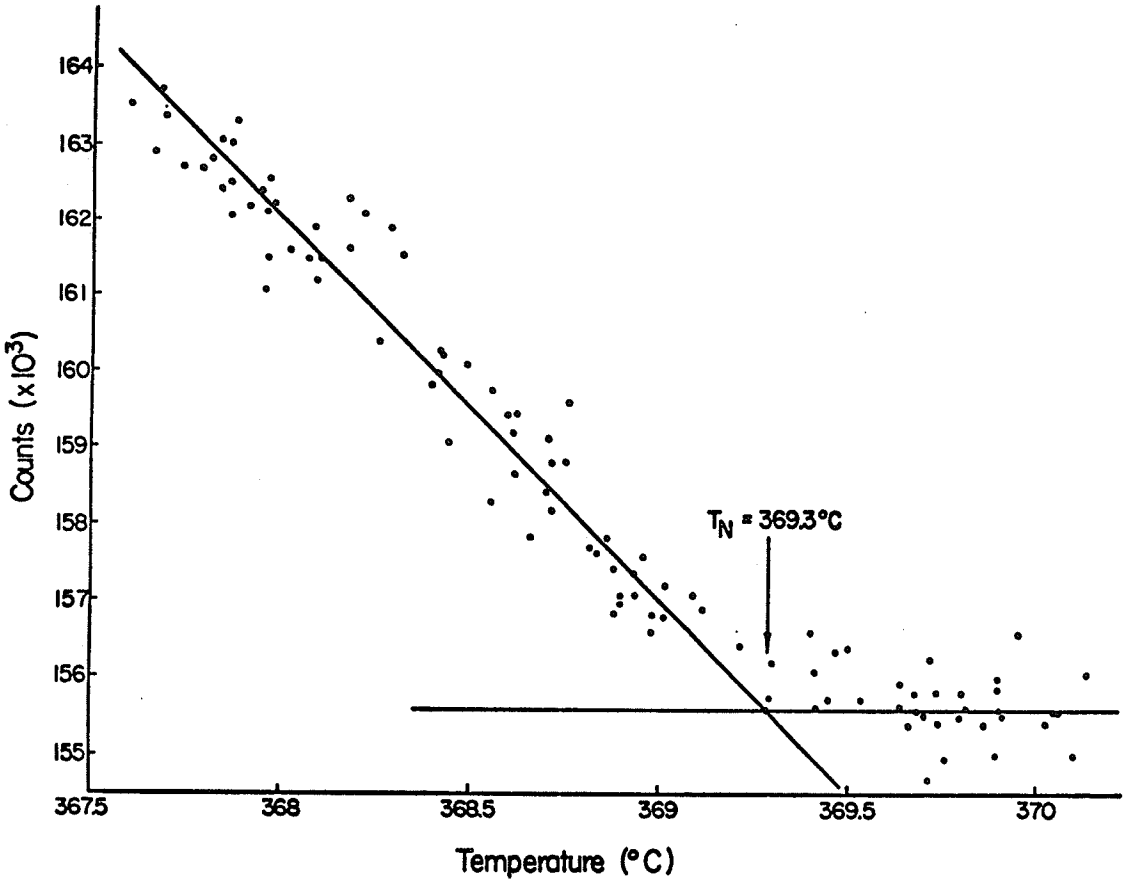

Figure 57. Determination of the Néel point from a thermal scan at 0.1 mm/s.

It is also worth plotting $H:(T_N-T)$ on a double logarithmic scale, as shown in figure 58. The critical exponent β may be found from the slope of the curve in various temperature ranges, since [119]

$$H = D(1-T/T_N)^{\beta} \tag{5.18}$$

In the decade $0.9 < (1-T/T_N) < 0.99$, we find $\beta = 0.337$, while in the decade $0.99 < (1-T/T_N) < 0.999$, $\beta = 0.346$. T_N was taken as 642.7°K, but if 642.5°K had been chosen, β would be 0.372 in the higher range, although the value in the lower range would be virtually unchanged.

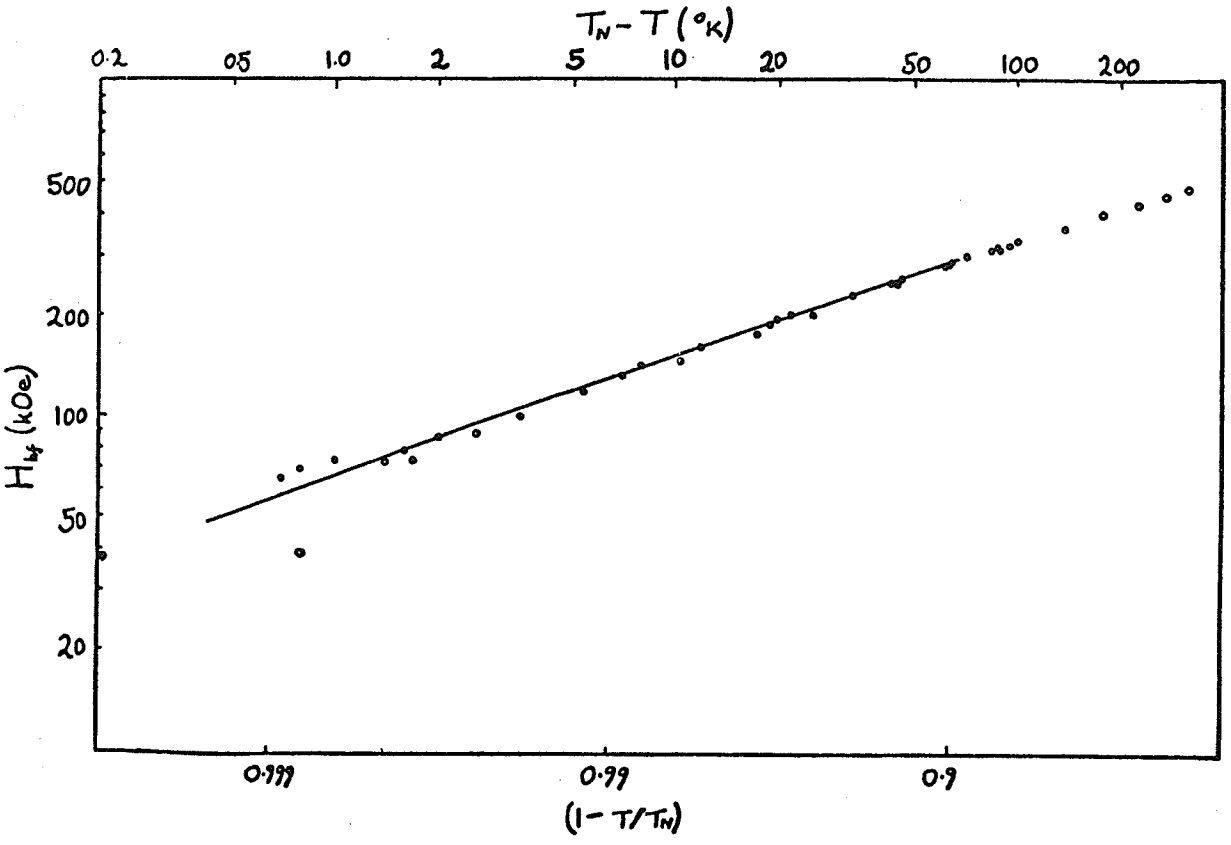

Figure 58. Plot for determining the critical exponent.

Mössbauer spectra are probably not a particularly good source of information about the critical exponents. Apart from the experimental difficulty of maintaining the sample at a homogeneous, uniform temperature, there is doubt whether H_{hf} is proportional to $\bar{S}_z$ in the critical region where dynamic effects may be important, and mixed spectra may appear.

2.3 Total Spectrum Shift.

The total spectrum shift is plotted as a function of temperature in figure 59. Many of the points are averages obtained from two spectra at almost the same temperature, and some typical error limits are marked. They are the sum of the error in the least-squares fit to the peak positions and the error in the position of the zero.

The curve does have the general shape expected. However there are some important discrepancies which will now be discussed.

In order to compare the observed temperature dependence of δ_t with the predictions of (5.14), it is first necessary to determine the Debye temperature. The mean square displacement $\langle x^2 \rangle$ of the Mössbauer nucleus which occurs in expression (1.1) for the recoilless fraction may be evaluated on the basis of the Debye model. The bracket in (1.1) is the Debye-Waller factor, often denoted as -2W. It is given by, [108],

$$2W = \frac{3E_\gamma^2}{Mc^2k}\left[\frac{1}{4} + \left(\frac{T}{\Theta}\right)^2 \int_0^{\Theta/T} \frac{x\,dx}{e^x - 1}\right] \qquad (5.19)$$

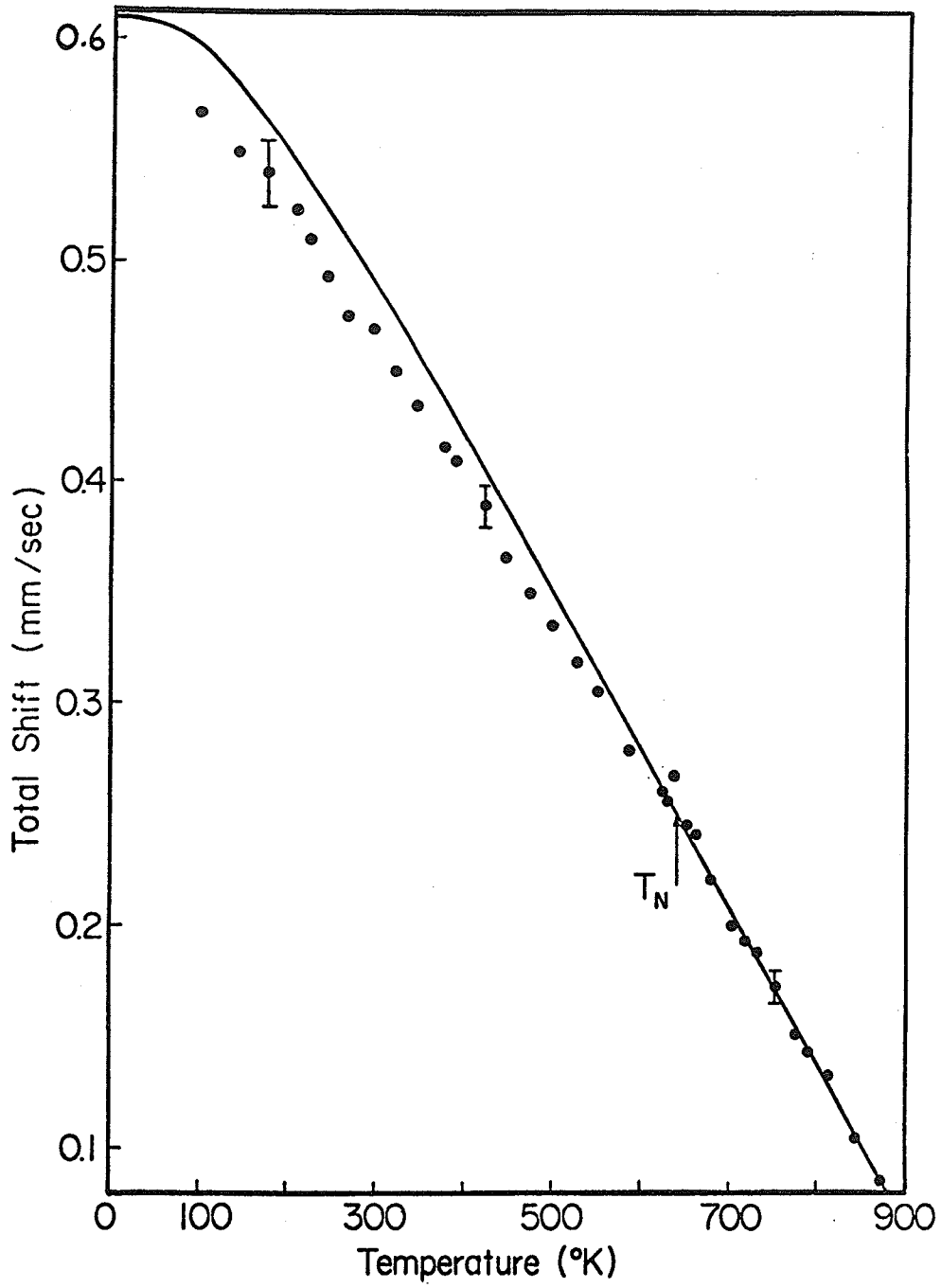

Figure 59. Temperature dependence of the total spectrum shift in $HoFeO_3$. The solid line corresponds to a Debye temperature of 457°K.

An approximation, accurate to within 7% for $T > \Theta/2$, is to set the bracket equal to T/Θ. Then

$$\langle x^2 \rangle = \frac{2W\hbar^2c^2}{E_\gamma^2} = \frac{3\hbar^2 T}{Mk\Theta^2} . \qquad (5.20)$$

A plot of ℓnf:T will have slope $-3E_\gamma^2/Mc^2k\theta^2$. Provided the absorber is thin, f is proportional to the area of the absorption peaks, and θ is easily deduced. A typical plot is shown in figure 60 for the temperature range 647 - 875°K, above T_N. The corresponding value of θ is 457 ± 9°K, the error being two standard deviations in the least-squares fit of a straight line to the points. Similar data was obtained in the range 320 - 550°K, below T_N, where an effective Debye temperature θ' = 540 ± 12°K was found. The errors do not take any account of possible systematic errors in inadequacies in the Debye model. The value of B_o, calculated from (5.15) and these values of θ and θ', is 0.67.

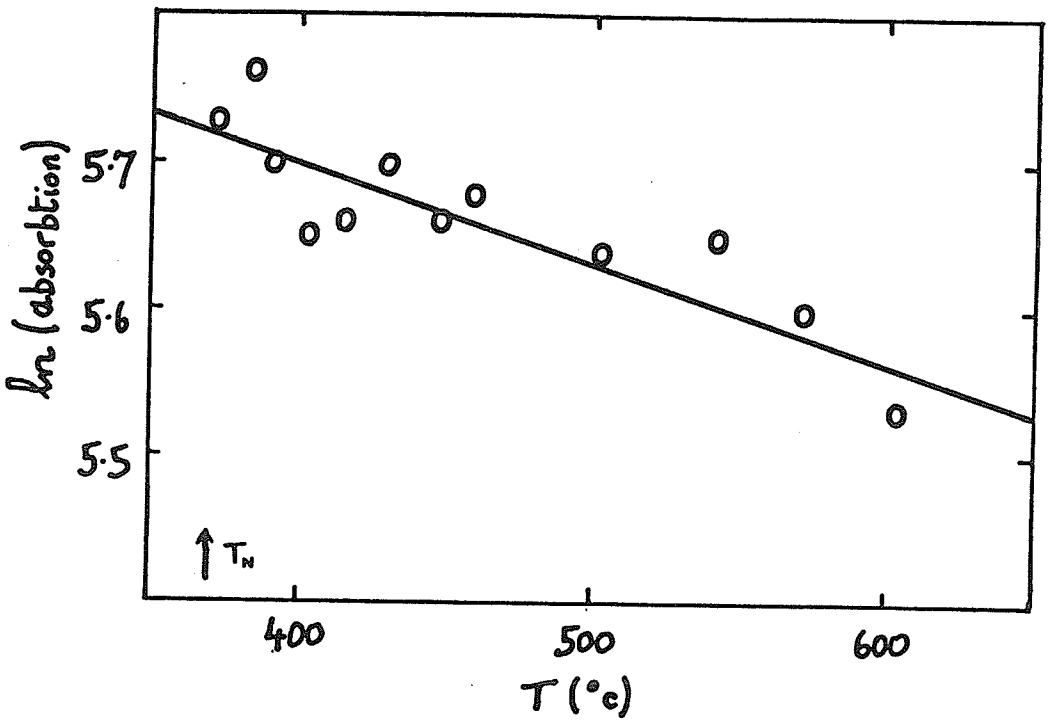

Figure 60. Determination of the Debye temperature from the variation of the recoil-free fraction in a range of temperature below T_N.

The high temperature part of the total spectrum shift curve, above T_N, was fitted to a straight line, and the slope is $-7.09 \pm 0.09 \times 10^{-4}$ mm/s/°K. The slope predicted by (5.10) in the same temperature range with $\Theta = 457$°K is -7.17×10^{-4} mm/s/°K, notably smaller than the limiting value given by (5.12), which is only attained at higher temperatures. We conclude that (5.10) gives a good fit to the data in the paramagnetic region, and the complete curve for $\Theta = 457$°K is drawn in figure 59.

The significant feature of the data is now apparent. Although the curve is a good fit to the paramagnetic points, every point but one in the antiferromagnetic region lies below it. The data is replotted on an expanded scale in figure 61 where the *deviation* from the $\Theta = 457$°K curve is given as a function of temperature.

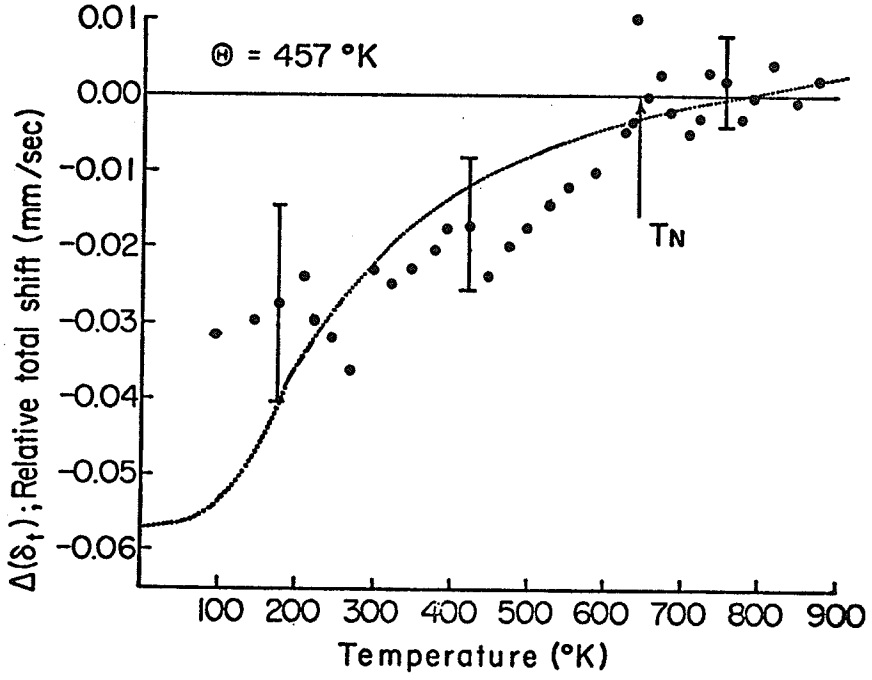

Figure 61. The total spectrum shift relative to the second order Doppler shift, calculated for a Debye temperature of 457°K. The dotted curve corresponds to a Debye temperature of 720°K.

By extrapolating the data in the regions just above and below T_N, it may be seen that any discontinuity in δ_t is less than 0.003 mm/s. This is in agreement with a result of Wertheim et al [120] who found the total spectrum shift of FeF_3 to be continuous to within ±0.002 mm/s. Continuity of δ_D is expected at a second order phase transition.

The observed influence of magnetic order on δ_t could have two explanations. Either the second order Doppler shift is magnetization dependent, as suggested by Bashkirov and Selyutin [112], or else the isomer shift is magnetization dependent. Both possibilities will be considered in turn, but first the dotted curve in figure 61 will be explained. It represents an attempt to fit all the data to (5.10) with a single Debye temperature. Although it is within the experimental errors of most of the points, it does not seem to have quite the right shape. However the decisive objection to this interpretation of the data is that the dotted line corresponds to a Debye temperature of 720°K, quite different from either of the measured values, and almost twice the Debye temperature deduced from low temperature specific heat measurements on another orthoferrite, $DyFeO_3$ [121].

The discrepancy between the data and the curve calculated from the simple Debye model (5.10) using the θ obtained in the high-temperature region begins at the magnetic transition temperature. This indicates that the effect really *is* connected with the magnetic

order, and is not just due to the inadequacy of the Debye model in describing the phonon spectrum. The insensitivity of the model was emphasized in the discussion of (5.13). The graph of figure 61 is repeated, for clarity in figure 62 with curves calculated for a magnetization-dependent sceond order Doppler shift or isomer shift.

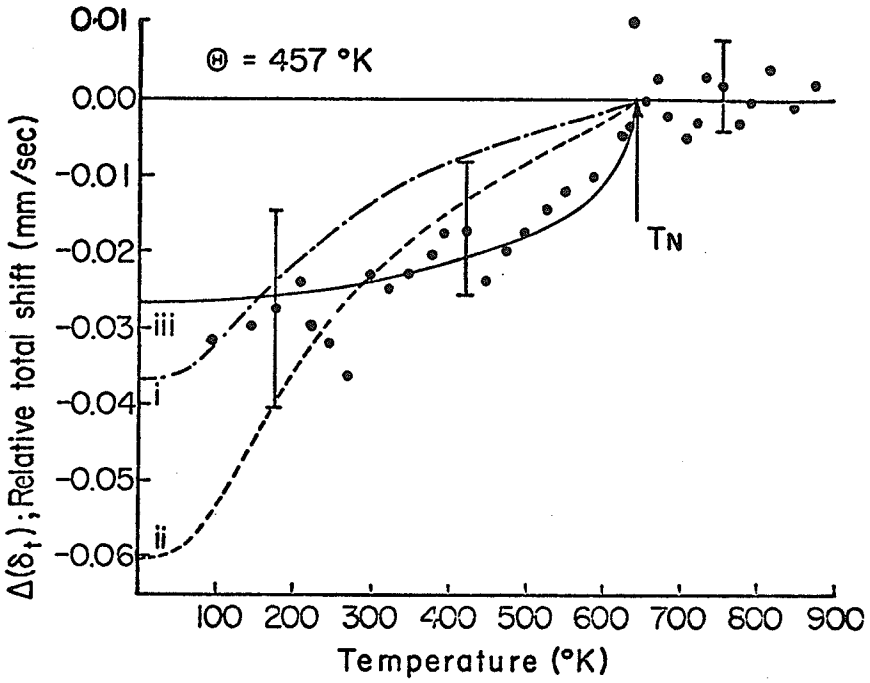

Figure 62. The same data replotted, with theoretical curves, i) for Θ'(0) = 591°K ii) for Θ'(0) = 676°K and iii) proportional to σ.

i is obtained from the magnetization-dependent Debye model (5.14) using the value of B_o deduced from the measurements of the Debye-Waller factor; ii is obtained from the same model by allowing B_o to vary to give the best fit to the data. B_o = 1.2, and Θ' is 676°K at T = 0. The average value of Θ' in the range 320 - 550°K is 597°K, compared to the measured 540 ± 12°K. Both of these two curves are just within the experimental error on most of the points, and either

could be taken as an adequate representation of the data. Nevertheless the agreement is not completely satisfactory.

iii is the best fit to the data, assuming a small extra contribution to the isomer shift proportional to σ, in conformity with (5.5). It appears to follow the shape of the data somewhat better than the others, although a term proportional to σ^2 would do just as well. The constant A is -0.027 mm/s which corresponds to a charge density difference ΔP of at least $0.05a_o^{-3}$, two orders of magnitude greater than the calculation in §1.1. In spite of the uncertainties in that calculation, it seems that the explanation of a magnetization-dependent isomer shift cannot be sustained.

The conclusion from the study of δ_t as a function of temperature is that there are measurable magnetic effects on the total spectrum shift in an insulator which may be explained fairly well on the basis of a magnetization-dependent Debye model. The other explanation, of a term in the isomer shift proportional to σ, lacks a theoretical justification.

3. RESULTS FOR $(Fe_{1-x}Rh_x)_2O_3$.

We now return to the iron-rhodium oxide system, which was the subject of the preceeding chapter. The measurements of the total spectrum shift of the system at 20°K and 296°K are illustrated in figure 63. The solid curves are just drawn to show the gist of the data, and they are not based on any calculation. The errors on the points are rather larger than in the previous experiment because

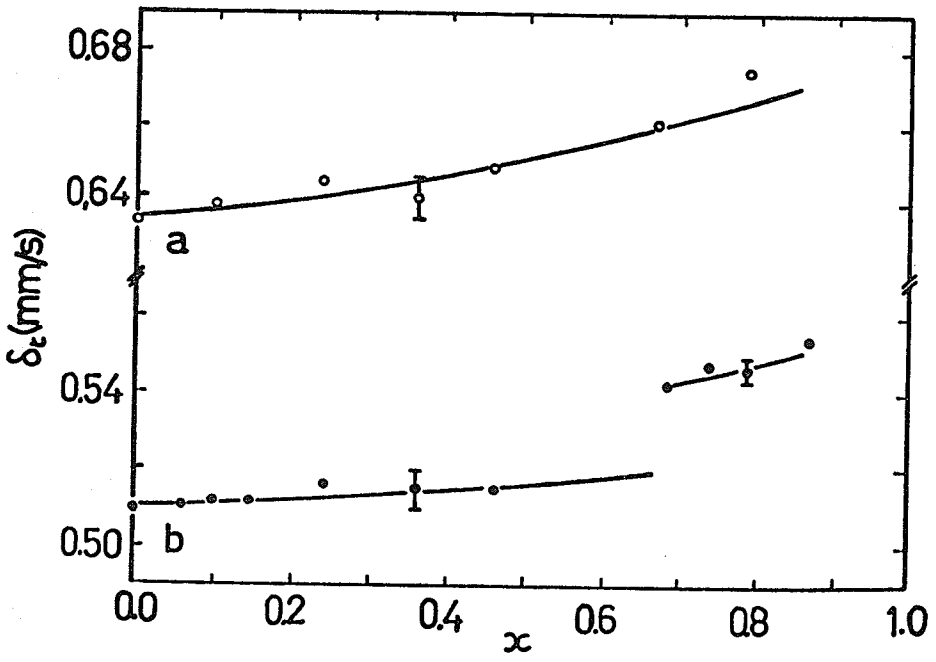

Figure 63. The average total spectrum shift of $(Fe_{1-x}Rh_x)_2O_3$ a) ○, at 20°K and b) ●, at 296°K. The solid lines just emphasize the trend of the data.

of the greater complexity of the fits in the antiferromagnetic region, and also because calibrations were not performed before and after every spectrum. Nevertheless, there is clearly a monotonic increase in δ_t with x at both temperatures, besides a distinct break between the magnetically ordered and disordered regions at room temperature. All the points for samples with $x \gtrsim 0.67$ at 296°K are deduced from paramagnetic spectra. The results for the temperature dependence of δ_t for the sample with x = 0.10, given in figure 42a, also show an increase in isomer shift in the paramagnetic region, as does the data for x = 0.36.

All these results may be compared with that of Bashkirov

et al [122], who found a *decrease* of 0.05 ± 0.02 mm/s in the total spectrum shift of αFe_2O_3 above its Néel point. We have no explanation of this difference between their result and ours, but it should be pointed out that the sign of the change they find at T_N is opposite to the sign they anticipate using their magnetization-dependent Debye model [112]. Moreover we will show that even the change of 0.025 ± 0.010 mm/s which we observe is too large to be explained in these terms.

It would be ideal if the shifts of the magnetically ordered and disordered phases could be measured simultaneously, for example in mixed spectra, like those shown in figures 37d or 47b. Unfortunately the magnetically split absorption lines are so broad and ill-defined that it is impossible to measure the centre sufficiently accurately.

We now consider the variation of δ_i and δ_D in the system in turn.

3.1 Isomer Shift.

The electron density at the nucleus is given by (3.14), except that the factor 6 must be replaced by the sum over Γ_a linkages. If we make the same assumptions as we did in the calculation of the variation of the quadrupole interaction, namely that the lattice parameters and the oxygen parameter vary uniformly with x, but the same iron parameter may be used throughout, then we can calculate the variation of P, and hence δ_i with x. The expansion of the lattice gives rise to a decrease in the electron

density at the nucleus and a corresponding increase in the isomer shift. If the isomer shift calibration of Simanek and Wong [101] is used, and a_{4s} is taken as 0.15 throughout, then the calculation gives the dashed lines in figure 64, where the same data is reproduced. The lines are normalised to 0.637 mm/s at 20°K and 0.512 mm/s at 296°K. The increase in isomer shift agrees moderately well

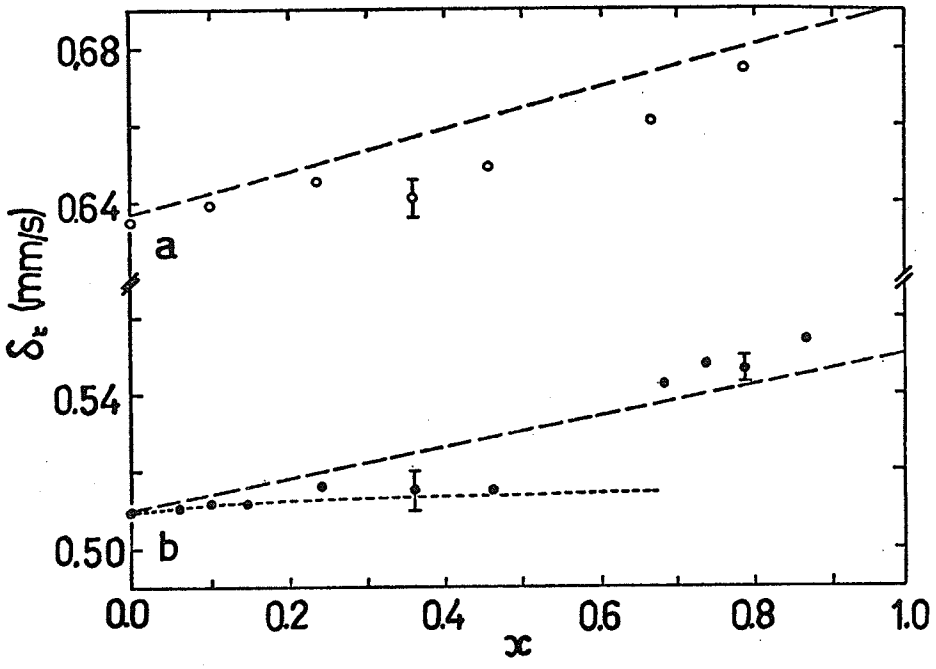

Figure 64. The same data as in figure 63. The dashed line shows the increase in isomer shift due to the change in lattice parameters. The dotted line gives the variation of the second order Doppler shift at room temperature.

with the data, in spite of the fact that we have not taken into account that some of the iron neighbours of the central iron ion have been replaced by rhodium, nor is any allowance made for the variation of the second order Doppler shift. Given the assumptions about the lattice parameters, there can be no discontinuity in the room temperature shift associated with the onset of magnetic order.

We can determine the difference between the total charge density at the iron nucleus in αFe_2O_3 and that of the free ion in much the same way as we did for spin density in IV 4. The free-ion value for an electron configuration $3d^5$ is given by the first terms in the modified (3.14). The remaining terms yield an increase in electron density of 6.3 a_o^{-3}. However the 3d occupation has also increased by 0.40 electrons. Using Watson's wave functions for Fe^{3+} and Fe^{2+}, there is a decrease in electron density of 1.76 a_o^{-3} on going from the ferric to the ferrous free ion. The overall increase in αFe_2O_3 is thus 5.6 a_o^{-3}, corresponding to a decrease in isomer shift of 0.84 mm/s. The isomer shift of a free Fe^{3+} ion would thus be 1.35 mm/s, relative to chromium.

3.2 Second Order Doppler Shift.

Before the possibility of explaining the data in terms of the second order Doppler shift can be considered, it is necessary to know the Debye temperatures. The Debye temperatures for αFe_2O_3 and αRh_2O_3 at room temperature may be deduced from the x-ray temperature factors, B_t. The Debye-Waller factor for the x-ray reflections is $B_t(\sin\theta/\lambda)^2$. (4.3) is analogous to (1.1) in that the intensities of the Mössbauer and x-ray lines both have the same functional dependence on $\langle x^2 \rangle$. On the Debye model, [123],

$$2W\left(\frac{\lambda}{\sin\theta}\right)^2 = B_t = \frac{48\pi^2\hbar^2}{Mk\Theta}\left[\frac{1}{4} + \left(\frac{T}{\Theta}\right)^2 \int_0^{\Theta/T} \frac{x\,dx}{e^x - 1}\right], \qquad (5.21)$$

a result which differs from (5.19) only in the numerical factor. We can make the same approximation as we did for (5.20), or else use the tabulated values of the function in the bracket, given by Guinier [123].

The temperature factors for iron and rhodium sesquioxides are 1.33 ± 0.12 and 1.2 ± 0.4. The factor for Fe_2O_3 applies only to the iron [72], while separate temperature factors for rhodium and oxygen in Rh_2O_3 were not obtained. However, the scattering factor of rhodium is more than thirty times greater than that of oxygen, so that no appreciable error is introduced if we take M in (5.21) as the cation atomic weight in both cases. The Debye temperatures are then 307 ± 12°K for Fe_2O_3, and 242 ± 40°K for Rh_2O_3. Assuming that θ varies linearly between these two extremes, it is possible to calculate the expected low temperature behaviour of δ_D from (5.11). If M is taken as $\bar{M}$, then δ_D increases with twice the slope of the 20°K data, whereas if M is taken as M_a, then the calculated increase is only half that of the data.

At room temperature, the data in the antiferromagnetic region is reproduced by the dotted line in figure 64, which is calculated from (5.10), assuming the linear decrease in Debye temperature. The difference between δ_t at 20° and 296°K for pure αFe_2O_3 is 0.125 ± 0.005 mm/s compared to 0.142 mm/s predicted from (5.10) with $M = M_a$. It is likely that a smaller value of M is appropriate at lower temperatures since $\bar{M} < M_a$, and the corresponding

difference would be even greater. A difference of 0.125 mm/s would correspond to Θ = 400°K with M = M_a throughout.

The data suggests that there is a decrease in δ_t of 0.025 ± 0.010 mm/s associated with magnetic ordering. Such a large change is inexplicable on the magnetization-dependent Debye model. Even if Θ' was 400°K in the ordered region, it would have to decrease to 0°K in the paramagnetic region to raise δ_t by just 0.02 mm/s. The increase in δ_t of 0.05 mm/sec associated with magnetic order in αFe_2O_3 reported by Bashkirov et al [122] would require that Θ *increases* by about 500°K near the Néel point, a result both unreasonable, and at variance with their theoretical prediction [112].

In conclusion, it is clear that the total spectrum shift in the $(Fe_{1-x}Rh_x)_2O_3$ system cannot be completely explained just by considering the second order Doppler shift. The calculation shows that some variation of the isomer shift with x must be expected, and there must also be a decrease of at least 0.017 mm/sec between 296°K and 20°K which could be explained by lattice contraction. The influence of magnetic order on δ_t, which is apparent in the room temperature data, could arise from a small change in z(Fe) at T_N, such as was invoked to explain the behaviour of the quadrupole interaction. In both experiments a decrease in δ_t of ∿0.01 mm/sec is attributable to magnetic ordering. The behaviour of $HoFeO_3$ may be adequately explained on the magnetization-dependent Debye model,

but not the behaviour of $(Fe_{1-x}Rh_x)_2O_3$. Further studies of the influence of magnetic order are called for. The most recent work by Wertheim et al on FeF_3 [111] was found to be consistent with (5.14). Absolute, mechanical spectrometers would be best for this work because the shifts of interest are less than 1/20 of a linewidth.

VI Central Peaks in Mössbauer Spectra of Magnetically Ordered Compounds

Le superflu, chose très nécessaire. - Voltaire.

In this chapter we will describe some experiments which were intended to elucidate the nature of the mixed spectra which we observed below the Néel point in the $(Fe_{1-x}Rh_x)_2O_3$ system. These mixed spectra have been observed in a number of pure [124-7] and substituted [38, 57, 61] compounds, and they are evidence of high-frequency spin relaxation. We noted earlier that it is impossible to explain these spectra, even in diamagnetically substituted compounds, on the basis of a static effective-field theory. However, it has been shown [7] that the appearance of a mixed spectrum does not necessarily imply that there are ferro- and paramagnetic regions coexisting in the same crystal. Mixed spectra can appear if there is a single value of τ_H, particularly in paramagnetic materials.

We will begin by mentioning some of the principles involved in relaxation processes, and we are particularly interested in the effect of an applied field on the Mössbauer spectrum. Experimental illustrations are given for a paramagnet and a superparamagnet. Then, experiments which show the influence of sample preparation

methods, and an applied field on the central peaks are reported and discussed.

1. RELAXATION PROCESSES

If the relaxation time of the ionic spin associated with an ^{57}Fe nucleus is longer than 10^{-7}s, then the full hyperfine interaction will be observed, regardless of whether the compound as a whole is magnetically ordered or disordered. Nuclear relaxation processes are assumed to be negligible on this time scale.

The main electronic relaxation effects arise from two interactions; i) The spin-spin interaction, which is associated with dipolar or exchange fields, and depends on the concentration of magnetic ions in the compound. ii) The spin-lattice interaction, which is particularly important for ions which are not in an S-state, and, unlike the spin-spin interaction, it depends strongly on temperature.

In ferromagnetic compounds at low temperatures, the spin waves ensure that the ions are distributed amongst the various m_s states in such a way that the lowest state is exclusively occupied at absolute zero. In an antiferromagnet there is a spin deviation. These spin-wave frequencies are of the same order as thermal frequencies, and at 1°K they are three orders of magnitude greater than the Larmor precession frequency of ^{57}Fe. Therefore, it is to be expected that the hyperfine field will follow the magnetization $\bar{S}_z$ in the region

of temperature where spin waves are present in the lattice [7].

Close to the magnetic ordering temperature, a different situation may prevail. Van der Woude and Dekker point out that if the spin fluctuation time, τ_H, becomes comparable with τ_L (or $\tau_{1/2}$, if it is the greater), then one may expect to see a spectrum with broadened outer lines whose splitting is *greater* than would be the case if the hyperfine field was proportional to the sublattice magnetization. The spectra may also show a central peak below the magnetic ordering temperature, provided the degree of magnetic order is small, and $\tau_H \lesssim \tau_L$ [7].

In paramagnetic compounds, the usual singlet or doublet spectrum arises because $\tau_H << \tau_L$, *and* the value of the spin of an ion is zero when averaged over the Larmor precession time in the instantaneous hyperfine field. If, instead, $\tau_H \sim \tau_L$, then a broadened paramagnetic peak appears, and in the extreme limit of $\tau_H >> \tau_L$, a set of hyperfine patterns, one for each value of m_s, will appear [6]. Sets of spectra, usually for S = 1/2, have been calculated by several authors [7-10].

1.1 Superparamagnetism.

Superparamagnetism is a phenomenon which was predicted and studied by Néel, particularly in connection with rock magnetism [128]. It has been observed in ultra-fine particles of several antiferromagnetic and ferrimagnetic materials using the Mössbauer effect [129-30]. Suppose a cluster of 10 - 10^6 magnetic ions is

coupled together,with any of the normal spin arrangements,to form a sub-domain-sized magnetic particle. If the temperature is sufficiently high, the net moment of the whole cluster may relax rapidly, and independently of the other particles, just like the ionic spin of a paramagnet. The relaxation time depends very much on the temperature. A simple model consists of two energy minima separated by an energy barrier of height E_B, due to anisotropy. It leads to the equation [131];

$$\frac{1}{\tau_1} = \frac{1}{\tau_0} \exp(-E_B/KT) \qquad (6.1)$$

τ_0 is usually set equal to the Larmor precession time in the anisotropy field. $E_B \simeq |C|v/\ell$, where C is the anisotropy constant and v is the volume of the particle; ℓ is 2 for uniaxial anisotropy, and 8 or 12 for cubic anisotropy. A more realistic model has been worked out by Aharoni [132].

Whether a particle appears superparamagnetic or not depends on whether τ_1 is less or greater than the characteristic time for the measurement. In the Mössbauer effect this is $\sim 10^{-7}$s, so that a blocking temperature, T_b, may be defined from (6.1) by putting $\tau_1 = \tau_{1/2}$. For magnetization measurements, the characteristic time is $\sim$10s, and the blocking temperature will be lower. It will not be much lower however, because the anisotropy depends on the magnetization, and thus on temperature. Magnetocrystalline anisotropy, in some instances, varies as M^{10}, whereas shape anisotropy varies as M^2 [133].

If it was possible to study a powder of identical superparamagnetic particles, the spectrum would change from a magnetically-split pattern just below T_b to a 'paramagnetic' pattern just above. In practice there is always a range of particle sizes, and mixed spectra are observed over a fairly wide temperature range [130].

1.2 Influence of an Applied Field on Relaxation.

An applied field has two distinct effects on a magnetic material, although in practice they may sometimes be difficult to distinguish; i) It introduces an energy gap between the opposite spin states of the ions, producing magnetic polarisation, and ii) It alters the energy barrier between the two energy minima of a superparamagnetic cluster, and hence the relaxation time. It may be shown [134] that the energy barrier for uniaxial anisotropy in the presence of a small field becomes

$$E_B' = \frac{1}{2}|C|v - MvH_{ap} + \frac{M^2v^2H_{ap}^2}{2|C|v} \qquad (6.2)$$

A more exact treatment of the problem has recently been given [135], which also predicts that the application of a field, such that $MH_{ap} \simeq |C|$, should decrease τ_1.

1.2.1 *Spin Polarisation of Paramagnetic* $Fe(ClO_4)_2.6H_2O$.

We return to our study of ferrous perchlorate, which serves to illustrate the effect of polarisation on the Mössbauer spectrum of a paramagnetic compound in which the spin relaxation time is

very short. The room-temperature spectra were previously discussed in II 2.1.2 as an illustration of the use of a magnetic field in determining the sign of the quadrupole interaction. The spectra at 4.2°K are shown in figure 65, and the sign of V_{zz} obviously is opposite to that for the 296°K spectra shown in figure 20.

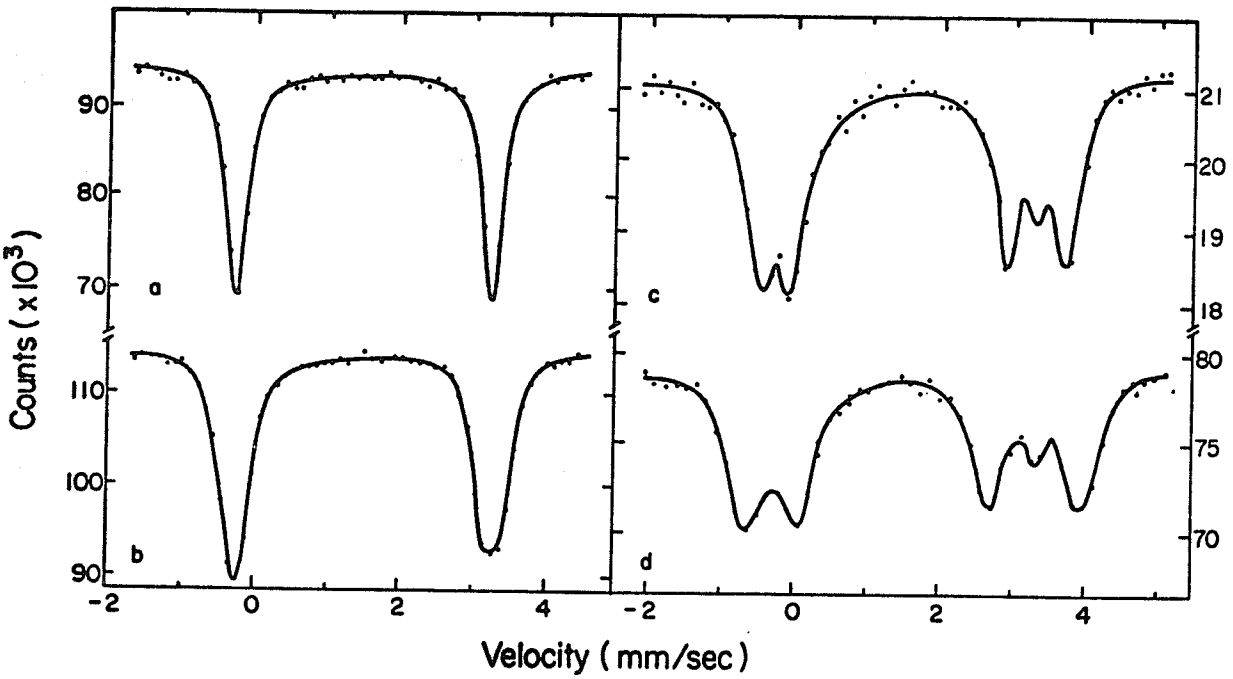

Figure 65. Mössbauer spectra of $Fe(ClO_4)_2 \cdot 6H_2O$ at 4.2°K in applied fields of a) 0 kOe, b) 10 kOe, c) 30 kOe, and d) 50 kOe.

The hyperfine field may be deduced from the splitting of the outer lines of the triplet [34]. The lines of the triplet are sharp, and there is no sign of broadening due to a slowing of the relaxation of the paramagnetic ions, even in 50 kOe. Although the ferrous ions are rather dilute in this compound, and the spin-spin interactions are weak, the spin-lattice relaxation times should be shorter than 10^{-8}s for a ^5D ion, even at 4°K. The applied fields and the magnitudes of the measured hyperfine fields at several

Table 13. Hyperfine Fields in Ferrous Perchlorate.

Applied Field	Measured Field		
kOe	kOe		
	4.2°K	80°K	296°K
10.0	13.3 ± 1.0	-	-
19.4	-	-	16.0
30.0	32.2	-	23.6
50.0	50.2	25.6	40.5

temperatures are listed in table 13. The hyperfine fields at 296°K and 80°K are consistently lower than the fields that are applied. A similar effect has also been observed in a ferric dimer [136].

The explanation of the data is to be found in the susceptibility curve of figure 66. The moment induced per Fe^{2+} ion at 4.2°K in a 10 kOe field is $0.48\mu_B$, compared to the saturation moment of about

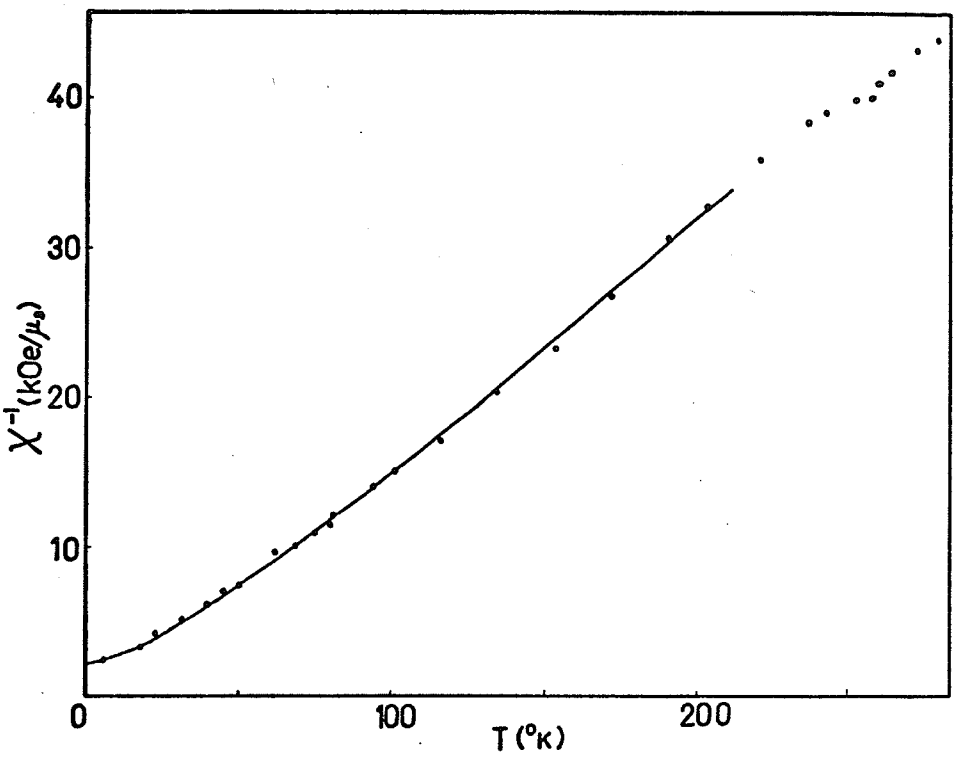

Figure 66. Temperature dependence of the inverse susceptibility of polycrystalline $Fe(ClO_4)_2.6H_2O$

$5.4\mu_B$. A field of 50 kOe would induce almost half the saturation moment. The observed hyperfine field would thus be 50 kOe, less about half the full hyperfine field in this compound at T = 0. The data of table 13 is plotted in figure 67. In this chapter we will

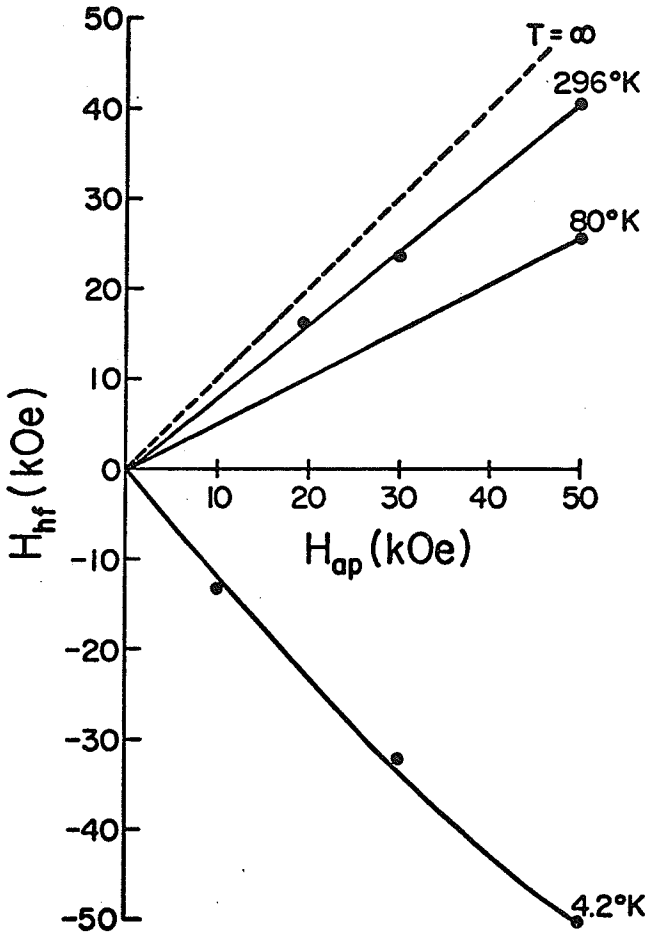

Figure 67. The effective hyperfine field in $Fe(CO_4)_2.6H_2O$ as a function of applied field, at several temperatures.

take the sign of H_{hf} into account in the figures. The difference between the observed field at a particular temperature and that at T = ∞ (the applied field) should be proportional to the induced moment. The ratio of the hyperfine fields induced by polarisation at 4.2°K, 80° and 296°K is 5.0:1.1:0.4 compared to the ratio of

the induced moments which is 5.0:0.9:0.2. The agreement is quite good. From the inverse susceptibility curve, this compound may be expected to order antiferromagnetically at about 2°K. The hyperfine field at T = 0 should be about 250 kOe, which is reasonable for a ferrous salt.

It can be seen from figure 67 that at some temperature between 80° and 4°K, the application of a field should have no influence on the Mössbauer spectrum, because the induced hyperfine field is equal and opposite to the applied field. It may be possible to use this device to study the influence of a large magnetic field on spin relaxation time in a suitable material, since the applied field produces no net field at the nucleus.

This experiment shows clearly that a hyperfine field can be observed in a Mössbauer spectrum when τ_H is very short. In the course of the nuclear lifetime, the ionic spin is more often aligned parallel to the applied field than antiparallel, and a hyperfine field proportional to this polarisation is seen by the nucleus. Since these polarisation effects are pronounced in paramagnets at low temperatures, it is to be expected that they will be even more important in superparamagnets.

1.1.2 Superparamagnetic γFe_2O_3.

We will now describe a material which we know to be superparamagnetic, and show the influence of an applied field on its Mössbauer spectrum.

Colloids containing fine particles of magnetite in suspension are used in the optical study of domain patterns [137]. To make these fine particles [138], stoichiometric quantities of $FeCl_2$ and $FeCl_3$ were dissolved, the solution was heated to 40°C, and NaOH was added. The black precipitate was washed, filtered and dried in air, and the final product was reddish-brown. The x-ray powder pattern of the material showed very broad lines, and those at high-angles could not be distinguished. However the low-angle lines belonged to the spinel pattern of Fe_3O_4 or else γFe_2O_3. The material was identified as γFe_2O_3 from its Mössbauer spectra.

The spectra are shown in figure 68. The broad, triangular

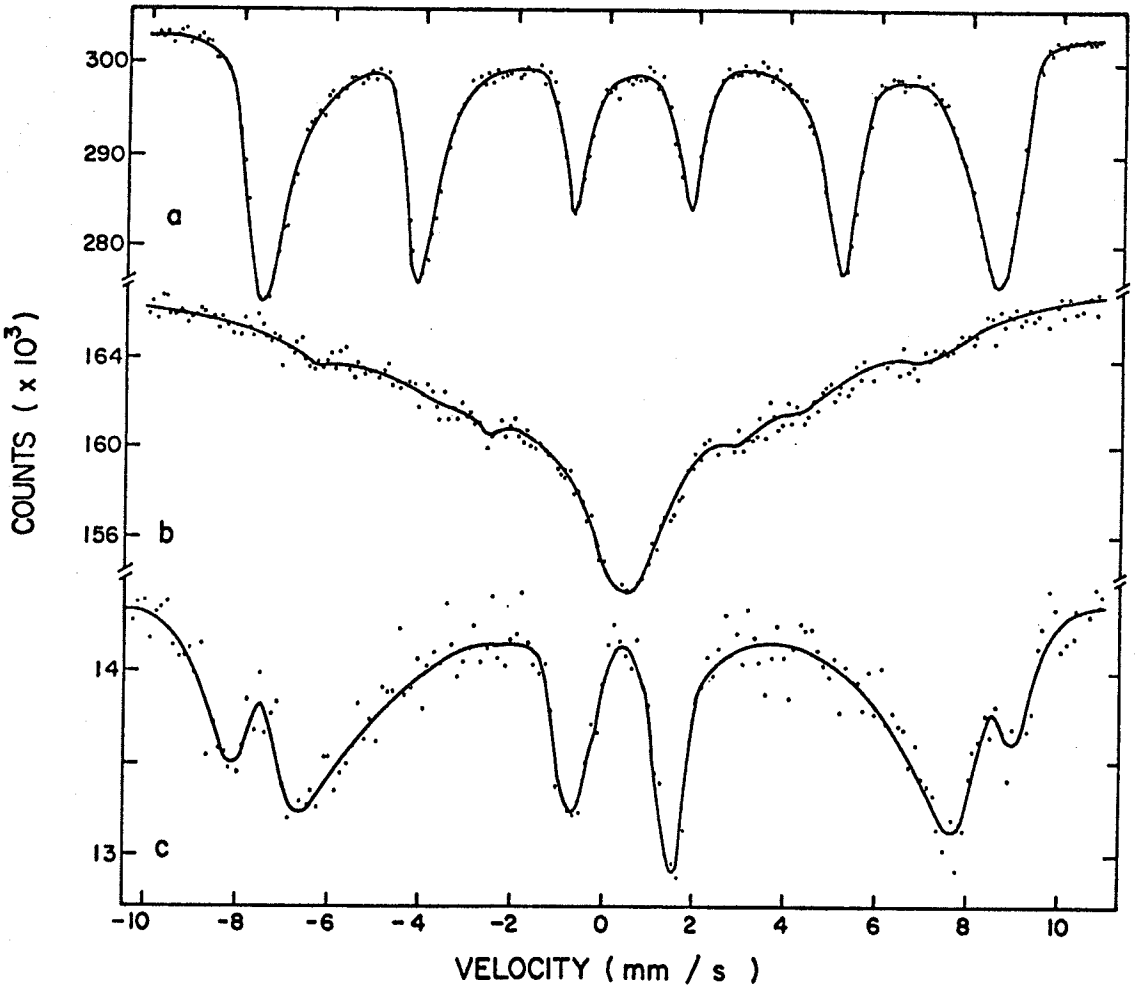

Figure 68. Mössbauer spectra of γFe_2O_3 with a crystallite size of 90Å; a) at 80°K, b) at 296°K, c) at 296°K in an applied field of 50 kOe.

spectrum of figure 68b was obtained at room temperature. At 80°K the spectrum has resolved itself into the six-line pattern with some line broadening, shown in figure 68a. The effect of a 50 kOe field on the 296°K spectrum is shown in figure 68c; it is resolved into two broad, unequal four-line patterns. These patterns may be compared to those shown in figure 69 for well-crystallised γFe_2O_3. The compound is certainly ferrimagnetic, and if it was magnetite, some of the lines in the 80°K spectrum would be split. Since they are not, the material must be γFe_2O_3.

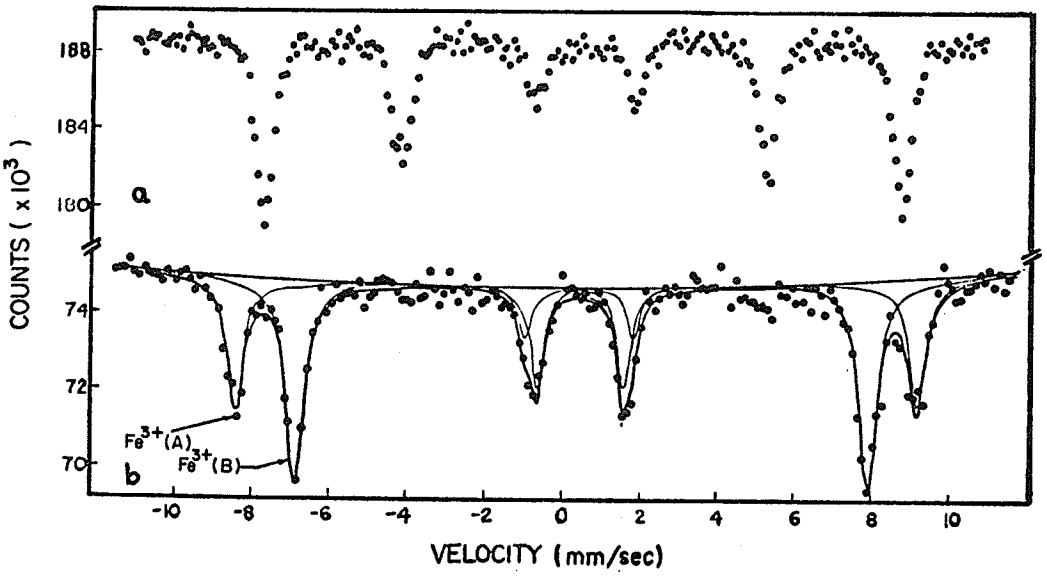

Figure 69. Mössbauer spectra of well-crystalised γFe_2O_3 at 296°K; a) without, and b) with an applied field of 50 kOe.

The 296°K spectrum is very like the one calculated by Van der Woude [8] for paramagnetic iron with S = 5/2 and $\tau \simeq 10^{-9}$s. It seemed likely that the material was superparamagnetic at this temperature, and confirmation was provided by the room temperature magnetization curve, shown in figure 70 which resembles a Langevin function corresponding to $S \sim 10^3$. If the γFe_2O_3 is not superparamagnetic

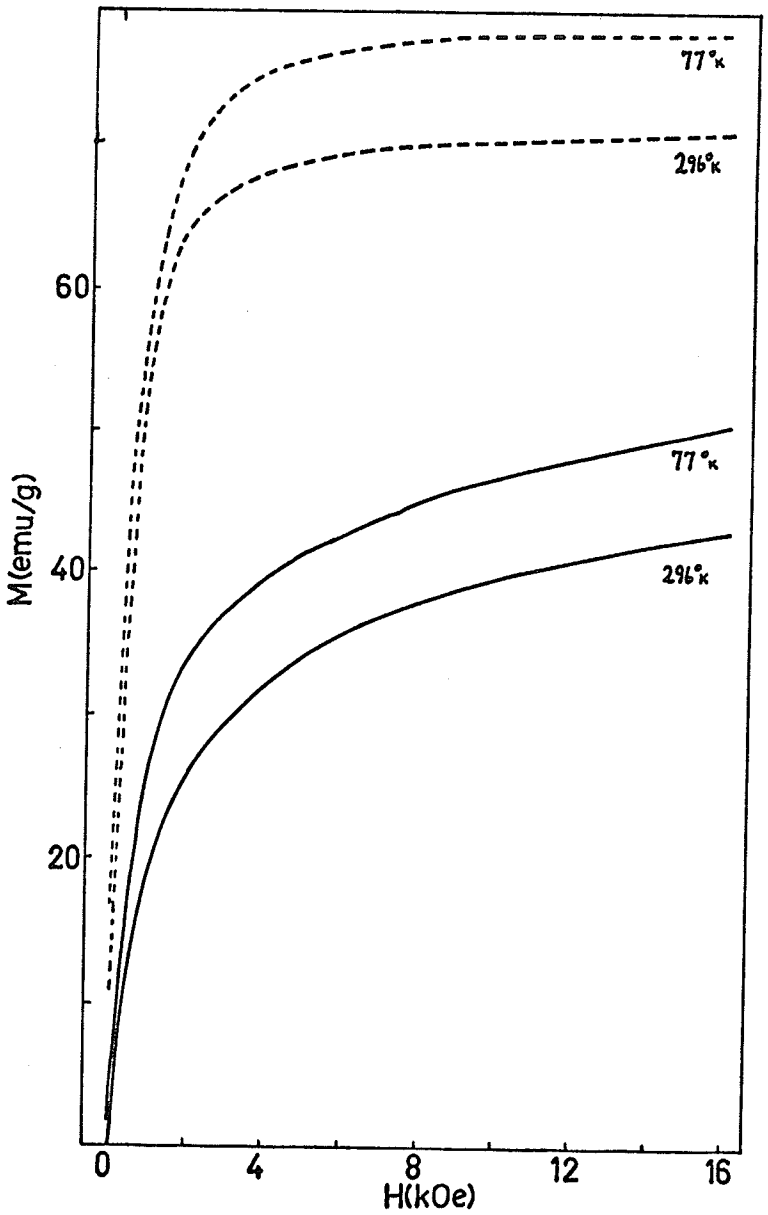

Figure 70. Magnetization curves for γFe_2O_3 at various temperatures. The solid lines are for the material with a crystallite size of 90Å, and the dotted lines are for well-crystalised material.

in a magnetization measurement it will certainly not be superparamagnetic in a Mössbauer measurement.

A good criterion for determining the blocking temperature is the disappearance of the remanence. This should occur at a lower temperature than the temperature at which a well-resolved

six-line spectrum appears. However, because of the range of particle sizes, the remanence disappears in a region of temperature between 4° and 100°K. The range of particle sizes is probably mainly responsible for the shape of the 296°K spectra, both with and without the applied field. The smaller particles will be much less saturated by the field than the larger ones, and give rise to the sloping inside edges on the outer lines. An explanation in terms of a slow superparamagnetic relaxation time is also possible, but the polarisation effect is undoubtedly predominant since the compound has about 70% of its spontaneous magnetization in a field of 50 kOe.

2. MÖSSBAUER SPECTRA of PURE COMPOUNDS near their MAGNETIC ORDERING TEMPERATURE.

There has been some discussion in the literature about the observation of central peaks in the spectra of pure compounds close to their magnetic ordering temperature. Bertelsen et al [126] found that $\tau_b = 0.98$ for a 99% pure FeF_3 crystalline powder. However, Wertheim et al [120] subsequently studied a high purity microcrystalline powder of the same material, and found $\tau_b > 0.999$. In the orthoferrites, Eibschütz et al found $\tau_b \simeq 0.993$, whereas we obtained a value of 0.996 in our experiments on $HoFeO_3$. The fluoride results may be explained by the lack of purity of the material used by the Danes. However, the Israelis have proposed an explanation of their orthoferrite results in terms of 'critical superparamagnetism' [127]. They suppose that their samples are not perfectly homogeneous, but

are composed of independent magnetic regions with an effective volume, v_{eff}, which is sufficiently small for the energy barrier Cv_{eff} to be low enough to allow superparamagnetic behaviour just below T_N. Mixed spectra could also be caused by a range of Néel temperatures in different parts of the crystal, or else a slow spin-relaxation time in the paramagnetic state, just above T_N.

Any discussion of mixed spectra and reduced temperatures begs the question, of how the magnetic ordering temperature is to be defined . If the iron ions are actually paramagnetic at the temperature of the mixed spectra, then T_N is the temperature at which they first appear. Alternatively, if the iron is superparamagnetic at the temperature of the mixed spectra, and if the material is taken as ordered if it has a non-zero *instantaneous* spin-spin correlation function in some arbitrary volume, then T_N is the temperature at which the last trace of the magnetically-split spectrum disappears, or possibly even higher. If, instead of taking the instantaneous value of the correlation function, it is averaged over a finite time, then different values of T_N will, in general, be found for different times and volumes. It is easy enough to propose an operational definition such as 'the temperature at which half the absorption is in the magnetically-split pattern' or 'the temperature at which the extrapolated spontaneous magnetization reaches zero', but it is more difficult to know how much short-lived, short-range order is included. The experiments on pure and diamagnetically substituted yttrium-iron oxides will shed some light on this problem, but a complete answer will not be given.

2.1 $YFeO_3$.

$YFeO_3$ was prepared from Fe_2O_3 and Y_2O_3 of the highest available purity. The iron oxide[14] had a total metallic impurity content of less than 10 parts per million, while the yttrium oxide[13] was supposed to be 99.9999% pure. The purpose of the experiment was to discover whether the central peaks are present in highly pure orthoferrites, and if so, whether the firing atmosphere has any influence on them. We used atmospheres of nitrogen and oxygen, which may be expected to have an effect on crystallite size or

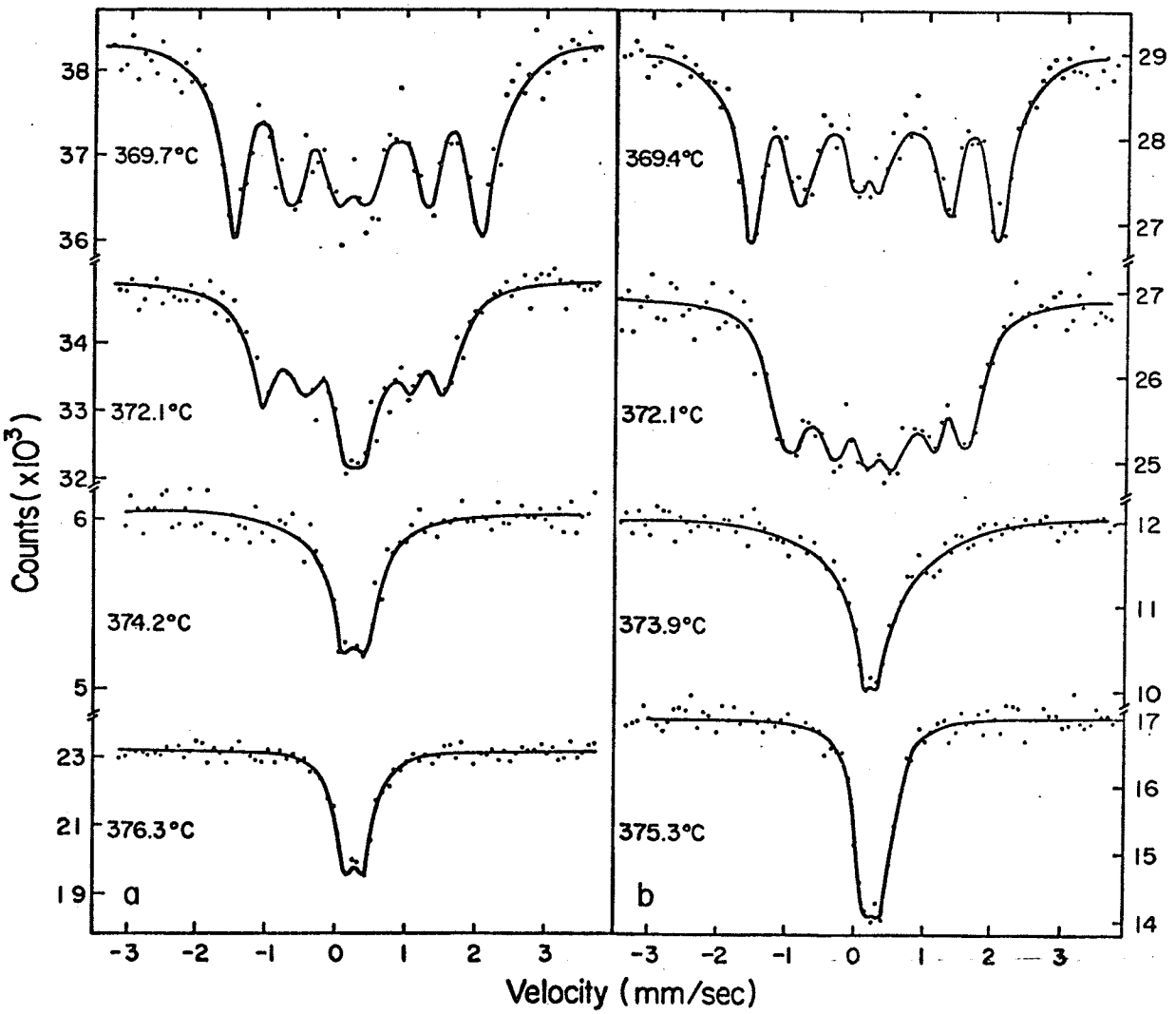

Figure 71. Mössbauer spectra of $YFeO_3$ near the Néel point; a) fired in an oxygen atmosphere, and b) fired in a nitrogen atmosphere.

oxygen stoichiometry, but we did not determine these effects. The powders were ground, pelleted and prefired for four hours in air at 900°C. The sample was then reground, divided in two, and each half was repelleted and fired for ten hours at 1400°C in an atmosphere of either nitrogen or oxygen.

The spectra were collected using the 20mC source and the scintillation counter. Each one was acquired for about an hour, during which time the temperature was stable to within 0.1°C. Some typical spectra are shown in figure 71. They are identical for the two different samples at almost all temperatures. The hyperfine

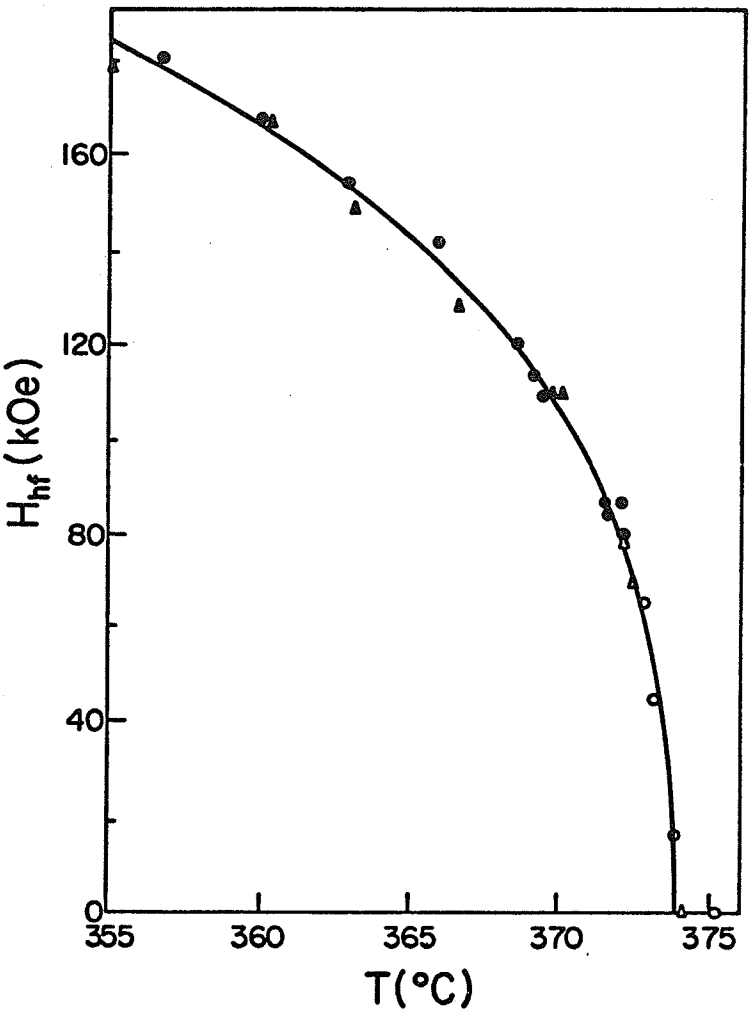

Figure 72. Hyperfine fields in $YFeO_3$ near the Néel point; ▲, fired in an oxygen atmosphere, and ●, fired in a nitrogen atmosphere.

field as a function of temperature is shown in figure 72. It is the same for both, and T_N is 374.0°C. Nevertheless some slight differences do emerge when $\tau > 0.995$. Spectra with central peaks are denoted by open symbols on figure 72. The nitrogen-fired sample does not show distinct central peaks until $\tau_b = 0.998$, whereas they occur in the oxygen-fired sample when $\tau_b = 0.996$. The two spectra at 372.1°C ($\tau = 0.997$) in figure 71 may be compared directly. We suppose that the 373.9°C spectrum is still below T_N because the intensity of the peak is less than it is in the paramagnetic region, for example at 375.3°C.

The conclusion is that these pure oxides do show central peaks just below τ_N, and a slight influence of firing atmosphere has been detected.

2.2 $Y_3F_5O_{12}$.

Yttrium-iron garnet was prepared from the same high-purity oxides as the orthoferrite. The powders were prefired for twelve hours at 950°C, and then given a final firing for six hours at 1450°C in oxygen. We have made Mössbauer and magnetization measurements on the sample, mainly for comparison with the diamagnetically substituted garnets discussed in the next section.

The formula of yttrium-iron garnet may be written

$$Y_3^{3+}(Fe^{3+})_2[Fe^{3+}]_3O_{12}^{2-}$$

The round brackets denote cations on the octahedral a-sites, and the square ones, cations on the tetrahedral d-sites. The a- and

d-sublattices are coupled ferrimagnetically, so the net 'spin only' moment is 5 μ_B per formula. The two six-line patterns from iron on the two sites are well resolved in the room temperature spectrum of figure 73. The a-site ions have a hyperfine field of 485 kOe, while that of the d-site ions is 395 kOe. In fact there are two slightly different d-site spectra with an intensity ratio of 3:1

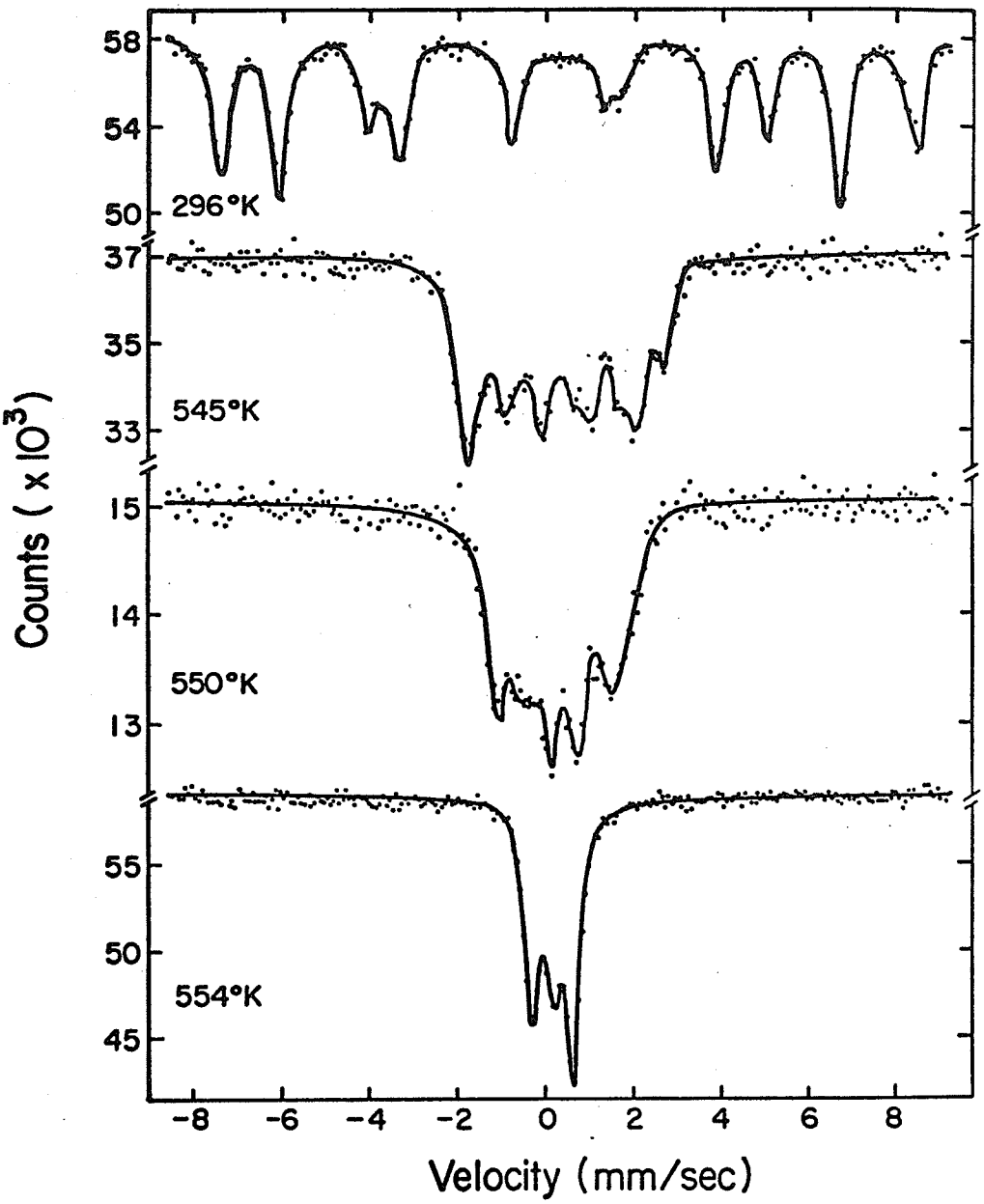

Figure 73. Mössbauer spectra of pure yttrium iron garnet at various temperatures.

because there are two possible angles, ϕ, between the magnetic axis, and the principal axis of the electric field gradient [139]. The ferrimagnetic ordering temperature was determined by extrapolating the hyperfine fields as a function of temperature, shown in figure 74, to $H_{hf} = 0$. It is 553°K, and there is little sign of 'paramagnetic peaks' in the 550°K spectrum. There is no pronounced absorption at the velocity corresponding to the lowest energy line in the paramagnetic spectrum. In other words, $\tau_b \gtrsim 0.995$.

We also measured the spontaneous magnetization, by

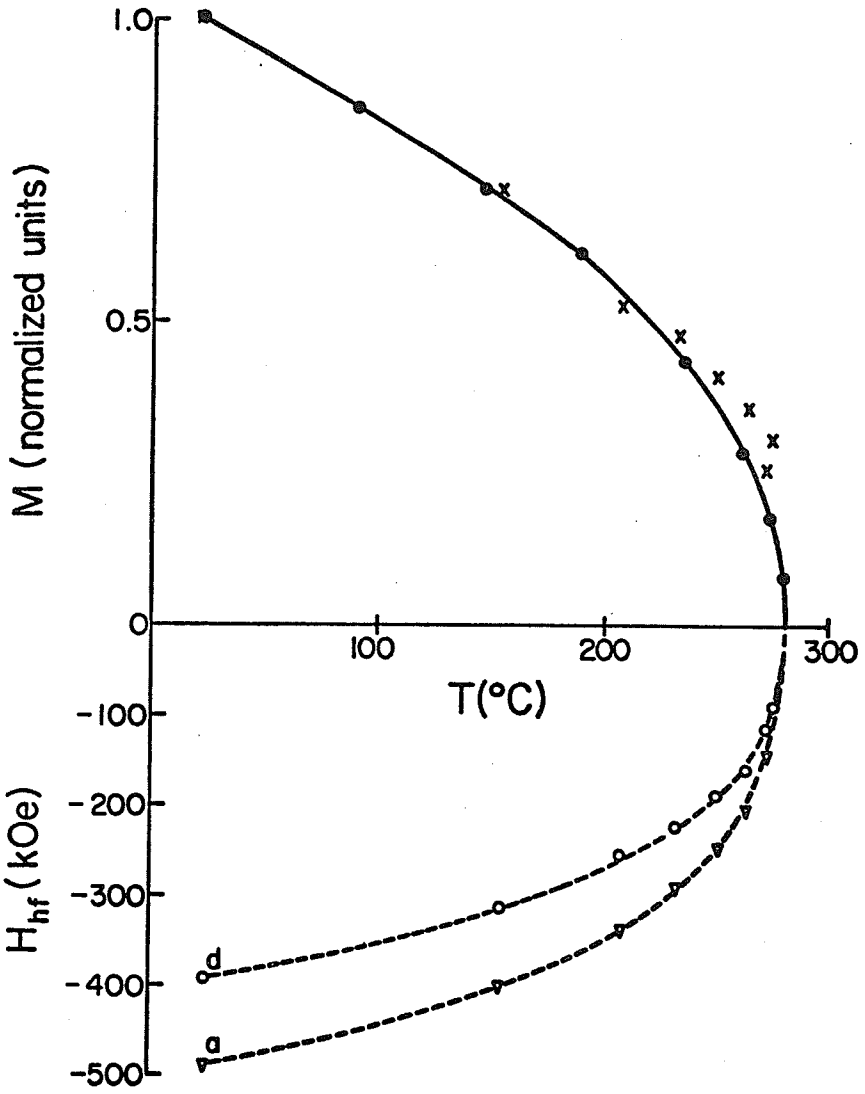

Figure 74. Comparison of the static magnetization of $Y_3Fe_5O_{12}$ with the net moment deduced from the hyperfine fields. The dotted lines show the temperature variation of the hyperfine field on the two iron sites.

extrapolating the moment in the range 8-16 kOe to zero field. The result is shown by the solid line in figure 74, and an ordering temperature of 551°K is inferred. This agrees with the hyperfine-field value within the errors of the thermocouple calibrations, and the extrapolations themselves. Since the shapes of the magnetization and hyperfine field curves, shown in figure 74, appear dissimilar, we calculated the temperature dependence of the magnetic moment on the assumption that the sublattice moments are proportional to the hyperfine fields. That is,

$$M \propto 3\sigma(d) - 2\sigma(a). \qquad (6.3)$$

The resulting value of M was normalised to the measured magnetization at room temperature, and the other values are denoted by crosses in the figure. Near the critical temperature, they all lie above the magnetization curve, and this may be evidence for a spin flip time τ_H which is greater than τ_L. Van der Woude and Dekker suggested that this may be possible in the region just below the ordering temperature [7].

3. MÖSSBAUER SPECTRA of YTTRIUM-IRON GARNET with DIAMAGNETIC SUBSTITUTIONS.

We have studied a number of diamagnetically substituted yttrium-iron garnets. These compounds were prepared in the same way as the pure garnet, except that suitable quantities of high-purity sesquioxides of diamagnetic cations were added to the mix.

Samples were made containing small amounts of Ga^{3+} and Al^{3+}, which are known to prefer the d-sites, and with small amounts of Sc^{3+} and In^{3+}, which prefer the a-sites [140]. We also made a sample with some Rh^{3+}, whose Mössbauer spectrum at room temperature resembled those of the compounds containing Sc or In. This shows that rhodium has the same octahedral site preference in garnets that it has in spinels. An attempt to make $Y_3Rh_2Fe_3O_{12}$ failed, because most of the Rh_2O_3 decomposed to metallic rhodium, and failed to react with the other oxides. The decomposition of Rh_2O_3 begins at 1100°C in air.

The room temperature spectra of the compounds $Y_3(Fe_{0.9}M_{0.1})_2[Fe]_3O_{12}$, with M = Sc, In, or Rh all show a slightly broadened a-site pattern, but the d-site absorption is split into two fairly well resolved patterns with an intensity ratio of about 5:2, and hyperfine fields of 385 and 345 kOe. The spectrum can be understood on the principles explained in chapter III. The d-site iron ions have four a-site superexchange neighbours, and 10% of these sites are occupied by diamagnetic ions. The probabilities of a d-site having 4, 3 or 2 a-site iron neighbours are 0.66, 0.29 and 0.05, so the two d-site spectra correspond to iron in environments with four and three magnetic neighbours. The broadening of the a-site lines are either a result of a-a interactions, which are not usually regarded as being significant in garnets, because the Fe-O distances are 2.00 and 4.41Å, or else the broadening may occur because not all the diamagnetic ions are on a-sites, but some are on d-sites.

Yet another explanation would be that the distribution of a-site hyperfine fields arises because their d-site super-exchange neighbours do not all have the same magnetization, on account of their different possible a-site environments. The idea is the same as the one in II 1.1.2.

The spectra of $Y_3(Fe)_2[Fe_{0.9}M_{0.1}]_3O_{12}$, with M = Ga or Aℓ show a virtually unaltered d-site pattern, compared to $Y_3Fe_5O_{12}$, and a broadened a-site pattern. The explanation is quite analogous to that for the garnets with a-site substitutions, except that the effects are not so pronounced, because each a-site has six d-site superexchange neighbours, compared to the four neighbours of the d-site. The $\sigma(Z)$ curves for consecutive values of Z are less separated when N = 6 than when N = 4.

The spectra shown in figure 75 are for garnets with a 25 'site-percent' substitution of Sc or Ga. These compounds should be magnetically comparable, even though there are half as many diamagnetic ions again in the gallium-doped garnet as there are in the scandium-doped one.

At room temperature, $Y_3(Fe_{0.75}Sc_{0.25})_2[Fe]_3O_{12}$ has a broad d-site pattern, which is fairly well resolved from the narrower a-site pattern. The rather square d-site line shape is explained by the probabilities $P_4(Z)$, which are 0.32, 0.42, 0.21 and 0.05 for Z = 4, 3, 2 and 1. The last trace of the magnetically-split spectrum disappears at 449°K in the absence of an applied field,

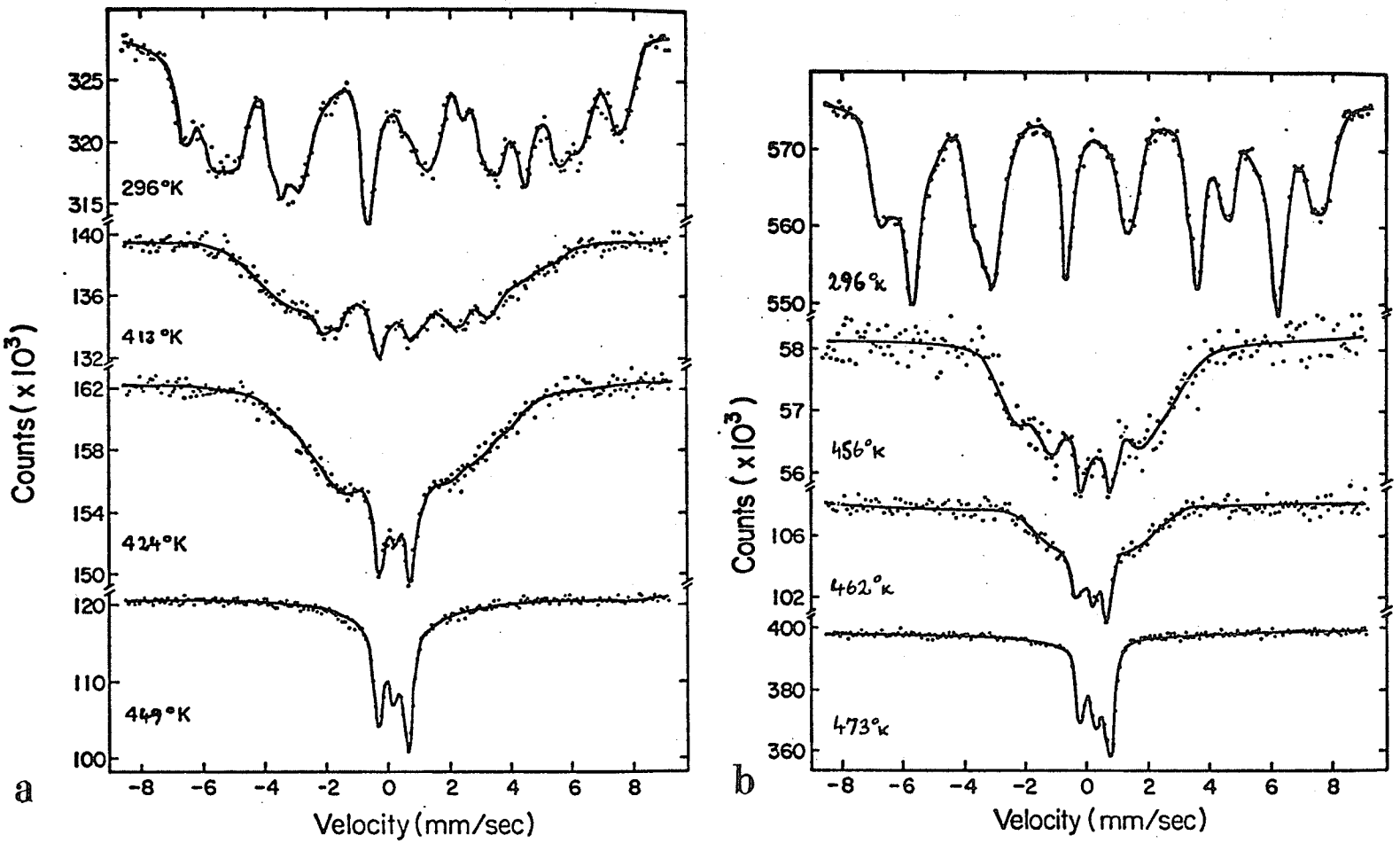

Figure 75. Mössbauer spectra of a) $Y_3(Fe_{0.75}Sc_{0.25})_2[Fe]_3O_{12}$ and b) $Y_3(Fe)_2[Fe_{0.75}Ga_{0.25}]_3O_{12}$ at various temperatures.

and the 'paramagnetic peaks' appear at 421°K (τ_b = 0.96).

The room-temperature spectrum of $Y_3(Fe)_2[Fe_{0.75}Ga_{0.25}]_3O_{12}$, shown in figure 75b, has broad a-site lines, for the reasons given above. 'Paramagnetic peaks' appear at 457°K (τ_b = 0.975), and they have taken over the entire spectrum at 469°K. These spectra suggest that there might be a relation the size of the region in which mixed spectra are observed, and the magnetic co-ordination number, particularly since τ_b should be lower for the gallium-doped sample, if all other factors were negligible, because it contains a higher concentration of diamagnetic ions. In other words, the greater the number of neighbouring sites on the sublattice with the diamagnetic substitution, the greater τ_b.

The purpose of making these garnets was not so much to study their low-temperature spectra, which serve as another illustration of the principles of chapter III, but rather to look at the mixed spectra in an applied field, using the furnace described in II 2.2. We had previously taken spectra of $(Fe_{0.34}Rh_{0.66})_2O_3$ and εFe_2O_3 at 296°C in an applied field of 50 kOe. The iron-rhodium oxide spectrum, shown in figure 37c, has a pronounced central peak, whereas the εFe_2O_3 has a six-line pattern, the lines of which are rather broad and asymmetrical, possibly due to relaxation effects. Both are antiferromagnetic , and the applied field had very little effect on either spectrum.

The garnets are ferrimagnetic, so it should be possible to

test whether the central peaks are paramagnetic or superparamagnetic. If the iron ions contributing to the central peaks are paramagnetic, then a field applied parallel to the γ-ray direction should have little influence on the mixed spectra, apart from removing lines 2 and 5, if the spin arrangement is colinear. The polarisation induced by a 10 kOe field would be completely negligible. However, if the central peaks are actually superparamagnetic, the applied field will polarise the superparamagnetic iron strongly. Considerable magnetic splitting should result, and the intensity of the central peaks should decrease. This superparamagnetic iron may be localised in distinct magnetic regions of the crystal, as suggested by Levinson et al [139], but it could just as well be in small clusters of short-range order which are not confined by any set of grain boundaries and lattice defects, but are continually changing in spatial extent and position.

The spectra shown in figure 76 were taken at two temperatures at which mixed spectra are observed in $Y_3(Fe_{0.75}Sc_{0.25})_2[Fe]_3O_{12}$. Spectra are shown at each temperature with and without an applied field of 10 kOe. The applied field has a very marked effect on the spectra, greatly reducing the intensity of the 'paramagnetic peaks', and producing a greater splitting of the magnetically ordered pattern. Data has also been obtained at 448°K and at 455°K. The latter temperature is above the magnetic ordering temperature, judged by the disappearance of the magnetically split spectrum in zero field,

nevertheless it is possible to induce a hyperfine splitting of more than 100 kOe by applying a field of 10 kOe even at that temperature. The conclusion is that *the central peaks in mixed spectra are superparamagnetic peaks.*

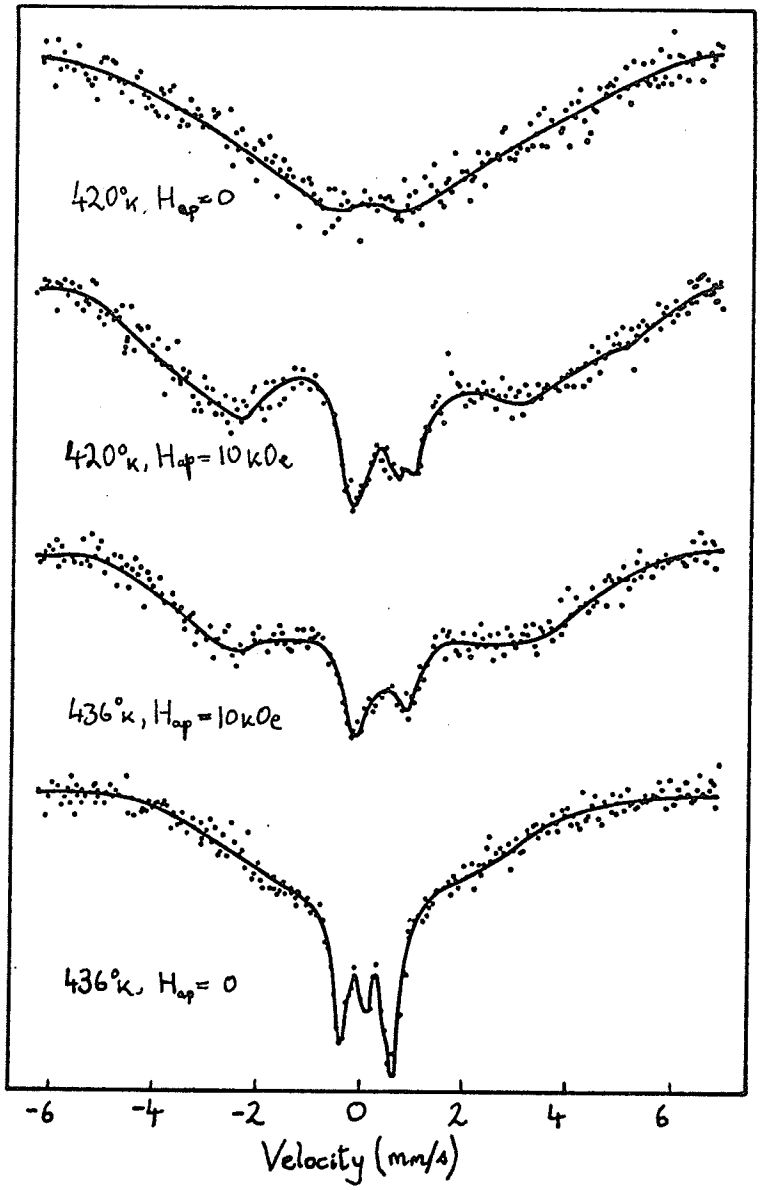

Figure 76. *Mössbauer spectra of $Y_2(Fe_{0.75}Sc_{0.25})_2[Fe]_3O_{12}$ close to its ordering temperature with and without an applied field of 10 kOe.*

The spontaneous magnetization of the 25% Sc and Ga garnets are shown in figure 77. M is obtained by extrapolating the part of the magnetization curve with 16 kOe $< H_{ap} <$ 10 kOe to $H_{ap} = 0$. The

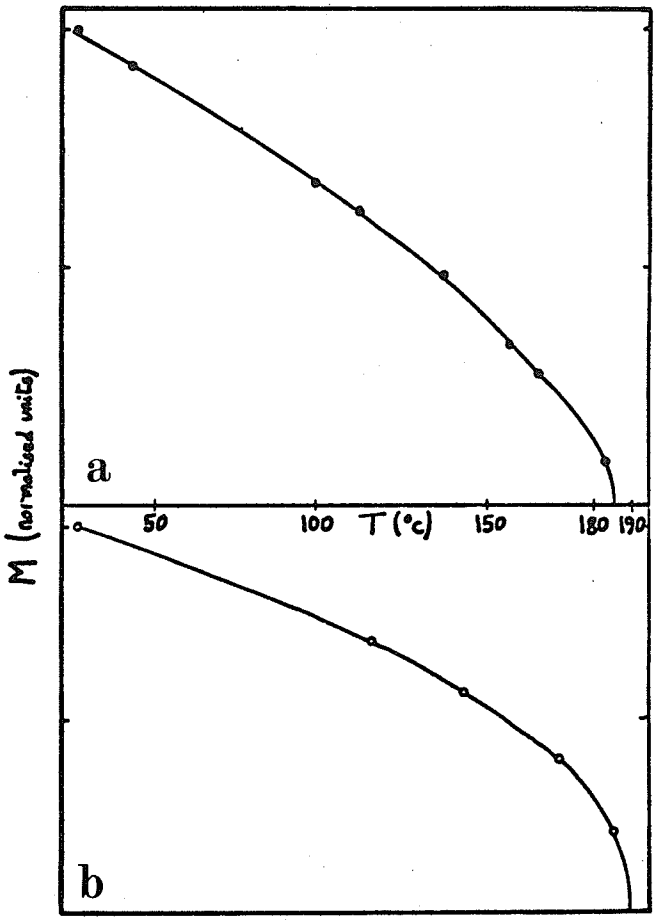

Figure 77. Temperature dependence of the magnetization of a) ●, $Y_3(Fe_{0.75}Sc_{0.25})_2[Fe]_3O_{12}$ and b) ○, $Y_3(Fe)_2[Fe_{0.75}Ga_{0.25}]_3O_{12}$.

Table 14. Magnetic Ordering Temperatures in Some Garnets.

	Spontaneous magnetization disappears at °C	Last trace of magnetic splitting in the Mössbauer spectrum disappears at °C
$Y_2(Fe)_2[Fe]_3O_{12}$	282	280
$Y_2(Fe_{0.9}In_{0.1})_2[Fe]_3O_{12}$		238
$Y_2(Fe_{0.75}Sc_{0.25})_2[Fe]_3O_{12}$	186	176
$Y_2(Fe)_2[Fe_{0.9}Ga_{0.1}]_3O_{12}$		247
$Y_2(Fe)_2[Fe_{0.75}Ga_{0.25}]_3O_{12}$	190	196

ordering temperatures for pure and substituted garnets, deduced from magnetization measurements and Mössbauer spectra are shown in table 14. The temperatures, obtained in the two different ways, agree for pure yttrium-iron garnet, but there are interesting differences for the two doped materials.

We have found that the scandium-substituted garnet is superparamagnetic above 176°C. Extrapolating a superparamagnetic magnetization curve like the one shown in figure 70 will give a finite value of M, and hence a higher value for the ordering temperature than the one deduced from Mössbauer spectra. However a higher ordering temperature is deduced from the Mössbauer spectra of the gallium-substituted garnet than from its magnetization curve. This may be because the characteristic time for the Mössbauer measurement is much less than for the magnetization measurement, and magnetic order persists on a time scale of 10^{-8} seconds to higher temperatures than it does on a scale of 10 seconds. The difference in behaviour with substitutions on the two sites is curious, and may be related to the difference in co-ordination, or the greater concentration of gallium.

4. DISCUSSION of the CENTRAL PEAKS.

In figure 78, the values of τ_b measured in the $(Fe_{1-x}Rh_x)_2O_3$ system and in the diamagnetically substituted garnets are shown.

The appearance of the central peaks in a Mössbauer spectrum means that some, or all of the iron has a spin relaxation

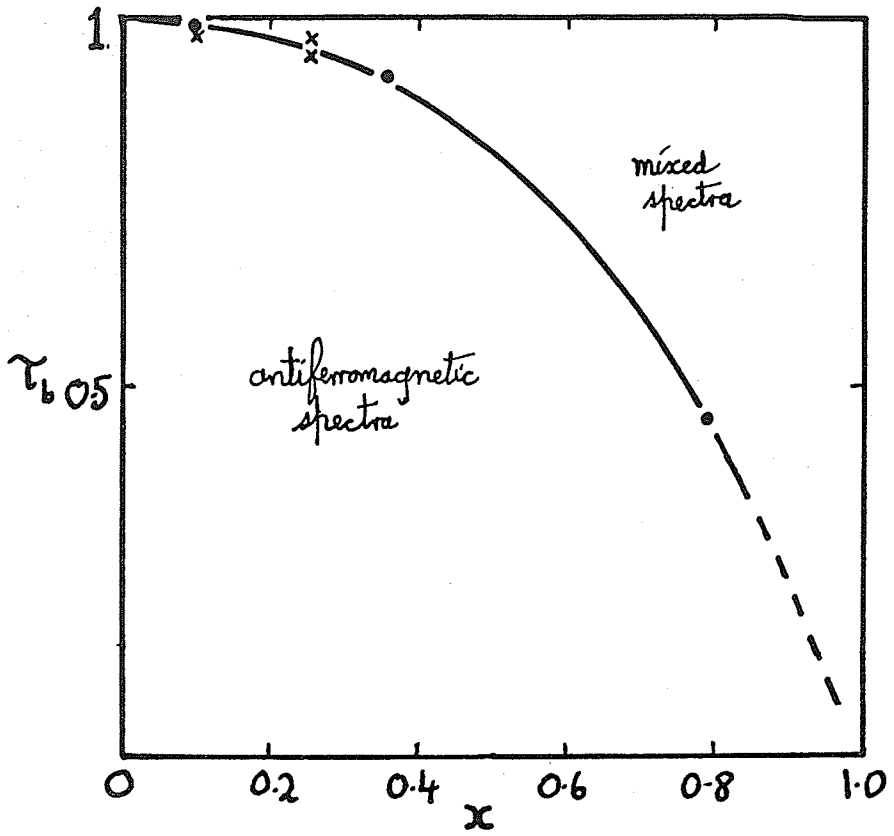

Figure 78. Variation of τ_b; ● in the iron-rhodium oxide system, and × in diamagnetically substituted garnets.

time comparable to the Larmor precession time. Three possible explanations will be considered; i) The impurity distribution is inhomogeneous, and different regions of the crystal have different ordering temperatures, so that paramagnetic and magnetically-ordered regions coexist at some temperatures. ii) Lattice imperfections, or clusters in the randomly-substituted lattice, define distinct magnetic regions with a range of volumes, so that superparamagnetic and magnetically-ordered regions coexist at some temperatures. iii) Around the ordering temperature there are clusters of evanescent short-range

order with a correlation time of at least 10^{-8}s. If these regions were small, they would appear superparamagnetic, even though they are not tied to some region of the lattice.

The first explanation requires that different regions of the crystal, perhaps different crystallites, have different impurity concentrations. We found a linear variation of T_N with x in the $(Fe_{1-x}Rh_x)_2O_3$ system (Figure 35). Consider the 99% pure FeF_3 as an example: If we suppose that the crystallites have substitutional impurities in the range 0 - 2%, then the central peaks should begin to appear at $\tau = 0.98$, because the regions with 2% impurity become paramagnetic at this temperature. In the $(Fe_{1-x}Rh_x)_2O_3$ system, the crystallite size is of the order of 500 Å, and the statistical variation of x from one crystallite to the next is less than 10^{-3}. In order to explain the mixed spectra of $(Fe_{0.64}Rh_{0.36})_2O_3$, x would have to vary from 0.34 to 0.40. Such a gross irregularity in the distribution of the rhodium seems unlikely, and would probably be detected in the x-ray powder photographs. However, it is difficult to see why regions containing 10^5 cations, which would have a statistical variation of x of the right magnitude, should be magnetically independent. In the random cubic lattice, almost all the magnetic ions have magnetic nearest-neighbours when $x < 0.65$, except for a few small, isolated clusters, and there is certainly no tendency to form large clusters. In an effective field theory, there is a single ordering temperature for each crystallite or large

cluster.

It seems to be unnecessary to go to great lengths to try to find regions of inhomogeneous doping, in view of the result of figure 76. We found there that the central peaks are not paramagnetic, as they would be if the first explanation was correct, but instead they show that either superparamagnetism or short-range order exist near the ordering temperature. In other words, they are not due so much to a range of concentration in the magnetically-ordered regions, as the size of the regions themselves. If the anisotropy is very low, as it is likely to be close to the critical temperature, then the volume of the region may be quite large. At Mössbauer frequencies, the factor τ_0 in (6.1) is critical. However, if it is taken as 10^{-10}, then $|C|v \gtrsim kT$, and particles with dimensions of thousands, or tens of thousands of Angstroms may be superparamagnetic. The clusters which occur naturally in the random lattice cannot explain the behaviour shown in figure 78. If they did, superparamagnetic peaks would only occur in compounds with $x > 0.7$. It is possible that at lower values of x, there may be weak points in the block of connected magnetic ions. For example, in Table 4, two large clusters which are connected by only one superexchange bond are counted as one. A cluster may be better defined as having at least a certain ratio of bonds at its surface to members within, and the ratio chosen should depend on temperature.

There seems to be no reason why the superparamagnetic

regions should necessarily be confined in a particular place in the lattice. They could be continually changing in extent and position, and still give the observed Mössbauer spectra. The explanation in terms of short-range order avoids the need to define magnetically-independent regions in the lattice.

VII Conclusions

Deus dat incrementum

1. SUMMARY.

The local molecular field theory of the cubic lattice with strong nearest-neighbour interactions, and a random distribution of magnetic and non-magnetic ions, was developed to help explain the Mössbauer spectra of diamagnetically substituted magnetic oxides. The theory is likely to be valid when the diamagnetic concentration is less than (N-2)/N, and the temperature is well below the magnetic ordering temperature. In these circumstances, the predicted spectra have the same form as those observed, provided that due account is taken of the different magnetic environments possible for the neighbours of a given magnetic ion, and a small, long-range interaction is included.

The behaviour of the Mössbauer spectrum of the $(Fe_{1-x}Rh_x)_2O_3$ system as a function of temperature for some x, is similar to its behaviour as a function of x at constant temperature. Three regions can be distinguished: At high temperatures, a normal paramagnetic spectrum is seen. At temperatures around and below the magnetic ordering temperature, however defined, mixed spectra occur, which

are a combination of the paramagnetic pattern with a broad, magnetically-split pattern. At yet lower temperatures, the central peaks disappear, and a magnetically-split pattern remains, whose broad lines show some structure. The broadening decreases with decreasing temperature, but persists even at T = 0.

The spectra at the lower temperatures may be explained in terms of the local molecular field theory in a randomly-substituted lattice, provided that a spread of local fields of 8 kOe per magnetic neighbour is permitted at absolute zero. The main source of this spread is the supertransferred hyperfine field, and it was possible to calculate the ferric charge and spin from its numerical value. Two exchange constants were calculated from the hyperfine fields in different magnetic environments, deduced from the room-temperature spectra.

The mixed spectra were studied in some diamagnetically-substituted garnets, and the central peaks were found to be due to small ferrimagnetic clusters with a rapid relaxation time for the net moment. Short-lived magnetic order persists, even when all trace of a magnetically-split spectrum has disappeared. Hence, different criteria for measuring the magnetic ordering temperature give appreciably different results.

Abrupt changes in the quadrupole interaction and the total spectrum shift at the Neel point of members of the $(Fe_{1-x}Rh_x)_2O_3$ system suggest a slight change in the lattice paramaters, associated

with magnetic ordering. The temperature-dependence of the total spectrum shift in $HoFeO_3$ was studied in detail above and below T_N. The small differences between the two regions are best explained in terms of a magnetization-dependent Debye model for the thermal shift. Thus, magnetic order may bring about measurable changes in either the second order Doppler shift or in the isomer shift.

The magnetic polarisation produced by an applied field was observed in the Mössbauer spectrum of both a paramagnetic and a superparamagnetic compound. There should be a 'compensation temperature' in paramagnetic iron salts at which the applied field does not split the spectral lines.

The quadrupole interaction changes sign at the 240°K transition in ferrous perchlorate. A large applied field was also used to resolve the hyperfine patterns in $SrFe_{12}O_{19}$, and to uncover a separate Fe^{3+}(B) spectrum in non-stoichiometric magnetite.

2. SUGGESTIONS for FURTHER WORK.

Most of the following proposed work is an extension or development of the work reported in thesis, although some of it is unrelated.

i) A better study of the geometry of the randomly-substituted lattice, from a magnetic viewpoint, is desirable. The random inhomogeneity, or cluster distribution, should be investigated without the strict requirement of nearest-neighbour interactions.

The magnetic interactions between the ions might be simulated on a computer, and it may be possible to find different magnetic behaviour in different regions of the lattice.

ii) Further tests of the assumption of a random distribution of cations should be made. These are best done from the spectra of compounds in which the iron has only four neighbouring superexchange sites. These sites are occupied by a mixture of magnetic and non-magnetic cations, and the probabilities of the five possible environments may be deduced from the structure of the Mössbauer spectrum. Truly random solid-solutions are most likely between oxides with the same crystal structure and cell dimensions, containing cations of the same valence and ionic radius, for which direct cation-cation interactions are weak.

iii) It may be worthwhile repeating the experiments of chapter IV on a system where there is definitely only one dominant superexchange interaction. The uncertainties about the best approximation to use to fit the data would then be eliminated. Iron-iron interactions could be studied in the distorted pervoskites $La(Fe_{1-x}Rh_x)O_3$, or the spinels $(Fe^{2+}_{1-x}A^{2+}_x)[B^{3+}]_2O_4$ or $(A^{2+})[Fe^{3+}_{1-x}B^{3+}_x]_2O_4$, where both A and B are diamagnetic cations. Ferrous spectra are usually more difficult to analyse than ferric ones, because of their large quadrupole interaction, and it is unfortunate that there are no spinel oxides with Fe^{3+} exclusively on A-sites, and diamagnetic ions on B-sites. These would be the ideal compounds for a study of

A-A interactions, with the aid of the Mössbauer effect.

iv) The compounds $FeRh_2O_4$ and $FeRh_2S_4$ would make a good comparison, if they could be synthesised. If ferrous rhodate is similar to some other transition-metal rhodates, it will show a Jahn-Teller distortion at low temperatures [86, 87]. The tetragonal distortion of the spinel lattice will disappear at higher temperatures, when the distortion presumably becomes dynamic.

v) Apart from further experiments to detect the influence of magnetic order on the total spectrum shift, it would be interesting to make accurate measurements of δ_t as a function of temperature in a para- or diamagnetic compound with a single-line spectrum. If the atomic weight of the Mössbauer ion is quite different from the average atomic weight of an ion in the crystal, it should be possible to see the transition from the short to long-phonon wavelength limits of the second order Doppler shift.

vi) A study of the central peaks found in the Mössbauer spectra of some well-crystallised defect-structure compounds, far below their ordering temperatures, may be illuminating. Fe_7Se_8 and Fe_3S_4 (Smythite)[125] are examples. The central peaks require a quantitative explanation, and the conditions necessary for them to occur should be more precisely characterised than has been possible in the present work.

vii) If a superparamagnetic compound with a uniform grain-size could be produced, it would be interesting to study the

sharpness of the transition from well-ordered to superparamagnetic behaviour. Also the influence of applied fields of the same order of magnitude as the energy barrier should be studied, to see if the superparamagnetic relaxation time increases or decreases.

viii) The final suggestion for further work is a novel application of the Mössbauer effect: to limnology. Not very much is known about the mineralogy of lake sediments, because they are intimate mixtures of dozens of organic and inorganic phases, many of them too poorly crystallised to give good x-ray diffraction patterns. The Mössbauer effect could perhaps identify the iron phases present in the sediment and help to clarify the iron cycle in lakes. Annual redox reactions could also be studied. There is sufficient iron, approximately 5% of the inorganic fraction of the sediments, give good Mössbauer spectra.

References

1. R.L. Mössbauer, Z. Phys., 151, 124 (1958); Naturwiss., 45, 538 (1958); Z. Naturforsch., 14a, 211 (1959).

2. J.R. Gabriel and S.L. Ruby, Nucl. Instr. and Meth. 36 23 (1965)
W. Kündig, ibid, 48, 219 (1967).
L. Dabrowski, J. Piekoszewski and J. Swalski, ibid 91, 93 (1971).

3. S.S. Hanna, J. Heberle, G.J. Perlow, R.S. Preston, and D.H. Vincent, Phys. Rev. Lett., 4, 513 (1960).

4. R.E. Watson and A.J. Freeman, Phys. Rev., 123, 2027 (1961).

5. F. van der Woude, G.A. Sawatzky, and A.H. Morrish, Phys. Rev., 167, 533 (1968).
H.Pinto, G. Shachar and H. Shaked, Solid St. Comm., 8 597 (1970).

6. G.K. Wertheim and J.P. Remeika, Phys. Lett., 10, 14 (1964).
F.E. Obenshain, L.D. Roberts, C.F. Coleman, D.W. Forester and J.O. Thomson, Phys. Rev. Lett., 14, 365.

7. F. van der Woude and A.J. Dekker, Phys. Stat. Sol., 9, 775 (1965).

8. F. van der Woude, Thesis; University of Groningen (1966), Chapter 2.

9. M. Blume, Phys. Rev. Lett., 14, 96 (1965).
M. Blume and J.A. Tjon, Phys. Rev. 165, 446 (1968); ibid, 165, 456 (1968).
M.J. Clauser and M. Blume, Phys. Rev. B, 3, 583 (1971).

10. H.H. Wickman, M.P.Klein and D.A. Shirley, Phys. Rev., 152, 345 (1966).
Moss. Eff. Meth., 2, 39 (1966).

11. L. M. Levinson and M. Luban, Phys. Rev., 172, 268 (1968).

12. H.Schwegler, Phys. Stat. Sol., 41 353 (1970).

13. H. Kofperman, Nuclear Moments, Academic Press, (1958), p. 127.

14. G.A. Sawatzky and J. Hupkes, Phys. Rev. Lett., 25, 100 (1970).

15. J.J. Spijkerman, J.C. Travis, D.N. Pipkorn and C.E. Violet, Phys. Rev. Lett., 26, 323 (1971).

16. M. Tinkham, Group Theory and Quantum Mechanics; McGraw-Hill, (1964) p. 309.

17. R.M.Sternheimer, Phys. Rev., 80, 102 (1950); 84, 244 (1951); 86, 316 (1952); 95, 736 (1954); 105, 158 (1957).

18. P. Zory, Phys. Rev., 140, A1401 (1965).

19. S.L. Ruby and P.A. Flinn, Rev. Mod. Phys., 36, 351 (1964). See also [34].

20. J.B. Goodenough, J. Appl. Phys., 31, 359S (1960); Phys. Rev., 117, 1442 (1960); Magnetism and the Chemical Bond; Interscience (1963), p. 165-84.

21. A.V. Shubnikov and N.V. Belov, Coloured Symmetry; Pergammon Press (1964).
S.C. Miller and W.F. Love, Tables of Irreducible Representations of Space Groups and Corepresentations of Magnetic Space Groups; Pruett Press (1967).

22. E.F. Bertant, Magnetism III; Academic Press (1963), p. 149.

23. G.A. Sawatzky, Thesis; University of Manitoba (1969).

24. R.J. Armstrong, A.H. Morrish and G.A. Sawatzky, Phys. Lett., 23, 414 (1966).

25. J.M.D. Coey, M.R. Spender and A.H. Morrish, Solid St. Comm., 8, 1605 (1970).

26. J.M.D. Coey, A.H. Morrish and G.A. Sawatzky; J. Phys., 32, C1-271. (1971).

27. E.J.W. Verwey, P.W. Haayman and F.C. Romeijn, J. Chem. Phys., 15, 181 (1947).
J.M. Daniels and A. Rosencwaig, J. Phys. Chem. Solids, 30, 1561 (1969); Can. J. Phys., 47, 2309 (1969).

28. K. Yosida and M. Tachiki, Prog. Theor. Phys., 17, 331 (1957).
D. Adler, Solid St. Phys., 21, 4 (1968).
J.R. Cullen and E. Callen, J. Appl. Phys., 41, 879 (1970); Phys. Rev. Lett., 26, 236 (1971).

29. J.S. van Wieringen and J.G. Rensen, Z. Angew. Phys., 21, 69 (1966).

30. R.L. Streever, Phys. Rev., 186, 285 (1969).
K. Hareyama, K. Kohn and K. Uematsu, J. Phys. Soc. Japan, 29, 791 (1970).

31. I. Dezsi and J.M.D. Coey, to be published.

32. I. Dezsi and L. Keszthelyi, Solid St. Comm., 4, 511 (1966).

33. A. Okiji and J. Kanamori, J. Phys. Soc. Japan, 19, 908 (1964).
R. Ingalls, Phys. Rev., 133, A787 (1964).

34. R.L. Collins, J. Chem. Phys., 42, 1072 (1965).
R.L. Collins and J.C. Travis, Moss. Eff. Meth., 3, 123 (1967).

35. M.J. Evans and P.J. Black, J. Phys. C, 3, 2167 (1970).

36. U. Shimony, Nucl. Instr. and Meth., 37, 348 (1965).
M. Celia Dibar Ure; in press, Moss. Eff. Meth., 7 (1971).

37. D.A. Shirley, M. Kaplan and P. Axel, Phys. Rev., 123, 816 (1961).

38. L. Czer, I. Dezsi, I. Gladkih, L. Keszthelyi, D. Kulgawczuk, N.A. Eissa and E. Sterk, Phys. Stat. Sol., 27, 131 (1968).

39. A. Kostikas, A. Simopoulos and N.H.J. Gangas; to be published.

40. W. Hall and T. Wolfram, Phys. Rev., 143, 284 (1966).
D. Hone, C. Callen and L.R. Walker, ibid 144, 283 (1966).

41. M.A. Gilleo, J. Phys. Chem. Solids, 13, 33 (1960).

42. A.H. Morrish, The Physical Principles of Magnetism, Wiley (1965), Chapters 6, 8 and 9.

43. A. Herpin, Théorie du Magnétisme, Presses Universitaires de France (1968), p. 242.

44. M. Kao, in Proceedings of the Brandeis Institute in Theoretical Physics, New York (1968), and Proceedings of the N.A.T.O. Summer School in Mathematical Physics, Istanbul (1970).

45. P.W. Anderson, Phys. Rev., 86, 694 (1952); Concepts in Solids, Benjamin (1963) p. 175.

46. S.W. Lovesey, J. Phys. C, 1, 408 (1968).

47. H.P. van de Braak, Physica, 42, 137 (1969).

48. J. Solyom and J. Bergou; J. Phys. 32, C1-89 (1971).

49. H.P. van de Braak and W.J. Caspers, Phys. Stat. Sol., 24, 733 (1967).

50. J. Owen and D.R. Taylor, Phys. Rev. Lett., 16, 1164 (1966).
N.L. Huang, R. Orbach and E. Simanek, Phys. Rev. Lett., 17, 134 (1966); Phys. Rev., 156, 383 (1967).

51. S. Sugano and R.G. Shulman, Phys. Rev., 130, 517 (1963).

52. K.P. Belov and I.S. Lyubutin, J.E.T.P. Lett., 1, 16 (1965).
B.J. Evans, Moss. Eff. Meth., 4, 139 (1968).

53. I. Nowik, E.R. Bauminger, J. Hess. A. Mustachi and S. Ofer, Phys. Lett., 34A, 155 (1971).

54. E. Simanek and Z. Sroubek, Phys. Rev., 163, 275 (1967).

55. F. van der Woude and G.A. Sawatzky; to be published.

56. J. Owen and J.H.M. Thornley, Rep. Prog. Phys., 29, 675 (1966).

57. I. Dezsi, G. Erlaki and L. Keszthelyi, Phys. Stat. Sol., 21, K121 (1967); I. Vincze, L. Czer and D.L. Nagy, Phys. Stat. Sol., 37, K51 (1970).

58. J.M. Trooster and A. Dymanus, Phys. Stat. Sol., 24, 487 (1967).

59. D.C. Dobson, J.W. Linnett and M.M. Rahman, J. Phys. Chem. Solids, 31, 2727 (1970).

60. G.A. Sawatzky, F. van der Woude and A.H. Morrish, Phys. Rev., 187, 747 (1969).

61. P. Raj and S.K. Kulshreshtha, J. Phys. Chem. Solids, 31, 9 (1970).

62. J.M. Daniels and A. Rosencwaig, Can. J. Phys., 48, 381 (1970).

63. P. Bratinka, Internal Report of the Reactor Institute, Delft (1969).

64. J.M.D. Coey, to be published.

65. E. Kren, P. Szabo and G. Konczos, Phys. Lett., 19, 103 (1965).

66. G. Lunde, Z. Anorg. Allg. Chem., 163, 345 (1927).

67. N.V. Belov, Akad. Nauk. S.S.R., Izvestia Sektor Platiny i Drugich Blagorodnych Metallov, 18, 113 (1945).

68. R.L. Blake, L.W. Finger and T. Zoltai; cited in [92].

69. R.D. Shannon and C.T. Prewitt, J. Solid St. Chem., 2, 134 (1970).

70. A. Wold, R.J.Arnott and W.J. Croft, Inorg. Chem., 2, 972 (1963).

71. H.T. Evans, Acta Cryst., 14, 689 (1961).

72. R.L. Blake, R.E. Hessevick, T. Zoltai and L.W. Finger, Amer. Min. 51, 123 (1966).

73. R.E. Newnham and Y.M. de Haan, Z. Krist., 117, 235 (1962). M. Marezio and J.P. Remeika, J. Chem. Phys., 46, 1862 (1967).

74. C.T. Prewitt, R.D. Shannon, D.B. Rogers and A.W. Sleight, Inorg. Chem., 8, 1985 (1969).

75. A.N. Guthrie and L.T. Bourland, Phys. Rev., 37, 303 (1931).

76. C.W. Searle and G.W. Dean, Phys. Rev. B, 1, 4337 (1970); and C.W. Searle, private communication.

77. A.H. Morrish and J.A. Eaton, J. Appl. Phys., 42, 1495 (1971).

78. M.A. Gilleo, Phys. Rev., 109, 777 (1958).

79. E.J. Samuelsen and G. Shirane, Phys. Stat. Sol., 42, 241 (1970); J. Phys., 32, C1-1064 (1971).

80. F. van der Woude, Phys. Stat. Sol., 17, 417 (1966).

81. J. Schrage and W.G. Perdok, to be published.

82. J.S. Smart, Effective Field Theories of Magnetism, Saunders (1966), p. 43.

83. D. Schroeer and R.C. Nininger, Phys. Rev. Lett., 19, 632 (1967). V. Yamamoto, J. Phys. Soc. Japan, 24, 23 (1968).

84. R. Brout, Phys. Rev., 115, 824 (1959).

85. G.A. Murray, Proc. Phys. Soc., 89, 111 (1966).

86. G. Blasse and D.J. Schipper, Phys. Lett., 5, 300 (1963); G. Blasse, Philips Res. Repts., 18, 383 (1963).

87. F. Bertaut, F. Forrat and J. Dulac, Comptes Rendus, 249, 726 (1959). S. Miyahara and S. Horiuti, Proc. Int. Conf. Magnetism, Nottingham, I.P.P.S. (1964) p. 550; J. Phys. Soc. Japan, 19, 423 (1964).

88. G. Blasse, Phys. Lett., 19, 110 (1965).

89. R.E. Watson, Phys. Rev., 111, 1108 (1958).

90. R.E. Watson, private communication.

91. E. Clementi, IBM J. Res. Develop., 9, 2 (1965).

92. J.O. Artman, A.H. Muir and H. Wiedersich, Phys. Rev., 173, 337 (1968).

93. G.A. Sawatzky, F. van der Woude and J. Hupkes; J. Phys., 32, C1-276 (1971).
R.R. Sharma, Phys. Rev. Lett., 26, 563 (1971).

94. R.S. Preston, S.S. Hanna and J. Heberle, Phys. Rev., 128, 2207 (1962).

95. R.S. Preston, Phys. Rev. Lett., 19, 75 (1967); J. Appl. Phys., 39, 1231 (1968).

96. S. Alexander and D. Treves, Phys. Lett., 20, 134 (1966).
R. Ingalls, Phys. Rev., 155, 157 (1967).

97. J.M.D. Coey, G.A. Sawatzky and A.H. Morrish, Phys. Rev., 184, 334 (1969).

98. J.M.D. Coey and G.A. Sawatzky; in press, J. Phys. C, (1971).

99. L.R. Walker, G.K. Wertheim and V. Jaccarino, Phys. Rev. Lett., 6, 98 (1961).

100. V.I. Goldanskii, Proc. Dubna Conf. Moss. Eff., Consultants Bureau (1963) p. 17.

101. E. Šimaněk and Y.C. Wong, Phys. Rev., 166, 348 (1968).

102. J.J. Spijkerman, F.C. Ruegg and L. May, Moss. Eff. Meth., 2, 85 (1966).

103. C.L. Herzenberg, Moss. Eff. Meth., 5, 209 (1969).

104. G.K. Wertheim, J.P. Remeika and H.J. Guggenheim, to be published.

105. R.V. Pound and G.A. Rebka, Phys. Rev. Lett., 4, 274 (1960).

106. B.D. Josephson, Phys. Rev. Let., 4, 341 (1960).

107. M. Eibschütz, S. Shtrikman and D. Treves, Phys. Rev., 156, 562, (1967).

108. A.J.F. Boyle, D. St. P. Bunbury, C. Edwards and H.E. Hall, Proc. Phys. Soc., 77, 129 (1961).

109. Y.A. Iosilevskii, J.E.T.P., 27, 495 (1968).

110. G.A. Sawatzky, F. van der Woude and A.H. Morrish, Phys. Rev., 183, 383 (1969).

111. G.K. Wertheim, D.N.E. Buchanan and H.J. Guggenheim, Phys. Rev. B, 2, 1392 (1970).

112. S.S. Bashkirov and G.Y. Selyutin, Phys. Stat. Sol., 26, 253 (1968).

113. P. Coppens and M. Eibschütz, Acta Cryst., 19, 524 (1965).

114. J. Chappert and P. Imbert, J. Phys. 24, 412 (1963).

115. G. Gorodetsky and D. Treves, Proc. Int. Conf. Magnetism, Nottingham, I.P.P.S. (1964) p. 606.

116. A.H. Bobeck, Bell. Sys. Tech. J., 46, 1901 (1967).
W. Strauss, J. Appl. Phys., 42, 1251 (1971).

117. M. Eibschütz, Acta Cryst., 19, 337 (1965).

118. R. Kubo, Phys. Rev., 87, 568 (1952).

119. H.E. Stanley, Introduction to Critical Phenomena, OUP (1971).

120. G.K. Wertheim, H.J. Guggenheim and D.N.E. Buchanan, Phys. Rev., 169, 465 (1968).

121. A. Berton and B. Sharon, J. Appl. Phys. 39, 1367 (1968).

122. S.S. Bashkirov, G.Y. Selyutin and V.A. Chistyakov, Sov. Phys. Doklady, 13, 449 (1968).

123. A. Guinier, X-Ray Diffraction in Crystals, Imperfect Crystals and Amorphous Bodies, Freeman (1963) p. 189.

124. F. van der Woude and A.J. Dekker, Phys. Stat. Sol., 13, 181 (1966).
C.E. Johnson, J. Phys. C., 2, 1996 (1969).

125. E.F. Makarov, A.S. Marfunin, A.R. Mkrtchyan, G.N. Nadzharyan, V.A. Povitskii and R.A. Stukan, Sov. Phys. Sol. St., 11, 391 (1969).

126. U. Bertelsen, J.M. Knudsen and H. Krogh, Phys. Stat. Sol., 22, 59 (1967).

127. L.M. Levinson, M. Luban and S. Shtrikman, Phys. Rev., 177, 864 (1969).

128. L. Neel, Comptes Rendus 228, 664 (1949); Ann. Geophys., 5, 99 (1949); Adv. Phys., 4, 191 (1955).

129. T. Shinjo, J. Phys. Soc. Japan, 21, 917 (1966).

130. D.W. Collins, J.T. Dehn and L.N. Mulay, Moss. Eff. Meth., 3, 102 (1967).
M. Eibschütz and S. Shtrikman, J. Appl. Phys., 39, 997 (1968).
R.H. Lindquist, G. Constabaris, W. Kündig and A.M. Portis, ibid, 39, 1001 (1968).
U. Gonser, H. Wiedersich and R.W. Grant, ibid, 39, 1004 (1968).
A.M. van der Kraan, J. Phys., 32, C1-1034 (1971).

131. I.S. Jacobs and C.P. Bean, Magnetism III, Academic Press (1963) p. 271.

132. A. Aharoni, Phys. Rev., 135, A447 (1964).

133. A.H. Morrish, The Physical Principles of Magnetism, Wiley (1965) p. 310-21.

134. A.H. Morrish, op. cit. p. 429.

135. A. Aharoni, Phys. Rev., 177, 793 (1969).

136. A.N. Buckley, B.D. Rumbold, G.V.H. Wilson and K.S. Murray, J. Chem. Soc., (A) (1970), 2298.

137. F. Bitter, Phys. Rev., 38, 1903 (1931).
J.A. Eaton, Thesis, University of Manitoba (1970).

138. S. Chikazumi, Physics of Magnetism, Wiley (1964).

139. C. Alff and G.K. Wertheim, Phys. Rev., 122, 1414 (1961).
J.J. van Loef, J. Appl. Phys., 39, 1258 (1968).

140. S. Geller, J. Appl. Phys., 31, 30S (1960).

FOOTNOTES.

1. Elscint Ltd., P.O.B. 5258, Haifa, Israel.

2. Nuclear Data Inc., P.O.B. 451, Palatine, Illinois, U.S.A.

3. New England Nuclear Corporation, 575 Albany Street, Boston, Massachusetts, U.S.A.

4. 20th Century Electronics Ltd., King Henry's Drive, New Addington, Surrey, England.

5. Harshaw Chemie N.V., de Meern, Holland.

6. Westinghouse Electric Corporation, Cryogenic Systems Department, Pittsburgh 35, Pennsylvania, U.S.A.

7. Perfection Mica Company, 740 Thomas Drive, Berserville, Illinois, U.S.A.

8. Made by SODERN, 10 rue de la Passerelle, Suresnes (Seine), France.

9. Made by N.V. Philips' Gloeilampenfabrieken, Eindhoven, Holland.

10. Made by Princeton Applied Research Corporation, Princeton, New Jersey, U.S.A.

11. Obtained from Alpha Inorganics, 8 Congress Street, Beverly, Massachusetts, U.S.A.

12. Produced by Oak Ridge National Laboratory, Oak Ridge, Tennessee, U.S.A.

13. Prepared by American Potash and Chemical Corporation, 258 Ann Street, West Chicago, Illinois, U.S.A.

14. Prepared by Johnson Matthey Chemicals Ltd., 74 Hatton Garden, London E.C.1, England.